

Advanced X-ray Analytical Methods for the Characterization of Buried Interfaces with Relevance for Energy Conversion Devices

vorgelegt von

Master of Science

Jonas Baumann

geboren in Berlin

von der Fakultät II - Mathematik und Naturwissenschaften

der Technischen Universität Berlin

zur Erlangung des akademischen Grades

Doktor der Naturwissenschaften

Dr. rer. nat.

genehmigte Dissertation

Promotionsausschuss:

Vorsitzender: Prof. Dr. Norbert Esser

Gutachterin: Prof. Dr. Birgit Kanngießer

Gutachter: Prof. Dr. Klaus Rademann

Tag der wissenschaftlichen Aussprache: 30. August 2017

Berlin 2017

Contents

Abstract	1
Zusammenfassung	2
1. Introduction	3
2. Methodological Bases	7
2.1. X-ray Fluorescence Analysis	7
2.1.1. Calculation of Fluorescence Intensities	8
2.1.2. Quantification Approaches	9
2.2. Grazing Incidence and Grazing Emission XRF	10
2.2.1. The Complex Refractive Index	13
2.2.2. Shallow Excitation	13
2.2.3. Shallow Detection	17
2.3. Scanning-Free GEXRF	19
2.3.1. Single Photon Counting with a CCD - Energy Resolution	19
2.3.2. Geometry Considerations - Angular Resolution	23
2.4. Software for (AR)XRF Evaluation	26
2.4.1. xrfLibrary and xrlfupa for X-ray Fluorescence Calculations	26
2.4.2. Depth Profiling	28
2.5. Soft X-rays in Scanning-Free GEXRF Analysis	30
2.5.1. Application of Soft X-rays	30
2.5.2. Production of Soft X-rays	31
3. Thermoelectric Nanofilms	35
3.1. Sample Preparation and Surface Characterization	35
3.2. Investigation of Lateral Homogeneity by means of Laboratory-based XRF	37
4. Synchrotron Radiation based Analysis	43
4.1. Instrumentation	43
4.1.1. Beamlines	43
4.1.2. Endstations	44

CONTENTS

4.2. Data Recording and Treatment	45
4.3. Integral Quantification	48
4.4. Qualitative GIXRF-NEXAFS	52
4.5. Depth Profiling with GIXRF	57
4.5.1. 1-Layer Model	61
4.5.2. <i>N</i> -Layer Model	63
4.5.3. <i>N</i> -Layer Model with Contamination	68
5. Development of Laboratory Scanning-Free Soft X-ray GEXRF	77
5.1. Grazing Incidence vs. Grazing Emission XRF Spectrometer Concept . . .	78
5.2. Principle Setup	80
5.2.1. Laser-Produced Plasma Source	81
5.2.2. Multilayer Optics	83
5.2.3. Spectroscopy Chamber	85
5.2.4. Charged Coupled Device	86
5.2.5. Alignment Procedures	86
5.3. Calibration of the Angular Scale	94
5.3.1. Calibration with GEXRF profile	95
5.3.2. Absolute Angular Calibration	96
5.4. Single Photon Analysis	100
5.4.1. Split Event Recombination	102
5.4.2. Numerical Simulations	108
5.5. Compilation of GEXRF Profiles	116
5.5.1. Region of Interest Method	116
5.5.2. Spectra Deconvolution Method	116
6. Feasibility Study of Laboratory Scanning-Free Soft X-Ray GEXRF	119
6.1. Multilayer Sample	119
6.1.1. Structure Analysis with Complementary Methods	120
6.1.2. GEXRF Simulations	122
6.2. First Beamtime - Proof of Principle	125
6.2.1. Setup Description and Alignment	125
6.2.2. Data Recording and Image Processing	129
6.2.3. Integral XRF Spectrum	130
6.2.4. Angular Calibration	133
6.2.5. GEXRF Profiles	136
6.3. Second Beamtime - Setup Development and Characterization	143
6.3.1. Setup Development	143

6.3.2. Measurement Stability and Reproducibility	144
6.3.3. GEXRF Profiles of the C/Ni-multilayer	151
6.3.4. GEXRF Profiles of Thermoelectric Nanofilms	159
7. Summary	167
7.1. Methodological Development of the Laboratory Scanning-Free GEXRF Setup	168
7.2. Thermoelectric Nanofilms	170
7.3. Future Perspective	174
Appendix	175
A. Angular Limits of the Sherman Equation	176
B. Atomic Force Micrographs of the Silicon Substrate for the Thermoelectric Nanofilms	177
C. Estimation of Uncertainties for Fluorescence Calculations	177
D. Effective Solid Angle of Detection for an Off-Axis Sample Surface	178
E. Estimation of Efficiency of GI- and GEXRF Spectrometer Concepts	179
F. Effect of Tilted CCD on Distance Calculation	181
G. Study on the Influence of Noise Thresholds on CCD Spectra using the Clustering Method	182
H. Simulated Intensity Distribution of SPEs on a CCD Mesh	184
I. Choose ROIs	185
J. Sample Alignment with a CCD	186
List of Figures	191
List of Tables	193
Nomenclature	195
Bibliography	210
Danksagung	213

Abstract

The efficiency of devices for novel renewable energy sources, like solar cells and thermo-electric generators (TEGs), is strongly increasing since the advent of nanotechnology. Synchrotron radiation-based advanced X-ray fluorescence (XRF) techniques, like grazing emission (GE-) or grazing incidence (GI-) XRF, offer non-destructive and quantitative access to elemental depth profiles in the nanometer range. Using soft instead of hard X-rays not only increases the sensitivity for light elements, but also enhances depth-resolving capabilities due to the stronger attenuation of the radiation. Clearly, material research could be accelerated by a better availability of those methods, which demands the development of an efficient laboratory setup.

In this thesis, the first X-ray fluorescence spectroscopy measurements by excitation with a laser-produced plasma (LPP) source are presented. Moreover, the highly brilliant source allowed to design a spectrometer concept, which enables laboratory-based, scanning-free GEXRF measurements in the soft X-ray range for elemental depth profiling of nano-scaled materials.

The scanning-free GEXRF approach requires a precise calibration of the measurement geometry and the accurate evaluation of single photon events to exploit the properties of two-dimensional, energy-dispersive detectors. Both is achieved in this thesis, leading to excellent angular and good energy resolution of the GEXRF measurements. The spectrometer concept is validated by evaluation of the Kossel lines in the GEXRF profile of a C/Ni-multilayer sample.

Furthermore, the setup is applied to the characterization of gold-doped copper oxide nanofilms, which can be used in TEGs. The sample structure is thoroughly characterized by various XRF measurements in the laboratories of the Physikalisch Technische Bundesanstalt at the synchrotron radiation facility BESSY II in Berlin. Complementary measurements with the laboratory scanning-free GEXRF setup show similar results obtained in comparable measurement times with respect to SR-based GIXRF. This demonstrates the feasibility of the spectrometer concept for elemental depth profiling of samples with relevance for renewable energy sources.

Zusammenfassung

Seit der Anwendung von Nanotechnologien in Geräten zur Nutzung erneuerbarer Energiequellen, wie Solarzellen oder thermoelektrische Generatoren (TEG), konnte deren Effizienz stark gesteigert werden. Die Nutzung hochentwickelter, auf Synchrotronstrahlung (SR) basierender Röntgenfluoreszensanalyse (RFA), wie GIXRF oder GEXRF (engl.: grazing incidence bzw. grazing emission X-ray fluorescence analysis) ermöglicht es, Elementtiefenprofile mit Auflösungen im Bereich von Nanometern zerstörungsfrei und quantitativ zu bestimmen. Wird weiche statt harter Röntgenstrahlung genutzt, erhöht dies die Sensitivität für leichte Elemente und verbessert die Tiefenauflösung der Messmethode durch die stärkere Absorption der Strahlung. Die Entwicklung effizienter Laborgeräte für diese Analysemethoden ist Voraussetzung für eine verbreiterte Nutzung derselben, wodurch die Entwicklungsprozesse neuer Materialien beschleunigt würden.

In der vorliegenden Arbeit werden die ersten RFA-Messungen unter Anregung mit einer laserinduzierten Plasmaquelle (LPQ) vorgestellt. Zudem wird diese hochbrillante Quelle für weiche Röntgenstrahlung genutzt, um ein laborbasiertes, scanfreies GEXRF-Spektrometer zu entwerfen, welches die Elementtiefenprofilierung von nanoskaligen Materialien ermöglicht.

Damit die Eigenschaften des verwendeten zweidimensionalen, energiedispersiven Detektors im scanfreien GEXRF-Aufbau voll ausgenutzt werden können, muss die Messgeometrie exakt bekannt und müssen Einzelphotonenereignisse präzise auswertbar sein. Beides wird in dieser Arbeit erreicht und führt zu einer sehr guten Winkel- und einer guten Energieauflösung. Das Spektrometerkonzept wird durch die Messung von Kossel-Linien in den GEXRF-Profilen einer C/Ni-Vielschichtprobe validiert.

Weiterhin wird das Spektrometer für die Untersuchung von golddotierten Kupferoxid-nanoschichten genutzt, welche in TEGs Anwendung finden können. Die Proben werden mit verschiedenen SR-basierten RFA-Methoden in den Laboren der Physikalisch Technischen Bundesanstalt bei BESSY II in Berlin charakterisiert. Die komplementären Messungen mit dem scanfreien GEXRF-Spektrometer ergeben bei vergleichbaren Messzeiten ähnliche Ergebnisse zu den SR-basierten GIXRF Messungen. Dies demonstriert erfolgreich die Anwendbarkeit des Spektrometers für Elementtiefenprofilierung von Proben, welche relevant für die Gewinnung von erneuerbaren Energien sein können.

1. Introduction

The United Nations Intergovernmental Panel on Climate Change (IPCC), established in 1988, is gathering and summarizing the scientific findings concerning climate change and its impacts. While clear evidence of anthropogenic influence on global climate could not be provided in the first Assessment Reports [1, 2, 3], climate modeling and the necessary scientific data improved over the decades. In their Fourth Assessment Report, published in 2007, the IPCC states that global warming is unequivocal and most of the observed global average temperature increase is caused by increased anthropogenic greenhouse gas concentrations [4]. Especially CO₂ from fossil fuel use plays a major role in the global anthropogenic greenhouse gas emissions, which is why renewable energy sources have been found to be an important part in greenhouse gas mitigation [5, 6].

Nano-scaled materials, like nanoparticles, nanowires, nano-structured films or nano-films, show significant differences in their physical and chemical properties with respect to bulk materials on the one hand or single atoms and molecules on the other hand. Furthermore, by precisely controlling the shape, structure or composition of these materials, the properties can often be adjusted to desired applications. Nanotechnology led to recent advancements with respect to efficiency, cost and stability of renewable energy sources like photovoltaics [7] and thermoelectric generators [8], thus being valuable for greenhouse gas mitigation strategies.

Understanding of nanomaterial properties must be accompanied by precise analytics, providing structural, compositional and chemical information on the nanometer scale. For the investigation of processing accuracy, stability or diffusion processes of buried interfaces or dopant profiles, invasive methods, like secondary ion mass-spectrometry (SIMS), transmission electron microscopy (TEM) or glow-discharge optical emission spectrometry (GD-OES), are frequently used [9, 10, 11]. One drawback is clearly the sample consumption. This prohibits repeated measurements on the same sample or direct comparison with complementary methods, which is “necessary for unambiguous and quantitative elemental distribution analysis of a thin film with unknown compositional in-depth distribution” [12].

X-ray fluorescence analysis (XRF) provides non-destructive and quantitative access to elemental compositions. However, analysis of nanomaterials is challenging due to

1. INTRODUCTION

typical attenuation lengths in the micrometer range and high demands on efficient X-ray optics for beam shaping. One possibility to overcome these limitations is the application of shallow excitation or detection schemes in advanced XRF analytical methods, i.e. grazing incidence (GI-) and grazing emission (GE-) XRF. Both methods can be used to analyze in-depth elemental profiles in the nanometer range, as was demonstrated for example by the analysis of CIGSe absorber layers of thin film solar cells [13], transparent conductive multilayer systems [14] or by metal thin film studies [15, 16].

To efficiently investigate light elements and increase depth-sensitivity, soft X-rays are preferable with respect to hard X-rays, because of larger photoionization cross sections and decreased attenuation lengths. In this energy range, the investigation of dopant profiles in ultra-shallow junctions [17, 18], sub-nanometer layers in transistor gate stacks [19] or nanoparticle analysis [20] was rendered possible by using 3rd generation synchrotron radiation. Yet, the need to apply for beamtimes delays the feedback time of analytical results in the development process of novel materials. Thus, readily available laboratory analysis improves research and development cycles and can reduce timescales for new technological inventions, which might e.g. help for future greenhouse gas mitigation.

As a second aspect, the wider the availability of a methodology, the faster is the advancement of the methodology itself. In GIXRF and GEXRF, evaluation strategies for quantitative analysis of depth profiles are still maturing and no best procedure for an arbitrary sample system exists*. Especially, providing reliable uncertainties in depth profiles is difficult, since the direct inversion of the measured angular profiles to depth profiles is an ill-posed problem and modeling strategies are applied. A better understanding of quantitative approaches with GIXRF and GEXRF will further improve the impact of the method.

In this thesis, a laboratory scanning-free GEXRF setup working in the soft X-ray range is developed, characterized and applied for depth profiling applications. To achieve the transfer of a synchrotron method to the laboratory, the lower brilliance of available laboratory sources requires highly efficient concepts in the excitation and detection channel. The developed spectrometer utilizes the laser-produced plasma (LPP) source at the Berlin Laboratory of Innovative X-ray Technologies (BLiX) in combination with focusing reflective multilayer mirrors, which allows efficient excitation in GEXRF geometry. Instead of the typically applied wavelength-dispersive detectors in (laboratory) GEXRF setups [21, 22, 23], the concept of scanning-free GEXRF [24] with a two-dimensional, energy-dispersive detector is applied to increase the overall solid angle of detection and

* Probably, a general method for arbitrary samples would scarcely be used. The usually applied fitting routines are much more robust with boundaries applied to the parameters and by limiting the number of parameters. Thus, prior knowledge, which strongly depends on each individual sample, is frequently applied.

dynamic range of the energy scale.

Further gain in efficiency is achieved by small sample-to-detector distances, which on the other hand demand an accurate angular calibration, to account for geometric effects of the distribution of fluorescence emission angles on the flat detector plane. This is achieved by accurately describing and measuring the whole detection geometry and precise setup and sample alignment. The developed methodologies allow the determination of an absolute angular calibration without the need of reference samples and show excellent reproducibility and high accuracy. The procedures are tested and validated with GEXRF measurements on a well-defined C/Ni-multilayer sample.

Moreover, a test of the applicability of the setup and methodology is performed on thermoelectric samples as scientific case with relevance for renewable energy sources. In the research group of Prof. K. Rademann at the department of chemistry of the Humboldt University of Berlin, gold-doped copper oxide nanofilms are tested for their applicability as thermoelectric generators. These regenerative energy devices convert temperature gradients to electrical power without the need of movable parts. They can be applied e.g. as energy source in wearable electronics [25] or for recuperation of thermal waste energy [26, 27].

In a first step, the thermoelectric samples are thoroughly characterized by synchrotron radiation-based near edge X-ray absorption fine structure (NEXAFS) and quantitative reference-free GIXRF measurements in the laboratories of the Physikalisch Technische Bundesanstalt (PTB) at the synchrotron radiation facility BESSY II. Then, GEXRF analysis of the sample system with the developed laboratory setup is performed. The results allow direct comparison between the synchrotron radiation-based GIXRF and the laboratory GEXRF methodologies and show the feasibility of elemental depth profiling of nano-scaled materials with the laboratory setup. Thus, the developed spectrometer can help in research for, amongst others, new materials with relevance for greenhouse gas mitigation.

2. Methodological Bases

2.1. X-ray Fluorescence Analysis

When an X-ray photon interacts with an atom, it can be scattered or absorbed and the probabilities of each process depend strongly on the atom number Z and the energy of the incident X-ray photon. While the cross sections for Rayleigh scattering, where the X-ray photon energy is preserved (elastic scattering), are larger for soft X-rays, Compton scattering cross sections (inelastic scattering) increase with higher photon energy and are more prominent in the hard X-ray regime. However, the interaction of X-rays with energies up to 100 keV with matter is dominated by photoionization. In this case, the photon energy E_{pr} is completely transferred to the atom and an inner shell electron with a kinetic energy $E_{\text{kin}} = E_{\text{pr}} - E_B$, where E_B is the binding energy of the electron in the atom, is ejected from the system. The excited atom goes now through a number of relaxation processes, where the initial core hole is filled with an electron from an upper shell and thus gradually moving towards the outer shells. During this cascade, radiative and non-radiative relaxation processes compete against each other.

Radiative transitions are most efficient for dipole transitions. For these, the selection rules imply that the quantum numbers of the atomic system must change according to $\Delta l = \pm 1$ and $\Delta j = 0, \pm 1$, with the orbital quantum number l and the total angular momentum j . This simplifies the observed X-ray spectrum and allows usually a direct assignment of element and transition specific fluorescence lines, making X-ray fluorescence (XRF) analysis sensitive to elemental compositions. Figure 2.1 exemplarily shows the possible dipole transitions and line assignments in the Siegbahn notation for copper. It has to be noted that also satellite lines with much lower intensities, which originate from quadrupole transitions, can appear in an X-ray spectrum.

In a non-radiative relaxation, the released energy can be transferred to an electron, which again leaves the atomic system. This is known as Auger effect and the electron is called Auger electron. In the special case that the core hole of an L-shell (or energetically higher shell) is filled with an electron from the same shell (but different subshell), the process is referred to as Coster-Kronig transition [28].

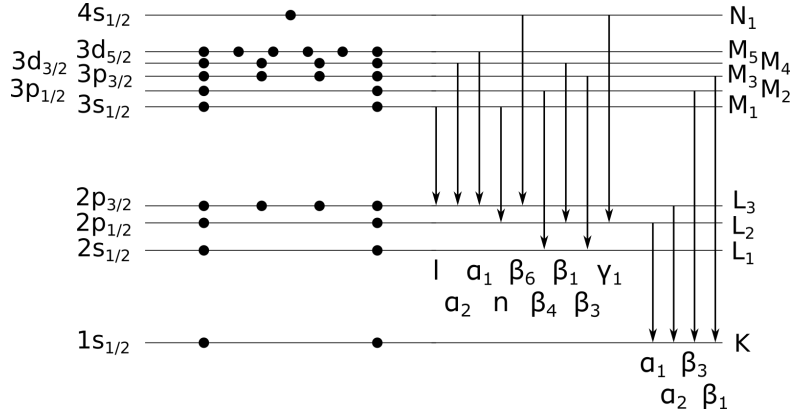


Figure 2.1.: Electron configuration and X-ray transitions for Cu. Only the allowed dipole transitions, i.e. which satisfy $\Delta l = \pm 1$ and $\Delta j = 0, \pm 1$, are shown.

2.1.1. Calculation of Fluorescence Intensities

Considering the case of a homogeneous layer, which is irradiated with a monochromatized, collimated X-ray beam, a fluorescence intensity of that layer, recorded by a suitable detector, can be calculated by the Sherman equation [29]. Here, the form as it is derived in [30] for primary, monochromatic excitation is given.

$$\begin{aligned}
 N_{i,j} &= N_{\text{pr}}(E_{\text{pr}}) G(E_{i,j}) \xi_{i,j,s}(E_{\text{pr}}) \rho C_i \int_0^d \exp(-\mu_{\text{tot}}^*(E_{\text{pr}}, E_{i,j}) \rho x) dx, \\
 &\text{with} \\
 G(E_{i,j}) &= \epsilon_{\text{det}}(E_{i,j}) \frac{\Omega}{4\pi \sin(\psi_{\text{pr}})} \\
 \xi_{i,j,s}(E_{\text{pr}}) &= \tau_{i,s}(E_{\text{pr}}) \omega_{i,s} p_{i,j} \\
 \mu_{\text{tot}}^* &= \frac{\mu_{\text{tot}}(E_{\text{pr}})}{\sin(\psi_{\text{pr}})} + \frac{\mu_{\text{tot}}(E_{i,j})}{\sin(\psi_{\text{fl}})}
 \end{aligned} \tag{2.1.1}$$

In Equation 2.1.1, $N_{i,j}$ is the count rate of detected fluorescence photons from transition j of element i . $N_{\text{pr}}(E_{\text{pr}})$ refers to the count rate of primary photons of energy E_{pr} irradiating the sample and $G(E_{i,j})$ accounts for the proportionality to most geometric parameters, combining the detector efficiency $\epsilon_{\text{det}}(E_{i,j})$, the normalized solid angle of detection $\Omega/4\pi$ and the incident angle of the primary radiation with respect to the sample surface ψ_{pr} . The photo production cross section $\xi_{i,j,s}(E_{\text{pr}})$ describes the fraction of produced fluorescence photons on the atomic scale. It is the product of the photoionization cross section $\tau_{i,s}(E_{\text{pr}})$ of subshell s with the fluorescence yield $\omega_{i,s}$ and the transition probability $p_{i,j}$. The integration variable x is the position along the layer surface nor-

mal and is varied in the integral from surface ($x = 0$) to d , where d is the thickness of the layer with density ρ and total mass attenuation coefficient of the layer μ_{tot} . The latter sums the cross sections of the possible photon-matter interaction processes, i.e. $\mu_{\text{tot}} = \tau + \sigma_{\text{coh}} + \sigma_{\text{inc}}$, with τ the photoionization cross section and σ_{coh} and σ_{inc} the cross sections for coherent and incoherent scattering. The integrand $\mu_{\text{tot}}^*(E_{\text{pr}}, E_{i,j})\rho x$ describes the attenuation due to Lambert-Beer's law of the incident primary photons up to a depth x and of the emitted fluorescence photons from depth x at an angle ψ_{fl} with respect to the sample surface.

The Sherman equation can be extended for polychromatic excitation by integrating over E_{pr} and for secondary fluorescence, i.e. X-ray fluorescence which follows after absorption of an initial fluorescence photon. In this thesis, secondary fluorescence enhancement is negligible, since the layer thicknesses of the analyzed samples are well below 100 nm [31]. However, details of the adapted formulas can be found e.g. in [31] or [30].

2.1.2. Quantification Approaches

Quantification of the composition of a bulk sample can be accomplished by using a calibration curve. In this case, X-ray fluorescence intensities of standards made from reference materials with accurate knowledge about the composition are measured. The dependency of the fluorescence intensities of an element and its concentration is the calibration curve, which should yield a linear relation in first approximation. Then, the concentrations of analytes in an unknown sample with similar composition, surface properties and microstructure can be directly determined by using the same measurement procedure as for the standards and interpolation of the calibration curve.

However, whenever (certified) reference materials are rare, which is e.g. the case for thin layers or novel nanomaterials, quantification methods based on fundamental parameters (FPs) and the Sherman equation become necessary. First, Equation 2.1.1 is considered again. The integral can actually be solved, which yields

$$N_{i,j} = N_{\text{pr}}(E_{\text{pr}}) G(E_{i,j}) \xi_{i,j,s}(E_{\text{pr}}) C_i \frac{1 - \exp(-\mu_{\text{tot}}^*(E_{\text{pr}}, E_{\text{fl}})\rho d)}{\mu_{\text{tot}}^*(E_{\text{pr}}, E_{\text{fl}})} . \quad (2.1.2)$$

Thus, the number of detected fluorescence photons can be correlated to the concentration C_i and the total mass deposition $\hat{m} = \rho d$. In the case of a single element layer, the mass deposition of that element can be directly computed with

$$\hat{m} = -\frac{1}{\mu_{\text{tot}}^*(E_{\text{pr}}, E_{\text{fl}})} \times \ln \left(1 - \frac{N_{i,j} \mu_{\text{tot}}^*(E_{\text{pr}}, E_{\text{fl}})}{N_{\text{pr}}(E_{\text{pr}}) G(E_{i,j}) \xi_{i,j,s}(E_{\text{pr}})} \right) . \quad (2.1.3)$$

2. METHODOLOGICAL BASES

As can be seen, if all geometric parameters of the setup and all FPs are known, the latter taken usually from databases like [32] or [33], the mass deposition of the single layer can be calculated without standards or references materials.

Such a reference-free quantification approach is e.g. used in Chapter 4 with the fully calibrated instrumentation of the Physikalisch Technische Bundesanstalt (PTB). In commercial XRF devices, like the one used in Chapter 3, often a FP based, standardless quantification is implemented. In this case, fundamental parameters from data bases are also used, but the instrumental parameters are determined by a calibration of the instrument with calibration samples. These calibrations samples do not need to be standards and thus do not need to be similar to the unknown samples, which are to be analyzed.

The reference-free and standardless quantifications can also be applied, when analyzing samples with more than one element in a single layer (e.g. alloys). Then, Equation 2.1.2 becomes a set of non-linear equations. These equations can be solved with various influence coefficients methods [30], where deviations from the linear correlation between measured count rate and analyte concentration due to e.g. matrix effects or secondary excitation can be corrected by influence coefficients. These coefficients are determined theoretically from fundamental parameter equations or empirically from standards.

In the case of several layers, which include the same elements, the above-mentioned approaches are no longer applicable. In these cases, quantification is carried out by non-linear least square fitting using a model sample, where the mass depositions of each layer are varied to match the calculated to the measured fluorescence intensities. Again, this approach can be used in a reference-free or standardless method and is similar to the quantification of angular resolved XRF profiles described in Section 2.4.2.

2.2. Grazing Incidence and Grazing Emission XRF

In Equation 2.1.1, a direct influence of the incident and detection angles ψ_{pr} and ψ_{fl} on the detected count rate $N_{i,j}$ is evident. For ever smaller ψ_{pr} or ψ_{fl} , the exponent decreases, dampening the integral. The physical meaning behind this fact is an increase of absorption either of the incident or the fluorescence radiation due to enlarged path lengths in the sample. Thus, the depth, from which fluorescence radiation is created and can reach the detector is adjustable by both angles and leads to depth resolving capabilities in angular resolved (AR) XRF measurements.

Experimentally, the angle of incidence or the detection angle is varied and for each angle an X-ray fluorescence spectrum is recorded. A plot of the recorded fluorescence line intensities against the incident and detection angle, respectively, yields the angu-

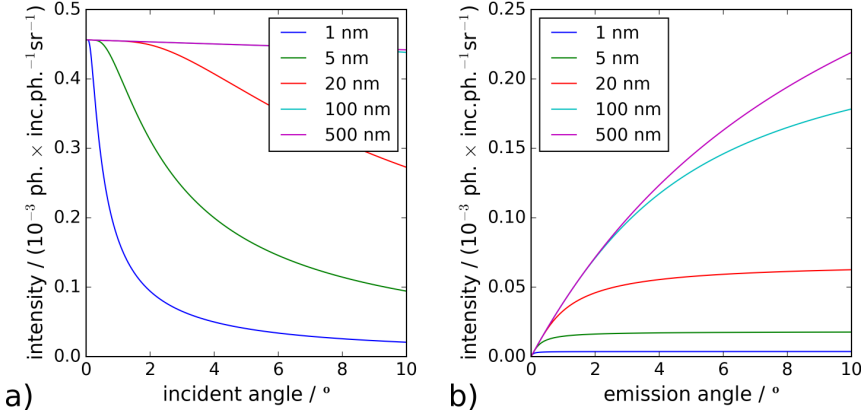


Figure 2.2.: Calculated Cu-L $_{\alpha_1}$ angular resolved XRF profiles of thin Cu layers (1 nm to 500 nm) excited with 1060 eV photons using Equation 2.1.2. a) shows the profiles for shallow incident angles and a detection angle of 90°. In b) the incident angle is fixed at 90° and the detection angle is tuned.

lar resolved XRF profiles. Figure 2.2 shows computed Cu-L $_{\alpha_1}$ ARXRF profiles using Equation 2.1.2 for a Cu layer of various thicknesses irradiated with a single 1060 eV photon / s. The curves are calculated for a fixed solid angle of detection of $\Omega = 1$ sr and setting the detection angle in the shallow excitation case in a) and the incident angle in the shallow detection case in b) to 90°. The fundamental parameters are taken from [32]. As can be seen, in both cases the ARXRF profiles of the different samples show not only a variation of absolute intensity but indeed different shapes of the curves. In the shallow excitation case in a), the fluorescence intensity increases towards smaller incident angles because of ever more efficient excitation in the thin layers. For $\psi_{\text{pr}} \rightarrow 0^\circ$, all curves converge to

$$N_{i,j} = \frac{1}{4\pi} \frac{\tau_{i,s}(E_{\text{pr}})}{\mu_{\text{tot}}(E_{\text{pr}})} \omega_{i,s} p_{i,j}, \quad (2.2.1)$$

as is shown in Appendix A. Since the attenuation coefficient $\mu_{\text{tot}}(E_{\text{pr}})$ is the sum of the cross sections for photoionization, coherent and incoherent scattering, the fraction in Equation 2.2.1 is the probability that the primary photon is absorbed in the sub-shell corresponding to the detected X-ray fluorescence line rather than being absorbed in another shell or scattered. Thus, the somewhat theoretical interpretation of Equation 2.2.1 is that in the ideal, infinite sample plane all incident photons interact with the first atomic layer of the sample and some fixed fraction depending on the atomic processes alone leads to the fluorescence radiation detected in 1 sr of the whole solid angle of 4π . Since only the first atomic layer is interacting with the primary photons, the

2. METHODOLOGICAL BASES

fluorescence intensity for $\psi \rightarrow 0$ is independent of the sample thickness. The decrease of fluorescence intensity for steeper angles in Figure 2.2 a) strongly depends on the sample thickness and is explained by the reduced interaction probability for thin layers. In the real world, two factors are actually decreasing the fluorescence intensity to zero for $\psi \rightarrow 0$. First, the sample plane and the excitation footprint are finite and second, external reflection might dominate for shallow ψ_{pr} . Both effects lead to losses in the excitation channel and are discussed in Section 2.2.2.

The interpretation of the ARXRF profiles in Figure 2.2 b) is more straightforward. The excitation conditions are the same for all detection angles ψ_{fl} but the number of fluorescing atoms increases with the layer thickness, as long as the thickness is in the range of the penetration depth of the primary photons. For ever shallower ψ_{fl} , the detected fluorescence radiation decreases with $\sin(\psi_{\text{fl}})$ due to self-absorption in the sample, leading to zero intensity at $\psi = 0$ (also see Appendix A).

Despite the differences in the ARXRF profiles in Figure 2.2 a) and b), the physical principles are the same and both types of angular scans can be used to extract information about the in-depth distribution of the elemental composition (elemental depth profiles) of the sample. Indeed, direct inversion of ARXRF profiles to get the elemental depth profile of the sample is in some special cases possible, but is still a severely ill-posed problem [34]. That means that more than one solution might exist and especially with the influence of experimental errors a direct inversion is highly unstable. Therefore, usually the elemental depth profiles of the sample are modeled and the expected angular dependent fluorescence intensities, considering the setup specifications, are calculated (forward calculation). Then, fitting the calculated and measured ARXRF profiles is performed by adjusting the sample parameters (back calculation). Thus, quantitative information about the sample is obtained only indirectly and the results, especially with respect to uncertainties, need to be considered carefully, as will be discussed further in Section 2.4.2.

For ever smaller incident or fluorescence emission angles, boundary effects such as reflection and refraction at interfaces can occur. These effects must be taken into account to correctly predict the fluorescence radiation intensity of a sample. On the other hand, the boundary effects, the occurrence of interference effects and thus the dependence on geometric length scales, makes the method sensitive to layer roughness, layer thicknesses and densities. Furthermore, local electrical field enhancements due to an X-ray standing wave (XSW) field can further increase the elemental sensitivity, as will be considered in the following.

2.2.1. The Complex Refractive Index

To describe X-ray scattering by a multi-electron atom, the complex atomic scattering factor f is used. It relates the scattered electric field amplitude to that scattered by a single, free electron. In the limit of short wavelengths (relative to the Bohr radius) or forward scattering, the complex atomic scattering factor $f^0 = f_1^0 - i f_2^0$ can be directly linked to the complex refractive index $n = 1 - \delta - i\beta$ via [35]

$$\begin{aligned}\delta &= \frac{n_a r_e \lambda^2}{2\pi} f_1^0 \\ \beta &= \frac{n_a r_e \lambda^2}{2\pi} f_2^0.\end{aligned}\quad (2.2.2)$$

Here, n_a is the average density of atoms, r_e the classical electron radius and λ the wavelength of the radiation. As can be seen when considering a plane wave propagating through matter, δ and f_1^0 respectively describe the phase shift relative to a wave propagating in vacuum and β and accordingly f_2^0 are responsible for the exponential decay of the intensity. Indeed, f_2^0 and thus β are directly linked to the photoelectric cross section τ through [35]

$$f_2^0 = \frac{\tau}{2r_e \lambda} \quad \text{and} \quad \beta = \frac{n_a \lambda \tau}{4\pi}. \quad (2.2.3)$$

In the whole X-ray regime, δ and β are small (usually positive) numbers of order 10^{-2} to 10^{-6} or less and β is usually smaller than δ . Therefore, reflection and refraction at interfaces between two materials is negligible for non-shallow angles and not further considered in conventional XRF analysis, where usually a single non-shallow incident and detection angle is used.

2.2.2. Shallow Excitation

Considering a plane X-ray wave propagating from a material with refractive index n_1 to a material with refractive index n_2 with $n_1 > n_2$ and neglecting absorption ($\beta = 0$), a critical angle for total external reflection ψ_c can be defined from Snell's law as

$$\psi_c = \arccos(n_{\text{rel}}^{-1}), \quad \text{with} \quad n_{\text{rel}} = \frac{n_1}{n_2}. \quad (2.2.4)$$

For incident angles below ψ_c , the incident wave is completely reflected and only an evanescent wave propagates along the surface with exponentially decreasing amplitude normal to the surface. The latter is not strictly true for lossy media ($\beta > 0$), where also a small wave vector component normal to the interface exists and absorption in the second

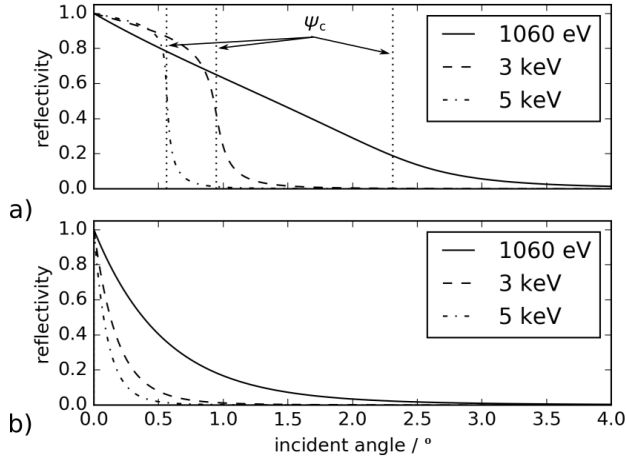


Figure 2.3.: Reflectivities for a) a vacuum-to-CuO and b) a CuO-to-Si interface and different photon energies. In a) total external reflection occurs and the critical angle ψ_c is indicated. Data for δ and β are taken from [39].

media occurs. Such interface effects at shallow excitation conditions need to be taken into account when calculating fluorescence intensities and reflectivity at the interface is significant. The requirements to allow specular reflection are a sample surface with small waviness and a root mean squared roughness (RMS) below a few nm (depending also on the wavelength and the incident angle) [36, 37].

An accurate description of the reflectivity at an ideal (sharp, no roughness) interface for perpendicular (R_s) and parallel (R_p) polarized light is given by the Fresnel equations [38]

$$\begin{aligned} R_s &= \left| \frac{n_{\text{rel}} \cos(\psi) - \sqrt{1 - n_{\text{rel}}^2 \sin^2(\psi)}}{n_{\text{rel}} \cos(\psi) + \sqrt{1 - n_{\text{rel}}^2 \sin^2(\psi)}} \right|^2 \\ R_p &= \left| \frac{\cos(\psi) - n_{\text{rel}} \sqrt{1 - n_{\text{rel}}^2 \sin^2(\psi)}}{\cos(\psi) + n_{\text{rel}} \sqrt{1 - n_{\text{rel}}^2 \sin^2(\psi)}} \right|^2 \end{aligned} \quad (2.2.5)$$

Figure 2.3 shows the calculated reflectivities (the results apply for R_s and R_p) for X-rays propagating from a) vacuum to CuO and b) CuO to Si for 1060 eV, 3 keV and 5 keV. Since the real part of the refractive index of vacuum is greater than that of CuO ($\Re(n_1) > \Re(n_2)$), the reflectivity for incident angles $\psi < \psi_c$ (with ψ_c from Equation 2.2.4) in Figure 2.3 a) is increasing strongly, reaching values close to 1 for 3 keV and 5 keV

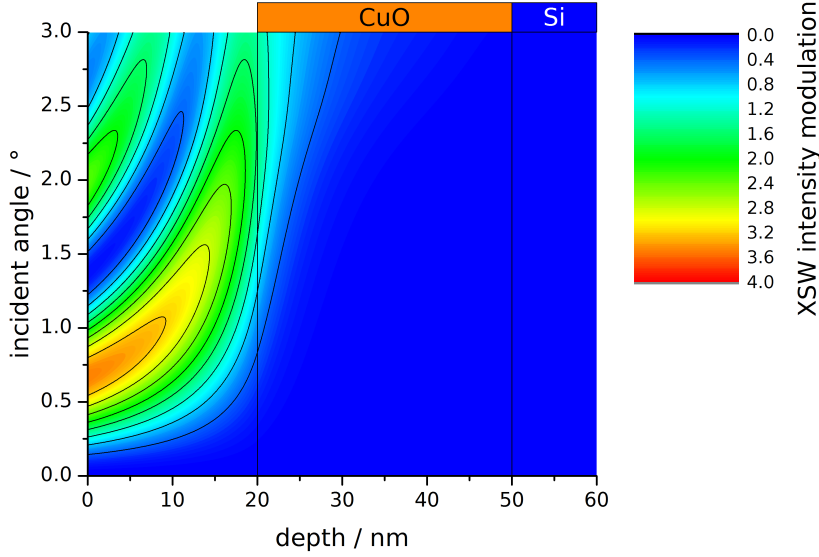


Figure 2.4.: XSW field intensity in front of and in a 30 nm thick CuO layer on a Si substrate. The density of the CuO layer is set to 6.31 g/cm³, Debye-Waller factor is zero and the incident X-rays have an energy of 1060 eV and are polarized parallel to the plane of incidence. The atomic scattering factors for the calculation are taken from [40].

photons. For incident angles above ψ_c the reflectivity quickly drops to zero. The soft X-rays at 1060 eV have a larger critical angle ($\psi_c = 2.31^\circ$) and thus significant reflection at larger incident angles compared to hard X-rays. However, the high absorption in the second material leads to losses in the reflected intensity, reducing the reflectivity well below 1 even for incident angles below ψ_c . In the case of the second interface in b) no total reflection occurs, since $\Re(n_1) < \Re(n_2)$. Here, the reflectivities for soft X-rays are usually larger than for X-rays with higher energies, leading to considerable values at steeper angles.

To correctly calculate the fluorescence intensities of a sample irradiated at shallow incident conditions, the mentioned boundary effects must be considered. L.G. Parratt developed an iterative algorithm to calculate the electric field amplitudes at each depth position for a sample of multiple homogeneous layers, using the Fresnel equations at each interface [41]. The resulting electric field amplitudes can render nodes and anti-nodes due to interference of incident and reflected radiation (schematically shown in Figure 2.5 a) top). Thus, the modulated field intensity, also referred to as X-ray standing wave (XSW) field, modulates the excitation intensity with depth. As an example, the XSW field of a 30 nm CuO layer on top of a silicon substrate is shown in Figure 2.4. The plot shows the

2. METHODOLOGICAL BASES

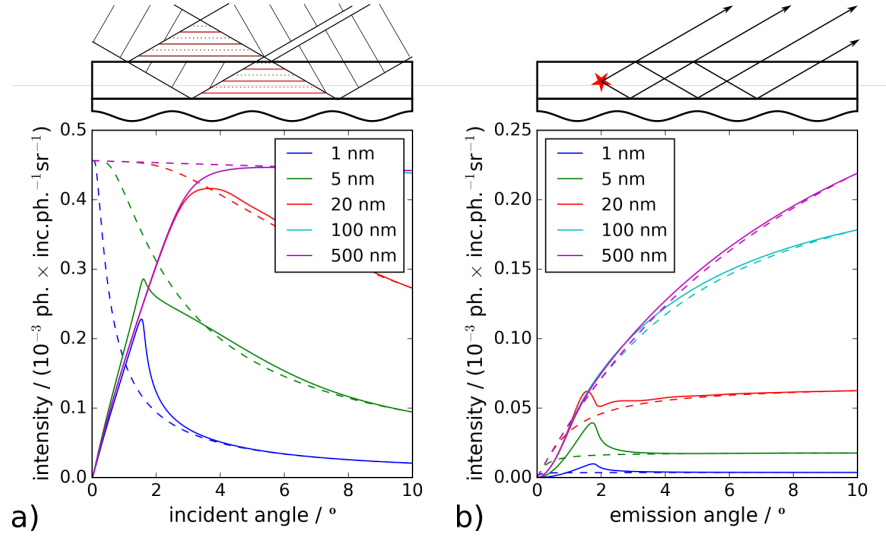


Figure 2.5.: Cu-L α_1 ARXRF profiles of thin Cu layers on a silicon substrate as in Figure 2.2. However, here the profiles are shown with (solid lines) and without (dashed lines) the boundary effects taken into account. On the top, the principles of GIXRF in a) and GEXRF in b) are schematically shown.

depth dependent (x axis) XSW field enhancement compared to the incident field intensity for various incident angles (y axis). Depth zero is defined as being 20 nm above the CuO surface, i.e. in vacuum. The CuO layer is at depth 20 nm to 50 nm and after a depth of 50 nm the first 10 nm of the silicon substrate are shown. The maximum enhancement close to a factor of 4 can be found for angles below 0.7° and at distances above 15 nm from the surface. In this region, the reflectivity of the incident beam at the first interface is above 70% (see Figure 2.3) but due to the phase shift after reflection, the XSW field maximum is a few nm above the surface. In principle, the nodes and anti-nodes of the XSW field can shift through the sample with varying incident angle. Thus, they can be regarded as nano-scaled sensors for X-ray fluorescence excitation, which further enhance depth resolution and sensitivity as compared to excitation without XSW field.

Figure 2.5 a) shows the GIXRF profiles of pure Cu layers on a Si substrate taking reflection and refraction into account and compares them with the results of the Sherman equation from Figure 2.2. Clearly, the effect of reflection of the primary radiation is seen for shallow incident angles, where the fluorescence intensity now drops to zero. But also, enhancement effects as compared to the case without XSW field are evident especially for the thin layers. Note that the high sensitivity in total external reflection XRF (TXRF) is partly due to this enhancement effect.

In a grazing incidence X-ray fluorescence (GIXRF) experiment, the incident angle of the excitation radiation ψ_{pr} is scanned in proximity of the critical angle for total

external reflection ψ_c (e.g. $0 < \psi_{pr} < 3\psi_c$). The incident beam needs to be collimated and monochromatized to guarantee a sufficient transversal and lateral coherence of the beam and permit the formation of an XSW field. This is easily done at synchrotron radiation facilities, where low divergence and high photon numbers are available. For divergent laboratory sources, e.g. multilayer mirrors and appropriate element filters can be applied at the expense of excitation intensity. Assuming a suitable incident beam, the projection of that beam on the sample surface (footprint) might extend the sample dimensions or detector field of view, leading to further efficiency losses. This effect is especially strong in the hard X-ray regime, where ψ_c , and therefore the probed angular range, is shallower than in the soft X-ray regime. On the other hand, the (usually) energy-dispersive detector can face the sample surface, which allows for the closest possible detector distance in an XRF experiment, maximizing the solid angle of detection. In addition, the steep detection angles minimize self-absorption of the fluorescence radiation. Thus, the probed depth region is defined by the absorption of the incident beam, which leads to most efficient excitation conditions at every probed ψ_{pr} . Whether the enhancing or deteriorating effects concerning efficiency dominate depends on the actual setup geometry and the probed sample.

Besides the setup requirements, a further analytical challenge in GIXRF analysis is the precise knowledge of the effective solid angle of detection. As mentioned, for short sample-to-detector distances d_{dist} , the footprint on the sample easily extends the field of view of the detector. In this case, regions of the footprint exist, where the detector chip is partly covered by the detector housing. This effect depends on the incident angle and distorts the GIXRF profiles. If the setup geometry is precisely known (ψ_{pr} , d_{dist} , detector configuration), the effective solid angle of detection can be calculated to correct the GIXRF profiles [42, 43].

2.2.3. Shallow Detection

In the case of shallow detection angles, the fluorescence radiation of the analytes in the sample can be reflected and refracted at the existing interfaces. Therefore, presuming smooth interfaces, the fluorescence at grazing emission (GE) angles is also modified as compared to the theoretical description by the Sherman equation. The direct comparison is shown in Figure 2.5 b), where similar to the shallow excitation case at small ψ_{fl} an additional decrease of the fluorescence intensity appears. Here, the fluorescence radiation is reflected at the sample-to-vacuum interface and cannot reach the detector. Less obvious is the appearance of fluorescence enhancement especially for the thin layers at $\psi_{fl} \approx 1.7^\circ$.

Considering a thin layer on a substrate, fluorescence radiation of that thin layer can

2. METHODOLOGICAL BASES

reach the detector directly or via an even number of reflections at the sample-to-vacuum and the sample-to-substrate interface (Figure 2.5 b) top). Due to the different possible detection paths, interference patterns and fluorescence intensity enhancement can occur in the GEXRF profiles. A direct calculation of GEXRF intensities by applying the Fresnel equations to the interfaces of a sample with several homogeneous layers is performed by Urbach and de Bokx [44]. The authors started by calculating the far field intensity at the detector due to a single fluorescing atom and integrated the result over a distribution of these atoms in depth. Thus, the interference pattern observed originates from the self-interference of the probability wave function of every fluorescence photon. This statement is also demonstrated in Section 6.2.5, where only single photons are detected but the predicted interference pattern is observed. It has to be emphasized again that no coherent excitation of the sample is necessary to obtain the enhancement from the interference pattern, which is beneficial for laboratory sources.

Already in 1983 R.S. Becker, J.A. Golovchenko and J.R. Patel compared and discussed the similarities in GIXRF and GEXRF measurements [45]. Later, in 1995, P.K. de Bokx and H.P. Urbach showed the physical similarities between GIXRF and GEXRF by applying the reciprocity theorem of optics in the calculation of GEXRF profiles [21]. The theorem states that the electric field from a dipole source at a detector is the same, if the positions of detector and source are exchanged. Therefore, instead of calculating the fluorescence intensity of a single fluorescing source in a sample directly, also the electric field at the position of the atom can be calculated assuming an X-ray beam incident on the sample. Only the incident angle has to be equivalent to the former detection angle and the photon energy needs to be the one of the detected fluorescence line. Thus, by calculating the X-ray standing wave field for an incident photon energy equal to the fluorescence energy and integrating over the source strength distribution in depth, also the GEXRF profiles can be obtained.

In comparison to GIXRF, the fundamental excitation conditions of GEXRF measurements are less efficient and self-absorption of the fluorescence radiation in the sample (due to shallow detection angles) is higher. Together with the usually better solid angle of detection due to the small sample-to-detector distance, detection limits in GIXRF are usually better by 2 orders of magnitude compared to GEXRF measurements [36]. On the other hand, there are several advantages of the GEXRF method. First, the angular profiles are depending on the X-ray fluorescence energy and not the excitation energy, which leads to a larger critical angle (Equation 2.2.4) and broader angular intensity patterns, reducing the requirements on the angular resolution. Furthermore, the incident beam does neither have to be monochromatic nor parallel and even particle excitation can be used [46]. Thus, also focusing optics or polychromatic excitation might be applied, which increase the efficiency in the excitation channel, especially for divergent

laboratory X-ray sources. Furthermore, due to the use of focusing optics, the lateral resolution in GEXRF experiments is superior to GIXRF, where for shallow angle excitation footprints with extensions of mm are reached.

The drawback in the excitation efficiency of GEXRF measurements can be compensated to some extend by also applying shallower incident angles, which becomes more important with decreasing layer thickness and for surface analysis. Depending on the sample system, a compromise between efficiency and lateral resolution can be found. However, the requirements on the angular resolution also demand small solid angles of detection, which is the second bottleneck for an efficient GEXRF setup. This latter disadvantage can be exploited by applying wavelength dispersive detectors with their inherent relatively small solid angle of detection to enhance the analytical capabilities of the setup [22, 47]. Alternatively, the overall solid angle of detection can be increased for an GEXRF setup, if the various fluorescence emission angles are not measured successively, but rather simultaneously with a scanning-free GEXRF approach.

2.3. Scanning-Free GEXRF

Kayser et al. showed the applicability of digital energy-dispersive area detectors to scanning-free GEXRF analysis [24]. The detector, a PILATUS 100 K, operates in a single photon counting mode to use the linear correlation between the number of created electron-hole pairs in the CCD chip and the photon energy, enabling energy-dispersive measurements. The spatial resolution of the area detector can directly be used to determine the emission angle of the detected fluorescence radiation, if the setup geometry is well-known. Indeed, every pixel can be regarded as a small energy-dispersive detector with small solid angle of detection allowing for high angular resolution. The high efficiency due to the large solid angle of the detection is achieved by the thousands or even millions of parallel working pixels. Besides the superior efficiency of the scanning-free GEXRF approach, also the stability of the setup can be expected to be improved with respect to an angular scan, due to the lack of moving parts during the measurement.

2.3.1. Single Photon Counting with a CCD - Energy Resolution

The key element of the scanning-free GEXRF method is a two-dimensional, energy-dispersive detector. After the late 1980s special high resolution area detectors like the pnCCD [48, 49], the Medipix [50] and PILATUS [51] detector have been developed, facilitating (semi-) energy-dispersive properties. However, the development of these devices was motivated by space missions and large-scale facility measurements, which enabled outstanding performance but up to date high cost and operational complexity. Conven-

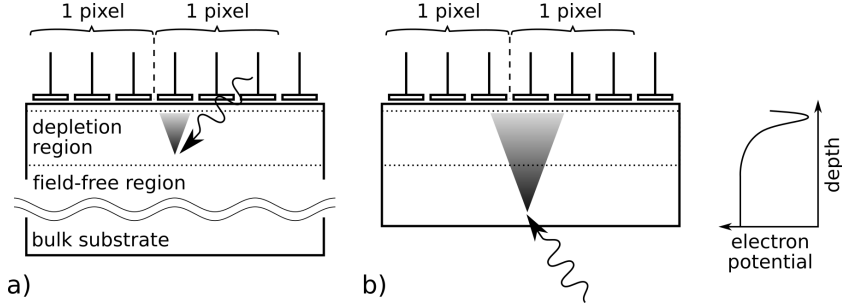


Figure 2.6.: Schematic view of a) front-illuminated and b) back-illuminated CCD. The absorbed photon creates a charge cloud, which drifts towards the potential well beneath the pixel structure.

tional CCDs, which are nowadays commercially distributed by a number of companies, are used for scientific X-ray analysis since the 1970s [52, 53]. Yet, exploitation of their energy-dispersive properties started just in the last decade [54, 55, 56]. The principle for differentiating photon energy is similar for all mentioned devices and is based on the proper analysis of deposited energy of every detected photon.

If an X-ray photon hits the absorber material of the detector chip, it can create a high energetic photoelectron by photoionization. This photoelectron interacts with the surrounding atoms and leads to electron impact ionization, creating further electron-hole pairs. The generated mean number of electron-hole pairs N_{eh} in the charge cloud depends on the chip material and the energy of the detected fluorescence photon E_{ph} by $N_{\text{eh}} = E_{\text{ph}}/W$, where W is the electron-hole pair creation energy, e.g. $W = 3.62 \text{ eV}$ for pure silicon [30]. This basic principle of energy discrimination can also be used in a conventional charge-coupled device (CCD) for X-ray applications, if operated in a single photon counting mode.

A general explanation of the working principles of CCDs can be found for example in [57]. The following description will focus on single photon detection and evaluation. A CCD consists of an absorber material with a fully depleted detector volume and a mesh of electrodes creating potential minima (pixels) in the substrate (Figure 2.6). The primary charge cloud created in the absorber has a size in the nm range [58] but due to diffusion processes on its way to the potential minima below the CCD pixel structure, it expands to diameters in the μm range. Depending on the path length of the charge cloud to the potential well, which is usually larger for back-illuminated CCDs, the charge cloud size can reach values in the order of the pixel size of the CCD [59, 60, 61, 62], with a two-dimensional shape well-approximated by a Gaussian curve [63]. This can lead to a splitting of the total charge to several neighboring pixels (split events), as illustrated in Figure 2.6 b). During image recording, charges are accumulated and stored in the

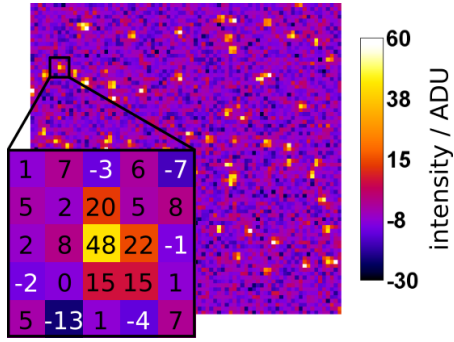


Figure 2.7.: Darkframe corrected image of soft X-ray single photon events detected with a commercial CCD. Computer algorithms are needed to evaluate the hundreds to thousands of events in every measurement frame.

pixel structure. Then, the charges are successively shifted to the read-out amplifier and subsequent analog-to-digital converter. By the exact knowledge of the shifting process, the spatial information for each measured charge is preserved.

The first challenge in the analysis of single photon events (SPEs) is to identify SPEs in the image. Figure 2.7 shows a section of a dark image corrected CCD frame (a frame with the same camera settings but without illumination is subtracted from the measurement frame) with a number of SPEs visible as bright spots. Many of the SPEs are split events consisting of up to 4 pixels, as is exemplarily shown in the enlarged frame. Also, the pixels without SPEs show intensity variations due to noise, thus, the signal-to-noise ratio in the frame already gives a lower boundary for the detectable SPE intensity, i.e. the accessible spectrum towards low photon energies. Furthermore, if a relevant number of split events occur, they need to be identified and either rejected or the actual charge cloud intensity from the intensity distribution in the split events has to be calculated.

Several approaches can be found in the literature to analyze single photon events, the algorithms also depending on the purpose of the measurement and applied CCD detector. SPE analysis is performed in wavelength dispersive measurements to increase the spatial resolution to the subpixel regime, by using center of gravity calculations [61, 60, 64]. In [64] the algorithm is described by finding pixels with intensity above an empirical threshold and using the $N \times N$ area ($N = 3$ or 5) centered at the pixel to calculate the center of gravity. The intensity of SPEs can also be facilitated to preselect valid events. They are filtered from the whole CCD image if their intensity is within a region of interest (for the expected measured energy range), which can enhance the signal-to-noise ratio of the wavelength dispersive spectra [65, 62]. Lawrence et al. [62] calculate for that purpose sum intensities of every 2×2 -pixel box of the images and

2. METHODOLOGICAL BASES

compare them with every overlapping box. SPEs are then defined for those boxes with maximum intensity in the comparison and subsequently the centroidal position and the SPE intensity are calculated for each box. The algorithm of Szlachetko et al. [65] works only for monochromatic radiation. Here, the SPEs without event splitting (1-px events) are used to get an estimate of the expected summed intensity of the split events, which are considered for up to four pixels. SPE evaluation can also be applied in full-field XRF imaging by using a pinhole camera with a CCD as energy-dispersive detector [55, 56]. While Alfeld et al. [55] just rejected every photon event, where less than 95% of the intensity is found in any of the single pixels of an SPE, the algorithm by Romano et al. checks a monotonic decrease of the neighboring pixels to identify an event. Energy-dispersive spectra of a CCD in a space mission are obtained in [66] by classification of the intensity distribution in 3×3 pixel boxes into 8 grades. Depending on the grade, intensities of the corner pixels in the box are used or rejected.

Summarizing, a large variety of SPE evaluation algorithms exists, all of them dealing in one way or the other with the direct shape of each SPE. However, often the descriptions, if given at all, lack details on the algorithm or on the criteria of choosing apparently applied thresholds. Especially in the soft X-ray range, where the signal-to-noise ratio (of pixel intensities) due to the smaller photon energy compared to hard X-rays is low, SPE treatment is crucial. Therefore, in Section 5.4.1 an own algorithm is developed, evaluated and adjusted for the performed soft X-ray fluorescence measurements.

Finally, some notes on noise in CCD images are given, since it not only defines the lower limit of the energy spectrum obtainable by the CCD, but also effects the energy resolution, as it is directly linked to the signal-to-noise ratio (see also Section 5.4.2). First, there might be inhomogeneous systematic offsets in every recorded CCD frame. These could result e.g. from insufficient charge transfer efficiency (probability that no electrons get lost when shifting charges during readout), unequal pixel efficiencies or hot pixels (increased dark current). If the effects are known, they can be compensated for or some pixels can be ignored during image processing. Furthermore, there are two significant statistical noise contributions, which can be influenced by the user via camera settings. On the one hand, during the recording time electron-hole pairs can be created by thermal excitation and accumulate in the potential wells. This dark current can be corrected for by subtracting a dark image, i.e. an image with the same recording parameters but without illumination. However, the dark current itself has a statistical deviation, which is why the dark current and the dark current shot noise is usually reduced by cooling the CCD chip. The second significant noise contribution is the on-chip amplifier noise or readout noise. It originates from the sampling of the data and increases with the readout frequency, for which often different settings can be chosen by the user. Especially for the GEXRF measurements with the conventional CCD, a

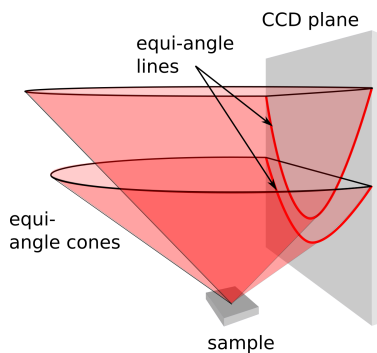


Figure 2.8.: Schematic illustration of positions on a CCD chip corresponding to the same fluorescence emission angle in a scanning-free GEXRF setup.

compromise has to be made between fast readout (reduced overall measurement time) and low noise level.

2.3.2. Geometry Considerations - Angular Resolution

Fluorescence radiation from a sample, which has the same emission angle ψ_{fl} with respect to the sample surface, is emitted in a cone-like shape, with an aperture of $2 \times (90^\circ - \psi_{\text{fl}})$. The equi-angle lines on a flat CCD detector are slice planes of the cones, having the shapes of hyperbolas (see Figure 2.8). If the position of the CCD detector is known with respect to the excitation spot on the sample (vertex of the cone), for each position on the CCD chip the respective emission angle of the fluorescence radiation can be calculated. During his PhD thesis in the research group Analytical X-ray Physics at the Technical University of Berlin, C. Herzog developed an algorithm to calculate ψ_{fl} for an arbitrary sample position and point in space, using simple vector calculations in 3-dimensional space. Furthermore, he implemented the algorithm of Asvestas et al. [67], which can compute the solid angle of any polygon with respect to a point in space. In the Bachelor's Thesis by F. Förste [68], both codes were applied to the calculation of corresponding fluorescence emission angles (angle maps) and solid angles of detection (solid angle maps) for every pixel on a CCD chip, given any detector geometry with respect to the sample.

Such calculations can be used to investigate the influence of the hyperbolic shape of the equi-angle lines on the CCD chip with respect to the angular resolution $\Delta\psi_{\text{fl}}$. For this purpose, angle maps are calculated for a conventional CCD as it is used in this thesis, i.e. 515×2046 pixels with $13.5 \times 13.5 \mu\text{m}^2$ pixel size. The geometry used in the calculations is sketched in Figure 2.9 and shortly described hereafter. The CCD chip is aligned with the larger aspect in the horizontal plane and the chip is perpendicular to

2. METHODOLOGICAL BASES

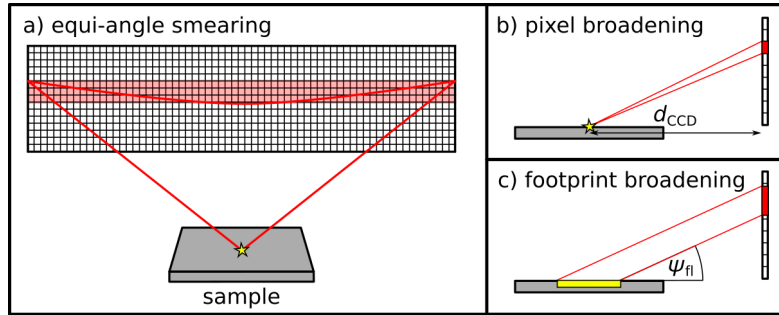


Figure 2.9.: Schematic illustration of geometric effects on angular resolution.

the sample plane. Also, the lower CCD edge is parallel to the sample plane and has zero distance to it. The closest distance of the CCD to the excitation position on the sample, which is also the sample-to-detector distance d_{CCD} , is situated at the center of that edge. Now, the number of pixel rows needed to confine an equi-angle line (equi-angle smearing, see Figure 2.9 a)) is calculated for every ψ_{fl} . The results for various d_{CCD} are shown in Figure 2.10 a). The y axis shows the various fluorescence emission angles of the CCD in a sample-to-detector distance on the x axis. The black corner to the top right arises from the limited extension of the CCD, so that these angles cannot be detected at large distances. The colorbar indicates the effect of the equi-angle smearing in units of pixel rows. As can be seen, for larger emission angles and smaller d_{CCD} , the equi-angle smearing increases. Already for $d_{\text{CCD}} = 10$ cm, the curvature of the equi-angle lines can be expected to influence the angular resolution, but even smaller sample-to-detector distances are envisaged to improve the overall solid angle of detection. However, if the geometry is known, then the angle maps can be calculated and pixels corresponding to the same fluorescence emission angle (or rather an angular range) can be combined for the evaluation. The calculations here are performed for a perpendicularly aligned CCD, which in an experimental setup might not always be possible (or desired). For a tilted CCD, the correct angle map calculation is even more important, since summing pixel intensities over rows or columns then leads to severe distortions of the GEXRF profile.

If the angle maps on the CCD detector can be correctly calculated, the angular resolution of the scanning-free GEXRF measurement is still limited by two more effects. First, the pixel size itself influences the angular resolution (pixel broadening), since every pixel detects a small fluorescence emission angle increment, as is shown in Figure 2.9 b). In a first order approximation, the angular resolution $\Delta\psi_{\text{fl}}$ depends on the pixel edge length d_{px} and the sample-to-detector distance d_{CCD} as $\Delta\psi_{\text{fl}} \approx d_{\text{px}}/d_{\text{CCD}}$. Thus, small pixel sizes are required, especially, if the sample-to-detector distance is to be minimized. However, there are technological limits for the pixel size, which might be overcome by using the subpixel resolution properties when carefully analyzing split events as is mentioned

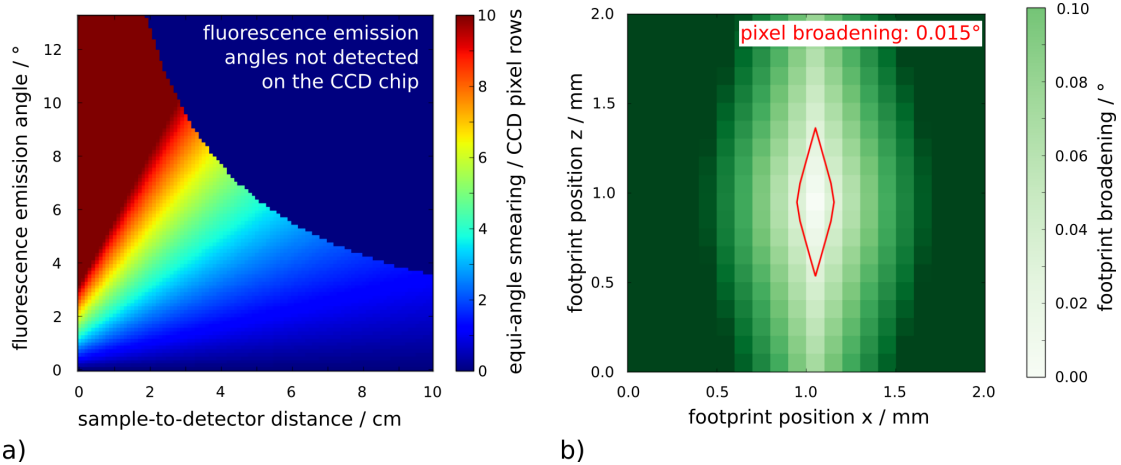


Figure 2.10.: a) Degradation of angular resolution due to equi-angle smearing for detectable fluorescence emission angles and different sample-to-detector distances. b) Degeneration of the angular resolution due to footprint broadening. For details please refer to the text.

above. The second degenerative effect on the angular resolution originates from the finite footprint size, i.e. the sample area from which fluorescence radiation is emitted. As is illustrated in Figure 2.9 c), radiation emitted from different spots in the sample plane with the same emission angle will hit the detector at different positions. The influence of this effect is estimated in Figure 2.10 b) for a CCD with the above-mentioned specifications and geometry but with $d_{\text{CCD}} = 5 \text{ cm}$ to emphasize the effect. Each grid point in the image represents a position in the sample plane with the center of excitation in the middle of the image. Now, for each point of the grid, the angle maps on the CCD are calculated as if all fluorescence radiation is emitted only from that point and compared to the angle map of the center position. Then, the pixelwise absolute difference of the two compared angle maps is calculated. The maximum of the angle differences is the value shown in Figure 2.10 b) for each grid point. It yields an upper estimate for the degradation of the angular resolution due to footprint broadening. As can be seen, the angular resolution degrades stronger with an extended footprint in the x axis, which is the direction towards the CCD detector. The red diamond like shape represents the footprint extension, which would just result in a resolution degeneration similar to the pixel broadening (0.015°). Thus, in the present case, the footprint in the sample plane should be confined to $100 \times 500 \mu\text{m}^2$ to prevent a significant decrease in the angular resolution. Of course, for every detector geometry, this effect should be considered separately, as is done for the different measurements in this thesis in Chapter 6.

2.4. Software for (AR)XRF Evaluation

2.4.1. **xrfLibrary and xrlfupa for X-ray Fluorescence Calculations**

In the research group Analytical X-ray Physics of the Technical University of Berlin exist two software packages to handle fluorescence calculations. The “xrlfupa” allows access to various published fundamental parameter databases like the compilation of Elam et al. [32] and Ebel et al. [33] for integral cross sections or Chantler [40] for atomic scattering factors. If necessary, the databases can be adjusted and extended to use new and more reliable values or such from measurements instead of theoretical calculations and interpolation. Furthermore, the xrlfupa is implemented into the “xrfLibrary”, the second software package, which allows to calculate the detected X-ray fluorescence of an arbitrary sample. The xrfLibrary can be used to simulate a complete XRF experiment, from e.g. calculation of a polychromatic X-ray tube spectrum, which can be altered by transmission filters or optics and used for the fluorescence excitation in the sample. The sample is modeled by discrete layers, each with its own composition, thickness and density. The Sherman equation is applied to all layers, considering absorption of primary and fluorescence radiation, as well as cascade effects and Coster-Kronig transitions in the fluorescence production itself. Optionally, secondary fluorescence can be calculated using the algorithm of de Boer [31].

If the number of fluorescence photons from a sample is to be calculated, which consists of several homogeneous layers, Equation 2.1.1 has to be applied to all the layers and for every layer the influence of the top layers (absorption of incident and fluorescent radiation) must be taken into account. Similarly, a continuous change of the sample composition can be approximated by subdividing the sample into N homogeneous layers, resulting in a step-wise change of the composition. For large N , this approximation can be reasonable.

Recently, L. Lühl and C. Herzog adapted the xrfLibrary to handle grazing incidence and grazing emission XRF calculations by taking into account refraction and reflection at interfaces as well as special detector geometries. For this purpose, the X-ray standing wave (XSW) field can be calculated for a sample defined in the xrfLibrary framework, following the work of de Boer [37], which is based on the equations of Parratt [41]. For GIXRF calculations, Equation 2.1.1 needs to be adapted. First, the absorption term in μ_{tot}^* for the incident radiation is removed, since the absorption of the incident radiation is already included in the XSW field. Second, the XSW field intensity I_{XSW} is introduced

as further excitation factor in the integral over depth. Both adaptions lead to

$$N_{i,j} = N_{\text{pr}}(E_{\text{pr}}) G(E_{i,j}) \xi_{i,j,s}(E_{\text{pr}}) \rho C_i \int_0^d I_{\text{XSW}}(E_{\text{pr}}, \psi_{\text{pr}}, x) \exp\left(-\frac{\mu_{\text{tot}}(E_{i,j})}{\sin(\psi_{\text{fl}})} \rho x\right) dx . \quad (2.4.1)$$

In practice, the integral is solved numerically by subdividing the layers of the samples into virtual, thin sublayers, for which the XSW field can be assumed to be constant (a typical thickness is 0.1 nm). For each sublayer, the absorption of the fluorescence in the superposed sublayers has to be accounted for.

For GIXRF experiments, the solid angle of detection is usually strongly affected by the tuned incident angle. In the xrfLibrary, the solid angle of a polygon shaded by another parallel polygon can be calculated, applying the formulas of Asvestas and Englund [67]. This is used to compute the effective solid angle of detection of e.g. an SDD detector consisting of chip and housing in front of the excited sample. Further details and a comparison to the solid angle of detection calculation of similar systems by Beckhoff et al. [42] can be found in [43].

The XSW field can also be applied for the calculation of GEXRF profiles as is rendered plausible by P.K. de Bokx and H.P. Urbach [21]. In this case, a virtual XSW field (there is no actual formation of an X-ray standing wave field, see Section 2.2.3) is calculated for every fluorescence energy and the produced fluorescence intensity of every virtual layer is modified by the respective virtual XSW field intensity in this layer. In contrast to the GIXRF case, now the absorption of the primary radiation is considered and the absorption of the fluorescence radiation, which is already included in the virtual XSW field, is omitted.

Since the calculation of the XSW field is already implemented in the xrfLibrary, also the GEXRF profiles calculated with the xrfLibrary use the approach of [21]. This also allows a straight-forward comparison of GI- and GEXRF measurements with the same sample model, as is applied in Section 4.5 and 6.3.4 for gold-doped copper oxide nanofilms.

For scanning-free GEXRF measurements, the xrfLibrary can also be used to calculate the solid angle of detection of every pixel on the CCD chip, again with the formulas of Asvestas et al. [67]. Especially for a tilted CCD, the solid angle of detection of each angular region used to compute the intensities of the GEXRF profile can vary drastically due to the different numbers of pixels included in these regions (e.g. the highest detected angles are confined to the corner of the CCD chip).

Both the xrlfupa and the xrfLibrary are programmed in C++ using an objective orientated approach, which makes the software highly adaptable. Also, an interface to

the high-level programming language Python is available for most functions, allowing easy data handling and access to the various well documented additional packages for example for fitting routines. This is notably of importance for depth profiling approaches.

2.4.2. Depth Profiling

So far, only the forward calculation of fluorescence intensities for a sample measured with tunable excitation or detection angles was described. Depth profiling from these angular resolved X-ray fluorescence (ARXRF) profiles (back calculation) can be performed by modeling the measured sample, comparing the calculated fluorescence intensity of the model with the measured fluorescence intensity and adjusting the sample parameters by a non-linear least square fit. The calculation of a GI- or GEXRF profile with the xrfLibrary can take several seconds up to minutes on a modern desktop PC, depending on the number (virtual) layer of the sample and the number of angles used for the profile. Thus, the whole back calculation procedure can take several minutes up to hours, depending on starting parameters and convergence of the fit. The back calculations in this thesis use χ^2 minimizations based on the Levenberg-Marquardt algorithm (if boundaries for the parameters are applied) or a Trust Region Reflective algorithm (if no boundaries are used), which are both implemented in the python function `curve_fit` of the package `scipy.optimize`. They will be further described later.

A χ^2 minimization, if successful, gives the maximum likelihood estimators of parameters, which are applied to a model that reflects the physical principle behind a measurement. However, this is only true if first of all, the model is a good approximation of the “real” physical principles responsible for the measurement results and second, if the measurement errors are normal distributed. This has to be kept in mind, especially when quantitative information is to be derived. In the case of ARXRF analysis, the model parameters a_0, a_1, \dots, a_{M-1} are the M parameters of the sample (like density, roughness, composition and thickness of the layers in the sample) and the weighted χ^2 -fit minimizes the sum of squares of the weighted differences of N measured (y_i) and calculated ($y(x_i|a_0\dots a_{M-1})$) fluorescence intensities [69]

$$\text{minimize } \chi^2 \equiv \sum_{i=0}^{N-1} \left(\frac{y_i - y(x_i|a_0\dots a_{M-1})}{\sigma_i} \right)^2. \quad (2.4.2)$$

Here, σ_i is the normal distributed error of measurement y_i .

There are differences in algorithms and quantitative statements, if the model function $y(x_i|a_0\dots a_{M-1})$ depends in a linear or non-linear way on the model parameters. Often, an estimated covariance matrix C for the best fit parameters is given by χ^2 fitting

algorithms. In the case of a linear χ^2 -fit and normal distributed uncertainties of the measurement values, the diagonal elements of the covariance matrix are directly linked to the parameter uncertainties Δa_j by

$$\Delta a_j = \sqrt{C_{jj}} \quad (2.4.3)$$

The models used for ARXRF fitting are usually non-linear. Even in these cases, the error estimations by the covariance matrix might hold, if the χ^2 -distribution close to the minimum can be approximated by a quadratic form. Then, the model function is approximately linear in the parameters [70, 69]. The approximation needs to be valid in the range of the uncertainties of the parameters given by Equation 2.4.3 themselves, which is already one reason why the results should be treated with care. Furthermore, the precondition of the measurement uncertainties being normal distributed needs to be kept in mind.

If some of the conditions are not fulfilled, the bootstrapping method might be applied. In this method, various new synthetic data sets are drawn from the actual measurement, fitted again with the same χ^2 -fit and the distribution of best-fit parameters is used for an uncertainty estimation [69]. Obviously, if a single fit needs already several minutes up to hours for convergence, the whole bootstrapping process can need days and is not applied in this thesis.

For the evaluation of GIXRF and GEXRF profiles in this thesis, the uncertainties of the fits as defined by Equation 2.4.3 are given and their analytical value is discussed. Often, the given uncertainties will be declared unreliable due to an insufficient model on the one hand, or a too complex model on the other hand. In the latter case, the introduced parameters might interfere with each other and lead to unreliable error estimates. Also, for the GIXRF measurements in Section 4.5, an additional large uncertainty originating from the solid angle of detection is introduced. This uncertainty is clearly not normal distributed, further diminishing the quantitative values of the result. Since the solid angle of detection has a stronger influence in GIXRF measurements than in GEXRF measurements, there might be an advantage for the latter concerning the analytical validity.

There exists a variety of algorithms to minimize χ^2 , which can be roughly grouped into local models, which will find a local minimum in the proximity of the starting values of the parameters and global methods, which strive to find a global minimum (and thus a probably better solution of the parameters). The Levenberg-Marquardt algorithm is a local minimization method. It decreases χ^2 with a steepest descent method if the parameters are still far from the parameters minimizing χ^2 and switches to a method

approximating χ^2 by an analytical function to directly approximate the minimum, if the parameters are close to the minimizing ones [70, 69]. This combination yields a good robustness and quick convergence, which is why the method has become a standard algorithm for least-squares fitting. However, if the starting parameters are far from the best-fit parameters, the step size (change of parameters) is rather small, since a steep decent (strong change in χ^2) is expected. Here, a Trust Region algorithm, which is closely related to the Levenberg-Marquardt method, can show a better performance with respect to conversion time. These methods tend to better estimate the necessary step sizes by estimating “trusted regions”, where the analytical estimation to the χ^2 -function is sufficient. Furthermore, the Trusted Region Reflective algorithm [71] can handle boundaries for the parameters and is used, when those are given. For further details also refer to the python documentation for `scipy.optimize.least_squares` in [72].

Global minimization methods as e.g. “particle swarm” have a better chance to find a global minimum of χ^2 . However, such algorithms often perform many more iterations than local minimization methods and thus the total fitting time is usually increased. This is not convenient for the fits in this thesis, where every single iteration step already takes several tens of seconds. However, in for instance the particle swarm algorithm, hundreds of the iterations are similar and independent of each other. Thus, parallel programming and efficient use of processing unites with multiple cores (probably ideally the graphics processing unit due to its thousands of cores), might decrease the fitting time drastically (ideally to the duration a single iteration takes) and make the whole evaluation processes more efficient in the future.

2.5. Soft X-rays in Scanning-Free GEXRF Analysis

There is no strict definition of soft X-rays with respect to exact energy limits of this electro-magnetic radiation. Here, the definition of [35] is followed, roughly defining the energy of soft X-rays to be in the range of 250 eV to several keV. Accordingly, the energy of hard X-rays ranges from several keV up to several 100 keV.

2.5.1. Application of Soft X-rays

The use of soft X-rays in GEXRF experiments has several advantages in comparison to excitation with hard X-rays. First of all, the photoionization cross sections for light elements can be 1-3 orders of magnitude higher, directly increasing the sensitivity for thin films or contaminants. Furthermore, the larger photoionization cross sections lead to a decrease in penetration depth for soft X-rays, which in principle increases depth-resolving properties. Also, the critical angle for total reflection typically increases with

the wavelength, so that the depth sensitive part of the GEXRF profile is extended over a wider angular range. In scanning-free GEXRF, this requires the detector to be placed closer to the sample, which is beneficial for the overall solid angle of detection and thus setup efficiency. Of course, the angular resolution degrades with closer sample-to-detector distances, but angular intensity patterns are broader in the soft X-ray regime. This is a result of the longer wavelength compared to hard X-rays, which directly affects the width of nodes and anti-nodes of the X-ray standing wave field patterns in the GIXRF case and similarly the (depth dependent) probability pattern for fluorescence detection in the GEXRF case.

The main drawbacks of a scanning-free GEXRF spectrometer operating in the soft X-ray range are, first of all, the limited access to heavier elements. For example, with a primary photon energy of 1 keV, K fluorescence radiation can be excited in elements with atomic numbers $Z \leq 10$ (Ne), while L shell fluorescence has to be used for the analysis of elements with $Z \leq 29$ (Cu). The latter exhibit usually higher uncertainties in the tabulated fundamental parameters, complicating fundamental parameter based quantification. Secondly, the fluorescence yield is small in the soft X-ray regime, i.e. non-radiative Auger decay is dominant and fluorescence production comparatively low. Finally, soft X-ray sources are rare compared to common X-ray tubes used in the hard X-ray range.

2.5.2. Production of Soft X-rays

Several types of sources enable the production of soft X-rays. For example, large-scale facilities like synchrotron radiation facilities or free electron lasers on the one hand and laboratory sources like soft X-ray tubes, discharge plasma sources and laser-based sources (e.g. high harmonic generators or laser-produced plasmas) on the other hand might be applied. In this thesis, measurements with synchrotron radiation and a laser-produced plasma (LPP) source are performed, which is why both source types are shortly described.

The probably most suited radiation for the application of soft X-rays in angular resolved XRF experiments is provided by synchrotron radiation facilities. Here, electron (or positron) bunches with velocities close to the speed of light are circulating in a storage ring and emit electro-magnetic radiation when deflected by a magnetic field [35, 73]. Due to the relativistic speed of the accelerated charges, the typical dipole emission characteristics is deformed to a narrow radiation cone. Furthermore, the high particle energies and strong magnetic fields enable spectral emissions from the infrared to the γ -ray region, depending on the specific device specifications. While bending magnets and wigglers create broadband emission, undulator radiation consists of discrete narrow

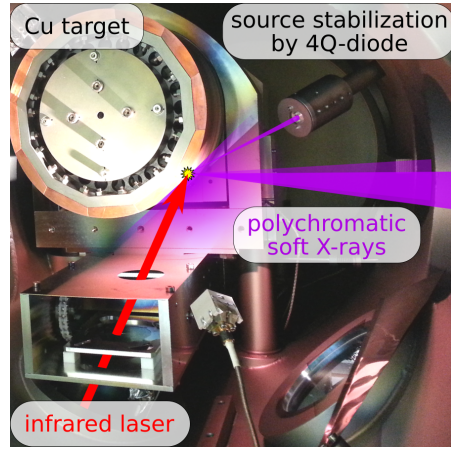


Figure 2.11.: Photograph of the copper cylinder in the plasma interaction chamber. The infrared laser, plasma position and emitted X-rays are illustrated.

peaks of high intensity (harmonics). Since the radiation already has small convergence and high monochromaticity (i.e. a high degree of spatial and temporal coherence), the intense undulator radiation is probably best suited for GIXRF experiments, since the relative losses due to the necessary beam shaping (monochromatization, parallelization) are relatively low. The latter is not critical for GEXRF experiments, where restrictions on beam convergence and monochromaticity are less tight. Indeed, focusing of synchrotron radiation to the nm range has been shown [74, 75], which could allow for the combination of nanometer depth resolution and nanometer lateral resolution in future beamlines by applying a scanning-free GEXRF setup. Besides the high photon flux, the second major advantage of synchrotron radiation is its energy tunability, enabling optimized excitation conditions for the analyzed elements. Details about specific beamlines and endstations, which are used in this thesis, can be found in Section 4.1.

When X-ray tubes are to be operated in the soft X-ray regime, first of all the entrance window must be especially thin or omitted to reduce absorption. Then, either L- or M-lines of high-Z anode material or anodes consisting of low-Z material have to be used. While using L- and M-lines reduces the overall efficiencies, the utilization of low Z-targets leads to insufficient thermal conductivity, limiting the applicable maximum power. An LPP overcomes this limit by intentionally consuming target material for the formation of a hot dense plasma, which can irradiate intense soft X-radiation [35]. Indeed, the amount of consumed target material is low and regenerative target systems like gas puffs [76], liquid jets [77], metal tapes [78] or rotating metal cylinders [79] can be applied.

At the Berlin Laboratory of Innovative X-ray Technology (BLiX) a LPP source with

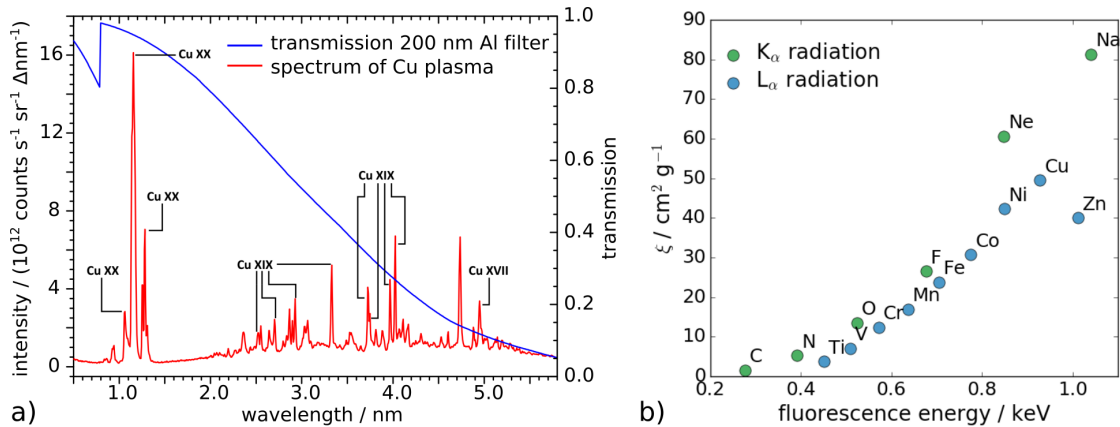


Figure 2.12.: a) X-ray spectrum emitted by the LPP source using a Cu target from [80]. The high intensity lines at 1.15 nm (1078 eV) of 20-fold ionized Cu are used for XRF experiments. The transmission of a 200 nm Al infrared filter is also shown. b) Photo production cross section ξ for K_{α} and L_{α} fluorescence from various elements excited with 1078 eV photons.

rotating copper cylinder is used. While a detailed description can be found in [79] and [81], here the properties, which are important for XRF analysis, are discussed. The LPP source is driven by a pulsed Yb:YAG thin disk laser with pulse energies up to 220 mJ, a pulse length of 1.2 ns and a repetition rate of 100 Hz. The laser is focused onto a rotating copper cylinder (see Figure 2.11), where the high laser intensity of $> 2 \times 10^{14} \text{ W/cm}^2$ [82] leads to the ionization and efficient heating of the target material, allowing the formation of a hot dense plasma. The plasma emits polychromatic radiation from the infrared to the soft X-ray region, which can be used for X-ray absorption in the 1-5 nm range [83] and X-ray fluorescence measurements [84]. The emitted soft X-ray spectrum is shown in Figure 2.12 a).

Due to the high absorption of soft X-rays in matter and the small differences of refractive indices, refractive optics are not applicable. Instead, multilayer reflective optics can efficiently collect and refocus the radiation on a sample. Since high reflectivities are only achieved for a single wavelength satisfying the Bragg equation (in first diffraction order), the multilayer optics are adapted to the intense plasma lines at 1078 eV (1.15 nm). Thus, the sample in the focus of the optics is excited with monochromatic radiation (the plasma intensity at photon energies of higher order Bragg reflexes is negligible). Figure 2.12 b) shows the photo production cross section ξ (which is directly proportional to the expected fluorescence intensity) of the elements, which can be excited with 1078 eV primary radiation. As can be seen, efficient excitation is possible for K_{α} radiation of light elements and L_{α} radiation of the 3d transition metals. The samples investigated in this thesis are composed of C, Ni, O, Cu and Au. Of these, Cu and Ni are especially

2. METHODOLOGICAL BASES

suited for excitation by the BLiX LPP source.

On the top right of Figure 2.11, a pinhole coupled to a 4-quadrant-diode (4Q-diode) is attached to monitor the source position. It is aligned in a way, that changes of the radius of the metal cylinder, e.g. by out-of-roundness of the target cylinder, a displacement of rotation axis to cylinder axis and temperature changes, can be detected by the 4Q-diode *Y* axis. Via a real-time feedback loop to a target motor controlling the vertical position of the target cylinder, these displacements can be corrected for. The 4Q-diode *X* axis is in first order approximation sensitive to a laser focus displacement. The feedback system allows for continuous and long-term operation with a stable source position, which is critical for scanning-free GEXRF measurements. Further details about operation conditions and exemplary stability measurements are given in Section 5.2.1 and 6.3.2.

3. Thermoelectric Nanofilms

Because of their earth abundancy, low cost and non-toxicity, transition metal oxides are promising material systems for the application in thermoelectric generators. K. Bethke investigated in his Diploma Thesis thermoelectric properties of several copper and silver compound nanofilms on soda-lime-silicate glass and found promising results for copper oxide nanofilms [85]. Therefore, research continued by increasing the electrical conductivity of these copper oxide nanofilms by doping the material with gold, which indeed increased the overall efficiency of the device. To improve the understanding of the thermoelectric properties of these materials it is of interest to obtain structural and chemical information of the nanofilms, i.e. information about lateral homogeneity and in-depth distribution of Cu and Au and depth dependent oxidation states of Cu with nm depth resolution. In this thesis, two of such gold doped copper nanofilm samples, one as deposited (DM0150A) and one thermally oxidized sample (DM0149A), are investigated with several laboratory and synchrotron based X-ray fluorescence methods to address the mentioned analytical questions. Furthermore, the comparison of grazing incidence (GI) XRF measurements performed at the synchrotron radiation facility and measurements with the herein developed scanning-free grazing emission (GE) XRF approach in the laboratory with the same sample allow for a validation of the method developed in this thesis and a direct comparison with state of the art GIXRF.

3.1. Sample Preparation and Surface Characterization

Sample preparation and first characterization measurements are performed by K. Bethke of the research group of Prof. K. Rademann from the department of physical chemistry at the Humboldt University of Berlin.

In a Cressington sputter coater 108 Auto (Figure 3.1), thin films of gold and copper are typically deposited on a soda-lime glass by magnetron sputtering. However, to reduce interferences from glass components in the XRF spectra and reduce the layer roughness (and thus increase the sensitivity of GI- and GEXRF due to X-ray standing wave (XSW) field effects), the samples used in this thesis are sputtered on an 800 μm thick silicon wafer with an area of approximately $18 \times 18 \text{ mm}^2$. As sputter target a 0.2 mm thick

3. THERMOELECTRIC NANOFILMS

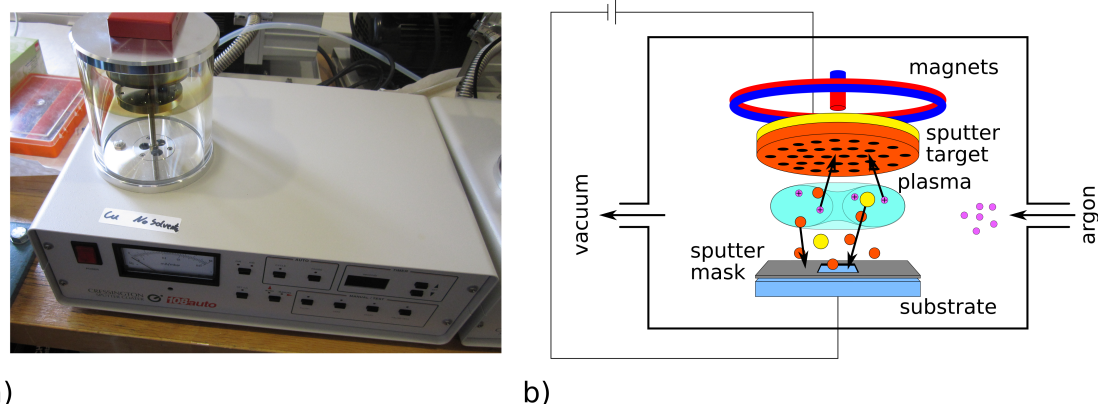


Figure 3.1.: a) photograph and b) schematic view of the magnetron sputter coater used for preparation of the copper oxide nanofilms. In an argon plasma, the ions are accelerated towards a sputter target, where they knock out atoms and ions of the target material. The ejected atoms can then condense on the substrate surface.

perforated Cu foil with a hole density of 5% is placed just beneath a 0.2 mm thick Au foil (Figure 3.1). The target has a distance to the substrate of 30 mm and directly on top of the substrate a sputter mask is placed to confine the sputtered area to $\approx 14 \times 14 \text{ mm}^2$. The process gas is AlphagazTM 1 Ar from Air Liquide, the current is 40 mA and the silicon wafers are sputtered for 2×40 s, rotating the sample about 180° after the first 40 s to make the sputtering more homogeneous.

Two samples, DM0150A and DM0149A are prepared as described one after another. Subsequently, only DM0149A is tempered in a tube furnace for 360 s at 300°C , to oxidize the copper layer. By investigating both the non-tempered and tempered sample, structural and chemical differences in the samples can be traced to the tempering process.

Figure 3.2 shows exemplarily an atomic force microscopy image of a non-tempered sample prepared with the same process parameters and substrate, which are used for DM0150A and DM0149A. Height variations of some tens of nm on a lateral scale of tens of μm are visible in the overview (right image). Such structures are force induced deformations of the substrate and are often visible in AFM images of large areas. In the first magnification (top left), valleys of ≈ 2 nm depth and extensions in the μm range can be seen. These structures probably originate from the substrate, which shows similar valleys (Appendix B). The local root mean squared (RMS) roughness determined in the two areas shown on the bottom left are about 1 nm, similar to the substrate roughness. Thus, the copper oxide layer seems to be homogeneously covering the substrate in the micrometer range.

The roughness of the sample is in the range of the wavelength of ≈ 1 keV photons, which are used in the GIXRF measurements in Section 4.5 and the GEXRF measure-

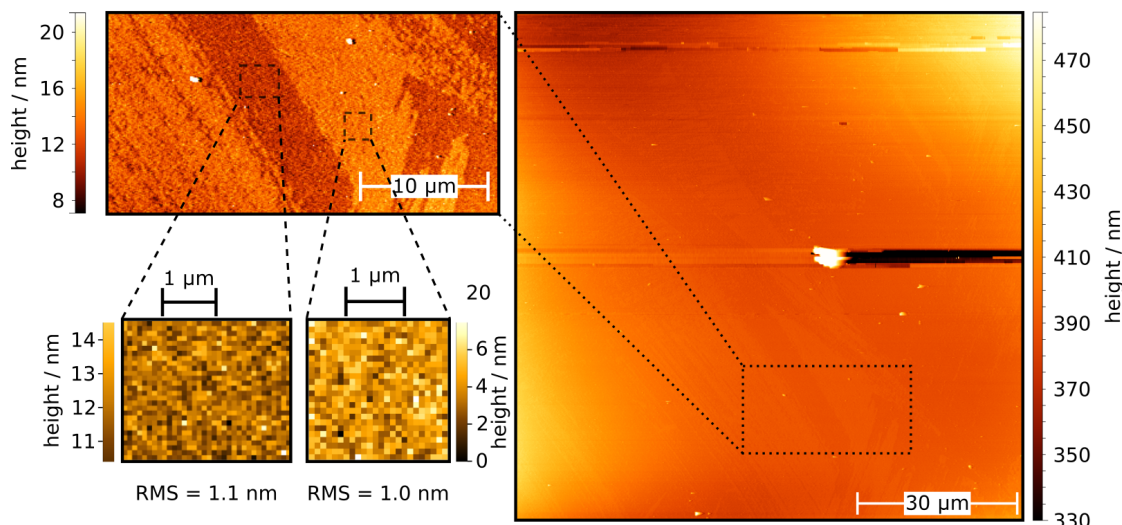


Figure 3.2.: Atomic force microscopic image of a gold-doped copper oxide nanofilm. The root mean squared (RMS) roughness on a micrometer scale is about 1 nm (bottom right).

ments in Section 6.3.4, so that the formation of an XSW field can be expected. Furthermore, particles or islands with a size of a few μm down to 100 nm are visible on the surface. This agrees with the findings in Section 4.5, where the GIXRF measurements imply the presence of carbon and oxygen rich particles with similar size.

3.2. Investigation of Lateral Homogeneity by means of Laboratory-based XRF

XRF measurements to investigate the absolute mass depositions of Au and Cu and their lateral homogeneity are performed with a commercial Fischerscope X-Ray XDV-SDD (Helmut Fischer GmbH). The X-rays are produced by a rhodium X-ray tube, operated with a high voltage of 50 kV and an anode current of 642 μA . 500 μm Al are used as primary filter and the collimated X-ray beam has a spot size of about 1 mm diameter on the sample surface. Spectra are recorded with a cooled silicon drift detector with a measurement time of 100 s for each measurement point. On both samples, DM0150A and DM0149A, 15 measurements are recorded at the same position close to the center of the sample to get information about the measurement reproducibility. Then, a grid of 10×10 measurements over the whole sample is measured once and a smaller grid of 5×5 measurement points close to the sample center is measured 6 times.

Mass depositions of the samples are quantified with a fundamental parameter based,

3. THERMOELECTRIC NANOFILMS

Table 3.1.: Quantification results of the thermoelectric nanofilms obtained from 15 single measurements on the same spot close to the sample center. The uncertainties are the ones given by the device. The standard deviation σ is calculated from the 15 single measurements.

	DM0150A		DM0149A	
	mean	σ	mean	σ
$\hat{m}_{\text{Au}} / (\text{ng} \times \text{cm}^{-2})$	600 \pm 300	76.2	600 \pm 300	72.7
$\hat{m}_{\text{Cu}} / (\text{ng} \times \text{cm}^{-2})$	23600 \pm 300	197.4	22100 \pm 300	309.4

standardless method (Section 2.1.2) implemented in the device software WinFTM of the manufacturer. The mean value for the mass depositions \hat{m} for Cu and Au of the 15 measurements of both samples are displayed in Table 3.1. Because of the very low quantities of Au, the uncertainties calculated by WinFTM are very high (50%) and indicate the limits of the device sensitivity. Assuming bulk density for Cu (8.96 g/cm^3), the quantified mass depositions can be used to roughly estimate a layer thickness of 26 nm and 25 nm for DM0150A and DM0149A, respectively. As will be seen in Chapter 4 and 6.3.4, the nanofilms are strongly oxidized, which reduces the layer density and leads to an increased geometrical layer thickness.

In Figure 3.3, the results of the 10×10 mapping are shown for sample DM0150A in a) and c) and for DM0149A in b) and d) for Cu and Au, respectively. Furthermore, the positions of the 5×5 area scan and of the 15 single measurements are indicated. To make statistically relevant deviations in the mass deposition visible, the color scale in the plot is graded in units of 4 times the standard deviation σ of the respective 15 measurements on the same spot (see Table 3.1). That means, for a mass deposition in the middle of the border of one color, a measurement of the same mass deposition will in $\approx 95\%$ ($\pm 2\sigma$ area) be displayed in the same color. As can be seen for the 10×10 mapping of Cu, the deposited material decreases slightly towards the edges. Obviously, a single rotation by 180° is not sufficient to account for the non-uniformity of the plasma during magnetron sputtering. In both the 10×10 mappings for Au in c) and d), the statistics is not sufficient for a statement concerning the homogeneity. Only the edges of the sample are visible, similar as in a) and b).

The results of the 5×5 mapping of both samples is shown Figure 3.4. Plotted are the mean values of the mass depositions of the 6 measurements on each of the 5×5 positions. The color scale is graded in units of 4 times the standard error of the mean $\sigma_m = \sigma / \sqrt{6}$, using again σ from the 15 measurements on the same spot. Thus, the results have a reduced statistical uncertainty and the probability of changes in the color of each measurement point due to statistics alone are again $< 5\%$. In Figures 3.4 a) and

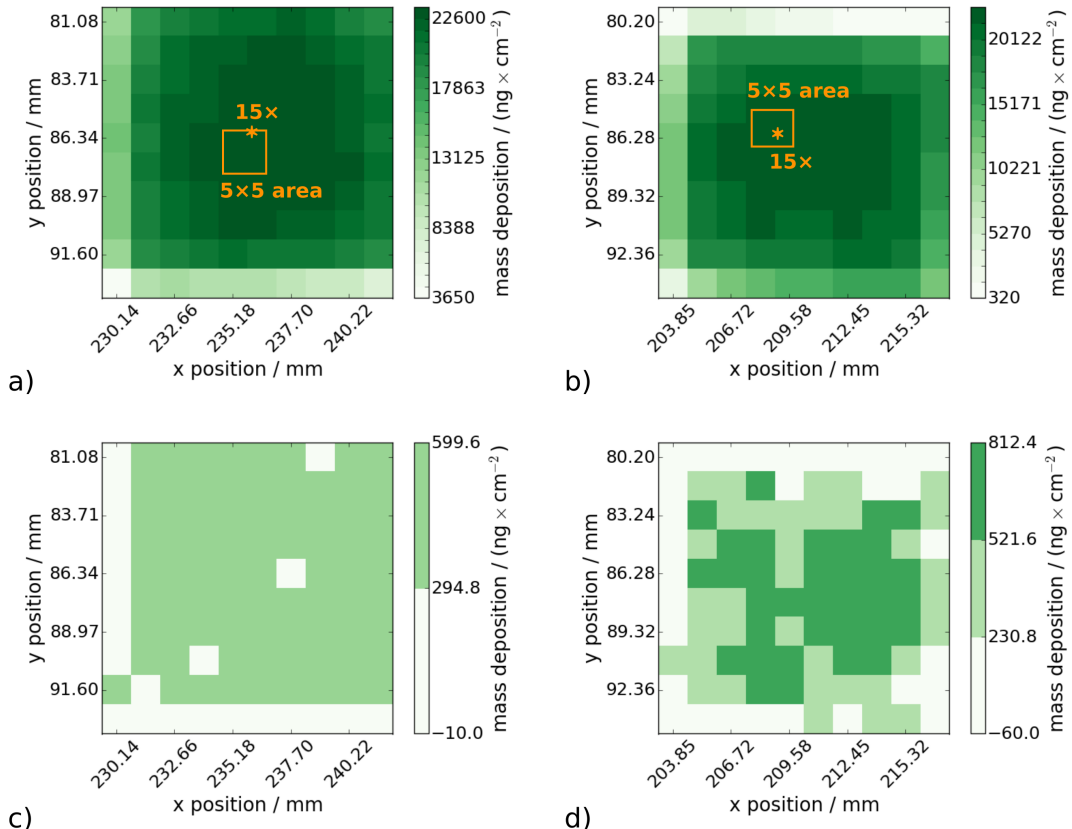


Figure 3.3.: 10×10 mappings of DM0150A (left) and DM0149A (right). The top graphs show the Cu and the bottom graphs the respective Au distributions. In a) and b) the areas of the 5×5 mapping and the position of the 15 measurements on the same spot are indicated.

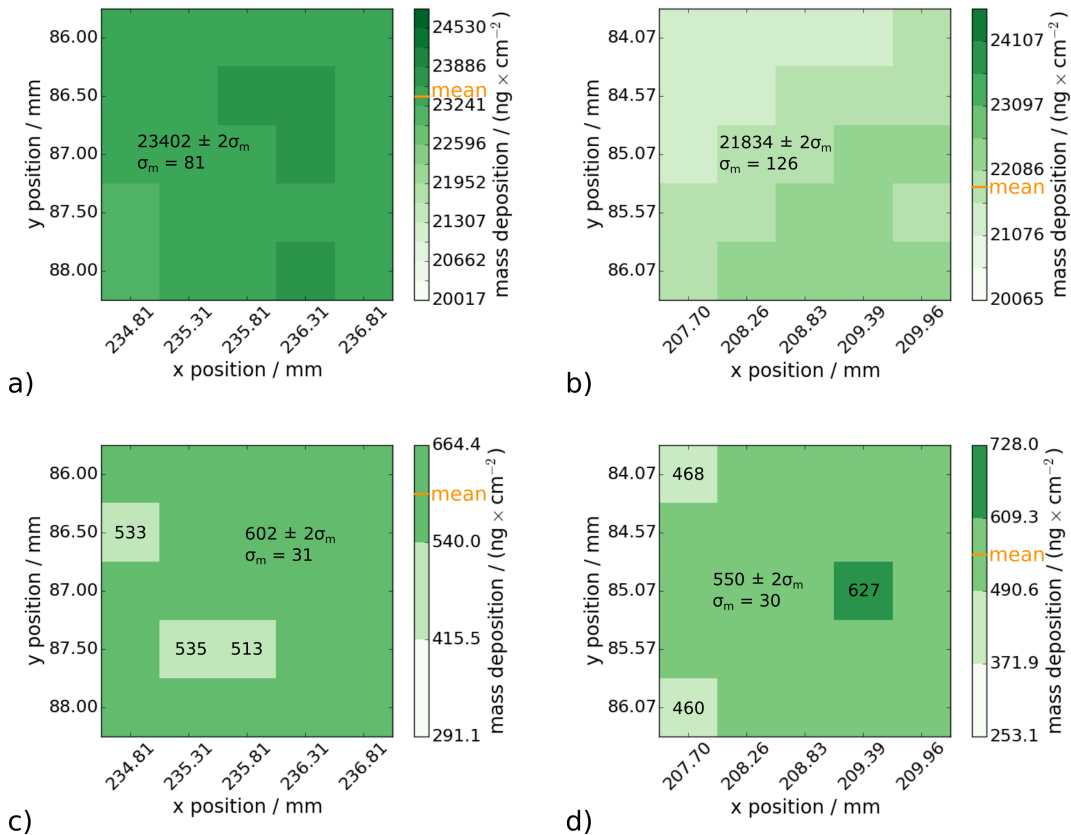


Figure 3.4.: 5×5 mapping of DM0150A (left) and DM0149A (right). For each position, the mean values of 6 measurements of the mass depositions for Cu (top) and Au (bottom) are displayed. The mean over the whole area is shown in the color bar.

b), the gradient of the Cu mass deposition is resolved, showing reduced values towards the bottom left for DM0150A and top left for DM0149A. This is consistent with the positions of the 5×5 grids indicated in Figure 3.3. Concerning the Au mass depositions in Figure 3.4 c) and d), the values are laterally homogeneous for both samples with respect to the statistical resolution. Only three values in both mappings are not within the $\pm 2\sigma_m$ confidence interval (deviation from mean value $< 10\%$), but would be included in a $\pm 3\sigma_m$ interval. Considering also the expected gradient of the mass deposition, there is no clear evidence for inhomogeneities of the Au mass deposition with respect to the resolution of the method. To enhance the latter, more extensive mappings on the sample could be performed. For example, to achieve in a 5×5 grid a $\pm 2\sigma_m$ confidence interval, which refers to $< 3\%$ of the mean value, the measurement must be repeated ≈ 60 times. This leads to vast measurement times of > 10 days, which is inconvenient, but possible with a laboratory setup and could be pursued in future work.

Also, the use of suitable standards could reduce the uncertainties of the determined mass depositions, which might be especially of interest for the amount of gold in the layers. However, appropriate reference materials are not readily available, yet.

4. Synchrotron Radiation based Analysis

So far, XRF analysis for the characterization of the thermoelectric nanofilms are performed in the hard X-ray range by tube excitation. Total mass depositions and their lateral homogeneity are investigated in the previous chapter, but neither access to the copper oxidation state nor to inhomogeneity in depth with nanometer resolution can be achieved with the available commercial equipment. These properties can be analyzed with soft X-rays for the effective excitation of light elements and by using advanced, angular and energy resolved XRF methods at synchrotron radiation facilities. In the scope of this thesis, grazing incidence (GI-) XRF and near edge X-ray absorption fine structure (NEXAFS) measurements are performed at the laboratories of the Physikalisch Technische Bundesanstalt (PTB) at the synchrotron radiation facility BESSY II in Berlin. Furthermore, the dedicated, fully calibrated instrumentation available there enables reference-free quantification (Section 2.1.2) in the soft and hard X-ray regime, which can be compared to the prior laboratory based approach. After describing the applied instrumentation and methodology, the following chapters will present quantitative and qualitative structural and chemical differences between the non-tempered and tempered thermoelectric nanofilms DM0150A and DM0149A.

4.1. Instrumentation

4.1.1. Beamlines

The analysis of the thermoelectric copper oxide nanofilms is carried out in the hard X-ray range to get access to Au-L and Cu-K fluorescence as well as in the soft X-ray range to efficiently excite O-K fluorescence. Therefore, measurements at three different beamlines at BESSY II in Berlin are performed, which are shortly described in the following.

The plane-grating monochromator (PGM) beamline [86] is using the radiation of the undulator U49. The beamline provides monochromatic X-ray photons with energies from 78 eV to 1870 eV and a resolving power $E/\Delta E$ from 1000 to 9000 [42], depending on the angular settings of the grating. Higher order contributions from the undulator and stray light are suppressed by total reflection at the mirrors acting as low-pass filters and further optional transmission filters and apertures. At a typical electron current in the

synchrotron storage ring of 200 mA, the photon flux reaches from 6×10^9 photons/s at 1.7 keV to 6×10^{11} photons/s at 400 eV [87]. The focus, which is usually the place where the sample in the endstation is aligned, has a size (FWHM) of 40 μm (vertical) \times 40–600 μm (horizontal), adjustable by means of an aperture. Further details can also be found in [88, 89].

The KMC beamline facilitates a four-crystal monochromator after the dipole magnet D71, providing monochromatic radiation between 1.75 keV and 10.5 keV [90, 91]. Due to the four Bragg reflections in InSb(111)- or Si(111) crystals, a resolving power $E/\Delta E$ of ≈ 4000 to 12000 can be achieved and again higher orders and stray light are suppressed by total reflection on various mirrors and transmission filters. The photon flux is about 10^{10} photons/s over the whole spectral range and can be monitored with a thin transmission diode when using X-rays with energies above 3 keV.

Finally, the BAMline beamline, operated by the Bundesanstalt für Materialforschung (BAM), uses a superconducting 7 T wavelength shifter to produce photons with energies from 6 keV to 60 keV [92, 93]. The beam is monochromatized either by a double-multilayer monochromator ($E/\Delta E \approx 40$) for high photon flux applications or by a double-crystal monochromator ($E/\Delta E$ up to 1000) if energy resolution is more important. In the beamline, a focusing mirror with variable curvature radius is applied, allowing for adjustable focus size in the horizontal direction from 185 mm down to 1 mm. The photon flux density with a focused beam reaches 5.7×10^{10} photons/(s \times mm 2) and can be monitored with an ionization chamber.

4.1.2. Endstations

All experiments are carried out under vacuum conditions to minimize absorption of primary and fluorescent X-rays. Two different vacuum chambers are used to realize the various geometries of the applied experiments with respect to incident beam position, sample alignment and diagnostics (see schematic in Figure 4.1). The measurements at the BAMline are carried out with the smaller of the two spectrometer chambers because of spatial restrictions. It is usually applied for reference-free quantification in conventional XRF geometry, i.e. with an incident and detection angle of 45° [87, 94]. To improve the excitation conditions for the thermoelectric nanofilms, the chamber is mounted to the beamline with a tilt of about 45°, enabling shallow incident angle conditions. The sample holder can only be moved in the sample plane, which permits precise angular resolved measurements.

The second, larger, spectroscopy chamber [95] is more flexible concerning the measurement geometry and is applied in the measurements at the KMC and PGM beamlines. The sample can be aligned and positioned with an 8-axes goniometer providing all 6

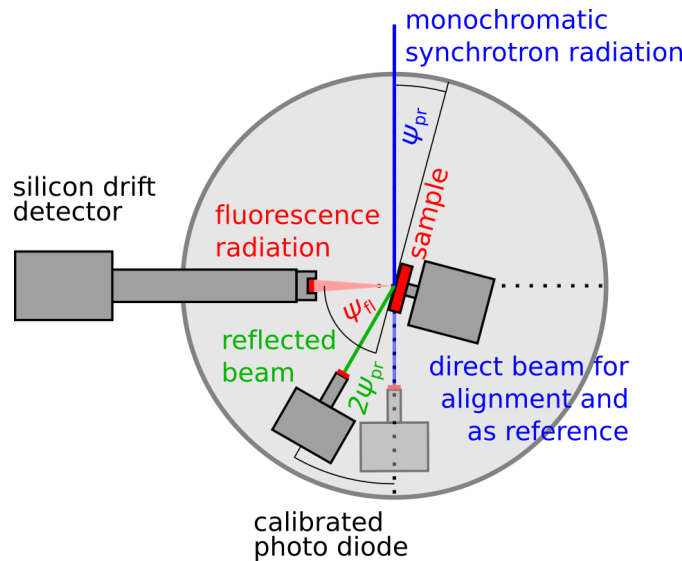


Figure 4.1.: Schematic view of the vacuum chambers and possible measurement geometries for the XRF experiments carried out at the laboratories of the PTB.

degrees of freedom for the sample (3 translational and 3 rotational axes) and two more axes for rotation and translation of a diode on a second goniometer arm. Therefore, not only GIXRF experiments can be performed by aligning the sample in the pivotal point of the goniometer and changing the incident angle of the radiation by a rotation of the sample. Also X-ray reflectometry measurements (XRR) can be applied simultaneously by changing the angular position of a photo diode on the second goniometer arm twice as fast as the sample angle. The whole vacuum chamber can be moved with respect to its base frame, which is of importance for the alignment with respect to the beamline and helpful to measure the sample-to-detector distance. The latter is important to calculate the solid angle of detection applied in GIXRF measurements and reference-free quantification.

4.2. Data Recording and Treatment

To quantify XRF spectra of a sample with a reference-free fundamental parameter approach, all the instrumental parameters in Equation 2.1.1 have to be known. These are the incident number of photons $N_{\text{pr}}(E_{\text{pr}})$, the detection efficiency $\epsilon_{\text{det}}(E_{i,j})$ (usually of a silicon drift detector) for all fluorescence photon energies $E_{i,j}$ used in the quantification and the setup geometry, i.e. the effective solid angle of detection Ω as well as the incident and detection angles ψ_{pr} and ψ_{fl} . Especially the geometry is of major importance for the analysis of GIXRF measurements, which is obvious for ψ_{pr} , but also Ω varies strongly

4. SYNCHROTRON RADIATION BASED ANALYSIS

with ψ_{pr} (for small ψ_{pr}) and affects the shape of the GIXRF profiles.

During the measurements, the incident flux on the sample is monitored by e.g. a thin photo diode, which is calibrated shortly before or after the measurement against the calibrated photo diode behind the sample. Thus, the absolute photon flux on the sample can be calculated. The fluorescence spectra are recorded with a calibrated SDD with known efficiency and detector response function. The life time of the measurement is derived from the zero peak of the SDD detector, which is increased by the SDD's electronics during the measurement.

To get access to Ω , ψ_{pr} and ψ_{fl} , a precise alignment of the spectroscopy chamber and of the sample is necessary. This is performed by routine procedures developed at the PTB X-ray spectrometry division. At first, the center positions of all samples mounted on the sample holder are aligned by horizontal and vertical line scans with the synchrotron beam. The center position is then defined by the middle of the edge positions of the line scans, which are indicated by the decrease of fluorescence intensity measured with an SDD. Thus, the measurement position of the thermoelectric copper oxide nanofilms is indeed the center of the sputtered area and not the center of the somewhat larger silicon wafer. The surface of the sample is aligned by radial scans and recording the direct synchrotron beam with a photo diode behind the sample, similar to a knife-edge scan, but with the whole sample surface. The aligned position concurs with an intensity drop by 50%. To align the sample surface parallel to the incident beam, the shadowing of the incident beam by the sample is minimized by rotating the sample about the vertical axis. To increase the accuracy, the two procedures (radial and rotational scan) can be repeated iteratively.

The solid angle of detection is determined by the detector geometry (chip size, aperture and distance) and the irradiated area on the sample (footprint). The footprint is stretched by a factor $1/\sin(\psi_{\text{pr}})$ in the horizontal direction because of the projection of the incident beam onto the sample surface. Therefore, for shallow angles and depending on the detector distance, the footprint might well exceed the field of view of the detector or the sample dimension itself. For example, with a typical horizontal beam diameter of 140 μm at the PGM beamline, below 0.6°, the footprint exceeds the 1.4 cm length of the thermoelectric nanofilms of DM0149A and DM0150A. This needs to be taken into account by calculating an effective solid angle of detection [42]

XRF spectra can be simulated with physical models of the background and delta functions for the fluorescence peaks, convolved with the measured detector response function of the SDD. This allows to fit simulated spectra to the measured spectra by adjusting the intensities of the fluorescence lines and the background functions. As background models, besides the Rayleigh scattered peak, resonant Raman scattering

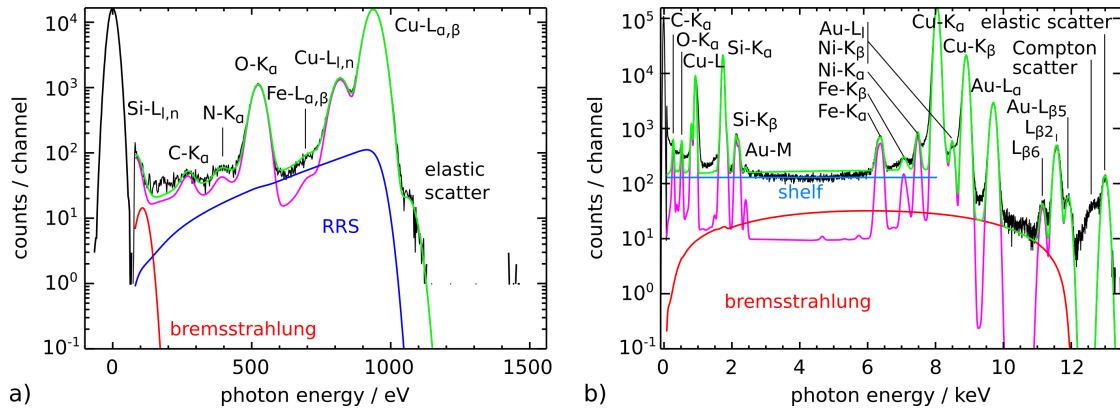


Figure 4.2.: Energy-dispersive spectra of sample DM0149A excited with a) 1060 eV at the PGM beamline and b) 13 keV at the BAMline beamline. Deconvolution is performed with physical background models and detector response functions.

(RRS) [96, 97] and bremsstrahlung [98] are calculated for sample matrices and incident energies as appropriate.

Figure 4.2 a) and b) show exemplarily the energy-dispersive spectra of sample DM0149A recorded at 1060 eV and 13 keV, respectively. In the spectra recorded at the PGM beamline (Figure 4.2 a)), the background due to bremsstrahlung is calculated for the copper oxide layer and resonant Raman scattering for the Si substrate. The fit of physical background and X-ray line contributions is in excellent agreement with the measured data. Besides the prominent contributions from $\text{Cu-L}_{\alpha,\beta}$, $\text{Cu-L}_{l,n}$, O-K_{α} and $\text{Si-L}_{l,n}$, minor contributions of carbon, nitrogen (surface contamination) and probably iron (perhaps originating from secondary excitation of the detector housing) might be present. The spectrum in Figure 4.2 b) is recorded at 13 keV at an incident angle of $\approx 0.05^\circ$. Because of the low transmittance of the thermoelectric nanofilm for the primary radiation at these shallow angles ($< 10\%$), the bremsstrahlung background is calculated for Cu. Furthermore, no RRS background appears, but a further detector shelf for the most intense line (Cu-K_{α}) has to be considered to achieve a satisfactory fit. In the low energy part of the spectrum (below 2 keV), further constant contributions to the background might improve the spectrum fitting in this region. They are not applied here, since only the high energy region is used for the quantification. In the spectrum, Cu-K_{α} , Cu-K_{β} , Au-L_{α} , Au-L_l , $\text{Au-L}_{\beta 2}$, Si-K_{α} and the Cu-L lines are prominent. Furthermore, contributions of C, Ni and Fe are visible, the latter two probably originating from the sample holder itself or as above from the detector housing. Note that the excitation energy is below the Au-L_2 edge, preventing fluorescence originating from Au-L_1 and Au-L_2 vacancies.

For the following quantification approaches, which are fully based on fundamental parameters (FPs), the overall uncertainties are dominated by the uncertainties of these

fundamental parameters. In Appendix C, a list of the applied FP uncertainties from Krause and the compilation of Zschornack [99, 100] is given. In principle, uncertainties are increased for light elements and low energy X-rays.

4.3. Integral Quantification

The absolutely calibrated instrumentation at the laboratories of the PTB allow to quantify mass depositions with XRF without the need of calibration standards. This is particularly of interest for sample systems, where such calibration standards are not readily available, as is the case for the thermoelectric nanofilms investigated in this thesis. For this purpose, measurements at the PTB laboratories are performed using 4 different excitation energies to optimally excite the components of the nanofilms, namely O-K and Cu-L lines at 1060 eV provided by the PGM beamline, Cu-K and Au-M lines at 10 keV of the KMC beamline and finally Cu-K and Au-L lines at 13 keV and 17 keV at the BAMline beamline. All spectra are deconvolved with the PTB software described above (Section 4.2) to get the net peak areas. The complete quantification is then realized in the following successive steps.

The measurements at the BAMline beamline are performed at 13 keV and 17 keV at shallow incident angles of about 0.05° to efficiently excite the thermoelectric nanofilm. Thus, the detection angle ψ_{fl} is almost 90° , minimizing self-absorption of the detected fluorescence radiation. For this beamtime, no absolutely calibrated instrumentation is applied. Therefore, the measurements cannot be used to quantify the gold and copper mass depositions directly. However, if Au is homogeneously distributed in depth in the copper oxide nanofilm and if self-absorption of the fluorescence radiation can be neglected, the Au to Cu atom ratio can be obtained from the measurements. The first condition is at least roughly fulfilled, as will be seen in the GIXRF measurements in Section 4.5. The latter condition is also true for both fluorescence energies (Cu-K_α and Au-L_α), since the transmission through even a solid 50 nm thick copper layer (which is a conservative estimate) is about 99% (calculated with FPs from [39]). By using initially the second condition, the absorption term of the fluorescence radiation in μ^* can be

neglected in Equation 2.1.1 in Section 2.1.1, resulting in

$$\begin{aligned}
 \text{I : } N_{\text{Au},j_1} &= N_{\text{pr}}(E_{\text{pr}}) G(E_{\text{Au},j_1}) \xi_{\text{Au},j_1,s_1}(E_{\text{pr}}) \\
 &\quad \times \int_0^d \rho(x) C_{\text{Au}}(x) \exp \left(- \int_0^x \frac{\mu_{\text{tot}}(E_{\text{pr}}, x') \rho(x')}{\sin(\psi_{\text{pr}})} dx' \right) dx \\
 \text{II : } N_{\text{Cu},j_2} &= N_{\text{pr}}(E_{\text{pr}}) G(E_{\text{Cu},j_2}) \xi_{\text{Cu},j_2,s_2}(E_{\text{pr}}) \\
 &\quad \times \int_0^d \rho(x) C_{\text{Cu}}(x) \exp \left(- \int_0^x \frac{\mu_{\text{tot}}(E_{\text{pr}}, x') \rho(x')}{\sin(\psi_{\text{pr}})} dx' \right) dx
 \end{aligned} \tag{4.3.1}$$

Note the second integral appearing in the factor responsible for the attenuation of the primary radiation due to Lambert-Beer's law, which is now valid for an (in depth) inhomogeneous layer. If gold and copper are similarly distributed in depth, i.e. $C_i(x) = C_i \times f(x)$, then the depth independent concentration factor C_i can be written in front of the integral, which is then the same for (I) and (II), resulting in

$$\begin{aligned}
 \text{I : } \frac{N_{\text{Au},j_1}}{N_{\text{Cu},j_2}} &= \frac{\epsilon_{\text{det}}(E_{\text{Au},j_1})}{\epsilon_{\text{det}}(E_{\text{Cu},j_2})} \times \frac{\xi_{\text{Au},j_1,s_1}(E_{\text{pr}})}{\xi_{\text{Cu},j_2,s_2}(E_{\text{pr}})} \times \frac{C_{\text{Au}}}{C_{\text{Cu}}} \\
 \Leftrightarrow \frac{C_{\text{Au}}}{C_{\text{Cu}}} &= \frac{N_{\text{Au},j_1}}{\epsilon_{\text{det}}(E_{\text{Au},j_1}) \xi_{\text{Au},j_1,s_1}(E_{\text{pr}})} \times \left(\frac{N_{\text{Cu},j_2}}{\epsilon_{\text{det}}(E_{\text{Cu},j_2}) \xi_{\text{Cu},j_2,s_2}(E_{\text{pr}})} \right)^{-1}
 \end{aligned} \tag{4.3.2}$$

The last row in Equation 4.3.2 shows that the Au-to-Cu mass ratio can be calculated by the ratio of the detected net peak areas $N_{i,j}$ corrected by the detector efficiency $\epsilon_{\text{det}}(E_{i,j})$ and normalized to the fluorescence production cross sections $\xi_{i,j,s}$. Dividing the Au-to-Cu mass ratio by the Cu-to-Au atomic weight ratio yields the relative number of atoms for gold and copper in Table 4.1. It can be stated that there is 1 gold atom for every 100 copper atoms in the sample.

The absolutely calibrated measurements at the KMC beamline at 10 keV can be used to quantify the absolute copper mass deposition directly and thus, with the information of the Au-to-Cu mass ratios, also the absolute mass deposition for gold. For the quantification, the Cu-K α line is used and its net peak area calculated from the deconvolved spectrum. The intensity is normalized with respect to incoming photon flux, measurement time, detector efficiency and solid angle of detection. Then, the xrfLibrary is used to calculate the fluorescence intensity of a single layered, single element sample for the fluorescence lines, which are not separable in the measured spectrum (Cu-K α_1 and Cu-K α_2). A fit of the mass deposition of that layer, so that the calculated and measured fluorescence intensities are the same, yields the quantification results for Cu

Table 4.1.: Quantification results for the relative atomic fractions of Au to Cu atoms obtained from the measurements on the thermoelectric nanofilms DM0150A and DM0149A (tempered) at the BAMline (BAM) and absolute mass depositions \hat{m} measured at the KMC beamline (KMC). \hat{m}_{Au} is not measured directly, but calculated from \hat{m}_{Cu} and the relative atomic fractions.

m	energy	DM0150A	DM0149A
$C_{\text{Au}}^{\text{at}} / C_{\text{Cu}}^{\text{at}}$	13 keV (BAM)	$1.04\% \pm 0.12\%$	$0.99\% \pm 0.11\%$
$C_{\text{Au}}^{\text{at}} / C_{\text{Cu}}^{\text{at}}$	17 keV (BAM)	$1.07\% \pm 0.12\%$	$0.98\% \pm 0.11\%$
$\hat{m}_{\text{Au}} / (\text{ng} \times \text{cm}^{-2})$	10 keV (KMC)	580 ± 80	560 ± 80
$\hat{m}_{\text{Cu}} / (\text{ng} \times \text{cm}^{-2})$	10 keV (KMC)	18900 ± 1400	18500 ± 1300

in Table 4.1*. The mass deposition for Au is calculated with the evaluated Au-to-Cu mass ratio.

The quantification for Au and Cu obtained from the measurements with the conventional laboratory setup in Chapter 3 resulted in $(23600 \pm 300) \text{ ng/cm}^2$ and $(22100 \pm 300) \text{ ng/cm}^2$ for Cu in the center of DM0150A and DM0149A, respectively. The gold mass deposition is for both samples $(600 \pm 300) \text{ ng/cm}^2$. Thus, there are small but significant discrepancies between the quantified Cu mass depositions with the laboratory setup and the fully FP based synchrotron measurements. Probably the uncertainties are slightly underestimated either for the FPs used in the reference-free approach and or the uncertainties of the commercial device. The latter is usually used for the determination of layer thicknesses in the 100 nm to μm range and probably working at its limit, when analyzing films with tens of nm thicknesses.[†] The quantification results for Au of both approaches (commercial setup and reference-free) agree within their uncertainties. Here, the commercial device gives huge uncertainties of up to 50%, indicating the limitation with respect to sensitivity. The results might be improved, if reference materials were available.

The next quantification step concerns the oxygen content in the two samples. Due to the tempering process applied to DM0149A, a difference in the oxygen concentration in both samples is expected. To get access to the oxygen concentration, XRF measurements need to be performed in the soft X-ray range.

The thermoelectric nanofilms DM0150A and DM0149A are deposited on silicon wafers.

* As fitting algorithm, the Levenberg-Marquardt least-squares fit implemented in the python function `curve_fit` of the package `scipy.optimize` is used.

[†] Interestingly, and as will be seen later in Section 4.5.2, the quantification approach of the Cu mass deposition with the GIXRF measurements ($(22600 \pm 800) \text{ ng/cm}^2$ for DM0150A and $(20500 \pm 1200) \text{ ng/cm}^2$ for DM0149A), which is less dependent on correct FPs, rather supports the values obtained by the commercial device.

Table 4.2.: Quantification results for atomic fractions and mass depositions of Au, Cu and O in the thermoelectric thin films DM0150A and DM0149A obtained at the PGM beamline with 1060 eV primary photons. Carbon rich contaminants with a mass deposition \hat{m}_C are presumably found on top of the thermoelectric layer. The quantification results for the oxygen mass deposition $\hat{m}_O(\text{SiO}_2)$ of the SiO_2 native layer on top of the Si wafer, measured next to the thermoelectric layers, are also shown.

	DM0150A	DM0149A
$\hat{m}_C / (\text{ng} \times \text{cm}^{-2})$	1600 ± 200	970 ± 120
$\hat{m}_{\text{Au}} / (\text{ng} \times \text{cm}^{-2})$	600 ± 170	560 ± 160
$\hat{m}_{\text{Cu}} / (\text{ng} \times \text{cm}^{-2})$	18000 ± 5000	18000 ± 5000
$\hat{m}_O / (\text{ng} \times \text{cm}^{-2})$	3800 ± 800	4300 ± 900
$C_{\text{Au}}^{\text{at.}\%}$	0.57 ± 0.17	0.51 ± 0.15
$C_{\text{Cu}}^{\text{at.}\%}$	50 ± 20	50 ± 20
$C_O^{\text{at.}\%}$	45 ± 9	48 ± 10
$\hat{m}_O(\text{SiO}_2) / (\text{ng} \times \text{cm}^{-2})$	200 ± 40	230 ± 50

Since the wafers have been stored in ambient conditions, a native silicon dioxide surface layer with nm thickness can be expected. To account for the oxygen signal originating from the SiO_2 , XRF measurements are performed just next to the sputtered sample area on the same wafer material for both samples DM0149A and DM0150A. The quantification is performed as above but for a single SiO_2 layer and using the mass deposition of oxygen as fitting parameter for the adjustment of the O-K_α fluorescence intensity. The results are shown in Table 4.2. The mass depositions can be calculated to more descriptive layer thicknesses, if assuming pure SiO_2 with a density of 2.65 g/cm^3 . In that case, the wafers of DM0149A and DM0150A have SiO_2 capping layers of $(1.6 \pm 0.5) \text{ nm}$ and $(1.4 \pm 0.5) \text{ nm}$, indicating no significant increase in the native oxide layer from the tempering process. The quantified SiO_2 layers will be included in the model for the oxygen quantification of the thermoelectric nanofilms. Furthermore, the spectra of the PGM beamline measurements show contributions from a carbon signal. This signal originates probably from some surface contamination (thin organic layer or dust particles) and is also quantified in a similar approach as the SiO_2 layers. The results (also shown in Table 4.2) show that there is approximately about 50% more carbon contamination present on DM0150A as compared to DM0149A. Assuming a homogeneous layer with a density of amorphous carbon of 2 g/cm^3 , the measured mass depositions refer to contamination thicknesses of $(4.9 \pm 0.6) \text{ nm}$ on DM0149A and $(8.0 \pm 1.0) \text{ nm}$ on DM0150A.

Because of the native silicon dioxide layer and non-negligible self-absorption in the

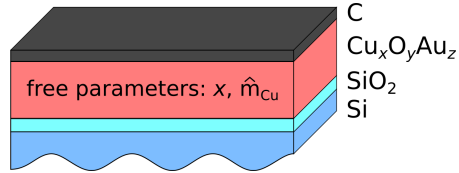


Figure 4.3.: Sample model used for the integral quantification of copper mass deposition \hat{m}_{Cu} and atomic fraction x .

sample matrix, a more complex model than a single layered, single element sample has to be applied for the quantification of the integral composition of the thermoelectric nanofilms. It consists of a carbon contamination layer, the gold doped copper oxide layer ($\text{Cu}_x\text{O}_y\text{Au}_z$) itself with a fixed Au-to-Cu ratio ($z = x \times C_{\text{Au}}^{\text{at}}/C_{\text{Cu}}^{\text{at}}$) and the measured native silicon dioxide layer on the silicon wafer (Figure 4.3). Since $y = 1 - x - z$, the atomic concentration of copper x and the mass deposition of copper \hat{m}_{Cu} are the only independent parameters. They can be calculated by a fit of the O-K $_{\alpha}$ and Cu-L $_{\alpha,\beta}$ intensities. The results of the quantification are also shown in Table 4.2. First of all, it can be stated that the quantified mass deposition of Cu is in agreement with the values obtained at 10 keV (Table 4.1). However, due to the high uncertainties of the FPs used in the quantification, uncertainties for the absolute quantified mass depositions reach up to almost 30%. Nevertheless, when comparing the results of both samples to each other, the similar excitation conditions and sample composition will also have similar effects on the actual FP values, so that uncertainties in the direct comparison can be expected to be much less. Thus, the increased measured oxygen concentration from 45 at.% to 48 at.% in the tempered sample DM0149A can be expected to be significant and is most likely resulting from ongoing oxidation during the tempering process. The results also show that even for the non-tempered sample a high oxygen concentration is found, indicating the oxidation of the Cu nanofilm due to the exposure to air, which is also described in [101, 16].

4.4. Qualitative GIXRF-NEXAFS

Already the results of the quantitative XRF analysis show an induced oxidation in the thin copper film of sample DM0149A due to the tempering process. This oxidation is further analyzed with qualitative near edge X-ray absorption fine structure (NEXAFS) measurements at the Cu-L₂ and Cu-L₃ edges with different shallow angles of incidence to tune the information depth. Since the Cu-L edges are probed, the measurements are performed at the PGM beamline. All samples are measured at their center positions. For each NEXAFS scan, the energy of the excitation radiation is scanned from 925 eV to

970 eV with energy steps of 0.25 eV. Measurement time is 15 s per point, resulting in a total measurement time of about 45 minutes. The fluorescence radiation is detected with an SDD detector in 90° geometry to the excitation beam. The recorded XRF spectra are deconvolved with the PTB software using a physical background (bremsstrahlung and resonant Raman scattering) and the detector response function. No normalization to detector efficiency or solid angle of detection need to be applied, since only relative fluorescence intensities are of interest.

To discuss and interpret the NEXAFS spectra, two reference samples, pure CuO and Cu₂O, are measured. For the references, powders of pure Cu₂O (from Sigma Aldrich) and CuO (from storage of the research group of Prof. Rademann) are pressed with potassium bromide to pallets, applying 5 tons pressure by a hydraulic lever press. They are mounted and aligned along with the two thermoelectric samples DM0150A and DM0149A on the sample holder. The references are measured with a shallow incidence angle of 5° to apply similar measurement conditions as for the thermoelectric nanofilms. The latter are also measured at several shallow incidence angles (0.8°, 3.4° and 15.0° for DM0150A and 0.8°, 1.5°, 3.4° and 15.0° for DM0149A) to tune the information depth.

By changing the energy of the incident radiation over the absorption edge of the main component of the thermoelectric nanofilms, the penetration depth of the radiation is varied. This leads to a variation of the number of excited Cu atoms during the energy scan. Therefore, the intensity of the Cu fluorescence is not purely dependent on the change of the absorption coefficient, but also on the number of Cu atoms in the excitation volume. This self-absorption effect of the incident radiation can deform the NEXAFS spectra and several approaches to correct for it can be found in the literature [102, 103, 104, 105]. Usually, the self-absorption correction is performed by using tabulated values or reference measurements of the attenuation coefficients and applying them to fluorescence calculations (using Equation 2.1.1) of a known sample composition. In the following, a less complex self-absorption correction is applied to the measured copper oxide nanofilms and shortly motivated.

A simple approximation for a self-absorption correction is performed by normalizing the fluorescence intensities of the Cu signal to the O-K_α intensities. Since in the scanned energy range the absorption coefficient for oxygen is almost constant, the normalization to the fluorescence intensity of O-K_α is effectively a normalization to the number of excited oxygen atoms. In the case of constant concentrations of O and Cu throughout the whole thermoelectric layer, this normalization would account for the variation of penetration depth of the incoming X-ray beam and thus correct for self-absorption, as can be seen by applying the assumptions to the Sherman equation. Before integration, the Sherman equation (Equation 2.1.1) in Section 2.1.1 yields

$$\begin{aligned}
 N_{i,j} &= N_{\text{pr}}(E_{\text{pr}}) G(E_{i,j}) \xi_{i,j,s}(E_{\text{pr}}) \\
 &\quad \times \int_0^d \rho(x) C_i(x) \exp \left(- \int_0^x \mu_{\text{tot}}^*(E_{\text{pr}}, E_{i,j}, x') \rho(x') dx' \right) dx,
 \end{aligned}$$

with

$$\mu_{\text{tot}}^*(E_{\text{pr}}, E_{i,j}, x') = \frac{\mu_{\text{tot}}(E_{\text{pr}}, x')}{\sin(\psi_{\text{pr}})} + \frac{\mu_{\text{tot}}(E_{i,j}, x')}{\sin(\psi_{\text{fl}})}, \quad (4.4.1)$$

if assuming a depth dependent sample composition for now.

Thus, because of the dependence of $\mu_{\text{tot}}^*(E_{\text{pr}}, E_{i,j}, x')$ on the primary photon energy, the detected number of fluorescence photons $N_{i,j}$ is not directly proportional to the absorption coefficient $\tau_{i,s}(E_{\text{pr}})$ in $\xi_{i,j,s}(E_{\text{pr}})$. In the following, the effect of the normalization to the oxygen fluorescence intensity is considered. First, self-absorption of the fluorescence radiation is small compared to the absorption of primary radiation, due to shallow incident and steep detection angles. If therefore approximating $\mu_{\text{tot}}^* \approx \mu_{\text{tot}}(E_{\text{pr}}, x')/\sin(\psi_{\text{pr}})$, the ratio of the copper and oxygen fluorescence is

$$\begin{aligned}
 \frac{N_{\text{Cu},j_1}}{N_{\text{O},j_2}} &= \frac{G(E_{\text{Cu},j_1}) \xi_{\text{Cu},j_1,s_1}(E_{\text{pr}})}{G(E_{\text{O},j_2}) \xi_{\text{O},j_2,s_2}(E_{\text{pr}})} \\
 &\quad \times \int_0^d \rho(x) C_{\text{Cu}}(x) \exp \left(- \int_0^x \frac{\mu_{\text{tot}}(E_{\text{pr}}, x') \rho(x')}{\sin(\psi_{\text{pr}})} dx' \right) dx \\
 &\quad \times \left(\int_0^d \rho(x) C_{\text{O}}(x) \exp \left(- \int_0^x \frac{\mu_{\text{tot}}(E_{\text{pr}}, x') \rho(x')}{\sin(\psi_{\text{pr}})} dx' \right) dx \right)^{-1} \quad (4.4.2)
 \end{aligned}$$

As can be seen, the outer integral cancels out, but only if indeed the concentrations $C_{\text{Cu,O}}(x)$ are constant for $0 < x < d$. This is surely true for the two reference samples, which are made of a single composition CuO and Cu_2O , respectively. During the NEXAFS experiment, only the primary radiation energy E_{pr} is changed. So with $\xi_{\text{O},j_2,s_2}(E_{\text{pr}}) \approx \text{constant}$ for oxygen in the considered energy range, it follows that the detected count rate ratio is proportional to the photoionization cross section of the Cu-L₃ shell.

$$\begin{aligned}
 \frac{N_{\text{Cu},j_1}}{N_{\text{O},j_2}} &\propto \xi_{\text{Cu},j_1,s_1}(E_{\text{pr}}) \\
 &\propto \tau_{\text{Cu},s_1}(E_{\text{pr}}) \quad (4.4.3)
 \end{aligned}$$

The results of the corrected and not corrected NEXAFS measurements are shown in Figure 4.4 and compared to data from literature [106]. The latter is obtained by X-ray absorption spectroscopy in the total electron yield, thus self-absorption effects should

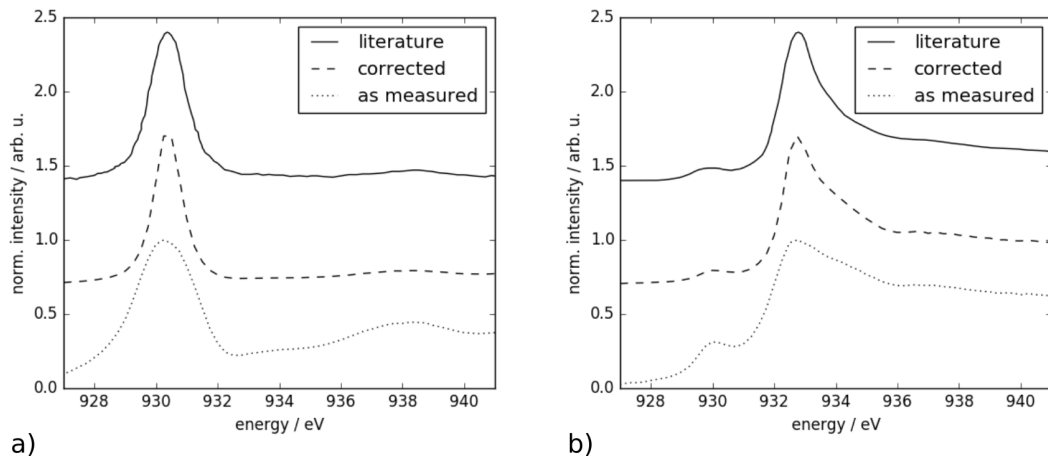


Figure 4.4.: Near edge X-ray absorption fine structure (NEXAFS) spectra at the Cu-L₃ edge of a) CuO and b) Cu₂O. After the applied self-absorption correction, the NEXAFS spectra measured at the PGM beamline (dashed) agree much better to literature [106] (solid) than the NEXAFS profiles without correction (dotted). The literature data is shifted by 0.85 eV to overlap the peaks.

be small [107]*. The energy axes of the literature spectra are both shifted by 0.85 eV to overlay the peak positions to those of the measured data. The energy resolution of the literature data is given with 0.4 eV, which implies that the absolute uncertainty is probably similar or even higher. For the measurements performed at the PGM beamline at BESSY II the energy resolution is similar, so that the energy offset in total might originate from the different energy calibrations. For both materials, the applied self-absorption correction leads to a better agreement of the measured NEXAFS spectra to the literature data, which indicates the validity of the method. The main peak in both, the CuO and Cu₂O spectra, is a transition from Cu 2p_{3/2} into empty d-states [108, 106]. In the spectrum of CuO (Figure 4.4 a)), the peak is at 930.4 eV. Thus, also the small peak at 930 eV in the spectra of Cu₂O (Figure 4.4 b)) might originate from some CuO contributions. This is likewise argued in [106], where also changes in intensity of this peak were detected for different samples. The main peak in the Cu₂O spectra is at 932.8 eV and has a broad shoulder on the high energy side, which is probably caused by a large Cu 2p core-hole potential [109]. Both spectra are well distinguishable and can be used as fingerprint for the two copper compounds in the following investigation of the thermoelectric nanofilms. Here, the normalization to the oxygen K_α fluorescence is applied, too. Even if the assumptions of negligible self-absorption of the fluorescence

* Self-absorption could appear, if shallow incident angles are used such that the excitation depth is comparable to the depth, where electrons are detected from. However, no glancing excitation conditions are mentioned in the respective paper, indicating no special effort by the authors to realize those.

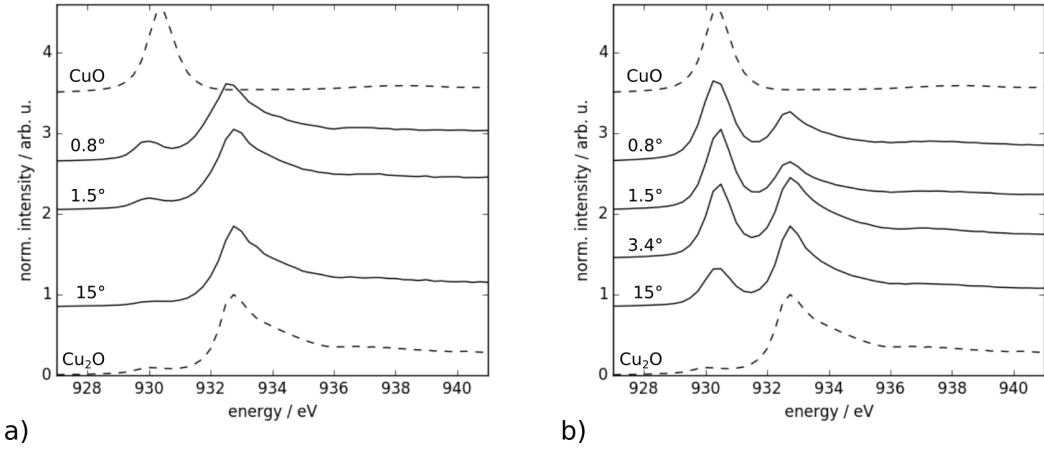


Figure 4.5.: NEXAFS spectra at the Cu-L₃ edge of a) DM0150A and b) DM0149A for various incident angles (solid lines). Also shown are the measured reference spectra for CuO and Cu₂O (dashed lines). All spectra are corrected for self-absorption (see text) and normalized to the intensity of the main peak.

radiation and constant copper and oxygen concentrations are not strictly valid, the normalization leads to a reduction of peak shift and damping induced by self-absorption, similar to the effect on the reference spectra in Figure 4.4.

The NEXAFS profiles of the Cu-L₃ edge for different angles of the incident beam are shown in Figure 4.5 a) for DM0150A and in b) for DM0149A. They are plotted together with the two reference measurements of CuO and Cu₂O with a different offset for each spectrum for reasons of clarity. The 3 spectra of DM0150A are clearly dominated by contributions from Cu₂O, showing that even the non-tempered sample is strongly oxidized, which is also found in the integral quantification in the previous Section 4.3. Only at shallow angles the slightly increasing peak at 930 eV indicates some minor contributions of CuO close to the surface.

In all 4 spectra of sample DM0149A, two peaks, referring to the strong resonances of CuO and Cu₂O, are visible. However, the peak ratio changes, indicating a CuO-rich phase close to the surface (shallow angles) and an increase of Cu₂O contributions with depth (increasing angles). Thus, also the NEXAFS measurements support the findings of the integral quantification (Section 4.3) that the tempering process induced further oxidation. Note that the appearance of both peaks (CuO and Cu₂O) at 15° does not necessarily mean that both oxides are present close to the silicon substrate, since the signal is an integrated information of the different compounds over the whole layer.

As expected, due to the changing concentrations of copper and oxygen in the thermoelectric layers, the applied self-absorption correction is not accurate enough to model

the various spectra by linear combination of references from Cu, Cu₂O and CuO. Especially for the sample DM0149A, where a strong compositional inhomogeneity is seen in the qualitative NEXAFS spectra, attempts of fitting are unsatisfactory. Also, all the other self-absorption correction algorithms mentioned above, can probably not lead to more reliable NEXAFS spectra which could be used for a more quantitative analysis, since they all require a known sample composition. In [89], a differential algorithm for the analysis of two subsequently buried titan oxide layers is validated. The basis of the analysis are NEXAFS measurements with varying incident angles, similar to the measurements performed here. It might be possible to apply an adapted algorithm for the present sample system, but the smooth variation of the composition in contrast to two well defined layers as used in [89] will increase the complexity of the analysis. Such an approach, which might be pursued in future work, is not in the scope of this thesis.

The NEXAFS measurements first of all indicate the progressed oxidation of the surface near region due to the tempering process in DM0149A. Secondly, they show the importance of synchrotron radiation based analysis, since chemical information with a depth resolution in the nm range is not available with a laboratory setup. However, a second approach to similar information is gained by analyzing stoichiometric changes with depth by angular resolved XRF. The potentials and limitations of the method, which is more easily adapted to a laboratory setup, are demonstrated by GIXRF investigations with synchrotron radiation in the following Section 4.5. Again, the thermoelectric nanofilms DM0150A and DM0149A are used for demonstration experiments.

4.5. Depth Profiling with GIXRF

Grazing incidence XRF measurements are performed during the beamtime at the KMC beamline at 2700 eV to investigate the angular profiles of Au-M_α, Cu-L_{α,β} and O-K_α qualitatively. The incident angle of the radiation is varied by tilting the sample. The vertical rotational axis intersects the measurement position and ensures a stationary excitation. The measurement angles range from -0.1° to 1.5° in steps of 0.025° and additionally from 1.6° to 4° in 0.1° steps. With a measurement time of 45 s, the total measurement time is a bit more than 1 h. Figure 4.6 shows the normalized GIXRF profiles for a) DM0150A and b) DM0149A. With increasing incident angle, the fluorescence intensity of all elements increases, passes the inflection point at about 0.9° and reaches an intensity maximum at about 1.1°. Then, the intensity drops, which is typical for a thin film. As can be seen, the GIXRF profiles of Cu, O and Au have a very similar shape and a similar position of the inflection point (Figure 4.6 c) and d)), which indicates a similar in-depth distribution of these elements. However, the oxygen signal in the

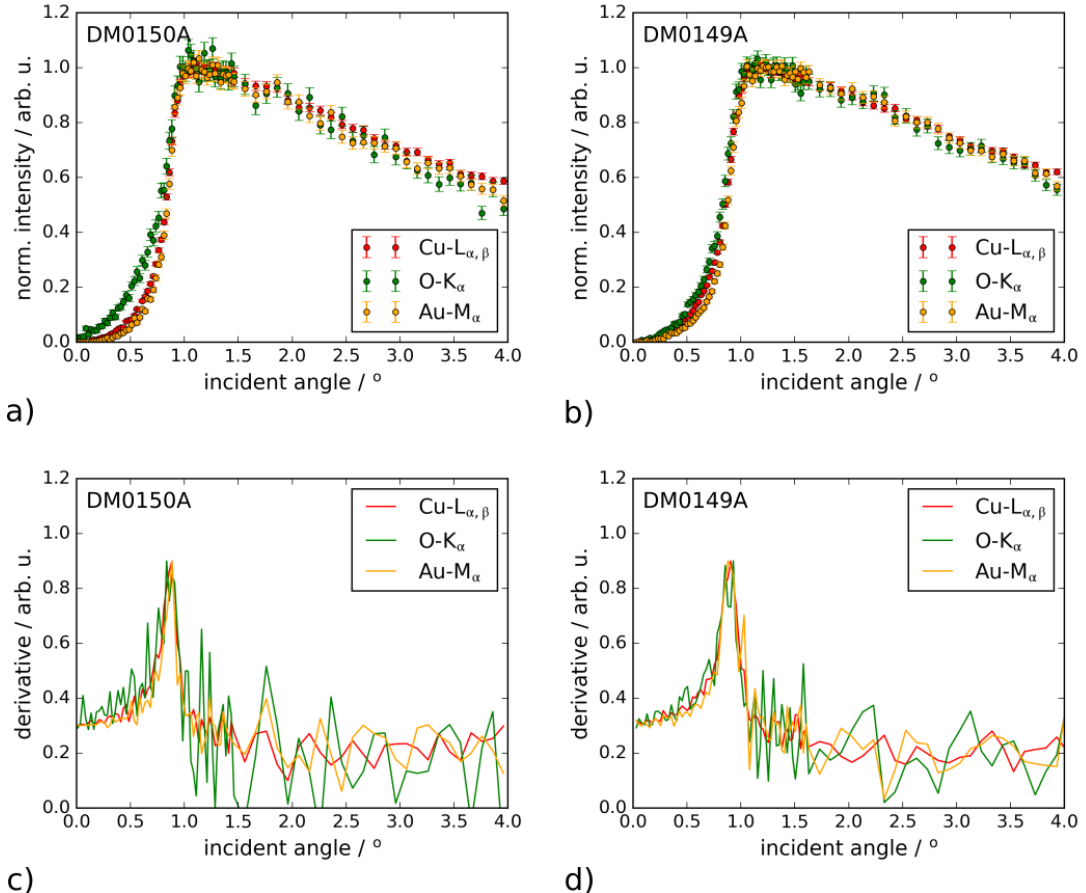


Figure 4.6.: Grazing Incidence X-ray Fluorescence (GIXRF) measurements of O, Cu and Au recorded at the KMC beamline with 2700 eV incident photon energy. The normalized GIXRF profiles and their derivatives are shown for the thermoelectric thin films DM0150A (not tempered) in a) and c) and for DM0149A (tempered) in b) and d).

GIXRF profile of DM0150A is increased for low angles. This signal might originate from organic contamination on the sample surface, which is clearly detected in the GIXRF profiles of the measurements at the PGM beamline, as will be shown in Section 4.5.3.

Actually, differences of the in-depth distribution of Cu and O are expected from the qualitative NEXAFS measurements in Section 4.4. Especially in sample DM0149A, concentration gradients for Cu and O should be present due to the induced oxidation by tempering. Therefore, measurements at the PGM beamline with an excitation energy of 1060 eV and thus increased depth sensitivity and sensitivity for light elements are used for a quantitative depth profiling approach.

Both samples DM0150A and DM0149A are measured at the same spot as is used for the quantification with conventional 45° geometry (Section 4.3). The focus size (FWHM) of the synchrotron beam at the PGM beamline is $40 \times 140 \mu\text{m}^2$ (vertical \times horizontal) and the horizontal footprint size is enlarged by $1/\sin(\psi_{\text{pr}})$. This leads to a horizontal footprint size of about 8 mm at an incident angle $\psi_{\text{pr}} = 1^\circ$ and $\approx 0.4 \text{ mm}$ at $\psi_{\text{pr}} = 20^\circ$. For every GIXRF scan, angles of the sample are varied from -0.4° to 8° in steps of 0.1° and subsequently from 8.5° to 20° in steps of 0.5° . The measurement time for each angle is 60 s resulting in a total measurement time of almost 2 h for every GIXRF scan.

Figure 4.7 shows the normalized GIXRF profiles for a) DM0150A and b)-d) DM0149A. The plotted uncertainties refer to counting statistics and an additional 1% uncertainty from the calculated incident flux determined with a calibrated photo diode [110]. In general, the GIXRF profiles of the main components of the thermoelectric layers, Cu and O, follow the typical trend of a thin layer. After reaching an intensity maximum at shallow angles (below 5°), the intensity drops because of the reduced absorption of the incident radiation in the thin layer. However, also some rather unusual features are present at shallow angles for the GIXRF profiles of O and C. In Figure 4.7 a), the high intensity for O and C below 2° indicates a strong surface contamination with probably organic compounds and water. Also, the rather constant C signal, even for high angles, is somewhat unusual. This behavior, as will be demonstrated in some detail in Section 4.5.3, can be explained by a large particle, whose fluorescence contributes with a constant signal to the GIXRF profiles shown here. A less strong signal from organic contaminants (C and O) is seen for the measurements on sample DM0149A (Figures 4.7 b)-d)) and also for steeper angles the C fluorescence seems to follow the expected trend of a thin layer. The 2 measurements in c) and d) are obtained at +2 mm and -2 mm vertical distance from the center position of DM0149A. The Cu and O signals are rather similar and indicate a homogeneous structure within at least 2 mm distance from the center. Only the GIXRF profiles for O and C at shallow angles differ significantly. Clearly, surface contaminants are not evenly distributed on the sample.

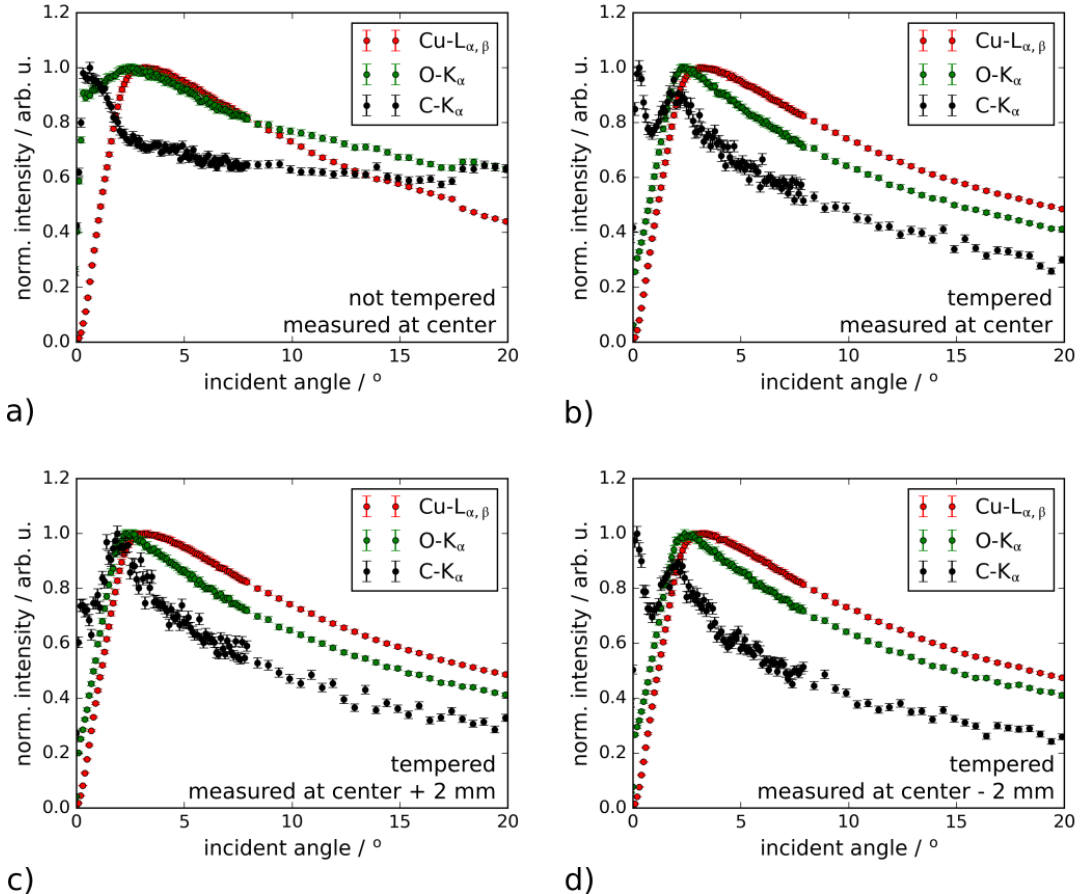


Figure 4.7.: Normalized GIXRF measurements of C, O and Cu performed at the PGM beamline with 1060 eV incident photon energy. a) shows the GIXRF profiles of the copper oxide nanofilm sample DM0150A (not tempered) and b) the GIXRF profile of DM0149A measured at the center position. c) and d) show the GIXRF profiles of DM0149A (tempered) measured in 2 mm horizontal distance to the center position.

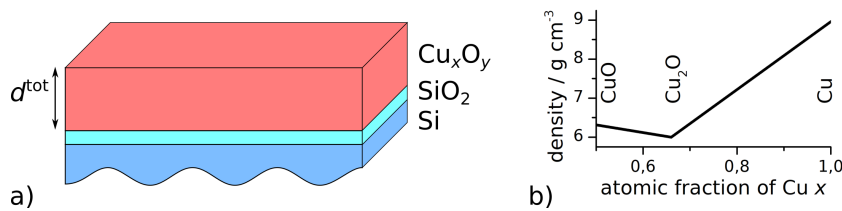


Figure 4.8.: a) Schematic of the 1-layer model used in the fitting procedure of the GIXRF profiles. **b)** Applied model for the density in the Cu_xO_y layer.

Several further differences between the GIXRF profiles of the non-tempered sample DM0150A in a) and tempered sample DM0149A in b) are visible. While the inflection point ($0.6^\circ \pm 0.1^\circ$) and the maximum position ($3.2^\circ \pm 0.1^\circ$) are the same for the Cu GIXRF profiles of both samples, the slope at higher angles is slightly steeper for DM0150A, indicating a lower mass deposition of Cu. However, the main differences are visible in the oxygen signal (apart from the contamination contributions below 2°), which displays a broader peak and a shallower decrease towards steeper angles for sample DM0150A. If these differences in the GIXRF profiles of the tempered and not tempered sample are indeed significant with respect to the sample depth dependent oxidation state, is analyzed in three subsequent steps. In these steps, the complexity of the applied model for the thermoelectric nanofilms is subsequently increased to better describe the GIXRF profiles and the analytical results concerning the sample structure are discussed.

4.5.1. 1-Layer Model

The easiest model of the sample consists of one single layer containing O and Cu on a Si substrate (Figure 4.8 a)). The small gold content in the thermoelectric nanofilms will be neglected for now and taken into account, when more quantitative results are envisaged. From XRF measurements on the substrate just next to the sputtered sample area, an oxygen mass deposition is quantified and a layer thickness for the native SiO_2 calculated (Section 4.3). This layer is added between copper oxide film and substrate for the models of sample DM0150A and DM0149A, respectively.

Figure 4.9 shows the simulated GIXRF profiles for the 1-layered model with a composition of pure Cu, Cu_2O , CuO and Cu_xO_y with x and $y = 1 - x$ being the atomic fractions of Cu and O as determined in Section 4.3. For all simulations here and hereafter, the influence of the samples optical properties (reflection and refraction at the interfaces) is taken into account by the XSW model described in Section 2.2.2. The density of the layer is set to bulk density of 8.94 g/cm^3 for Cu, 6.0 g/cm^3 for Cu_2O and 6.31 g/cm^3 for CuO . As density for the Cu_xO_y layer, a linearly interpolated value between the former pure compounds is used (Figure 4.8 b)). The densities of thin layers can indeed differ

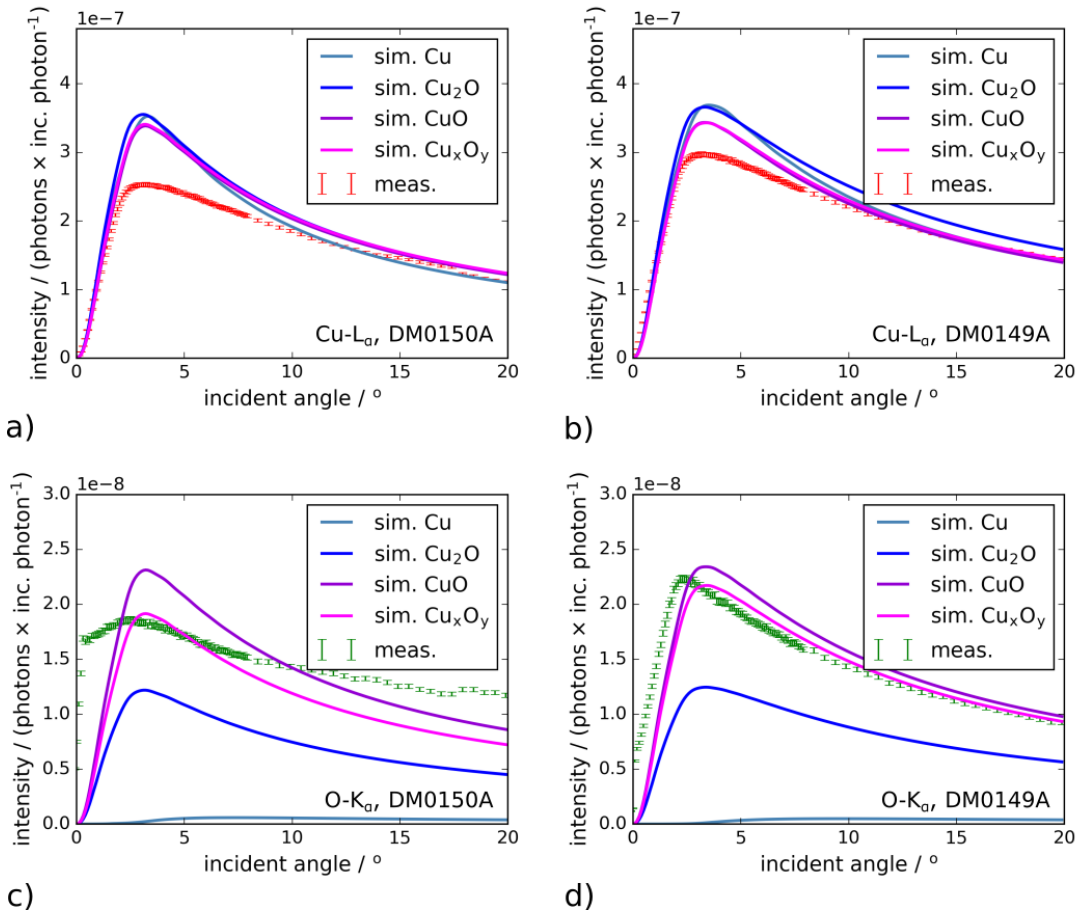


Figure 4.9.: Simulated and measured GIXRF profiles of Cu and O for the copper oxide nanofilms DM0150A (Cu-L_{α,β} in a) and O-K_α in c)) and DM0149A (Cu-L_{α,β} in b) and O-K_α in d)). The incident photon energy is 1060 eV.

from bulk densities by several percent. Such a difference affects here only slightly the inflection point of the curves at shallow angles and is neglected for the following simulations. Layer roughness, modeled by Debye-Waller factors, also show only small effects on the simulated curves and are set to zero for the present purpose. The fluorescence calculations are carried out for each measurement angle and normalized to the respective solid angle of detection.

The simulated curves in Figure 4.9 are fitted to the measurement at the steepest angle ($\approx 20^\circ$) by adjusting the layer thickness. At steep incident angles, geometrical and XSW effects are smallest and so are the uncertainties. For the fitting, here and hereafter, a weighted least square fit is used within a Python program (`curve_fit` from the package `scipy.optimize`, using a Trust Region Reflective algorithm for minimization [72]). As can be seen, a good agreement between measured and simulated value at 20° is only achieved for sample DM0149A with the simulation of Cu_xO_y , where the layer thickness is determined to (36.0 ± 0.6) nm. The given uncertainties of the fitting algorithm have to be used with some care and should probably be understood as lower limit, as will be discussed more detailed in Section 4.5.3. In all other curves, the Cu signal is overestimated and the O signal underestimated. This behavior is expected for all simulations but the simulation of Cu_xO_y with x and y taken from the integral quantification (Section 4.3), since the relative concentration of Cu to O do not fit. For the simulation of Cu_xO_y for sample DM0150A, an additional O signal from contamination is present, as is discussed in Section 4.5.3.

Overall, the results of the 1-layer model, when comparing the whole range of the GIXRF profiles, are not satisfactory. The maximum of the Cu GIXRF profiles for both samples is overestimated by all simulations. The same is true for the shallow angular regions of the O GIXRF profiles, even for the simulations of CuO and Cu_xO_y of DM0149A, where at least the slope of the curve above 4° seems to fit reasonably. The simulated curves for CuO are closer to the measurements than the curves for Cu_2O or pure Cu, indicating a strong progression of the oxidation process. However, this information might be misleading and actually originating from a wrong model of the GIXRF simulations. Indications for this can be found in the GIXRF-NEXAFS spectra (Section 4.4), where the main contribution originates from Cu_2O .

4.5.2. *N*-Layer Model

A change in the Cu oxidation state with depth in the copper oxide nanofilms is expected from the GIXRF-NEXAFS measurements. This implies a change of the major chemical compound to be found in a specific depth region and thus a change of the concentrations of the elements in depth. To account for such concentration changes in the present

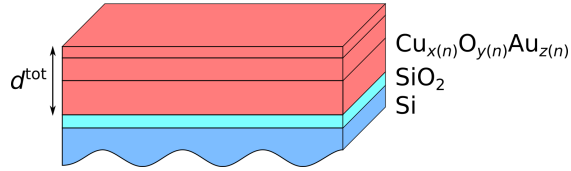


Figure 4.10.: Schematic illustration of the N -layer model with increasing sublayer thickness.

model of the copper oxide nanofilms, an N -layer model is tested (Figure 4.10). Instead of a single layer with variable thickness, now a sample model consisting of N discrete layers is used. Each layer consists of a $\text{Cu}_{x(n)}\text{O}_{y(n)}\text{Au}_{z(n)}$ compound, where $x(n)$, $y(n)$ and $z(n)$ are the atomic fractions of each element in layer n . However, only $x(n)$ is used as variable, since $z(n) = x(n) \times (C_{\text{Au}}^{\text{at}} / C_{\text{Cu}}^{\text{at}})$ is calculated from the quantification in Section 4.3 and $y(n) = 1 - x(n) - z(n)$. The density of each layer is again interpolated between the bulk densities of the pure compounds Cu, Cu_2O and CuO (Figure 4.8 b)). The thickness of each layer $d(n)$ depends on the layer number n and the summed thickness of all N layers d^{tot} according to

$$d(n) = d^{\text{tot}} \times \frac{n}{\sum_{i=1}^N i} \quad (4.5.1)$$

E.g. for $N = 5$ the layers have an increasing thickness $d(1) = d^{\text{tot}} \times 1/15$, $d(2) = d^{\text{tot}} \times 2/15$ etc., which is partly accounting for reduced information from lower layers due to the absorption in the layers on top. A similar approach is motivated in [43]. In the fitting procedure, only the total layer thickness d^{tot} is used as free parameter. Besides the $N + 1$ free parameters, $x(n)$ and d^{tot} , two more scaling parameters for the fluorescence intensities of copper and oxygen, s_{Cu} and s_{O} , are applied. They should account for the uncertainties of the absolute values of the fundamental parameters used in the photo production cross section $\xi_{i,j,s}(E_{\text{pr}})$ in Equation 2.1.1 in Section 2.1.1. Table 4.3 summarizes the fitting parameters, their starting values and the applied boundaries.

Simultaneous fitting of the Cu and O GIXRF profiles is carried out with the described model for various layer numbers $N \leq 10$ for both samples. Apparently, during the GIXRF measurements, the sample surface was radially misaligned by up to $60 \mu\text{m}$ from the pivotal point of the goniometer. This has a strong effect on the effective solid angle of detection for shallow incident angles, as is shown in detail in Appendix D. To consider this during the fitting procedure, an additional uncertainty, being the relative difference between the effective solid angle of detection with and without sample misalignment, is applied to the measured data.

Figure 4.11 shows the results of the fitted GIXRF profiles for $N = 1, 2, 5$ and 10 . The

Table 4.3.: Parameters and settings for the non-linear least square fit applied to the GIXRF profiles with the N -layer model. Besides intensity factors $s_{\text{Cu},\text{O}}$ and total layer thickness d^{tot} , for each of the N layers an atomic fraction $x(n)$ for Cu is fitted.

	starting value	boundary
$N \times x(n) / \text{at.\%}$	75	50 - 100
$d^{\text{tot}} / \text{nm}$	30	0 - 100
s_{Cu}	1.0	0.50 - 1.5
s_{O}	1.0	0.50 - 1.5

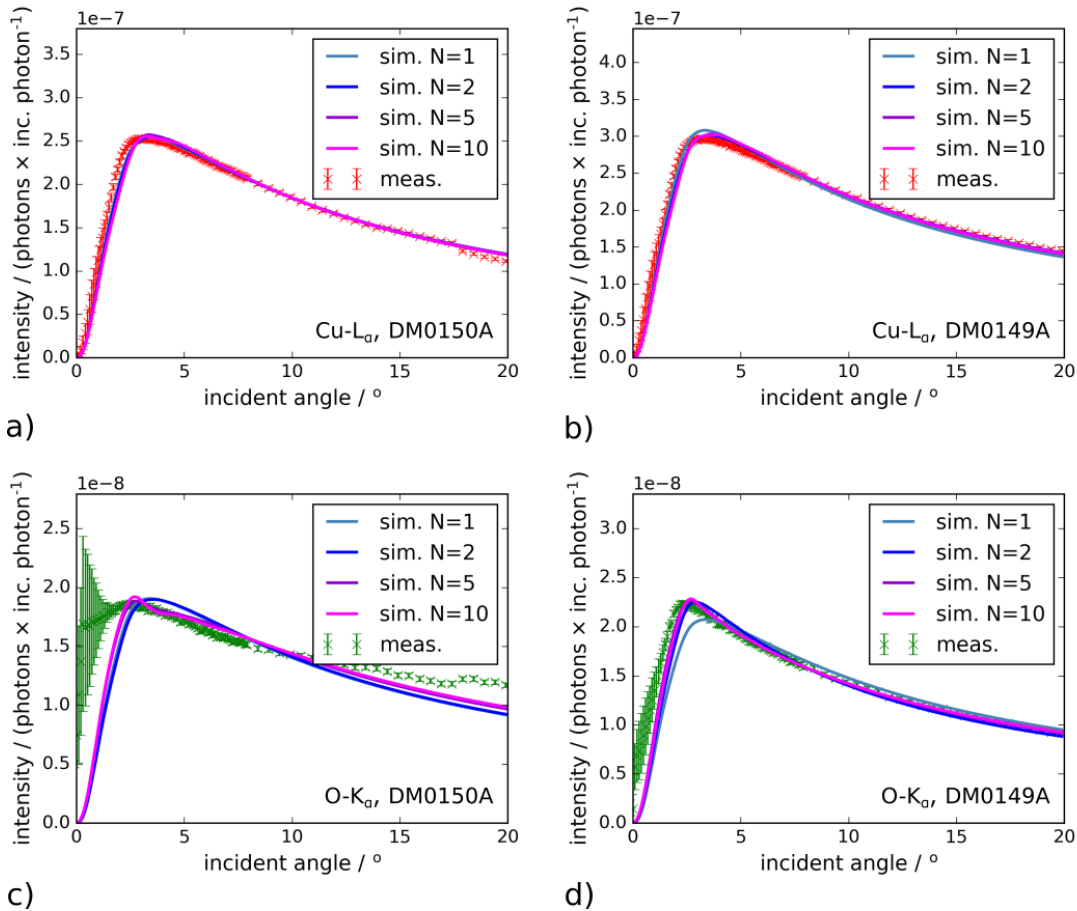


Figure 4.11.: Fitted and measured GIXRF profiles for Cu and O of the thermoelectric nanofilms DM0150A (a) and c)) and DM0149A (b) and d)), applying the N -layer model with $N = 1, 2, 5$ and 10 . The incident photon energy is set to 1060 eV. The fit is improved compared to the 1-layer model mainly because of the introduced intensity factors. However, it shows still some deviations in the shallow angular regime below 3° and overall for the O GIXRF profile of DM0150A (c)).

Table 4.4.: Results of the fitted parameters for the N -layer model with $N = 1$ for the thermoelectric nanofilm samples DM0150A (not tempered) and DM0149A (tempered). The uncertainties are derived from Equation 2.4.3 in Section 2.4.2 and should be understood as lower boundary because of the imperfect model and the non-normal errors applied to the measurement.

	DM0150A	DM0149A
$s_{\text{Cu}} / \%$	70.5 ± 0.5	86.2 ± 1.5
$s_{\text{O}} / \%$	127 ± 14	130 ± 40
$d^{\text{tot}} / \text{nm}$	43.5 ± 1.4	40 ± 3
$\hat{m}_{\text{Cu}} / (\text{ng} \times \text{cm}^{-2})$	22600 ± 800	20500 ± 1200
$\hat{m}_{\text{O}} / (\text{ng} \times \text{cm}^{-2})$	3490 ± 110	3350 ± 200
$\hat{m}_{\text{Au}} / (\text{ng} \times \text{cm}^{-2})$	740 ± 90	620 ± 80

simulated curves approximate the measurements visibly better than with the 1-layer model. However, since even the curves for $N = 1$ agree better with the measurements, the effect is mainly caused by the additional factors for the overall fluorescence intensity, s_{Cu} and s_{O} . They allow for an adjustment of the absolute fluorescence intensity, when changing the total layer thickness d^{tot} . The latter is similar to a change in the total mass deposition of the elements and dominates the shape of the slope above 3° . The fitting values for s_{Cu} and s_{O} together with d^{tot} and the corresponding mass deposition for $N = 1$ can be found in Table 4.4.

A few points of discussion arise from the results. First, the given uncertainties have to be discussed. They are derived from Equation 2.4.3 in Section 2.4.2. To be reliable, the model needs to be appropriate (see the discussion in Section 2.4.2) and the measurement uncertainties need to be normal distributed. The latter is not true because of the unknown, systematic uncertainties of the effective solid angle of detection due to misalignment. However, the uncertainties are given here nevertheless, but they should be understood as lower limits. They can be used to derive hints about the correctness of the model and are discussed in detail.

The Cu fluorescence intensity is reduced by 15-30% (s_{Cu}), not only for the fit with $N = 1$, but also for all tested layer numbers $N = 1, 2, 3, 5, 7, 10$. This seems reasonable with respect to the estimated uncertainties for L-shell fluorescence, which are in this work estimated with 26% (see Appendix C). For oxygen on the other hand, the signal is increased by 30% for $N = 1$, but also values at the boundary limit of 50% are reached in some fits. In addition to the high uncertainties given by the fit, the results for s_{O} are not accurate. As will be seen in the fitting procedure with the next model, a large part

of the oxygen fluorescence seems to originate from surface contamination and is thus not covered in the present model. Therefore, also all the values based on the oxygen signal (\hat{m}_O directly and d^{tot} via the applied density model) are not trustworthy and should be interpreted with care. Surely, the uncertainties of these values are strongly underestimated.

Nevertheless, the mass deposition results for Cu (and thus also Au) should be rather trustworthy, since they mainly depend on the slope above 3° , where neither large uncertainties in the solid angle of detection, nor effects due to contamination appear. The values support the quantification results of the commercial setup in Chapter 3 and are about 15% higher than the quantification results obtained at the KMC beamline with Cu-K α . This indicates an underestimation of the FP or instrumental uncertainties in the latter approach. By introducing a factor for the fluorescence intensity, the determination of the mass depositions does not rely on the precise knowledge of the solid angle of detection (which does not change drastically above 2° for the present setup), the incident photon flux or most fundamental parameters, leading to decreased uncertainties. Especially in the soft X-ray range, the fluorescence yield has high uncertainties, which directly affect the uncertainties of layer quantification, as is illustrated in Section 4.3. Thus, the shown results nicely demonstrate the advantages of reference-free, FP based quantification, using a range of incident (or emission) angles instead of a single measurement. This already indicates that even without a fully calibrated setup and with rather high uncertainties of the FPs in the soft X-ray range, single layered nanofilm quantification is feasible with the scanning-free GEXRF setup described later in Chapter 5. But even for synchrotron applications, the described quantification approach could be useful to decrease uncertainties.

The main sensitivity for in-depth compositional changes of the thermoelectric nanofilms is found in the GIXRF profiles at shallow angles. Figure 4.12 shows exemplarily an enlarged view of the GIXRF profiles of Cu and O for the tempered sample DM0149A. As can be seen in a), the model already fails to precisely describe the measured Cu GIXRF profile. This is even more pronounced for the O GIXRF profile in b), even though there is some improvement for fits with $N > 1$. The main reason is an additional contribution from contamination, which has to be described in the model accordingly. Otherwise, the contribution of the contamination interferes with the O GIXRF profile of the thermoelectric nanofilms and leads to wrong depth profiling results (also affecting the Cu GIXRF profile).

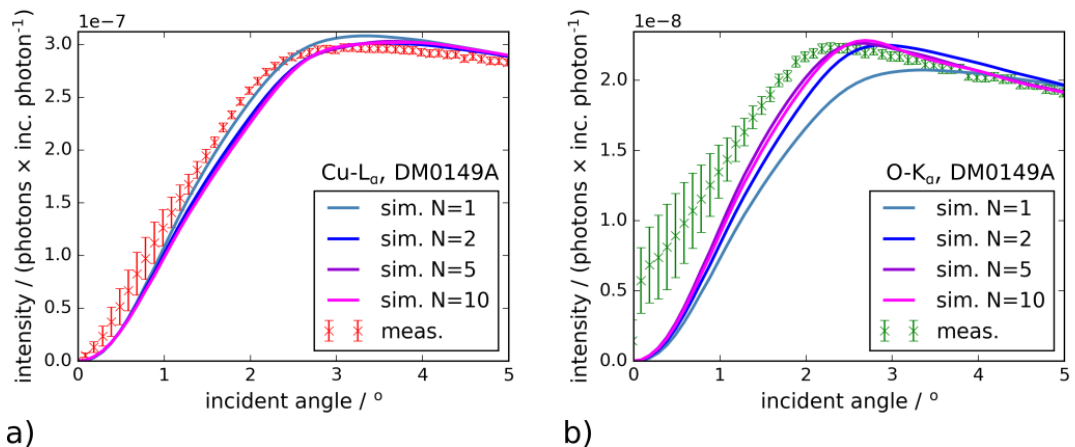


Figure 4.12.: Zoom to the shallow angular regime for a) the Cu and b) the O GIXRF profiles in Figure 4.11 b) and d), respectively.

4.5.3. *N*-Layer Model with Contamination

From the measurements shown in Figure 4.7 on page 60, the oxygen signal and especially the carbon signal at shallow angles strongly indicate surface contamination. To account for this in the simulated GIXRF profiles, several possibilities to introduce such a contamination are tested.

First, the XSW field above the copper oxide layer, which can excite the contamination layer, exhibits only low intensities at the first few nm above the surface for incident angles below 0.3° (Figure 2.4 in Section 2.2). Thus, the high carbon signal at about 0.1° cannot be explained with a smooth contamination layer on a reflecting surface. Therefore, some fluorescence intensity has to originate from contamination, which is not affected by the destructive interference of the XSW field in this angular and spatial region. This could be the case, either if the XSW field is disturbed by rough interfaces, or if fluorescence intensity of the contamination originates from a larger distance to the reflecting sample surface than a few tens of nanometers*. Therefore, the calculated fluorescence of a single layer without XSW field modification is added to the fluorescence of the model sample. The summed intensities are again weighted with the effective solid angle of detection of each incident angle. Note that the absorption of primary and fluorescence radiation in the contamination layer, which might affect the signal from the thermoelectric thin films, is negligible with respect to the overall uncertainties and not implied in the present

* The XSW field vanishes above the surface because of the finite temporal coherence of the synchrotron beam. Assuming a resolving power of $E/\Delta E = 5000$, the longitudinal coherence length $l_{coh} = \lambda^2/(2 \times \Delta\lambda)$ would be $\approx 3 \mu\text{m}$ for 1060 eV photons. That means, at a shallow incident angle of 1° , the XSW field should vanish at about 50 nm above the reflecting surface.

calculations.

A second possibility for the introduction of contaminants is a nm or sub-nm thick contamination layer, which is excited by the XSW field. The XSW field enhancement would be largest at about 2.2° (Figure 2.4 in Section 2.2) and indeed some peak at about 2° is visible for sample DM0149A (in Figure 4.7 on page 60). However, in the fitting attempts for sample DM0150A and DM0149A, this layer usually converged to a thickness below 0.5 nm and the contribution to the GIXRF profiles is small. To keep the numbers of free parameters small, this layer is not included in the final fitting procedure.

Since unexpectedly high intensities at very shallow angles are found for both, C-K α and O-K α , the composition of the contamination layers in the model is set to C_xO_{1-x} with atomic fractions x for carbon. The carbon content might originate from dust and oxygen probably from water, which adheres on the surface if the sample is stored in ambient conditions.

However, even with the additional contamination model described so far, the GIXRF profiles cannot be reproduced completely. Mainly the rather slow decrease of fluorescence intensity above 3° for C and O in the GIXRF profiles of DM0150A and for C in the GIXRF profiles of DM0149A cannot be simulated in this way.

Regarding the C GIXRF profile for sample DM0150A, the almost constant intensity signal with increasing angles is atypical for layered structures. Because of the decreasing path length in a thin layer with increasing incident angle, the absorption probability of the primary radiation should also decrease, leading to the typical decline of fluorescence intensities. However, if a spherical particle on a (nonreflecting) surface is fully irradiated for all incident angles, the fluorescence signal of that particle is indeed expected to be constant. Therefore, for the simulation of sample DM0150A, a constant contribution to the fluorescence intensities of C is added as fitting parameter, to simulate such particles (or particle). Since the contamination seems to consist of C and O (both elements showing high intensities below 3°) and also the O signal exhibits a very flat gradient at steeper angles (above 5°) an offset as fitting parameter is also added to the O GIXRF profile.

While the fitted simulation of the Cu GIXRF profile does not change much (not shown), the added parameters lead to much better agreement between simulated and measured C and O GIXRF profiles (Figures 4.13 a) and c)). The flat decline of the fluorescence intensities with steeper angles can now be described by the simulation, even with a 1-layer model for the copper oxide nanofilm. Also, at shallow incident angles below 3° (Figures 4.13 b) and d)), the simulated GIXRF profiles agree much better with the measurement than without the additional parameters for the contamination. This indicates that the contamination model applied is a sufficient estimate of the real

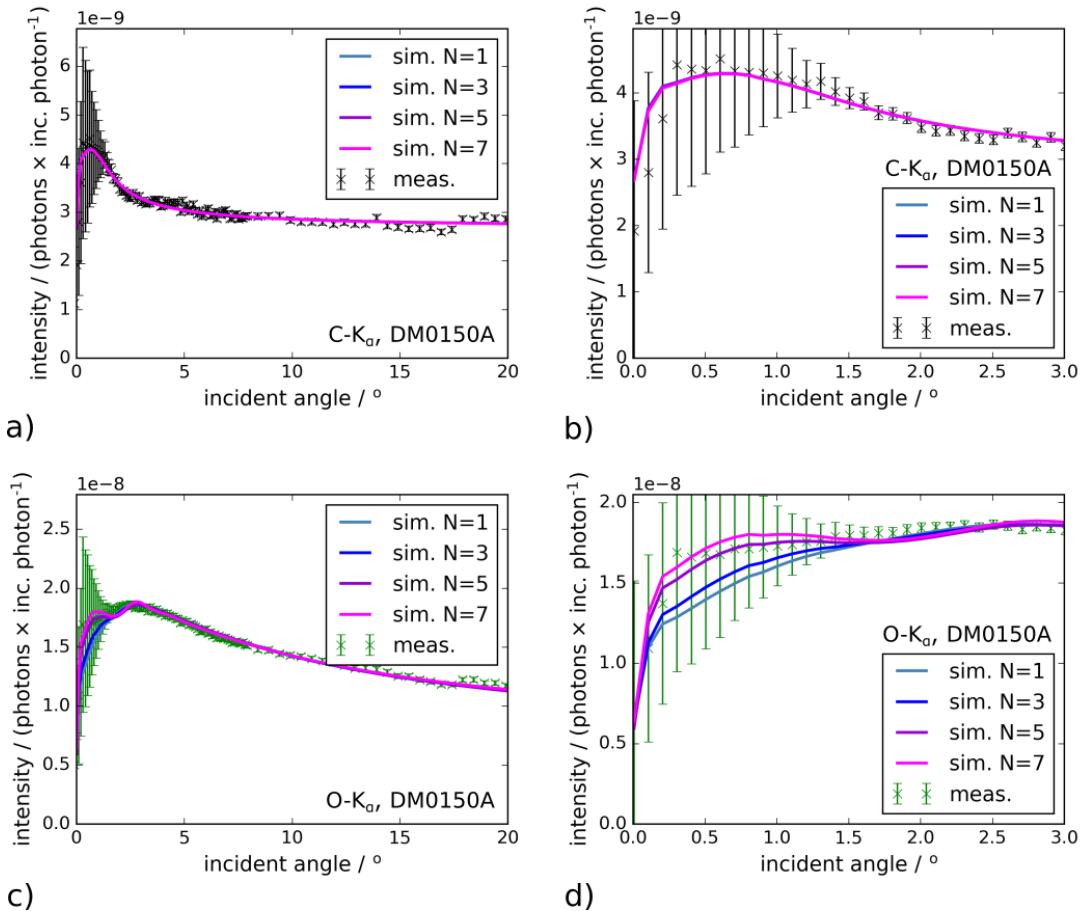


Figure 4.13.: Measured and fitted GIXRF profiles for a) C (close-up in b)) and c) O (close-up in d)) of the thermoelectric nanofilm sample DM0150A (not tempered) irradiated with 1060 eV photons and applying contamination contributions to the N -layer model.

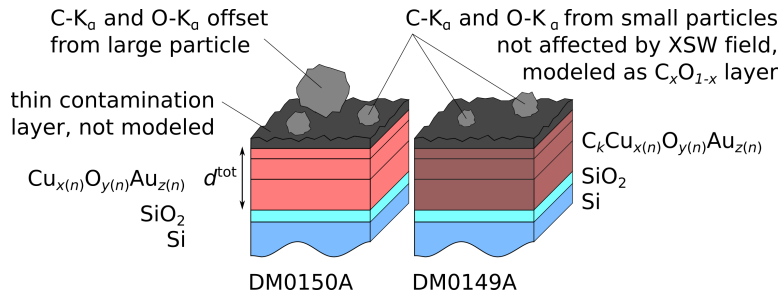


Figure 4.14.: Sketch of the N -layer model with contamination. A constant contribution to the fluorescence signal of O and C in the GIXRF profile of DM0150A might originate from one or several large particles. Small particles could give rise to a signal which would be expected without XSW field modifications of the excitation conditions. The measurements also indicate a thin surface contamination layer, which is not modeled (see text). In the tempered sample DM0149A, evidence for a C signal from the copper oxide matrix is present.

sample contamination, which is sketched in Figure 4.14. Here, the constant fluorescence intensity contribution is originating from the large particles and some fluorescence is emitted by smaller particles (extensions from surface should be larger than tens of nm), mainly unmodified by the XSW field. The latter is modeled as a layer and the X-ray fluorescence intensity is calculated without XSW field. Even though not modeled, the measurements show some C and O contribution to the GIXRF profiles from contaminants affected by the XSW field. This could be small particles of various shape and size in the nm or sub-nm range, forming a more or less closed, surface layer. The presence of particles with various diameters up to the μm range is also detected by atomic force microscopy (AFM) measurements shown in Figure 3.2 in Section 3.1, further supporting the sample model developed here.

Interestingly, the applied model for DM0150A does not lead to satisfactory results for the tempered sample DM0149A. The contamination layer thickness is always overestimated by the fit, to achieve a better agreement between measurement and simulation in the high angular regime. However, this leads to overvalued fluorescence intensities in the low angular range (red curve in Figure 4.15 a)). To get a better agreement of the intensity decrease above 3° in the C GIXRF profile, the signal must originate from carbon embedded in a matrix of a somewhat thicker layer than a few nm. Therefore, a constant carbon contamination is added into the copper oxide nanofilm matrix and its atomic fraction k is also fitted. The improved agreement between measurement and simulation is shown in Figure 4.15

Table 4.5 summarizes the resulting parameters of the final fitting approach with $N = 1$. The given uncertainties are again estimated by the fitting procedure and have to be

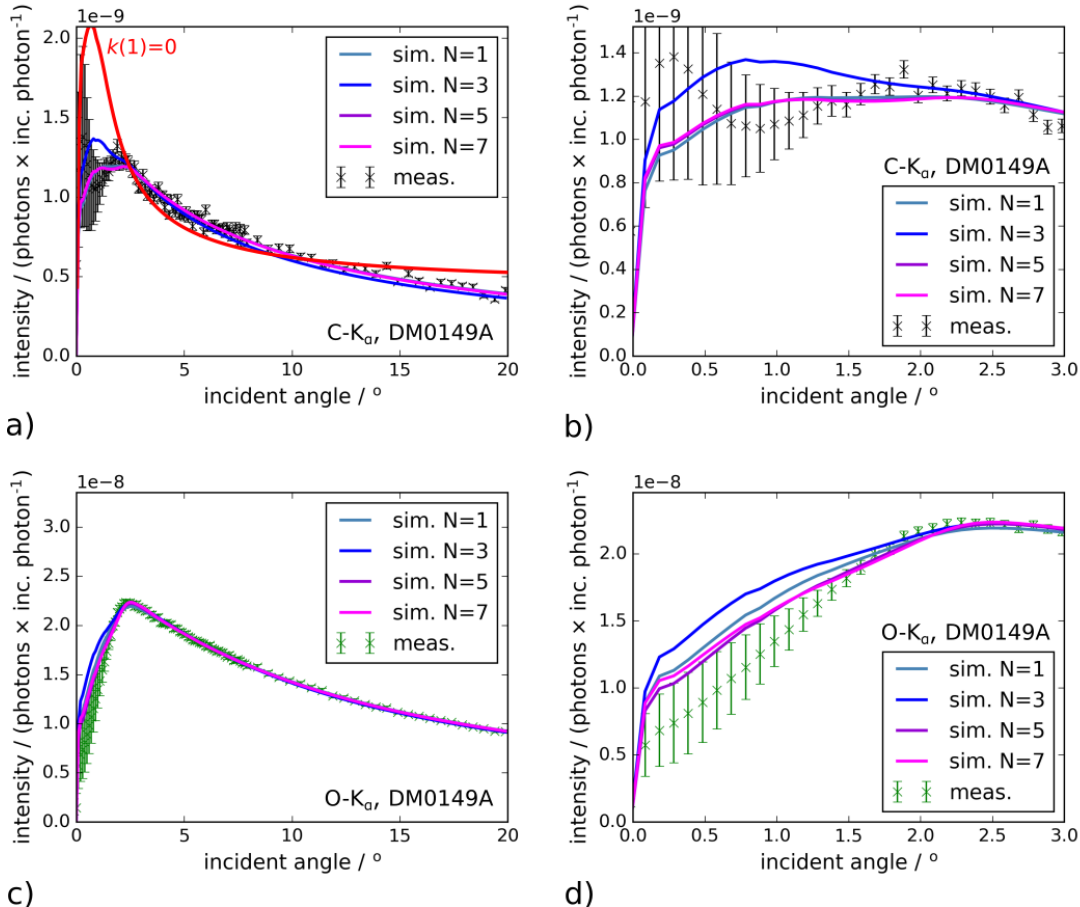


Figure 4.15.: Fit results of the GIXRF profiles for a) C and c) O with the N -layer model with contamination of the tempered thermoelectric nanofilm DM0149A. The red curve in a) is a fit ($N=1$) using only contaminants on top of the surface. The primary photon energy is 1060 eV. b) and d) show close-ups of a) and b), respectively.

Table 4.5.: Fit results of the approach with the N -layered model with contamination and $N = 1$. * in units of $(10^{-9}$ photons. \times inc. photon $^{-1})$

	DM0150A	DM0149A
$s_{\text{Cu}} / \%$	71.0 ± 0.2	83 ± 4
$s_{\text{O}} / \%$	77 ± 4	107 ± 110
$s_{\text{C}} / \%$	100 ± 700	100 ± 300
$x(\text{cont.}) / \%$	60 ± 120	50 ± 90
$d(\text{cont.}) / \text{nm}$	2 ± 7	1.8 ± 0.8
O-K $_{\alpha}$ offset*	8.5 ± 0.5	0.0 ± 0.4
C-K $_{\alpha}$ offset*	2 ± 12	not used
d^{tot}	41.0 ± 1.2	58 ± 2
$x(1) / \text{at.\%}$	65.7 ± 1.4	50 ± 2
$k / \text{at.\%}$	not used	20 ± 70

regarded with care. As expected, the fitted factor s_{Cu} for the Cu fluorescence intensity is similar to the values obtained without contamination (Table 4.4 on page 66), since the Cu signal itself is not strongly affected by the added contamination layer. This is not the case for the O GIXRF profile, which explains the change in s_{O} as compared to the results of the N -layer model. However, the value for s_{O} in the case of DM0150A (77%) is still reasonable with respect to the fundamental parameter uncertainties of 20%. Also, the thickness of the contamination layer with a couple of nm is plausible. For DM0150A, the offset in the O-K $_{\alpha}$ intensity seems indeed to be necessary to achieve a better fit of the simulated to the measured GIXRF profile, as is indicated by the rather low uncertainty of < 10%. On the other hand, the huge uncertainties for s_{C} , $x(\text{cont.})$, $d(\text{cont.})$ and the carbon offset probably indicate the somewhat strong coupling of these parameters, each variation leading to partly similar effects on the GIXRF profile for C. Also, the C GIXRF profile has the lowest counting statistics, which also contributes to the uncertainties given by the fit. For the same reasons, uncertainties for k in the model for DM0149A are also huge. Consequently, since k directly affects the composition of the thermoelectric thin film and thus also the attenuation coefficient of the matrix, the uncertainties of $x(1)$ and d^{tot} given by the fit are largely underestimated.

In conclusion, the measured GIXRF profiles can be described by simulations with a model of the sample including contributions of contamination. Furthermore, not only the presence of contamination can be shown, but also the high sensitivity of GIXRF especially in the surface-near region yields information about the nature of the contam-

ination. The tested models strongly indicate that carbon and oxygen rich particles with intermediate size ($>$ few tens of nm) are present on the surface. Their fluorescence signal can partly be modeled by a thin homogeneous layer without XSW field modification of the excitation. Also, a smooth film or very small particles containing C and O could be on the surface (this can be modeled by a thin layer being subject to the XSW field), but the signal is probably covered by the fluorescence of the intermediate particles. Then, also major differences of the C and O GIXRF profiles between DM0150A and DM0149A can be explained by further contributions from contaminants. In the measured spot on sample DM0150A, a large roughly round or cylindrical particle seems to be present, which is irradiated for the whole angular range up to 20° . In the spectrum used for quantification in Section 4.3, the C-K α intensity is much lower than expected from the interpolated GIXRF measurements, suggesting that the large particle or most of the large particles are outside of the smaller footprint at 45° . The GIXRF profiles of DM0149A on the other hand show no such behavior, but here the C GIXRF profile can be reproduced, if adding C to the copper oxide nanofilm matrix. Maybe the tempering process led to an integration of C into the copper thin film.

The NEXAFS measurements in Section 4.4 showed qualitatively a much stronger change of the Cu oxidation state close to the sample surface for the tempered sample DM0149A, than for the non-tempered sample DM0150A. This finding cannot be confirmed by the present GIXRF measurements. The main sensitivity to a change of oxygen concentration with depth is expected from the O-K α GIXRF profile. But since this profile is strongly distorted by the fluorescence originating from contamination, the sensitivity for compositional changes of the copper oxide is lost. In principle, also the Cu GIXRF profile is sensitive to the somewhat lower relative changes of the Cu concentration. The strongest effect is expected in the shallow angular range, but there the uncertainties of the effective solid angle of detection are highest. To compensate for these, GIXRF profiles of quotients of fluorescence lines from different elements in the matrix can be considered, as is shown in [43]. However, this approach cannot be used here, since only copper as undisturbed signal is present.

Even though the depth profiles of oxygen and copper cannot be determined with sufficient accuracy with the present measurements, the evaluation of the data surely illustrates the analytical possibilities of angular resolved XRF measurements and motivates the need for a laboratory setup. Often, unexpected results obtained from angular resolved XRF measurements are originating from the sample preparation process, making a quick feedback loop between analysis and sample preparation important. In the case of large facility measurements, this feedback loop is usually delayed by the need of applying for beamtime. In the next Chapter 5, the development of a laboratory setup for GEXRF measurements in the soft X-ray range is presented. After characterizing the

setup with a multilayer test sample in Sections 6.2 and 6.3, it will also be used to test the applicability with one of the thermoelectric thin film samples, namely DM0149A. For this purpose, the above developed N -layer model will be applied to the GEXRF case.

5. Development of Laboratory Scanning-Free Soft X-ray GEXRF

In the previous chapter, it has been shown that grazing incidence X-ray fluorescence (GIXRF) can give access to nanometer scaled structural information for complex samples. However, the shown measurements were performed at a synchrotron radiation facility to provide a highly collimated and intense excitation beam in the soft X-ray range and use was made of the absolutely calibrated instrumentation of the PTB. Such measurement conditions are difficult to achieve with a laboratory setup. On the other hand, a laboratory setup has the advantage of being readily available without the need of beamtime proposals and the related long latencies. And, probably more importantly, with a larger user and scientific community at hand, evaluation procedures for the inverse problem of GI- and grazing emission (GE) XRF measurements might evolve more rapidly, making the method even more powerful in general.

In the following, the development of a laboratory soft X-ray GEXRF spectrometer is presented with a short introduction dealing with the applicability of GI- and GEXRF in the laboratory. After describing the principle setup, special emphasis is placed on alignment procedures to enable precise measurements as well as an absolute angular calibration. Then, the evaluation of single photon events detected with a charge-coupled device (CCD) camera is investigated to make use of the energy-dispersive properties of a conventional CCD camera. Finally, angular calibration and energy-dispersive CCD images are both used to obtain GEXRF profiles.

Please note that setup design, adjustment, calibration and evaluation procedures are developed for soft X-ray GEXRF measurements with a laser-produced plasma source. Nevertheless, most of the ideas can be readily transferred to the hard X-ray range, where the sample can be excited e.g. by an X-ray tube equipped with a polycapillary lens, which further increases the impact of this work.

5.1. Grazing Incidence vs. Grazing Emission XRF Spectrometer Concept

Grazing incidence XRF and grazing emission XRF are related measurements, which give access to similar information. While the former allows for ideal excitation conditions with respect to excitation depth and self-absorption of the fluorescence radiation (Section 2.2), clear drawbacks are the high requirements regarding the excitation beam and the extended footprint on the sample for shallow angles. GEXRF measurements on the other hand can be applied by any, also convergent, ionizing radiation (X-rays, electrons, ions, etc.). This is not only preferable in terms of laboratory (mainly divergent) excitation sources, but can also be used to guarantee a small footprint and enhanced lateral resolution. However, the fluorescence radiation needs to be detected under shallow emission angles. This leads to self-absorption losses in the detected intensity and thus, a typically lower efficiency compared to GIXRF, which has to be compensated for.

At the Berlin Laboratory for Innovative X-ray technologies (BLiX), a laser-produced plasma (LPP) source is available for the generation of divergent soft X-rays [79]. Furthermore, a spectroscopy chamber designed for sample manipulation and realization of various spectrometer geometries can be used [111]. If the plasma interaction chamber and the spectroscopy chamber are combined in a spectrometer, the minimum distance between source and sample position is almost 1 m. This makes the application of X-ray optics necessary to increase the photon flux in the sample plane.

For a grazing incidence XRF spectrometer, parallelizing optics are necessary. Due to the long working distance (the optics needs shielding from plasma debris), multilayer optics are superior to e.g. polycapillary lenses. Such an optics might achieve a solid angle of acceptance of $\Omega_{\text{opt}}^{\text{GI}} = 3.1 \times 10^{-5}$ sr (see Appendix E). What is lost in the excitation channel is compensated for in the detection channel of typical GIXRF spectrometers. The detector, usually a silicon drift detector (SDD), can be aligned with less than 1 cm distance to the sample surface, resulting in achievable solid angles of detection of $\Omega_{\text{det}}^{\text{GI}} \geq 0.3$ sr. However, the electronics can only compute and differentiate photons in the microsecond range. Therefore, the pulsed radiation of the LPP source with pulse length of 1.2 ns leads to severe pile-up in the detector, limiting the usable count rate of the detector to only ≈ 100 counts/s (the repetition rate of the LPP source is 100 Hz).

In a grazing emission XRF spectrometer, the multilayer optics can have focusing properties. This allows for a higher angle of acceptance of $\Omega_{\text{opt}}^{\text{GE}} = 2.3 \times 10^{-3}$ sr (Appendix E), which means a factor 75 more flux in the excitation channel. Also, more than one optics might be used, further increasing the excitation intensity (as is applied in Section 5.2.2). This gain in intensity is diminished by the small solid angles of detection

5.1. GRAZING INCIDENCE VS. GRAZING EMISSION XRF SPECTROMETER CONCEPT

($\Omega_{\text{det}}^{\text{GE}} \approx 6 \times 10^{-7}$ sr) in a GEXRF spectrometer, which typically has to be applied to guarantee sufficient angular resolution. Only a scanning-free GEXRF setup can overcome both the limitations concerning pile-up (with an SDD) and insufficient solid angle of detection. The overall solid angle of detection with a CCD can easily be of the order of 0.05 sr and the pile-up is prevented by separating the photon events not only temporally (as in the SDD) but also spatially. Thus, a scanning-free GEXRF approach is clearly favorable compared to a GIXRF setup.

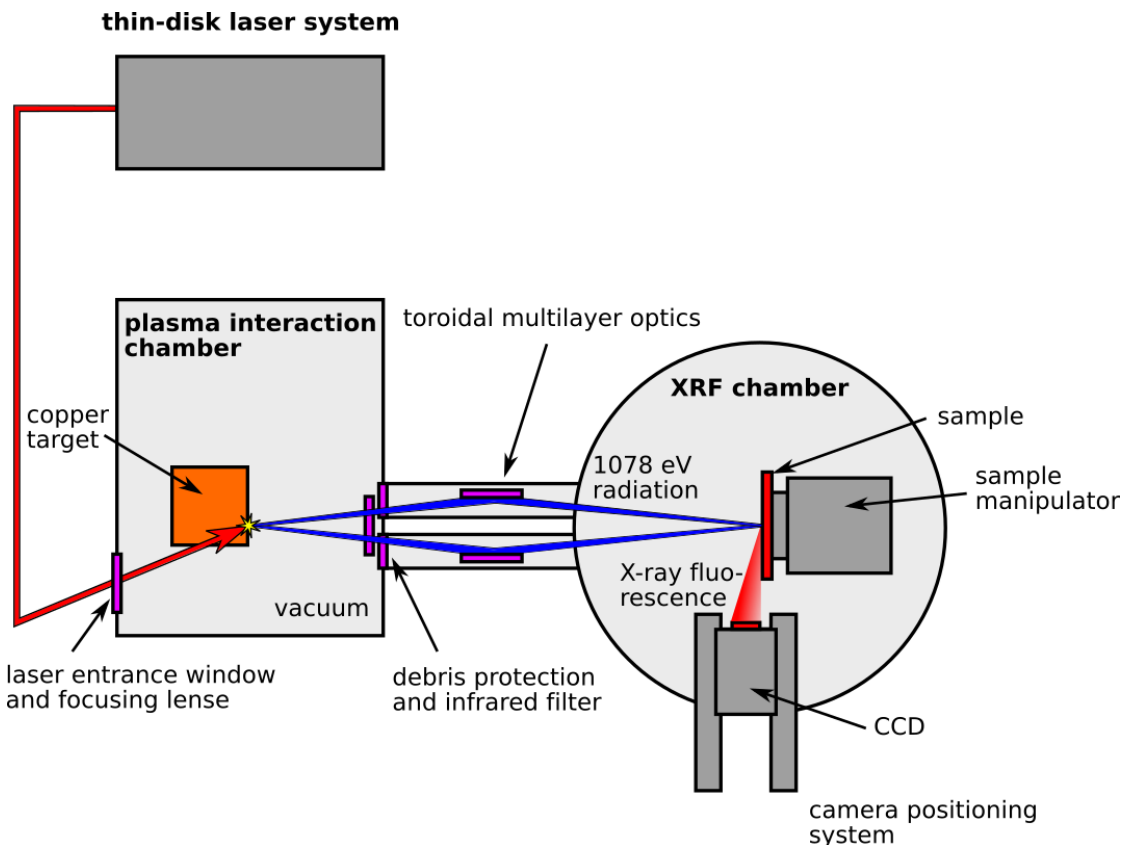


Figure 5.1.: Schematic setup for the laboratory scanning-free soft X-ray GEXRF measurements.

5.2. Principle Setup

The principle setup used for the GEXRF measurements is shown in Figure 5.1. The divergent radiation of the LPP source is focused onto the sample plane by means of a multilayer mirror optics. The optics were in a first beamtime two one-dimensionally focusing mirrors in Kirkpatrick-Baez (KB) geometry and in a second beamtime with improved setup and methodology two two-dimensionally focusing, toroidal shaped mirrors. The optics are shielded from debris by a thin polymer foil, sputtered with 100 nm of aluminum. Visible light is additionally prevented to reach the spectroscopy chamber by an aluminum filter with a thickness of 1.5 μm . The sample, positioned and aligned with a 7-axes goniometer in the spectroscopy chamber, is irradiated at about 90° and the fluorescence radiation at shallow emission angles is detected with an area detector operated in a single photon counting mode to enable energy-dispersive measurements.

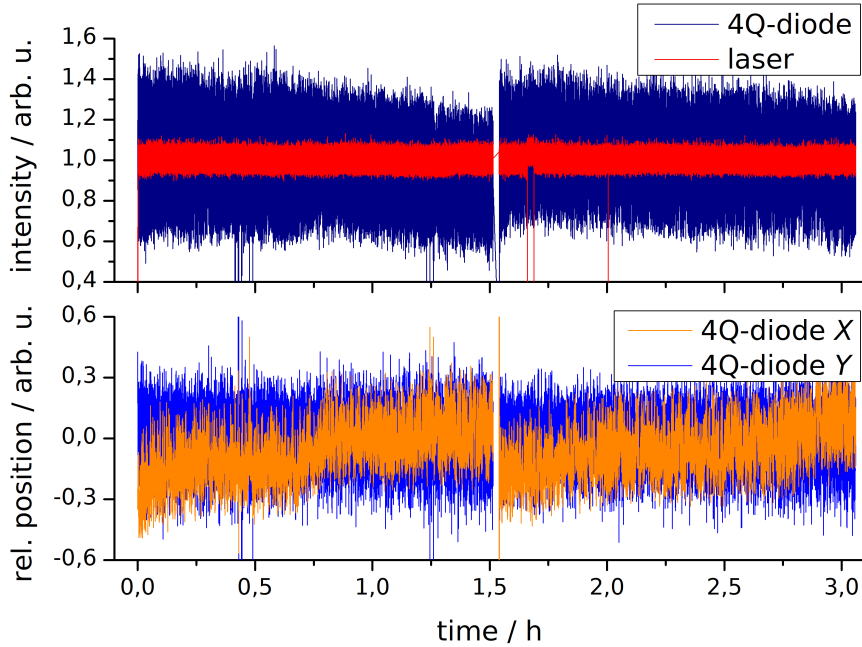


Figure 5.2.: Laser and plasma intensity (top) as well as X and Y values of the plasma position monitoring of the 4Q-diode (bottom) for 3 hours of LPP operation.

5.2.1. Laser-Produced Plasma Source

A short description of the laser-produced plasma (LPP) source is given in Section 2.5.2. For GEXRF measurements, the LPP source is operated in a continuous mode, providing 1.2 ns X-ray pulses every 10 ms. The pulse energy of the Yb:YAG laser is typically set to 150 mJ for alignment and 200 mJ for the GEXRF measurements, to effectively heat the plasma and generate X-rays with energies at 1078 eV from transitions in the 20-fold ionized copper. After up to 9 hours of operation, the copper target is replaced by a freshly polished target. This ensures high surface quality and improves position and intensity stability of the source. Furthermore, the debris protection foil in front of the beamline is sputtered with copper during operation, resulting in a reduced transmission of about 50% for the 1078 eV radiation after ≈ 9 hours. Therefore, after each target replacement, the debris-protection foil is renewed.

The GEXRF measurements shown in Chapter 6 are the first measurements, where the LPP source is operated continuously over several hours. Over the whole time, a high stability in the plasma position and a moderate stability with respect to X-ray intensity need to be guaranteed. While the former affects the footprint position on the sample and thus the angular resolution of the GEXRF measurements, the latter is less critical, since

5. DEVELOPMENT OF LABORATORY SCANNING-FREE SOFT X-RAY GEXRF

in the scanning-free GEXRF approach, the shape of the GEXRF profile is not affected by intensity instabilities.

The four-quadrant-diode (4Q-diode) proves to be a useful tool for stability monitoring. Figure 5.2 shows the plasma intensity measured with the 4Q-diode and the respective laser intensity for 3 hours of continuous operation. The laser intensity displays a very stable mean value and a standard deviation of 10% over almost the whole time. The summed intensity of the four quadrants of the 4Q-diode, measuring the plasma intensity, has a larger standard deviation of up to 40% and also the mean intensity is decreasing with time. The former can be explained by the high non-linearity and complexity in the plasma formation and the resulting sensitivity for changes of target position and roughness. Moreover, the 4Q-diode has insensitive areas between the quadrants, so that positional changes of irradiated area (influenced by position changes of the plasma) can affect the summed intensity. The decrease of mean intensity originates from debris, which is sputtered onto a protective glass disk in front of the laser entrance window. This leads to reduced laser intensity in the laser focus on the copper target and consequently reduced plasma temperature and X-ray intensity. After 1 h to 1.5 h of operation, the LPP source is shortly stopped for changing the glass disk in vacuum by means of a mechanical conveyer, to counter this effect.

Also, the position of the plasma source is monitored with the 4Q-diode. In the bottom panel of Figure 5.2 the X and Y values are displayed (see Section 2.5.2). While Y is used for the feedback loop and therefore shows a constant mean value, X drifts slightly in one direction during operation but is reset after changing the protective glass disk of the laser entrance window. This indicates a slight deflection of the laser beam depending on the sputtered copper on the protective glass disk. However, in other measurements (not shown here), X can drift rather arbitrarily, revealing a more complex behavior of the plasma position. Nevertheless, the absolute drift of the plasma position is negligible for the GEXRF measurements, as will be shown in Sections 6.2 and 6.3.

As is mentioned in Section 2.3.1, the noise level in each CCD frame of a GEXRF measurement needs to be as low as possible to detect and discriminate single photon events. Therefore, special care has to be taken to minimize stray light in the spectroscopy chamber. Besides visible light entering the spectroscopy chamber through window flanges, contributions from the LPP source itself might be detected. The former can be reduced by carefully sealing the window flanges. The latter, which is infrared and visible light from the LPP plasma and from the plasma reflected laser light, is typically blocked by a 1.5 μm aluminum filter (Goodfellow) in the X-ray beam path. However, a further significant reduction of stray light can be achieved by using a debris protection foil with an additional aluminum layer just at the exit of the plasma interaction chamber (see

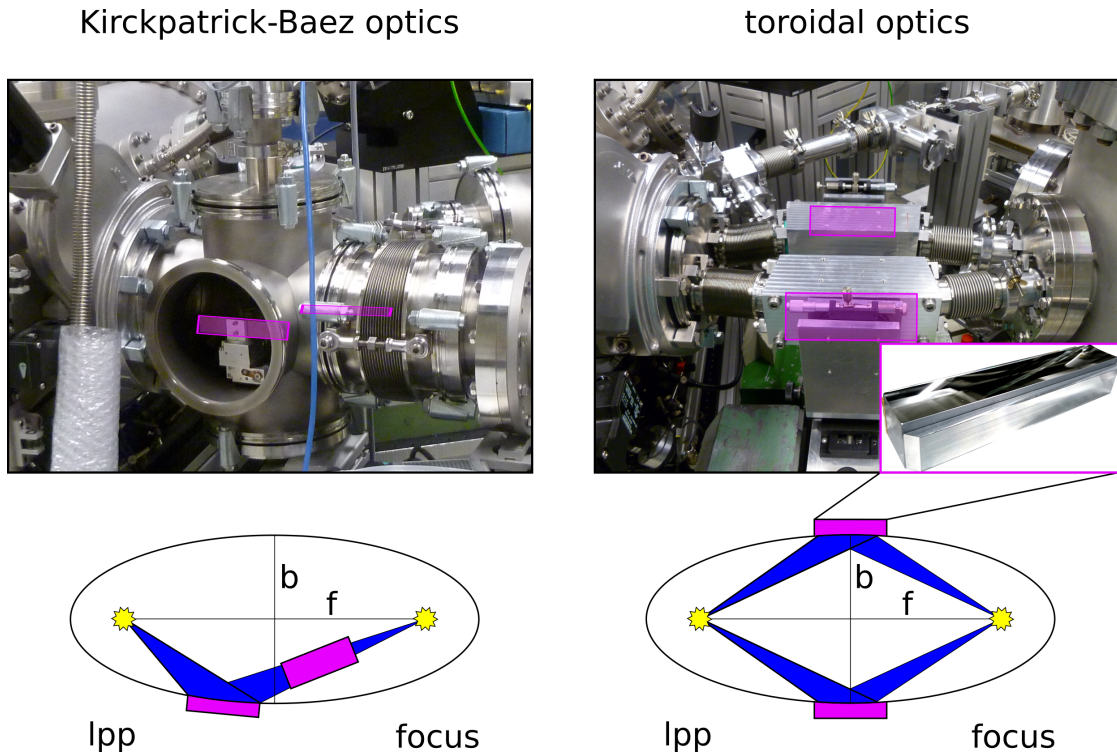


Figure 5.3.: Vacuum setup and positioning stages (photograph) and schematic ray path for the Kirkpatrick-Baez (left) and toroidal (right) optics. A single toroidal multilayer reflector is shown in the inset (bottom right of photograph).

Figure 5.1), e.g. 900 nm Mylar coated with 100 nm aluminum.

5.2.2. Multilayer Optics

The divergent and polychromatic X-radiation emitted from the LPP source needs to be efficiently transported to the sample plane, which has a distance of more than 100 cm from the source because of the size of the vacuum chambers, i.e. the plasma interaction chamber and the spectroscopy chamber. In the suggested setup, multilayer mirrors, offering a relatively high solid angle of acceptance, are used to collect, monochromatize and focus the radiation onto the sample plane. In a first approach (measurements in Section 6.2), two one-dimensionally focusing W/Si-multilayer mirrors, especially designed for the LPP source, are used in Kirkpatrick-Baez geometry (Figure 5.3 left panel). In a second development step (measurements in Section 6.3), they are replaced by two two-dimensionally focusing, toroidal-shaped multilayer mirrors (Figure 5.3 right panel), increasing the achievable photon flux on the sample.

Kirkpatrick-Baez Optics

In the Master's Thesis of A. Jonas the Kirkpatrick-Baez optics are characterized and aligned [112]. Here, the most important results for the GEXRF setup are shortly summarized. In a first characterization step, both multilayer mirrors are investigated separately. The focus size (measured as FWHM of the thin line focus) for both mirrors is (101 ± 14) μm over a focal length of about 1 cm. Spectra of the LPP source after reflection at a single KB mirror result in a Gaussian peak at 1078 eV (1.15 nm) with a FWHM of 66 eV, i.e. a bandwidth of 3%. Note that the Gaussian peak consists of three plasma lines at 1088 eV, 1069 eV, 1060 eV (i.e. 1.14 nm, 1.16 nm and 1.17 nm wavelength), which are not resolved in the measurement.

The alignment of the combined multilayer mirrors in KB geometry is performed with motorized stages in vacuum (Figure 5.3, left panel). Since there are only two axes (one rotational and one translational) for the alignment for each of the two mirrors, the desired focus size of $100 \times 100 \mu\text{m}^2$ (FWHM) could not be achieved. The focus is minimized in the more critical direction with respect to angular resolution, i.e. the horizontal axis pointing to the CCD (Section 2.3.2). With this alignment, the focus has a size of $100 \times 500 \mu\text{m}^2$ (FWHM). The intensity in the sample plane with KB optics is increased by a factor (gain) of 1470, if compared with the direct radiation of the LPP source in a pinhole with 500 μm diameter in the sample plane.

Toroidal Optics

In the second GEXRF beamtime (Section 6.3), toroidal multilayer optics instead of the KB optics are applied. These optics approximate the geometrically ideal ellipsoidal shape for a two dimensional focusing optics based on reflection. Since a single multilayer reflector is already focusing the radiation in both dimensions, the X-rays are reflected only once (instead of twice as in the KB geometry), leading to an increased efficiency. Furthermore, two optics are applied in the setup to increase the solid angle of acceptance, each aligned with 3 translational and 2 rotational stages, allowing to align both mirror foci at the same position in the sample plane. The optics are characterized in the Bachelor's Thesis of R. Reusch [113]. There it is shown that a single optics facilitates a focus size (FWHM) of $70 \times 80 \mu\text{m}^2$.

With a bandwidth of 4% and a maximum reflectance at 1078 eV, the spectral reflection properties of the two toroidal mirrors are similar to each mirror of the KB optics. The gain, as with the KB optics compared to direct radiation of the LPP in a pinhole with 500 μm diameter, is 27100 for one of the mirrors. Thus, the total number of photons in the sample plane is increased by a factor of 18 with one toroidal optics compared to

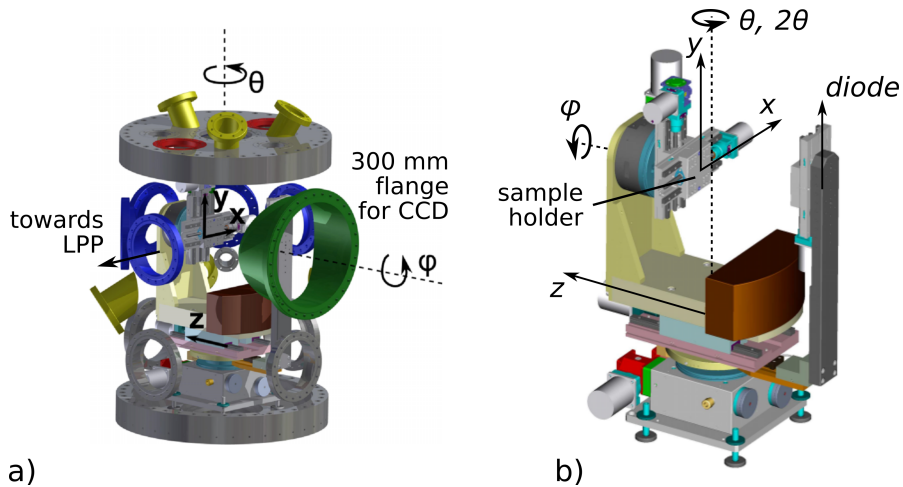


Figure 5.4.: a) Schematic view of the spectroscopy chamber with the sample manipulator (enlarged in b)) in the center. The sample can be moved in x , y and z direction and rotated against the axes θ and ϕ [111].

the KB optics, while the spot size is decreased. The huge intensity increase is mainly originating from a much easier optics alignment, enhanced coating properties because of a better substrate and adapted processing techniques, and a slightly larger optical area. In principle, a ring-shaped ellipsoidal optics could further increase the solid angle of acceptance, but setup and alignment requirements as well as the high cost make that concept unfavorable at the moment.

5.2.3. Spectroscopy Chamber

The spectroscopy chamber used for the GEXRF experiments is described in detail in [111]. It is evacuated with a turbomolecular pump with resulting pressures down to 5×10^{-8} mbar. The high-vacuum guarantees clean measurement conditions and negligible absorption of soft X-rays. In the center of the spectroscopy chamber, the sample manipulator is located (Figure 5.4). It allows to move the sample in 3 translational directions in a Cartesian coordinate system (x and y for movement in the vertical plane of the sample holder, z for movement radial to a vertical axis), which can be rotated about a vertical axis in the center of the spectroscopy chamber (θ) and a horizontal axis normal to the sample holder (ϕ). The latter is facing the θ -axis, such that the intersection of the θ -axis and the ϕ -axis defines the pivotal point of the goniometer and sample manipulator. Furthermore, another linear stage (“diode”) is mounted on a second rotational stage (“ 2θ ”) to mount and align e.g. an X-ray sensitive diode in the setup.

If the pivotal point of the goniometer is located on the sample surface, and the sample

is irradiated in this point, the excitation position will be fixed, even if the sample is rotated. The pivotal point will also be essential for the angular calibration procedures and serves as origin of the Cartesian coordinate system, in which the measurement geometry is defined (LAB system in Section 5.2.5). Therefore, also the sample needs to be excited in the pivotal point and the spectroscopy chamber needs to be aligned precisely with respect to the optics' focus, as is described in Section 5.2.5.

5.2.4. Charged Coupled Device

The CCD is integrated into the spectroscopy chamber with an adjustable positioning system at the 300-mm flange (see Figure 5.4). The system allows to tilt the CCD via a tripod and to traverse the CCD in the plane facing the flange. Furthermore, it is possible to move the CCD radially towards the center of the spectroscopy chamber. With the distance, also the angular resolution and the total solid angle of detection of the GEXRF measurements are adjusted. Due to the small pixel sizes in modern CCD chips and the more relaxed restrictions on angular resolution in soft X-ray GEXRF compared to hard X-ray GEXRF (Section 2.2.3), it is usually beneficial to move the detector as close as possible to the excitation spot on the sample. The smallest achievable distance with the sample surface perpendicular to the chip surface is about 15 cm, due to obstructive parts of the sample holder itself. However, this distance can be reduced further, if the sample is mounted on a 20° wedge, allowing to move the goniometer axis θ further away by 20° and giving way to the CCD positioning system. With this adaption, the distance of the pnCCD chip to the pivotal point in the first beamtime is 6.5 cm and in the second beamtime the CCD has a distance of 11.1 cm. The reason for the difference is an additional adapter flange and a different CCD housing of the conventional CCD.

5.2.5. Alignment Procedures

Various alignment procedures are developed during this thesis, which are crucial for the angular calibration of the GEXRF measurements. In principle, for every pixel of the CCD, the respective emission angle of the fluorescence radiation and solid angle of detection can be calculated (Section 2.3.2), if the positioning of the CCD with respect to the excitation position and sample surface direction is well-known. The excitation focus of the multilayer optics, the sample surface and the CCD camera are thus aligned with respect to the pivotal point of the goniometer, which defines the origin of the coordinate system used for the angle calculations.

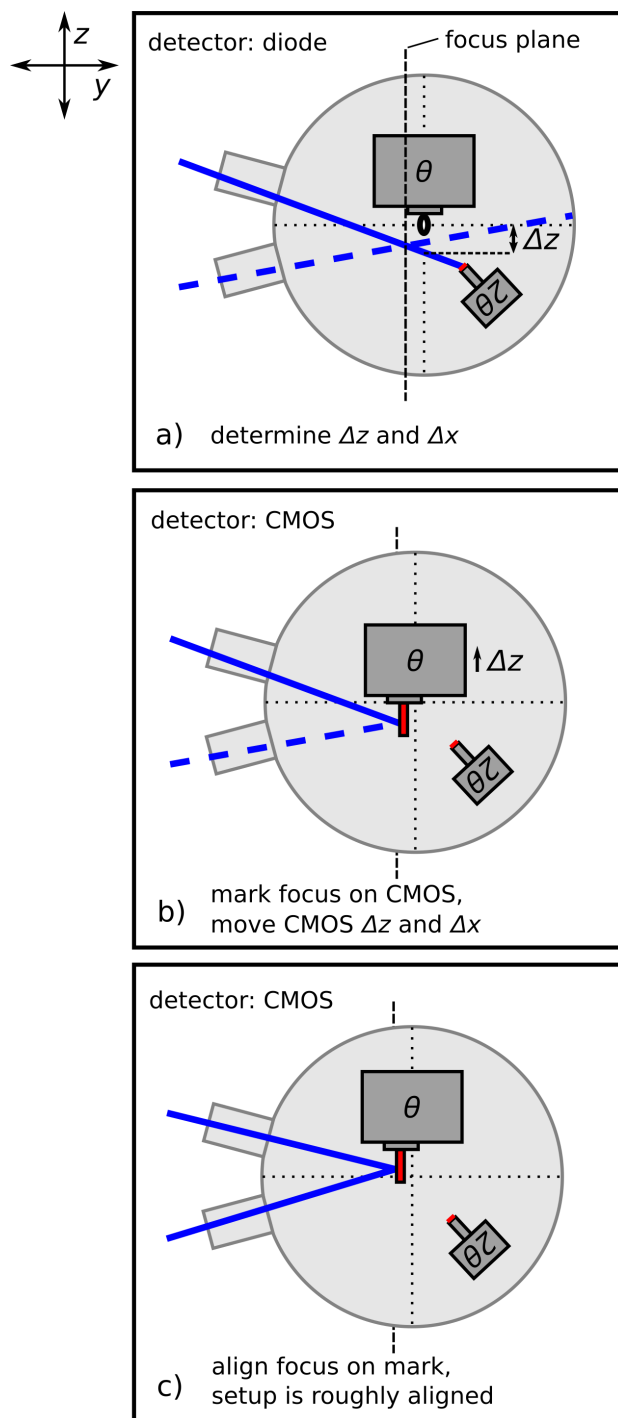


Figure 5.5.: Schematic of the alignment steps for the precise adjustment of the toroidal optics foci into the pivotal point of the goniometer. The dotted blue X-ray beam is not used at the alignment step. It can be easily aligned to a position, where it does not interfere with the other beam. For details about the alignment refer to text.

Goniometer Alignment

For the description of the goniometer alignment, the setup equipped with the superior toroidal mirrors is used. As requisite for the alignment of the goniometer with respect to the optics' focus, the two optics should be already adjusted and their foci overlapped. For beam diagnostics, a pinhole (diameter 500 μm) and a CMOS sensor (768×576 pixel of size $6.33 \times 6.33 \mu\text{m}^2$) are mounted on the sample holder, facing the direction of the convergent X-rays of the toroidal optics. The relative distance of the y position between CMOS chip surface and pinhole is roughly known (e.g. measured with slide gauge), as well as the y position of the pinhole, if it is roughly in the pivotal point.

In a first step, the vertical (here, the x axis is used, it could be the y axis, depending on the ϕ position), radial (z axis) and rotational (θ and ϕ) positions of the pinhole, when its normal intersects with the pivotal point of the goniometer, have to be found. This is done by scanning the X-ray beam, which is reflected by one of the optics, with the pinhole and an X-ray sensitive diode attached to the 2θ stage. Then, pinhole positions with maximum intensity transmitting through the pinhole have to be found before and after rotating θ and subsequently ϕ by 180° . The pivotal position is then the mean of the maximum positions for each axis. For further details about these scans see [114].

When the pinhole is in its pivotal position (Figure 5.5 a)), the optics focus must be shifted a distance Δz and Δx (i.e. vertical axis, which is perpendicular to the plane of projection in Figure 5.5) until it intersects with the pinhole's pivotal position. For this purpose, the X-ray focus on the CMOS detector is marked (Figure 5.5 b)) and the CMOS detector shifted by Δz and Δx . Now the optics can be focused again on the marked spot on the CMOS detector (Figure 5.5 c)). If the new focus position of the toroidal optics is too far from the optimum (i.e. the optics cannot be focused on the mark), the whole spectroscopy chamber, which is mounted on a motorized base frame, must be moved in the corresponding direction and the process repeated. Now the setup is roughly aligned. Depending on the accuracy of the pivotal position of the pinhole in y direction and the measurement of the distance between CMOS chip and pinhole, the focus is probably as close as 0.5 mm to the pivotal axis.

Fine adjustment is now performed by scanning θ (e.g. by 20°) at several y positions of the CMOS detector and recording the focus shift of one of the optics in the CMOS image (Figure 5.6 d)). The y position, at which the focus does not shift with changing θ is the position for which the CMOS surface is in the pivotal point of the goniometer. This position is the intersection point of two linear fits to the position dependent z shifts (Figure 5.6 d), right). If the beam spot is not stationary for θ scans at the determined z position, the alignment steps starting at a) need to be repeated. Now the whole spectroscopy chamber can be shifted in the direction of the y axis of the

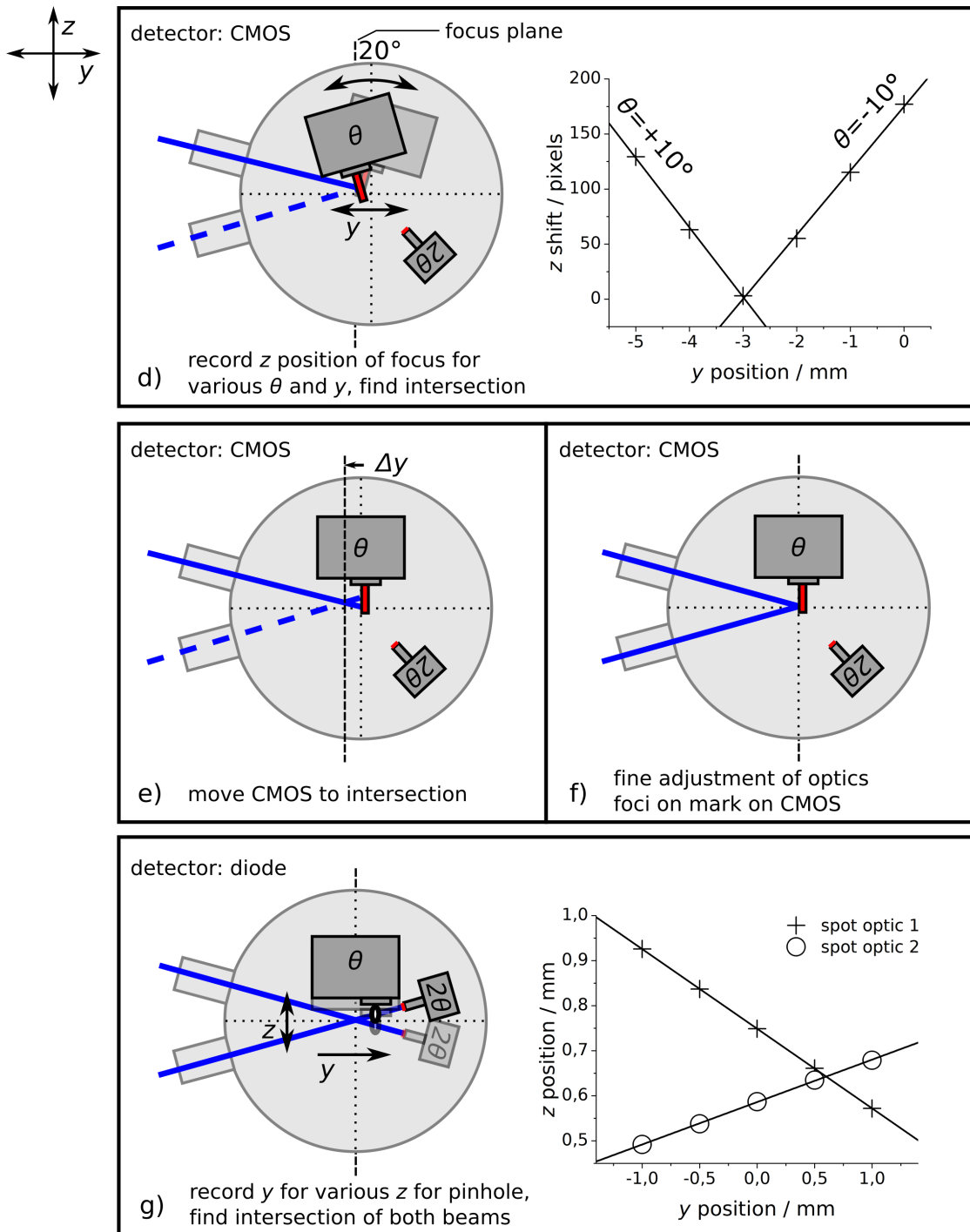


Figure 5.6.: Figure 5.5 continued.

goniometer by the distance between the pivotal y position of the CMOS detector and the y position when the two toroidal foci intersect (Figure 5.6 e)). The whole procedure can be performed with a ϕ scan to further adjust the height of the optics focus. However, since the beam in the setup is propagating almost in a horizontal plane, the alignment procedures performed so far should be sufficient for the x position of the optics' focus. Finally, the foci of both optics can be fine adjusted to the marked position on the CMOS chip (Figure 5.6 f)). The foci distance to the pivotal axis is now better than 50 μm in all directions.

The exact pivotal position of the pinhole in beam direction (y) can now be found by scanning the z axis at various y positions (Figure 5.5 g)) and at each marking the maximum intensity positions for both X-ray beams (of both toroidal optics). At the y position, where the two fitted linear curves intersect, the pinhole is in the pivotal position for y (Figure 5.6 g), right). Scanning the remaining axes yields then the pivotal pinhole position, also with an accuracy of about 50 μm .

Now, the focus position of the toroidal optics is well-defined. A sample with its surface in the pivotal point can be rotated, while the excitation spot on the sample is stationary. For the calculation of the angular scale on the CCD during the GEXRF measurements, the CCD needs to be aligned relative to that excitation position. To describe the CCD positioning, an optical axis must be defined, as is shown in the following chapter.

Defining the LAB System and CCD Alignment

For the alignment of sample and CCD, a Cartesian coordinate system (LAB system) is defined. Its origin is in the pivotal point of the goniometer, so that after the alignment of the spectroscopy chamber, this is overlapped with the toroidal optics focus position. An optical axis is defined and used for sample and CCD alignment by an optical adjustment laser ((Figure 5.7)). Since the direct laser spot will be imaged on the CCD chip for sample alignment and angular calibration purposes later, gray glasses and a mechanical shutter are deployed in the beam path outside the spectroscopy chamber to adjust the intensity and define exposure times. The laser is aligned through the pinhole in its pivotal position (determined in the previous chapter) rotated about θ by 90°. Indeed, the angle between excitation beam and optical laser does not have to be exactly 90° and might vary to enable an easier CCD positioning. The laser beam defines the x_{LAB} axis and the θ axis of the goniometer is parallel to the z_{LAB} axis of the LAB system.

After the CCD is in its measurement distance, the tilt of the CCD and the translational direction are aligned with respect to the optical laser. The laser spot, which will mark the angle line where the emission angle of the fluorescence radiation in the GEXRF measurements is 0°, should hit the CCD at the edge of the chip (but still fully on

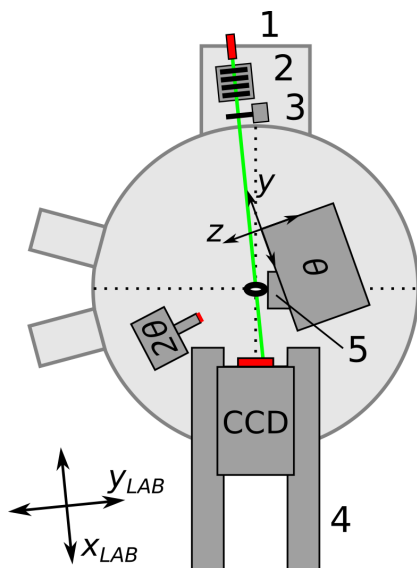


Figure 5.7.: Schematic top view of the spectroscopy chamber with the optical alignment laser (1), gray glasses (2), mechanical shutter (3) and the CCD positioning system (4). The adjustment laser is aligned through the pivotal point of the goniometer onto the edge of the CCD chip. In this final arrangement, it defines the LAB system. Also note the 20° wedge (5), which allows to move the sample holder further away from the CCD positioning system, while keeping the sample surface (here pinhole) aligned to the optical laser.

the chip), so that the angular scale can extend over most of the remaining chip area. Furthermore, it is important to measure the position of the laser beam reflected from the chip surface, to calculate the tilt angles of the CCD chip with respect to the optical axis, as will be shown in Section 5.3.2. Alternatively, the laser reflection can be adjusted back on the laser to align the CCD chip in the $y_{\text{LAB}}z_{\text{LAB}}$ plane.

Sample Alignment

The samples are mounted on a 20° wedge on the sample holder, allowing to set the θ motor of the goniometer 20° further away from the CCD detector, while keeping the position of the samples (see Figure 5.7). Thus, the detector can be aligned closer to the sample holder without touching the motors of the translational stage of the goniometer, increasing the solid angle of detection.

The alignment of the excitation position on the sample surface is carried out by movements relative to a fixpoint on the sample holder (pinhole position or a fluorescent screen). The relative positions can be measured with a slide gauge or a photograph containing a scale before load locking the sample holder and are accurate to about 0.5 mm. Now, the sample surface has to be aligned into the pivotal point of the goniometer with high accuracy, to assure that the excitation spot and thus the origin of the fluorescence radiation is in the origin of the LAB system. For this purpose, iterative scans with the θ and z motors of the goniometer can be used. Thus, the sample surface is aligned by moving it into the laser beam and monitoring the laser beam intensity on the CCD chip. If the shadowing leads to half of the maximum intensity, θ scans are used to maximize the laser intensity. Details can be found in the Bachelor's thesis of L. Bauer [114].

The application of the 20° wedge on the sample holder changes the alignment slightly. Now, the tilt of the sample surface with respect to the transitional axes y and z of the goniometer has to be considered. This results in combined y - z scans with step sizes $\Delta y = \Delta z \tan(20^\circ)$ instead of the pure z scans for the radial adjustment of the sample surface (see Figure 5.7). If this is not considered, the excitation spot on the sample surface would shift due to the alignment. Slightly depending on the sample extensions, this alignment procedure assures a positioning of the sample surface with respect to the pivotal point within about 50 μm . The zero angle of the sample, which is the θ position of the goniometer when the sample surface is parallel to the x_{LAB} axis of the LAB system, can be determined with an accuracy of better than 0.01° , as is demonstrated in Section 6.3. Of course, this value varies with the CCD and sample dimensions and positions. If necessary, further scans with the goniometer stages in the plane of the sample surface can be used to adjust the lateral excitation position on the sample with higher precision. However, it might be necessary to repeat the surface

adjustment afterward.

After the alignment of the sample is completed and the sample is set in its measurement position, the fluorescence emission angle to pixel assignment is defined and can be calculated by an angular calibration procedure (Section 5.3).

5.3. Calibration of the Angular Scale

Since GEXRF profiles are plots of fluorescence intensity with respect to the fluorescence emission angle, the control of the emission angle is crucial for the GEXRF experiment. If the fluorescence emission angle is scanned, for example by rotating the sample, the angular axis is defined by the motor steps of the rotational stage except for an offset of the angular scale. This offset is typically found by measuring a calibration GEXRF profile with a well-known feature, e.g. the inflection point in the GEXRF profile of Si-K α originating from a silicon wafer [23, 115]. The wafer can either be a different sample, or the substrate of the sample to be analyzed. Kayser et al. also use a calibration GEXRF profile (signal of the Ge wafer) in their scanning-free GEXRF experiments in [24]. The relative angular scale is calculated from the measured sample-to-detector distance and detector extension.

The use of a calibration GEXRF profile can lead to systematic uncertainties in the angular scale. First, if the substrate signal is used for calibration, the analyzed structure (thin layers or dopant profiles) can have an influence on the propagation of the fluorescence radiation, which might have to be taken into account. Since the properties of the analyzed structure, which affect the optical response (e.g. roughness, density or stoichiometry), might not be known a priori, this approach can lead to inconsistencies in the analysis. Second, if a well-known independent sample is applied for the angular calibration, there is an uncertainty in the alignment of the measurement samples with respect to the calibration sample.

The following considerations will focus on the angular calibration of a scanning-free GEXRF setup. If the sample-to-detector distance is large compared to the detector width, the detector can be aligned such, that each pixel column (or row) detects fluorescence of a well-defined emission angle (see Section 2.3.2, Figure 2.10 a)). However, especially in the soft X-ray regime, the restrictions to the angular resolution are more relaxed, allowing for a shorter sample-to-detector distance to increase the solid angle of detection and the analyzed angular range. In this range of large solid angles of detection, the actual hyperbolic shape of the equi-angle lines has to be taken into account. Furthermore, it is not sufficient to assume an average solid angle of detection for each pixel (or pixel row), but rather the opening angle of each pixel needs to be calculated, as is shown in Section 2.3.2.

For both GEXRF experiments shown in this thesis (Sections 6.2 and 6.3), the corresponding fluorescence emission angles and solid angles of detection for all pixels of the detectors are calculated as described in Section 2.3.2. To do so, the exact geometry of the detector with respect to the sample, defined by all the geometric parameters (GPs)

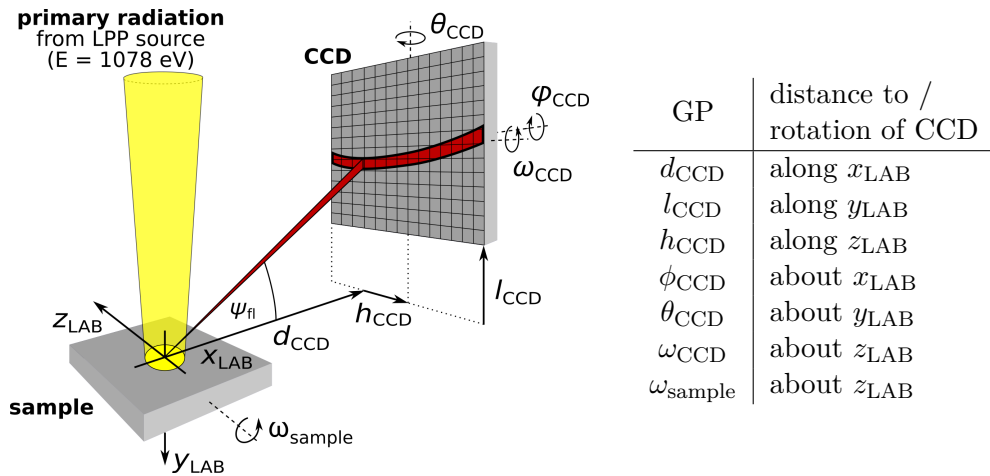


Figure 5.8.: Schematic view of the GEXRF measurement geometry and definition of the geometric parameters in the LAB system (see table). The $x_{LAB}y_{LAB}$ plane is approximately a horizontal plane. Indicated is also a hyperbolic equi-angle line on the CCD chip for a fluorescence emission angle ψ_{fl} .

in Figure 5.8, needs to be known. As mentioned in Section 5.2.5, x_{LAB} and z_{LAB} are parallel to an adjustment laser and the θ axis of the goniometer, respectively. The origin of the LAB system is the pivotal point of the goniometer and the sample surface is adjusted in the $x_{LAB}z_{LAB}$ plane. Then, 6 GPs (3 displacements of the edge center of the CCD and 3 rotations) need to be known to calculate the corresponding fluorescence emission angles and solid angles of detection of each pixel of the two-dimensional detector. To determine these parameters, a calibration sample is used in the first beamtime (Section 6.2) and in the second beamtime (Section 6.3) an absolute angular calibration is applied. The latter is achieved by measuring all the GPs with high precision by means of an optical laser setup.

5.3.1. Calibration with GEXRF profile

In principle, it is possible to fit all geometric parameters with an algorithm, which compares a measured GEXRF profile with a theoretical or well-known GEXRF profile. Each variation of the GPs leads to a change in the angular calibration of the measured GEXRF profile and therefore to a different form of that profile. If the measured and the theoretical GEXRF profile match, the fitted GPs describe the angular calibration correctly. However, the calculation of the whole angular distribution on the CCD chip is time consuming (tens of seconds to minutes on a modern desktop PC), since angle and solid angle are calculated for every pixel. This can be critical in a procedure with tens or hundreds of iterations if all 6 GPs are taken into account. Therefore, it is

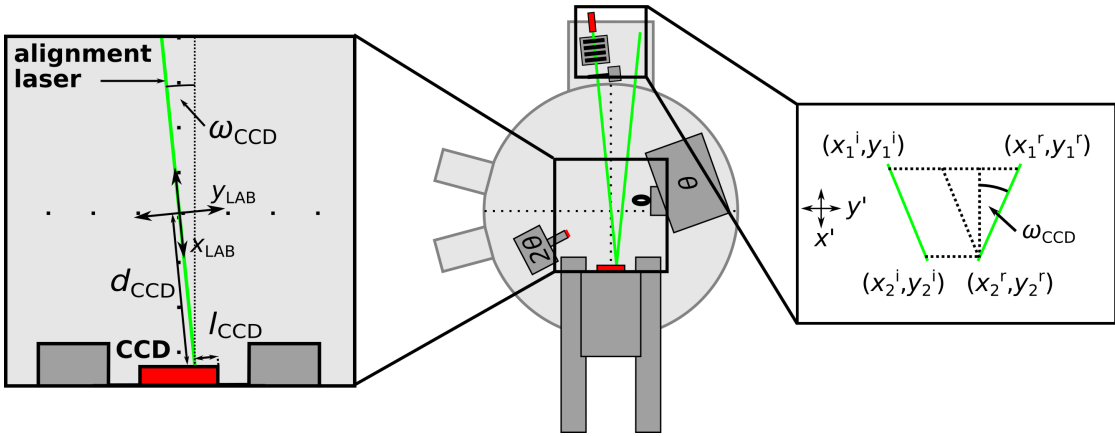


Figure 5.9.: Schematic view of the spectroscopy chamber. The aligned optical laser beam intersects the pivotal point of the goniometer and defines the LAB system (left). It is reflected at the CCD chip (center) and exits the vacuum chamber through the same window flange where it enters. Outside the vacuum chamber, the beam path can be measured to determine the tilt of the CCD camera (right).

helpful to combine the direct measurement of some of the GPs with a fitting routine, which determines for example only the GPs with the strongest influence on the angular scale. It has to be kept in mind that the fitting algorithm can only be as precise as the assumptions on the theoretical GEXRF profile. That means a wrong theoretical curve might still lead to a good fitting result, but induces a systematic error in the angular scale. Even more, a wrong geometry leads to a wrong normalization to the solid angle of detection for each angle, which could alter the shape of the GEXRF profile and lead to wrong depth profiling results.

5.3.2. Absolute Angular Calibration

The basic principle of measuring all relevant GPs to achieve an absolute angular calibration is worked out within the scope of the Bachelor's thesis of L. Bauer [114]. For the beamtime in Section 6.3, the evaluation procedure is automatized and refined. To apply the evaluation procedure, the setup needs to be aligned according to the description in Section 5.2.5. Then, all GPs can be derived in the following way.

The angles ω_{CCD} (see Figure 5.9 left) and θ_{CCD} (lies in $x_{LAB}z_{LAB}$ plane and is not shown in the image) might deviate from zero to achieve a smaller sample-to-detector distance in the alignment procedure. Both can be measured outside the spectroscopy chamber. For this purpose, the positions $(y^{i,r}, z^{i,r})$ of the incident and of the reflected optical laser beam need to be measured at two x' positions x'_1 and x'_2 (Figure 5.9 right).

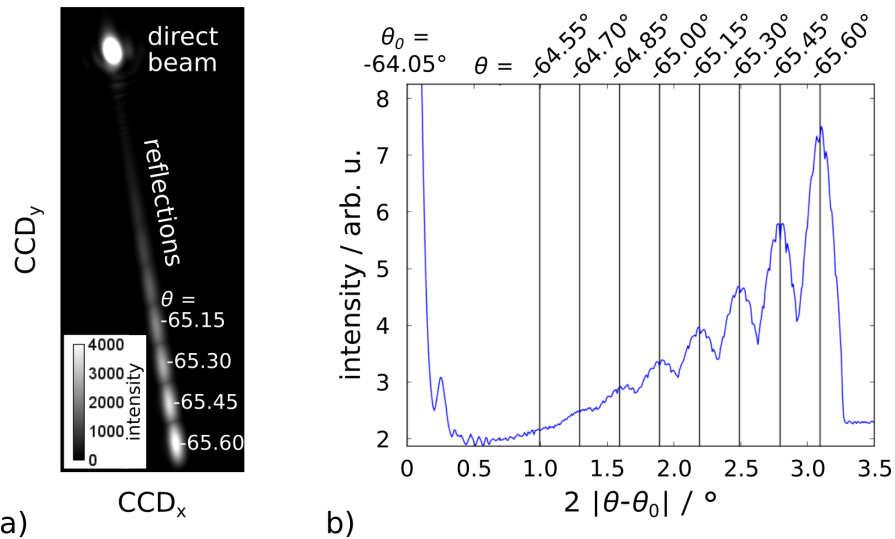


Figure 5.10.: a) Section of the maximum pixel intensities of 9 images of a θ scan. Besides the direct laser beam, the reflected beam positions are shown. In b) the intensities of the image in a) are summed along the equi-angle lines computed with the angular calibration.

Then, the tilt of the CCD with respect to x_{LAB} can be calculated with

$$\begin{aligned} \tan(\omega_{\text{CCD}}) &= \frac{|y_1^{\text{i}} - y_1^{\text{r}}| - |y_2^{\text{i}} - y_2^{\text{r}}|}{2 \times |x_1^{\text{i}} - x_2^{\text{i}}|} \\ \tan(\theta_{\text{CCD}}) &= \frac{|z_1^{\text{i}} - z_1^{\text{r}}| - |z_2^{\text{i}} - z_2^{\text{r}}|}{2 \times |x_1^{\text{i}} - x_2^{\text{i}}|}. \end{aligned} \quad (5.3.1)$$

The GPs l_{CCD} and h_{CCD} (displacement of edge center of the CCD with respect to y_{LAB} and z_{LAB}) are determined by a single recording with the CCD camera of the direct adjustment laser beam (shown in Figure 5.10 a)). The position $(\text{CCD}_x^0, \text{CCD}_y^0)$ can be measured with a two-dimensional Gaussian fit with sub-pixel accuracy. This, together with the known tilt angles ω_{CCD} and θ_{CCD} , yields the position of the CCD camera in the $y_{\text{LAB}}z_{\text{LAB}}$ plane.

Now, d_{CCD} and ϕ_{CCD} are extracted from the final θ scan of the goniometer from the sample alignment* (Figure 5.10 a)). For each scan position, an image of the adjustment laser beam reflected at the sample surface is recorded with the CCD camera. The positions of the reflected beam on the CCD chip can again be fitted with two-dimensional Gaussian functions, yielding the center positions $(\text{CCD}_x(\theta), \text{CCD}_y(\theta))$.

* It is important that the radial position of the sample (z axis) is already aligned

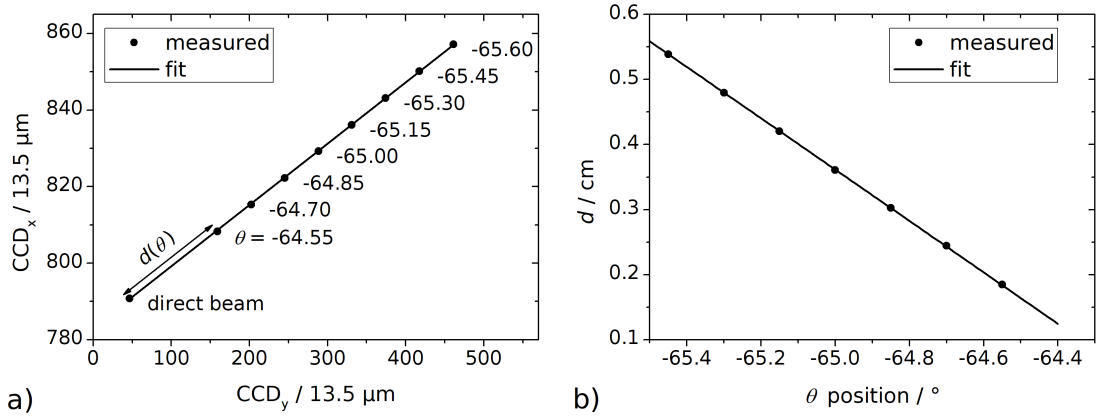


Figure 5.11.: a) Linear fit to the CCD positions of the adjustment laser reflected at the sample surface for various θ positions of the goniometer. b) Distances $d(\theta)$ of the reflected laser beam positions to the direct laser beam position on the CCD for various θ positions of the goniometer and the corresponding fit.

Plotting $CCD_x(\theta)$ over $CCD_y(\theta)$ and a linear fit of m and n in

$$CCD_y(\theta) = m \times CCD_x(\theta) + n$$

yields $\phi_{CCD} = 1/\tan(m)$ (Figure 5.11 a)).

The distance d_{CCD} can be calculated with the relation $d(\theta)/d_{CCD} = \tan(2\theta)$, $d(\theta)$ being the distances of each reflected laser beam position to the direct laser beam on the CCD chip for a tilt angle θ of the sample. In the case that the unobstructed adjustment laser beam is perpendicular to the CCD chip surface ($\omega_{CCD} = \theta_{CCD} = 0$), $d(\theta)$ can be calculated by the Pythagorean theorem $d(\theta)^2 = (CCD_x(\theta) - CCD_x^0)^2 + (CCD_y(\theta) - CCD_y^0)^2$. For a more general case, the tilt of the CCD has to be taken into account. The surface of the sample is in good approximation parallel to the θ axis of the goniometer, which is parallel to the z_{LAB} axis of the LAB system. Therefore, the plane of all (at the sample surface) reflected beams is parallel to the horizontal $x_{LAB}y_{LAB}$ plane of the LAB system and a tilt of θ_{CCD} does not affect the positions of the reflected laser spots. However, a tilt of ω_{CCD} needs to be considered with a correction factor $K(\omega_{CCD}, \theta)$ (see Appendix F), so that

$$\begin{aligned} d^K(\theta) &= d(\theta) \times (K(\omega_{CCD}, \theta))^{-1}, \text{ with} \\ K(\omega_{CCD}, \theta) &= \cos(\omega_{CCD}) + \sin(\omega_{CCD}) \tan(2\theta). \end{aligned} \quad (5.3.2)$$

With θ^0 being the position of the goniometer when the sample surface is aligned

parallel to the x_{LAB} direction of the LAB system, the following relation is valid:

$$d(\theta - \theta^0) = \tan(2|\theta - \theta^0|) \times d_{\text{CCD}} \times K^{-1}(\omega_{\text{CCD}}, \theta - \theta^0) \quad (5.3.3)$$

Figure 5.11 b) shows a fit of equation 5.3.3 to the measured distances $d(\theta - \theta^0)$ on the CCD with θ^0 and d_{CCD} as free parameters. Consequently, both, the alignment angle θ^0 and the sample-to-detector distance d_{CCD} can be obtained.

The knowledge of all 6 GPs and θ^0 allows now to calculate the corresponding fluorescence emission angle and the solid angles of detection for every pixel on the CCD chip for every goniometer position θ adjusted during a measurement. As proof of consistency, the image of the maximum pixel intensities of the θ scan is used and the intensities along the equi-angle lines from the angular calibration are summed. Figure 5.10 b) shows the resulting plot. If GEXRF data were used, the x axis would correspond to fluorescence emission angles. The expected reflection angles with respect to the x_{LAB} axis ($2|\theta - \theta_0|$) are indicated by the vertical lines for each θ value. They match with the maximum positions of the plot, demonstrating the validity of the calibration. The performance of this procedure with respect to reproducibility and stability will be presented along with the measurements of the second beamtime in Section 6.3.

5.4. Single Photon Analysis

After a careful setup and sample alignment, the recording of the raw data of the GEXRF experiment is straight forward. While the source is in operation and fluorescence radiation from the sample is excited, the CCD acquires images (GEXRF frames). The source intensity and camera parameters have to be adjusted in a way that the total intensity on each frame is low enough to detect and distinguish single photon events (SPEs) and that dark current and readout noise are minimized. Due to the typically short recording times (< 1 s) and low chip temperatures ($< -50^{\circ}\text{C}$), the readout noise is dominant and can be regulated by the readout frequency of the CCD, leading to a compromise between long readout times and low noise levels.

While for the first beamtime a pnCCD is used (Section 6.2), measurements in the second beamtime are performed with a conventional CCD (Section 6.3). The former is optimized to detect SPEs and the raw data treatment is carried out by PNSensor GmbH. The treated data provides already information about position and intensity of each detected photon. For the measurements with the conventional CCD, this information is not readily available. Therefore, the methods developed to analyze the raw data from the second beamtime are explicitly described in the following.

For the measurements with the conventional CCD, it is useful to record e.g. $n_{\text{dark}} = 3$ dark images every $n_{\text{meas}} = 50$ GEXRF frames to monitor the noise level in the dark frames (which is a function of chip temperature due to dark current, see Section 2.3.1). The GEXRF frames are dark frame corrected with a “master” dark (MD) image, which can be e.g. the median image of the n_{dark} dark images prior to the n_{meas} measurements. Thus, long-term instabilities of the camera temperature can be monitored and accounted for. For the measurements used in this thesis, the standard deviation of the dark frames σ_{dark} changed by less than 0.5% over a whole GEXRF measurement.

In Figure 5.12, a clean GEXRF frame (after subtraction of a MD frame) is shown. The detected fluorescence radiation originates from a C/Ni-multilayer irradiated with 1078 eV photons from the LPP source, so that mainly Ni-L $_{\alpha}$ radiation reaches the detector. SPEs can be seen in the magnified image on the bottom left panel. Different shapes of the photon events can be differentiated. On the one hand, one-photon events are shown consisting of up to four pixels (labeled 1-px, 2-px etc.). The SPEs, which consists of more than one pixel are split events (see Section 2.3.1). On the other hand, two examples for photon events which consist of more than four pixels are labeled as pile-up. These events are usually created by more than one photon, as will be seen in the next evaluation steps.

Of each photon event, the position, where the photon was absorbed in the CCD chip,

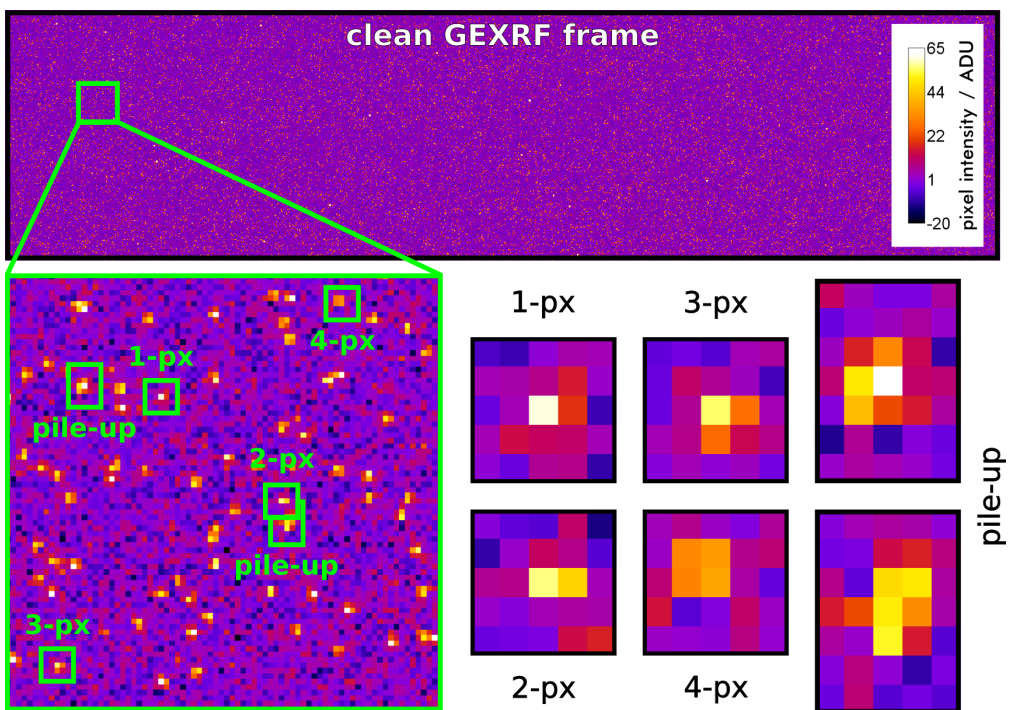


Figure 5.12.: Single photon events detected with a CCD camera. Top: Whole dark frame corrected CCD frame. Bottom: Enlarged view of indicated image section. Different patterns of single photon events can be discriminated.

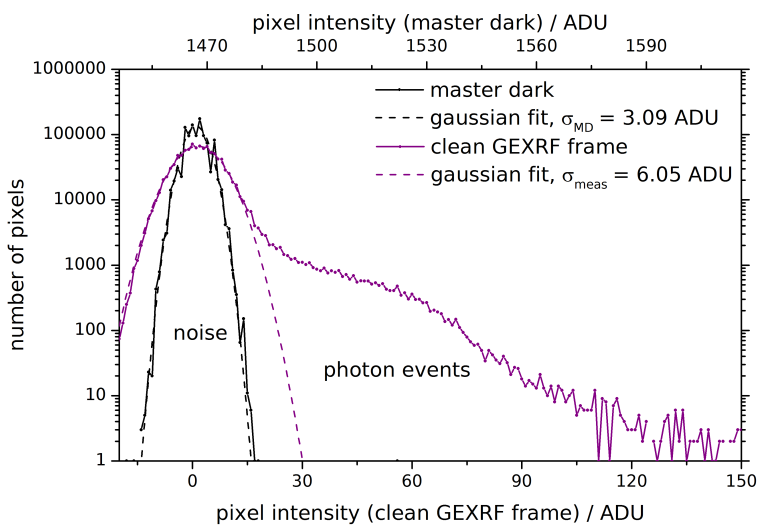


Figure 5.13.: Histogram of master dark frame (top axis) and clean GEXRF frame (bottom axis). A region dominated by noise and a high pixel intensity shoulder originating from photon events can be identified in the plot.

and the energy of the detected photon are of interest. If all photon events were 1-pixel events (i.e. no split events are present), both properties are retrieved straight forward by the pixel coordinate and the pixel intensity. In this case, an energy-dispersive spectrum is identical to an (energy calibrated) plot of the number of detected SPEs against their intensity (histogram). For the CCD image in Figure 5.12, such a histogram is shown in Figure 5.13.

At zero intensity, a Gaussian-shaped peak is visible in the histogram of the clean GEXRF frame (or “SPE frame” hereafter, purple curve). Its height and width depend on the actual noise contribution. The Gaussian-shaped noise in the MD frame (black curve) has a standard deviation of $\sigma_{\text{MD}}=3.09$ ADU. The Gaussian-shaped noise in a single dark frame yields a standard deviation of $\sigma_{\text{dark}}=4.67$ ADU and is assumed to be similar to the noise in the SPE frame*. Thus, from error propagation it follows that the noise in the clean SPE frame is expected to be

$$\sigma_{\text{meas}} = \sqrt{\sigma_{\text{dark}}^2 + \sigma_{\text{MD}}^2} = 5.63 \text{ ADU}. \quad (5.4.1)$$

However, the measured value of $\sigma_{\text{meas}} = 6.05$ ADU (from Gaussian fit in Figure 5.13) is slightly higher, indicating a further noise contribution, maybe due to visible light from the LPP source. The noise level in the SPE frames is crucial to the split event recombination, influencing the final energy resolution and the analyzable low energy region, as will be investigated in Section 5.4.2.

At higher pixel intensities (> 30 ADU), the histogram of the clean SPE frame shows contributions, which originate from the detected fluorescence radiation. However, no clear fluorescence peak of the expected Ni-L α radiation from the C/Ni-multilayer sample can be differentiated in the histogram, since the total fluorescence photon intensity is most often randomly distributed over more than 1 pixel. This indicates the need for precise split event recombination.

5.4.1. Split Event Recombination

The main challenge in SPE detection in the soft X-ray range with the conventional CCD applied in this thesis is the low signal-to-noise ratio. Firstly, the total number of created charge carriers is relatively small compared to the case with hard X-ray photons and secondly, these charge carriers are also distributed over more than one pixel, further reducing the signal of a single pixel. In addition, the applied CCD camera is not optimized for single photon detection concerning gain and dynamic range. Therefore, a

* The noise in the SPE frame cannot be measured by simply taking the standard deviation of the image, since the SPEs influence that value.

Ni-L _{α} photon with an energy of 849 eV, which creates on average $849 \text{ eV} / 3.62 \text{ eV} = 234.5$ electron-hole pairs in pure silicon, is only detected with a signal of ≈ 120 ADU, although the dynamic range is about 50000 ADU. In the case of split events, the discrimination of pixels dominated by noise and those giving information about the detected photon is not always possible, especially for fluorescence radiation with yet lower energy.

Clustering

The first approach to recombine split events is a clustering method. The algorithm to identify SPEs and to find the corresponding pixels in the clean SPE frame is illustrated in Figure 5.14. In a first step (top row), all pixels in a clean SPE frame are searched for, whose intensity is above a certain threshold. The threshold is defined by a multiple n'_σ of the estimated noise level σ_{meas} in the clean SPE frame according to equation 5.4.1. Typical values of n'_σ are 3 to 8, in the example $n'_\sigma = 3$ is chosen. If pixel positions x and y are found such that the pixel intensity $I(x, y) > n'_\sigma \times \sigma_{\text{meas}}$, it is checked if this pixel has the highest intensity in a 3×3 area centered at (x, y) . If not, the conditions are checked for the next pixel. Otherwise (2nd row), the neighboring pixels $P(x - 1, y)$, $P(x + 1, y)$, $P(x, y - 1)$ and $P(x, y + 1)$ are investigated. If their value is above a second threshold $n''_\sigma \times \sigma_{\text{meas}}$ ($1 \leq n''_\sigma \leq n'_\sigma$), these pixels are assigned to the same cluster N_{ev} and the neighboring pixels are again investigated in the same way iteratively, leading finally to an n -px event, n being the number of pixels in the cluster. In the end, a total number N_{ev}^t of clusters is found in the image, each consisting of $n(N_{\text{ev}}) \geq 1$ pixels. The total intensity of each cluster is then

$$I(N_{\text{ev}}) = \sum I(x, y), \quad P(x, y) \in N_{\text{ev}} \quad (5.4.2)$$

Furthermore, a center of gravity can be determined with the coordinates

$$\begin{aligned} X(N_{\text{ev}}) &= \frac{\sum x \times I(x, y)}{I(N_{\text{ev}})}, \quad P(x, y) \in N_{\text{ev}} \\ Y(N_{\text{ev}}) &= \frac{\sum y \times I(x, y)}{I(N_{\text{ev}})}, \quad P(x, y) \in N_{\text{ev}}. \end{aligned} \quad (5.4.3)$$

The center of gravity in principle yields a better spatial resolution than the pixel size, i.e. a better angular resolution for the scanning-free GEXRF measurements. However, for the measurements shown in Section 6.3, the angular resolution is not critical and therefore no sub-pixel resolution will be introduced. Investigations on the possible sub-pixel resolutions can be found in [64, 59]. The calculated intensity can be used to

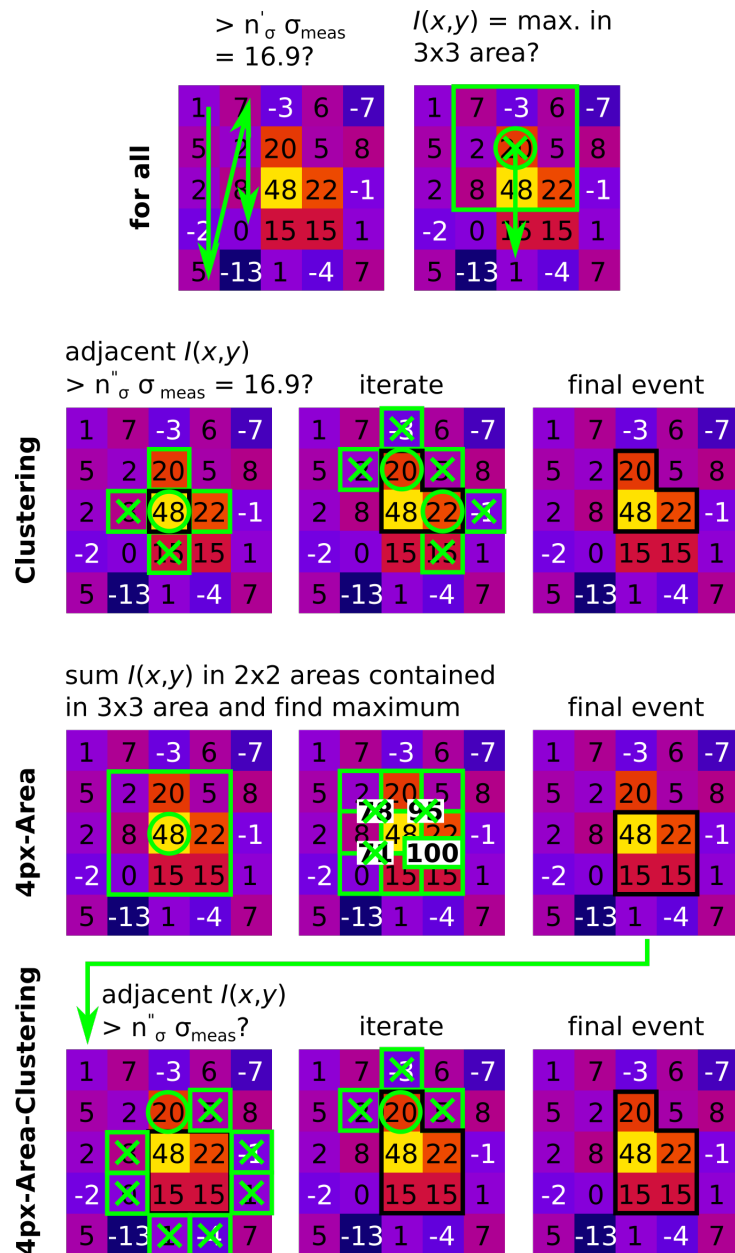


Figure 5.14.: Exemplary description of the three investigated split event recombination methods: Clustering, 4px-Area and 4px-Area Clustering. The identification of the most intense pixel of an SPE is the same for all methods (top row). The threshold factors are $n'_\sigma = n''_\sigma = 3$ and $\sigma_{\text{meas}} = 5.63$ ADU. For a complete description, please refer to the text.

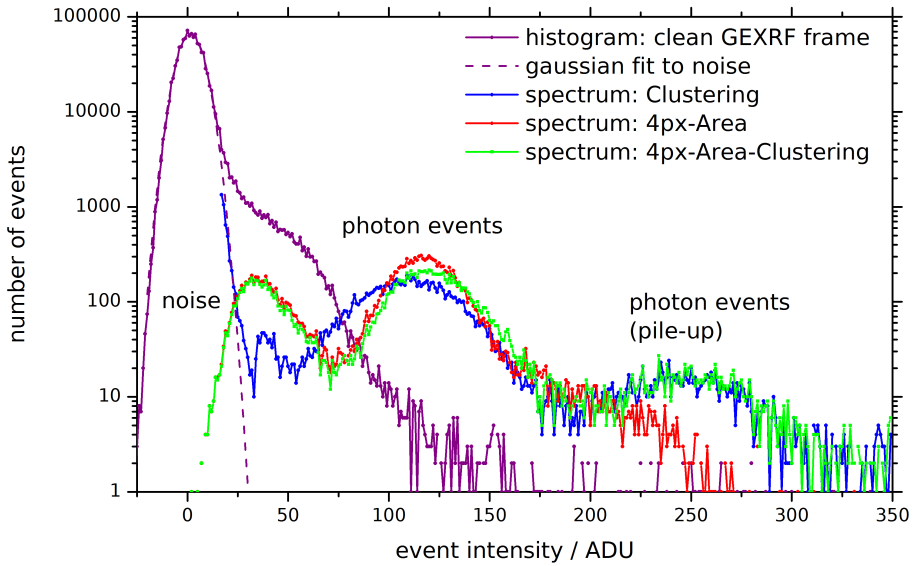


Figure 5.15.: Energy-dispersive spectra (uncalibrated) created with the three SPE recombination methods from the clean SPE frame and its histogram for comparison. In the spectra of all three methods a peak for Ni-L_α fluorescence is visible. The two clustering methods also handle pile-up.

create an energy-dispersive spectrum from the detected SPEs, if the number of SPEs is plotted with respect to their intensity. Such a spectrum for the Clustering method (and subsequent methods) is compared in Figure 5.15 to the plain histogram of the clean SPE frame. For the present and the following analysis in the chapter, the two threshold factors for the analysis are set to $n'_\sigma = n''_\sigma = 3$. The high number of events at low event intensities (≈ 25 ADU) can be attributed to noisy pixels with high noise intensities, as shows the comparison to the Gaussian peak fitted to the noise peak in the histogram. At about 35 ADU, a small, narrow peak appears. This peak can also be attributed to noise events, as will be shown later. The actual fluorescence peak of the Ni-L_α is located at $x_0 = 109.7$ ADU with a full width at half maximum of $\Delta x_{\text{FWHM}} = 57$ ADU. This yields a resolving power $E/\Delta E = x_0/\Delta x_{\text{FWHM}} = 1.9$ at Ni-L_α. Note that at 243 ADU a second broad peak with much lower intensity is visible, originating from pile-up events (also shown later).

The energy-dispersive spectrum can also be analyzed with respect to the type of cluster the spectrum is composed of. Figure 5.16 a) shows the contributions of n -px events to the total number of detected clusters. For $n > 4$ the number of photon events drastically decreases, but also n as large as 14 is detected. In Figure 5.16 b), the contribution of the 1-px to 6-px events (filled curves) to the total spectrum (blue curve) is shown. It

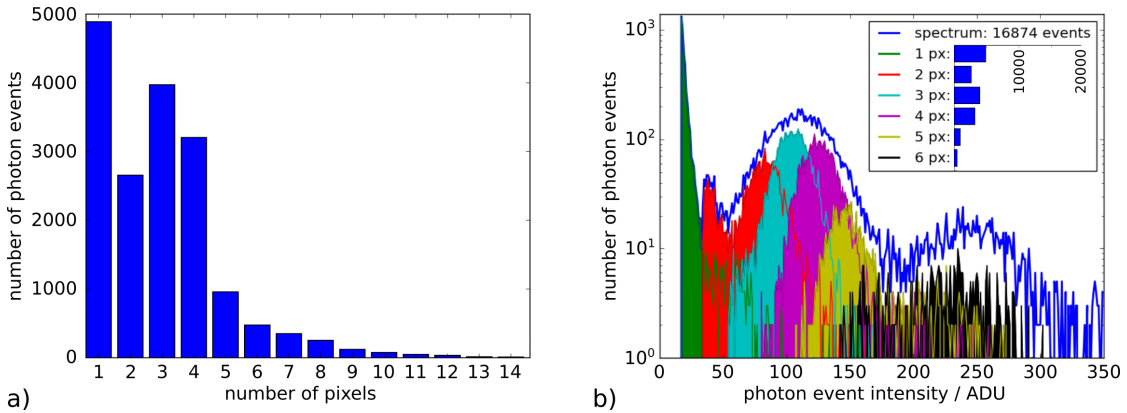


Figure 5.16.: a) Histogram of SPE types (1-px, 2-px ...). The probability decreases strongly for the appearance of 5-px events and larger ones. b) Share of the n -px events in the total spectrum shown for $n \leq 6$. The histogram in the inset is the same as in a).

can be seen that the high intensity peak in the low energy range, starting at 16.9 ADU $\approx 3 \times \sigma_{\text{meas}}$, is only containing 1-px events, supporting the explanation that these are pure noise pixels. The second peak at about 35 ADU $\approx 2 \times 3 \times \sigma_{\text{meas}}$, consists of mainly 2-px events. This in addition to the shape and position of that peak indicate that it is also an artifact in the spectrum originating from two pixels with high noise levels. The actual photon peak consists of mainly 2-px, 3-px, 4-px and 5-px events, each displaying a much narrower but shifted peak in the spectrum. This shift in the n -px spectra results in the large width of the combined spectrum and is responsible for the low energy resolution of the Clustering method. Theoretically, for a photon event split in e.g. 2 pixels, on average it should make no difference for the calculated intensity (i.e. position in the spectrum) if further noise pixels are contributing to the cluster of the SPE. Yet, this is only true if the mean intensity of the added noise pixels is zero, which is not valid since the pixels have to be above the threshold $n''_\sigma \times \sigma_{\text{meas}}$ to be accepted. A more detailed study on the influence of the two thresholds n'_σ and n''_σ on the n -px spectra is presented in Appendix G. It is shown and rendered plausible that the spectra can be shifted to overlay the peaks of all the n -px spectra, resulting in a slightly better resolving power for the peak in the combined spectrum. However, since the effect on the linearity of the energy scale is not clear (to simultaneously overlay the pile-up peaks the abscissa would need to be stretched, too), this approach will not be followed further. Instead, a second approach is pursued for SPE recombination in the following section. Finally, please note that the peak at about 243 ADU is composed of n -px events with $n > 4$, which supports the interpretation as pile-up.

4px-Area

The main idea in the 4px-Area method is that the charge cloud of an SPE has a finite size. Indeed, already by visual inspection of Figure 5.12 it can be seen that a great part of the detected photon events consist of more than one pixel, but usually of less than 2×2 pixels. This is expected, if the detected charge cloud is of the size of the pixels, which is true for the shown measurements, as will be investigated in Section 5.4.2. Therefore, an approach is tested in which always 4 pixels are regarded as the whole photon event.

Similar to the Clustering method, all pixels with an intensity greater than $n'_\sigma \times \sigma_{\text{meas}}$ are searched for, which have also the highest intensity compared to their neighboring pixels (Figure 5.14, top row). Then, all 8 surrounding pixels are regarded further and the summed intensity of the four 2×2 -pixel areas are compared (Figure 5.14, third row). The 2×2 pixel area with the highest summed intensity is assigned to the photon event. SPE intensity and position can be calculated according to equations 5.4.2 and 5.4.3.

The spectrum obtained with the 4px-Area method is printed as red curve in Figure 5.15. The first peak is centered at 35 ADU and can be assigned to noise events. Its slope is much shallower compared to the noise peak in the Clustering method, since always four pixels contribute to the noise events (i.e. a corresponding Gaussian-shaped noise peak would have twice the width). As expected, the fluorescence peak is narrower compared to the Clustering method, resulting in a resolving power of $E/\Delta E = x_0/\Delta x_{\text{FWHM}} = 3.4$ at Ni-L α . The peak is also slightly shifted to higher event intensities compared to the Clustering method because of the on average higher number of pixels assigned to the SPEs.

Since all evaluated SPEs consist of four pixels, pile-up events might be counted in a wrong way. If the charge cloud of two photons strongly (but not completely) overlap, the two events will be counted only as one with a photon event intensity of less than the sum of the two SPEs. This leads to a broadened and shifted pile-up background as compared to the Clustering method (high energy tail in Figure 5.15), making it difficult to use the pile-up events in the evaluation. However, with respect to measurement time it could be useful to allow a specific level of pile-up events be recorded during the measurement, if these events can be evaluated correctly. Therefore, in a third SPE recombination method, the superior energy resolution of the 4px-Area method is coupled to the better pile-up detection of the Clustering method.

4px-Area-Clustering

Figure 5.14 shows the principle of split event recombination with the 4px-Area-Clustering method in rows 3 and 4. The start is the same as in the 4px-Area method. Then, for all

Table 5.1.: Evaluation of the fluorescence peak position x_0 , its width Δx_{FWHM} and the resulting resolving power $x_0 / \Delta x_{\text{FWHM}}$ for the Ni-L α peak. The 4px-Area method yields the best resolving power, but pile-up events cannot be handled correctly.

	x_0 / ADU	$\Delta x_{\text{FWHM}} / \text{ADU}$	$x_0 / \Delta x_{\text{FWHM}}$
Clustering	109.7	57	1.9
4px-Area	117.1	34.5	3.4
4px-Area-Clustering	120.2	41.4	2.9

four pixels, the adjacent pixels are investigated and assigned to the same cluster if their intensity is above a second threshold $n''_\sigma \times \sigma_{\text{meas}}$, just as in the Clustering method. This process is iterated until no more pixels above the threshold are found. The example in Figure 5.14 shows the difference in the resulting pixel assignment for all three methods (last column). Here, the 4px-Area-Clustering method seems to lead to the most complete event recombination. As can be seen in the resulting spectrum in Figure 5.15 and in Table 5.1, the resolving power of $E/\Delta E = 2.9$ is better than for the Clustering method while the spectrum still allows to identify pile-up events. The broadening of the Ni-L α fluorescence peak as compared to the peak in the 4px-Area method is caused by the on average higher number of pixels contributing to the recombined SPEs.

Figure 5.17 summarizes the results of the 3 different split event recombination methods. The first column illustrates the differences of the pixel-to-cluster assignment for all three methods, the green circle indicating the example of Figure 5.14. All three methods detect the same photon events, but assign different pixels to each event. The spectra for the 4px-Area and 4px-Area-Clustering method are shown in Figure 5.17 d) and e), respectively. Of course, the former is composed of only 4-px events, resulting in the best energy resolution. The decreased energy resolution of the 4px-Area-Clustering method compared to the 4px-Area method originates from a contribution of 5-px events, as can be seen in Figure 5.17 e). The choice of the threshold factors n'_σ and n''_σ affects the resolution and depends on the actual data. This will be shortly investigated for one of the measurements in Section 6.3.

In the final part of this chapter, the influence of various camera and charge cloud properties are numerically simulated to evaluate optimal properties for soft X-ray SPE evaluation.

5.4.2. Numerical Simulations

Dark frame corrected CCD frames with single photon events (SPEs) can be simulated by a 2-dimensional array, the entries representing the pixel intensities. SPEs are sim-

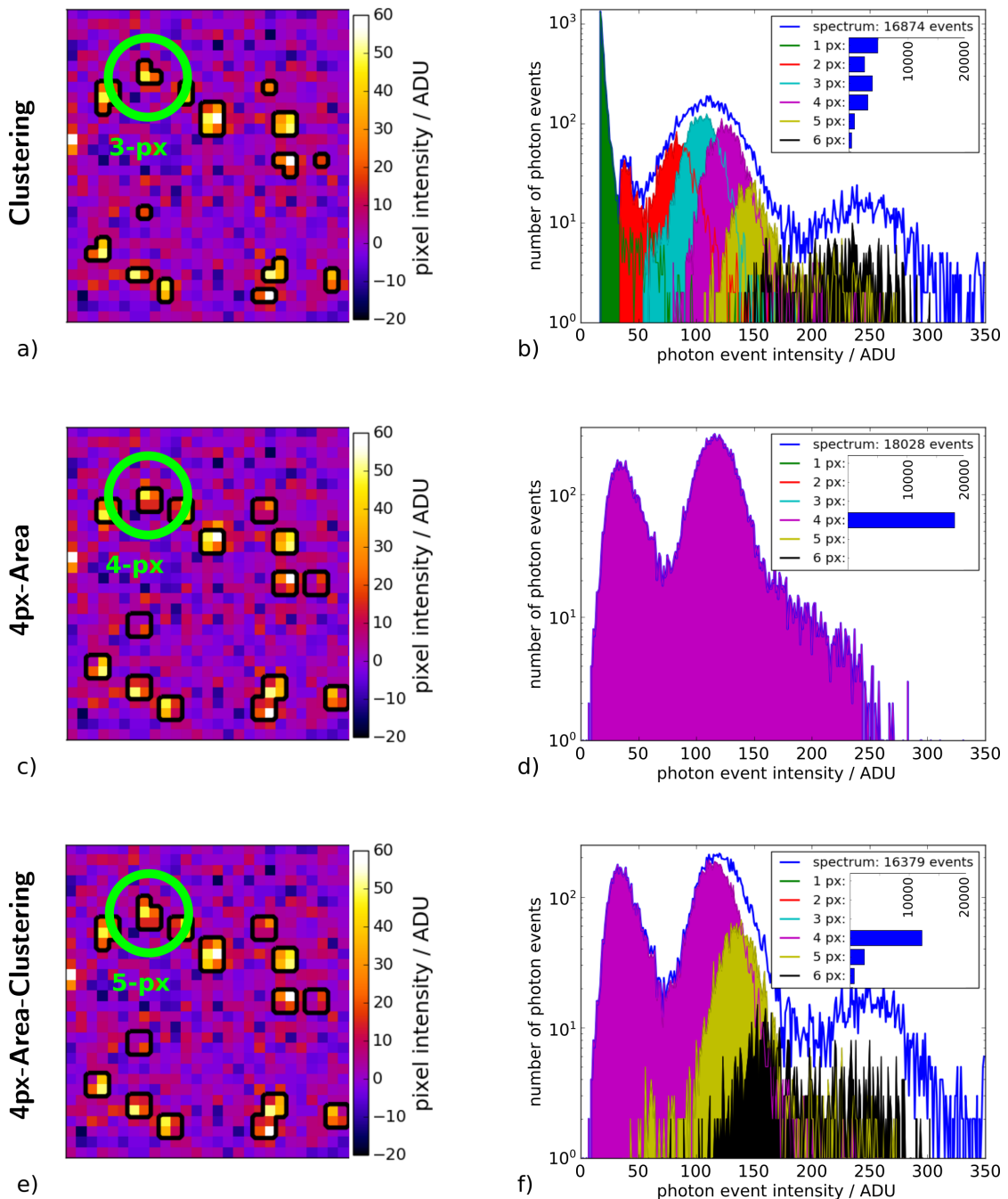


Figure 5.17.: Comparison of the evaluation with the three SPE recombination methods.

The left column (figures a, c and d)) shows the resulting pixel to cluster assignment of the methods. Circled is the area of Figure 5.14. The right column (figures b, d and f)) compares the calculated spectra. The contribution from the various split event types is shown. Of course, no 1-px to 3-px events appear in the 4px-Area and 4px-Area-Clustering method.

ulated with a Monte Carlo approach. Each simulated photon N_{ph} creates a Gaussian-distributed total intensity $I_{\text{ph}}(N_{\text{ph}})$ in the CCD chip with an average intensity of \bar{I}_{ph} and a standard deviation of $\sigma_{\text{ph}}(\bar{I}_{\text{ph}}, E_{\text{ph}})$ given by

$$\sigma_{\text{ph}}(\bar{I}_{\text{ph}}, E_{\text{ph}}) = \bar{I}_{\text{ph}} \times \frac{\sqrt{F \times \frac{E_{\text{ph}}}{3.62 \text{ eV}}}}{\frac{E_{\text{ph}}}{3.62 \text{ eV}}}. \quad (5.4.4)$$

In equation 5.4.4, E_{ph} is the energy of the detected photon, $E_{\text{ph}}/3.62 \text{ eV}$ the number of electron-hole pairs created by such a photon in pure silicon [30], and F the Fano factor, which is for silicon 0.115. The latter takes into account the deviation of the statistical charge carrier creation from a pure Poisson process. Thus, the energy resolution is assumed to follow the behavior of an ideal semiconductor radiation detector [116].

The algorithm randomly distributes a number $n(N_{\text{ph}})$ of such photons N_{ph} homogeneously on an initially empty CCD mesh with 2046×515 pixels and a pixel size of $13.5 \times 13.5 \mu\text{m}^2$, similar to the conventional CCD used for the measurements shown above. The total intensities $I_{\text{ph}}(N_{\text{ph}})$ are split to several adjacent pixels, if the charge cloud created by the photon is of the size of the pixels or the hit position close to a pixel border. The charge cloud is modeled by an axially symmetric two-dimensional Gaussian distribution with a standard deviation of σ_{cc} and centered at the exact photon hit position. The intensity for the individual pixels is calculated by an integration of the Gaussian distribution over the pixel dimensions of each pixel (Appendix H). Finally, a random, Gaussian-distributed noise intensity with a width of σ_{dark} is added to each pixel of the simulated CCD image.

The first simulations shall match the single photon event measurements in Section 5.4, where mainly fluorescence radiation of Ni-L α is detected. The size of the charge cloud is derived from these measurements, using the plateau height of the difference-ratio histogram as proposed by Lawrence et al. [62]. This method yields a value of $\sigma_{\text{cc}} = 7.6 \mu\text{m}$ (FWHM = $17.8 \mu\text{m}$), as is shown in the Master's thesis of S. Staech [117]. Furthermore, it is found that the charge cloud size calculated with this approach is consistent with simulated data representing the present measurement conditions. The noise value of the dark images $\sigma_{\text{dark}} = 4.67 \text{ ADU}$ is also chosen according to the values of the actual measurement and a total mean intensity of $\bar{I}_{\text{ph}} = 145 \text{ ADU}$ is set for the monochromatic 849 eV photons. Three dark images (without single photon events) and a single SPE frame are created. A master dark is calculated by taking the median image of the three dark frames. The master dark is subtracted from the SPE frame to get a clean SPE frame, which is then evaluated by the 4px-Area-Clustering method using noise thresholds $n'_{\sigma} = n''_{\sigma} = 3$.

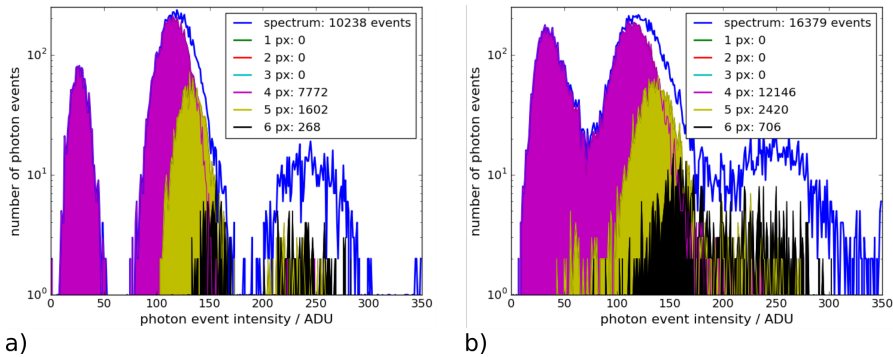


Figure 5.18.: Spectrum of SPE evaluation with the 4px-Area-Clustering method for a) simulated and b) measured data. In the spectrum a noise peak, a fluorescence peak of Ni-L_α lines and a pile-up peak are visible. The peaks in the measurement are broader than in the simulation.

Figure 5.18 compares the spectra of the SPE evaluation for a single frame of measured and simulated data, the latter performed with 10000 SPEs in the SPE frame. Clearly, the main features, a noise peak below 50 ADU, the fluorescence peak at ≈ 120 ADU and a pile-up peak at ≈ 250 ADU are visible. Furthermore, the ratio of 4-px events to 5-px events is similar, indicating a correctly simulated charge cloud size. Indeed, the main difference in the two spectra is a broader peak width and a more intense noise peak in the measured data, which seems to originate from an additional noise contribution to σ_{dark} in the SPE frame, as is already suspected above. Therefore, in the next step, additional noise is introduced by increasing σ_{dark} in the SPE frame only.

Figure 5.19 a) shows how the spectrum evolves with increasing noise in the SPE frame only. The noise is increased by 10% from bottom to top, resulting in a good match of simulated and measured data for the Ni-L_α fluorescence peak and pile-up peak at an increase of about 30% (red curve). However, it becomes obvious that some additional background contribution below 80 ADU is present in the measurement, which cannot be explained by the simulation. This contribution cannot be assigned to further fluorescence lines, since they would have been detected in the measurements with the pnCCD, where similar excitation conditions and a much better energy resolution are applied (Figure 6.7 in Section 6.2.3). C-K_α and O-K_α are present in the spectrum, but with intensities about 2 orders of magnitude lower than the Ni-L_α intensity. Possible background contributions might be introduced due to stray light or detector artifacts, but no satisfactory explanation has been found, yet. Indeed, an enhanced energy resolution would not only be beneficial in terms of photon discrimination, but would also help to better understand the recorded spectra and identify noise contributions.

To study the parameters that might influence the energy resolution, SPE frames are

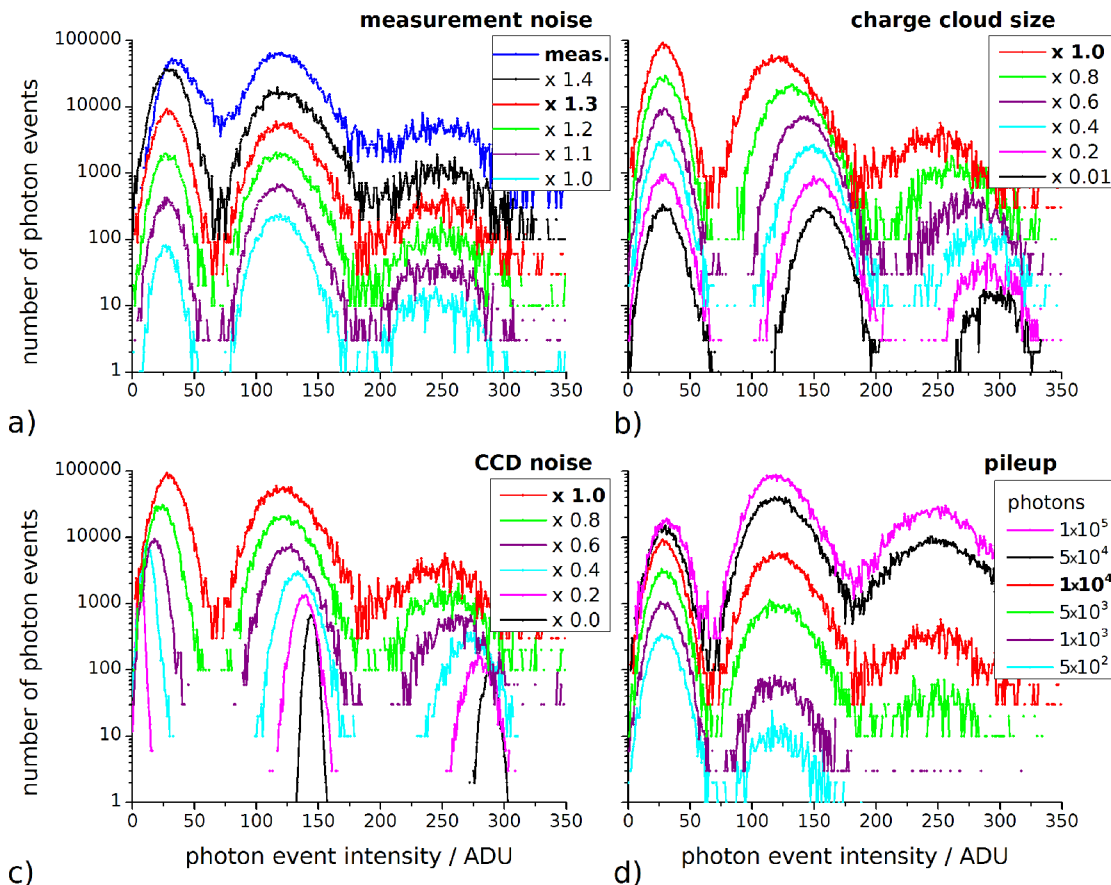


Figure 5.19.: Spectrum evolution for variation of several parameters. The spectra are separated by an offset for reasons of clarity. In a) the noise σ_{dark} is increased in the SPE frame only (and not in the master dark image) in 10% steps with respect to $\sigma_{\text{dark}} = 4.67 \text{ ADU}$ in the dark frames. The red curve with an increase of 30% is the starting point for all further simulations. This curve is also present in b)-d) painted in red. In b) the charge cloud size σ_{cc} and in c) the noise level σ_{dark} is decreased in 20% steps. d) shows spectra with different numbers of SPEs simulated on the CCD chip to investigate pile-up.

simulated with varying charge cloud size, reduced CCD noise and different photon numbers. The starting point for the variation of the parameters is always the red curve in Figure 5.19 a), where the noise in the SPE frame is increased by 30% with respect to the dark frames. Figure 5.19 b) and c) show the evolution of the spectrum with decreasing charge cloud size (σ_{cc}) and decreasing CCD noise (σ_{dark}) in steps of 20%. The reduction of σ_{cc} leads to a blue shift and narrowing of the fluorescence (and pile-up) peak. The reason for this is that split events become less probable and the total charges $I_{ph}(N_{ph})$ are collected more thoroughly, since less pixels below the noise level appear. The noise peak is rather unaffected. When reducing σ_{dark} , as is shown in Figure 5.19 c), the fluorescence and pile-up peak also get narrower and blue shifted. Besides the more complete charge cloud collection, also noise for every pixel contributing to the SPE is reduced and therefore the width of the lines. Furthermore, also the width of the noise peak decreases and the noise peak is red shifted. This leads to a reduced background in the low energy part of the spectrum, which is helpful for the analysis of light elements. Finally, in Figure 5.19 d) it can be seen that a change of photon numbers and thus of pile-up probability does not affect the energy resolution in the spectra after split event recombination. However, for spectra with several fluorescence lines pile-up will increase the background and lead to intensity losses. This is especially critical for GEXRF profiles, where the pile-up probability depends on the fluorescence emission angle and thus might distort the profile.

The enhancement in resolving power is now investigated in a more quantitative way. For all curves in Figure 5.19 b) and c) the fluorescence peak is fitted with a Gaussian function and a value for the resolving power at this peak is calculated by $E/\Delta E = x_0/\Delta x_{FWHM}$. Figure 5.19 shows the results not only for the 4px-Area-Clustering method, which is used above, but also for similar investigations performed with the Clustering method. In Figure 5.19 a), the change of the resolving power with decreased charge cloud size in units of the measured charge cloud size $\sigma_{cc} = 7.6 \mu\text{m}$ is shown. For the 4px-Area-Clustering method, the resolving power seems to increase linear up to a maximum for negligible σ_{cc} , the value of the maximum resolving power being influenced by equation 5.4.4 and the noise in the images. The Clustering method shows also a linear behavior for small σ_{cc} , but the curve flattens for values approaching the measured charge cloud size. Interesting to note is the intersection of both curves at about 0.4. For smaller charge cloud sizes, the split event recombination of always at least 4 pixels (as in 4px-Area-Clustering) is no longer beneficial, since most of the charge cloud is more likely contained in a smaller number of pixels. However, for large charge cloud sizes, the 4px-Area-Clustering method is superior with respect to resolving power.

In Figure 5.19 b), the dependency of the resolving power on the noise in the image is illustrated. It is strongly nonlinear with a strong increase of resolving power for

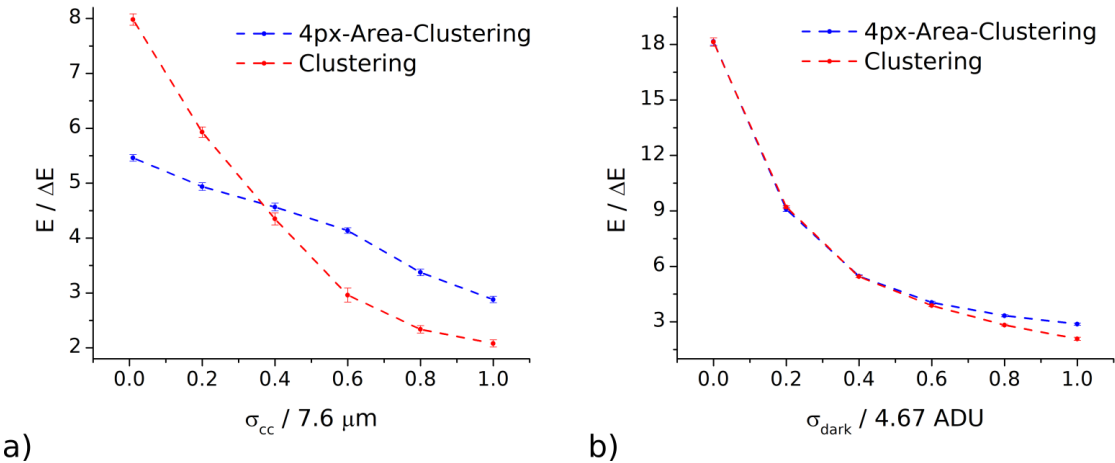


Figure 5.20.: Increase of resolving power when a) σ_{cc} or b) σ_{dark} are reduced in simulated data. Split event recombination is performed with the 4px-Area-Clustering and the Clustering method.

ever smaller noise levels, reaching almost the theoretical limit of $E/\Delta E = 19.2$ given by Equation 5.4.4 (a conversion factor for the FWHM width of 2.35 has to be applied). The determined resolving power of the simulations is slightly reduced because only natural numbers are allowed in the calculation of pixel intensities in the split events. This leads to some discrimination noise in the simulation, which limits the resolving power to 18.2 but hardly affects the energy resolution when other noise contributions dominate. The overall behavior for the 4px-Area-Clustering and the Clustering method is very similar for noise levels reduced by more than 40% with respect to the noise of the measurement. In this regime, the charges can be differentiated from noise similarly well, while for higher noise levels, the Clustering method results in a less complete charge collection.

Summarizing, the benefits of the 4px-Area-Clustering method over the Clustering method with respect to charge collection for the measurement parameters are demonstrated. Therefore, this method is used in Section 6.3 for split event recombination. Furthermore, it has been found that the noise level, e.g. readout noise and thermal noise of the CCD system, more drastically affects the energy resolution than the charge cloud size, or more precisely the charge cloud size to pixel size ratio. Since angular resolution plays a major role in GEXRF analysis, a rather extended charge cloud size to pixel ratio and the use of sub-pixel resolution methods (e.g. by determining the center of gravity [64, 59]) might be beneficial. Instead of absolute noise level, rather the signal-to-noise ratio is of importance, i.e. $\bar{I}_{ph}/\sigma_{meas}$. This also explains why SPE recombination is much easier for hard X-rays, where the photons create more charges in the detector, then for soft X-rays. However, in [61] an Electron Multiplying CCD is

presented, which is pre-amplifying the charges before readout, so before readout noise is added to the signal. Thus, not only the overall signal-to-noise ratio is increased, but also high readout frequencies can be preserved, efficiently reducing measurement time.

5.5. Compilation of GEXRF Profiles

The measured data of a full GEXRF measurement at one sample position consists of typically several hundred CCD images, where single photon events can be discriminated. To each SPE, an intensity (corresponding to the photon energy) and a hit position on the CCD mesh can be attributed with the algorithms described in the previous Section 5.4. Furthermore, the angular calibration (Section 5.3) can be used to assign a fluorescence emission angle and a solid angle of detection to each pixel of the CCD. All this information can now be combined to obtain GEXRF profiles, i.e. the angular dependent fluorescence intensity normalized to the solid angle of detection for each angle, for distinctive (element specific) fluorescence lines (Figure 5.21). To achieve this, two evaluation options are described in the following and applied later for the compilation of the GEXRF profiles of the two beamtimes in Sections 6.2 and 6.3.

5.5.1. Region of Interest Method

With this method, the integral spectrum of the GEXRF measurement is used to define regions of interest (ROIs) of SPEs that are evaluated for a GEXRF profile. This could be for example all SPEs with intensities within the FWHM (or a multiple) centered around a peak position. Then, according to the angular calibration, regions on the CCD grid are defined, where the corresponding fluorescence emission angle is $\psi_{fl} \pm \Delta\psi_{fl}$. Note that since the equi-angle lines are not parallel to the CCD pixel rows or columns, $\Delta\psi_{fl}$ can be chosen smaller than the angular resolution corresponding to a single pixel and still pixel positions might be found belonging to the (small) angular area. However, only with the determination of the SPE hit position with sub-pixel resolution (using the center of gravity) a real gain in angular resolution is achieved. Now, the number of SPEs of a ROI are summed in each angular region for each GEXRF image, yielding the detected photon numbers (of the specific ROI) for all fluorescence emission angles ψ_{fl} . Finally, this number can be normalized to the solid angle of detection of each angular area, which is also given by the angular calibration. A plot of the (normalized) photon numbers with respect to ψ_{fl} results in the GEXRF profiles.

5.5.2. Spectra Deconvolution Method

While the region of interest method is computationally quick and straight forward, spectral background contributions or line overlaps can lead to distortions of the GEXRF profile. In this case, it might be necessary to deconvolve each spectrum belonging to angular regions on the CCD chip, which correspond to fluorescence emission angles

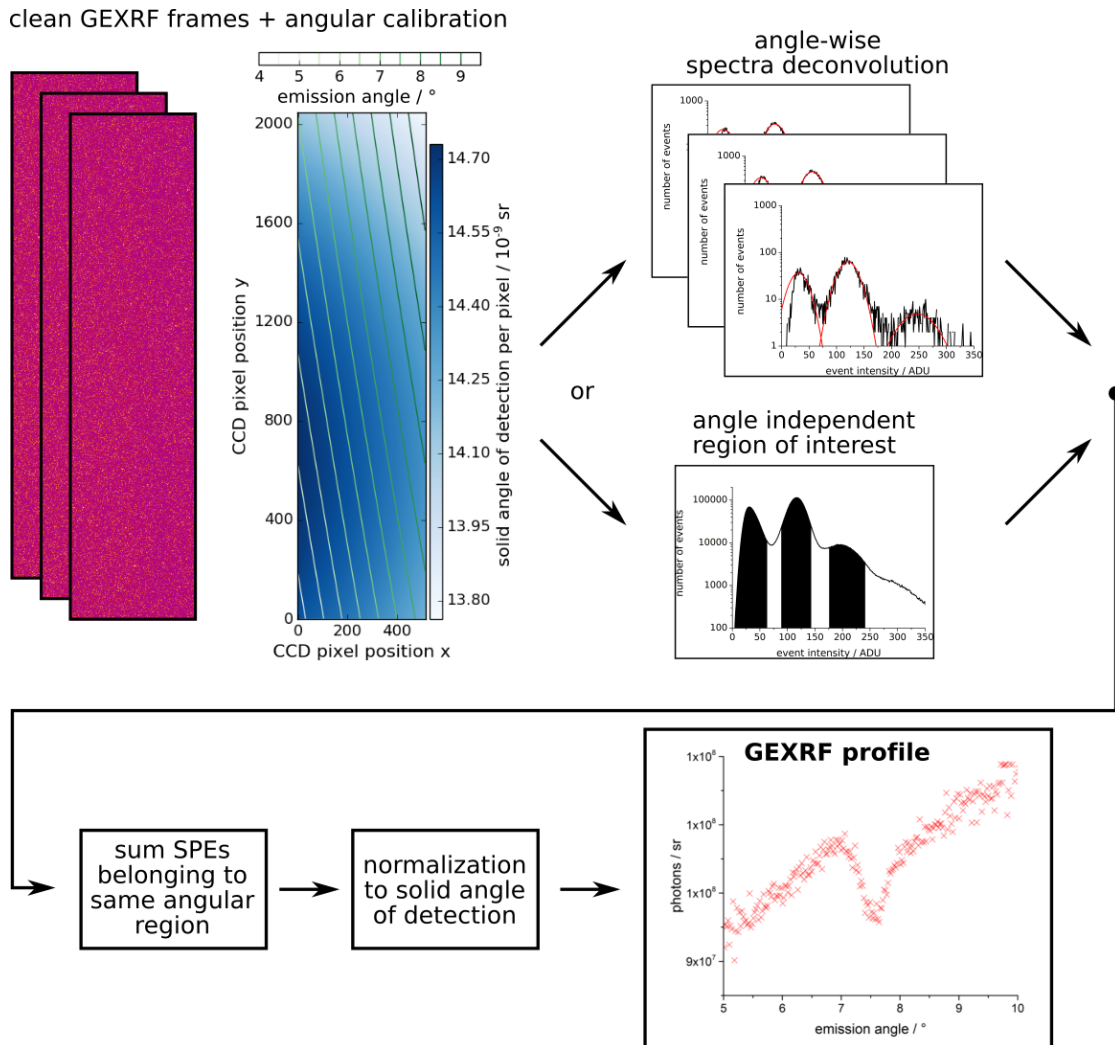


Figure 5.21.: Evaluation chart describing the steps necessary to compute GEXRF profiles from the clean GEXRF frames and the angular calibration.

5. DEVELOPMENT OF LABORATORY SCANNING-FREE SOFT X-RAY GEXRF

$\psi_{\text{fl}} \pm \Delta\psi_{\text{fl}}$. At first, the spectra are created by calculating the number of SPEs with equal SPE intensities for each angular region. Then, these spectra are deconvolved with, e.g., Gaussian functions for the noise, fluorescence and pile-up peaks and a suitable background model. This is applied and compared to the ROI method for the evaluation of the second beamtime. Here, only few spectral features are present, but these features are somewhat distorted due to high noise levels and small energy resolution (see Section 6.3 for details). In general, it is also possible at this step to use external software for spectra deconvolution, e.g. PyMca [118]. The result of the spectral deconvolution should be the number of SPEs in the fluorescence lines of interest. These numbers can again be normalized to the solid angle of detection of the angular region and displayed as GEXRF profile.

6. Feasibility Study of Laboratory Scanning-Free Soft X-Ray GEXRF

The first test of the suggested laboratory, scanning-free, soft X-ray GEXRF setup described in the previous Chapter 5 is performed with a C/Ni-multilayer sample, typically used as an X-ray mirror. The well-controlled fabrication process and a standard characterization of the multilayer by X-ray reflectometry (XRR) is performed by AXO DRESDEN GmbH. Thus, the sample structure is well-known, which makes it applicable for proof of principle measurements.

Moreover, besides as X-ray optics, multilayers are e.g. used as protective coatings or as ceramic capacitors and development of novel multilayer structures and adapted material systems is ongoing [119, 120, 121, 122]. Amongst others, this development is accompanied by investigations of diffusion processes, layer roughness and layer thicknesses using GI- or GEXRF methods at synchrotron radiation facilities [123, 124], indicating exemplarily the approachable analytical questions with these techniques. Since multilayers are a representative of technical stratified materials, such as thin-film solar cells [43], thermoelectric devices, transistor gate stacks [19] or gas sensors [125, 126], investigations on multilayers further indicate the analytical potentials of a laboratory scanning-free GEXRF setup for the above-mentioned material systems.

After describing in detail the structure of the multilayer sample and its modeling for the GEXRF forward calculations in Section 6.1, the results of two beamtimes with the laboratory scanning-free GEXRF setup are presented. While in Section 6.2 the description and evaluation of the very first measurements are shown, the second beamtime (Section 6.3) focuses on the characterization of setup and methodological improvements.

Most of the findings of Sections 6.1 and 6.2 are published in a paper by this author and co-authors in [84].

6.1. Multilayer Sample

The multilayer structure under investigation is fabricated by Dual Ion Beam Deposition (DIBD) and consists of 15 bilayer pairs of carbon and nickel on a silicon wafer. Its struc-

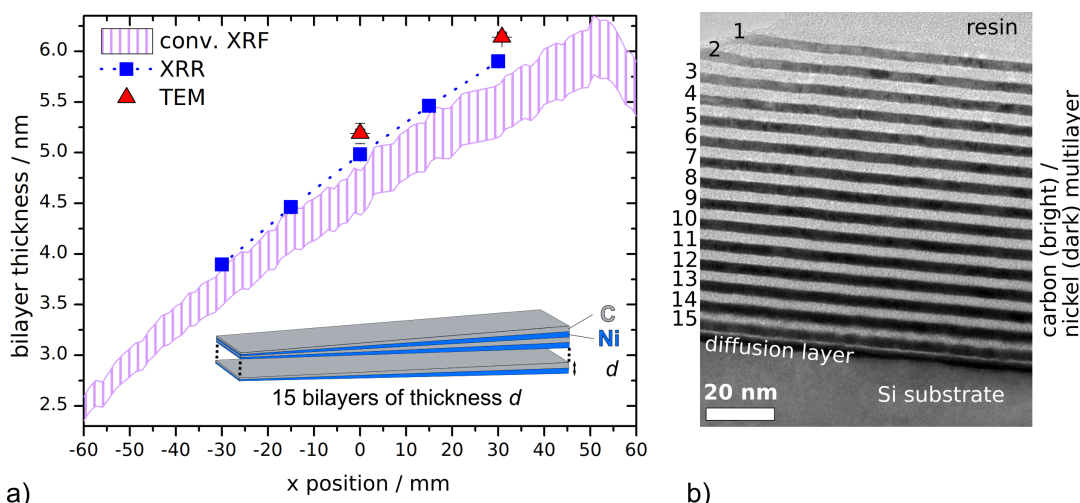


Figure 6.1.: a) Transmission electron microscopy (TEM) image of the periodic C/Ni-multilayer structure used in the GEXRF analysis. b) Analytical results of the bilayer thickness of the multilayer obtained with conventional XRF, X-ray reflectometry (XRR) and TEM measurements. A schematic of the sample is shown in the inset.

ture has a wedge-shaped form with a bilayer thickness changing from 5 nm to 6 nm over a sample length of 40 mm. Since such structures are fabricated to be used as X-ray mirrors, interfaces need to be sharp and with low roughness and the in-depth thickness variation needs to be less than a few per mill to achieve good reflectivities. The quality of the multilayer structure is also confirmed by transmission electron microscopy (TEM) measurements (Section 6.1.1) carried out at the Zentraleinrichtung Elektronenmikroskopie (Zelmi) of the Technical University of Berlin.

The size of the whole multilayer stripe is 13 cm × 5 mm. To mount it properly on the sample holder, the sample is cut at +3 mm distance to the center into two parts. In the following, zero mm marks the middle of the multilayer, the bilayer thickness is increasing at the positive scale. A schematic of the multilayer structure is shown in the inset of Figure 6.1 a).

6.1.1. Structure Analysis with Complementary Methods

Besides GEXRF, the multilayer sample is also characterized with X-ray reflectometry, conventional XRF and transmission electron microscopy, the results of which are shown in Figure 6.1 a).

The XRR measurements are performed by AXO DRESDEN GmbH with a twin mirror arrangement (TMA) using the characteristic Cu-K α radiation of an X-ray tube. The sample is irradiated at 5 positions (-30 mm, -15 mm, ... 30 mm) with the plane of

incidence parallel to the thickness gradient. To confine the footprint on the sample, i.e. the probed thickness range, a slit system is used, resulting in an effective footprint length of 1.2 mm at about 1° incidence angle. The probing width perpendicular to the thickness gradient is of the size of the sample width (5 mm). The measured reflectivity curves are fitted with simulated curves of a model of the sample using the software IMD. In the fit, density, roughness and thicknesses of the layers are used as free parameters. The thickness of the bilayers in the fit is mainly dependent on the position of the Bragg peak at about 1° incidence angle. Because of the fairly linear thickness gradient, mainly a broadening of the Bragg peak in the reflectivity measurements is observed due to the extended footprint length, instead of a peak shift. This ensures the accuracy of the determined bilayer thickness for a given position on the multilayer.

Conventional XRF analysis is carried out with a Fischerscope X-Ray XDV-SDD (Helmut Fischer GmbH), using a tungsten anode and a 100 μm Al filter in the excitation channel. The high voltage is set to 50 kV. The sample is measured in 3 parallel lines with a distance of 1.5 mm and a spot size of about 1 mm diameter. Each line scan consists of 135 points over a total of 12 cm length of the multilayer. In each point, spectra are recorded (the live-time is 120 s per measurement), deconvolved and evaluated with the WinFTM software implemented in the Fischerscope. For the calculation of bilayer thicknesses, a sample model consisting of a single Ni layer on top of a Si substrate is assumed, since absorption of primary and fluorescence radiation in the C layers is negligible for hard X-rays*. The layer thickness is then divided by the number of bilayers of the multilayer and the relative thickness ratio for nickel $\Gamma = d_{\text{Ni}}/d_{\text{bilayer}} = 0.45$ to deduce a bilayer thickness for every measurement point. Inherently, the Fischerscope measures a mass deposition, which is converted to a layer thickness by the software, given a density of the layer. In Figure 6.1 a), an extended area for the conventional XRF results is plotted rather than precise measurement points. The lower border indicates the results, if bulk density is assumed for the Ni layers. However, the XRR measurements showed that the layer density is reduced by up to 10%. To illustrate the influence of this effect, the upper border of the area corresponds to a Ni layer in the sample model with such a density reduction. Statistical uncertainties given by the Fischerscope evaluation are negligible. As can be seen, the XRF values underestimate the XRR measurements, even with the reduced density taken into account. Therefore, probably a further uncertainty of the XRF analysis due to the fundamental parameter based evaluation of the WinFTM software has to be considered. Alternatively, also the Ni layer density could be smaller than is found with the XRR measurements. Since layer density and layer roughness have similar effects on the calculated XRR curve, both values can to some extend compensate

* For example, the transmission of Ni-K α through 1 μm C is larger than 99.9% [39].

each other. Nevertheless, the bilayer thickness gradient (i.e. the slope of the curve) is in good agreement with the XRR measurements and further extends the curve towards the edges of the multilayer sample. There, strong deviations from the linear profile are measured, which originate from the production process.

TEM measurements are performed at two sample positions at the Zentraleinrichtung Elektronenmikroskopie (ZELMI) of the Technical University of Berlin. For this purpose, cross-sections have to be prepared, making a sample consumption of about 5 mm length at the positions to be measured unavoidable. For the preparation of the cross-sections the 5-mm long sample piece is cut in two halves at the measurement position and glued with a hot resin (130° for 30 min.) face to face. A thin slice is cut from the stack and is further thinned by polishing and ion milling parallel to the direction of the interface, to create a dimpled shape. At the center, the sample provides positions with thicknesses in the range of 10 nm, sufficient for TEM microscopy. The TEM micrographs are recorded with a FEI Tecnai G² 20 S-TWIN at up to ten positions of the two sample cross-sections. An example of a micrograph is shown in Figure 6.1 b). Due to the mass contrast, the nickel layers are visible as dark lines with the brighter carbon layers in between and the silicon substrate on the bottom of the picture. The layers appear smooth, homogeneous and equidistant. Only at the silicon substrate interface a 16th nickel layer with less homogeneous thickness is visible. The origin of this layer is probably diffusion from the 15th nickel layer (which also appears a bit brighter than the layers on top) through the thin carbon layer on the substrate. Whether this diffusion is induced during the sample fabrication or during the preparation of TEM cross-sections cannot be verified. However, the bilayer thickness results should not be affected, since the signal in GEXRF and XRR measurements of the top layers is dominant and for the conventional XRF analysis the total mass deposition is measured. For the TEM measurements, the bilayer thickness is deduced from the intensity profiles along the normal of the layers and the magnification factor. Uncertainties are estimated from statistical deviations of the bilayer thickness measurements. The results are shown in Figure 6.1 a).

6.1.2. GEXRF Simulations

For the simulations of the GEXRF profiles a model of the multilayer sample is used in the xrfLibrary framework (Section 2.4.1), which is in accordance to X-ray reflectometry measurements. In the evaluation of these measurements it is found that the thickness ratio of nickel is $\Gamma = d_{\text{Ni}}/d_{\text{bilayer}} = 0.45$. The layer densities are 8.21 g/cm^3 for nickel, which is a reduced density of 7.5% compared to bulk and 2.75 g/cm^3 for carbon, which fits rather to amorphous carbon than diamond-like carbon (both can in principle be deposited with DIBD). Furthermore, for the GEXRF simulations with the xrfLibrary,

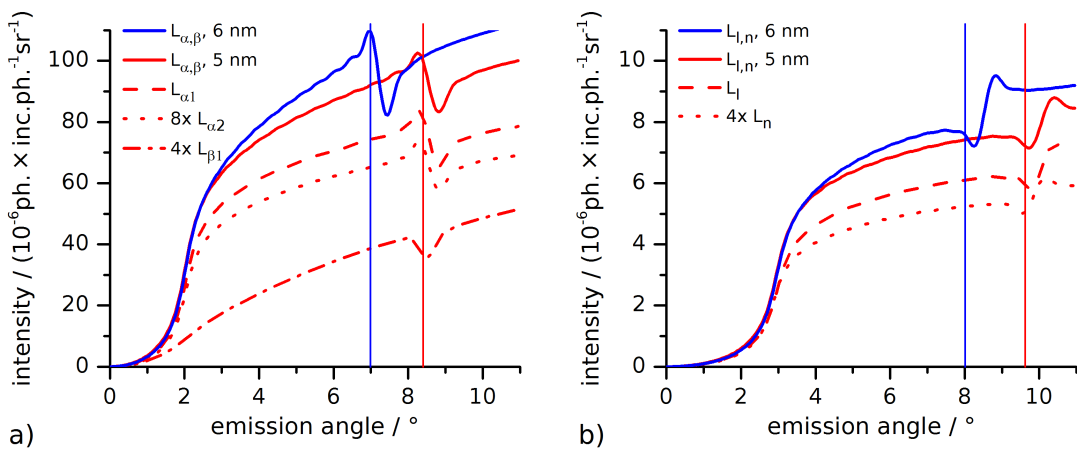


Figure 6.2.: a) Ni-L_{α,β} and b) Ni-L_{l,n} GEXRF profiles for two bilayer thicknesses of the C/Ni-multilayer sample. Also shown are the intensities of each contributing line (dashed lines) and the position of the respective Bragg angle (vertical line).

atomic scattering factors are used from Chantler et al. [40]. Because of the energy resolution of the measurements, GEXRF profiles for Ni-L_{α,β} and Ni-L_{l,n} can be separated in the first beamtime (Section 6.2). These two profiles are simulated with summed contributions from L_{α1}, L_{α2} and L_{β1} for Ni-L_{α,β} and L_l and L_n for Ni-L_{l,n}. The relative intensities are calculated using subshell photoionization cross sections from Ebel et al. [33] and transition probabilities and fluorescence yields from Elam et al. [32].

The simulations of the Ni-L_{α,β} and Ni-L_{l,n} GEXRF profiles for two different bilayer thicknesses $d = 5$ nm and $d = 6$ nm of the C/Ni-multilayer are shown in Figure 6.2 a) and b). Up to 2° , the intensity of the fluorescence line increases strongly because of the reduced reflection at the interfaces of the sample, preventing the radiation from leaving the sample. The further, shallower intensity increase results from reduced self-absorption when the path length in the sample is reduced. Then, near the first order Bragg angle $\alpha = \arcsin(\lambda/2d)$ of the multilayer sample with the respective photon wavelength λ and bilayer thickness d , a local intensity maximum followed by a minimum (vice versa in b)) appears. For the respective angles, intensity maxima (and minima) of the XSW field used for the calculations emerge in the nickel layers. This means that for fluorescence photons from atoms located at these positions, the probability to reach the detector is increased (reduced) due to self-interference of the probability wave functions of each photon (Section 2.2.3). This interference effect in multilayers is similar to the Kossel effect, which describes the diffraction pattern of X-rays originating from sources inside a crystal [127, 128]. Therefore, the features in the GEXRF profiles of multilayers are also called Kossel lines. They are used to get information about the structure factor of

crystals [129].

The simulated GEXRF profiles will be used in the next chapters for the evaluation of the measured GEXRF profiles and in the angular calibration for the measurements of the first beamtime.

6.2. First Beamtime - Proof of Principle

The first beamtime serves as proof of principle for the suggested laboratory scanning-free GEXRF setup. For this purpose, a pnCCD of PNSensor GmbH is applied, providing reliable single photon analysis. As test sample, the multilayer described in the previous Section 6.1 is used. The following chapters focus on the setup alignment (Section 6.2.1), the first measured integral XRF spectrum with the setup (Section 6.2.3), the angular calibration (Section 6.2.4) and finally the compilation and evaluation of the measured GEXRF profiles (Sections 6.2.5). The raw data handling, performed by PNSensor GmbH is described shortly in Section 6.2.2.

6.2.1. Setup Description and Alignment

The principle setup and setup alignment is discussed in Section 5.2. In the following, only deviations to this setup and alignment procedures are described, which are applied in the first beamtime. As optics, the Kirkpatrick-Baez (KB) mirrors are used and the detector is a pnCCD of PNSensor GmbH. The CMOS sensor, beneficial for alignment and beam diagnostics, and the optical laser for precise definition of the measurement geometry and sample alignment are only available in the second beamtime. Therefore, goniometer and sample alignment here is carried out relative to the beam of the KB optics with a pinhole and an X-ray sensitive diode and the angular calibration is performed with a reference measurement.

Goniometer Alignment

Goniometer alignment is carried out relative to the beam of the KB optics with a pinhole on the sample holder and an X-ray sensitive diode on the 2θ axis behind the pinhole. Firstly, the diode is positioned in the direct beam of the LPP source. Then, the position of the KB focus is found by scanning the radiation with the pinhole. The pivotal point position for the pinhole is known from former measurements. Therefore, the two axes of the pivotal point perpendicular to the beam direction can be adjusted by moving the motorized base frame of the spectroscopy chamber in the calculated position. However, the movement of the spectroscopy chamber changes the forces pulling on the vacuum chamber containing the KB optics and induces a shift in the focus position due to a slight misalignment of the KB optics. Therefore, the procedure needs to be repeated iteratively. The position of the pivotal point of the goniometer parallel to the beam of the KB optics is defined by the setup, which is performed in accordance to a CAD model of the whole setup. Since the focal length of the focus of the KB optics is in the range of 1 cm, the focus is not further adjusted parallel to the LPP radiation. After all adjustment

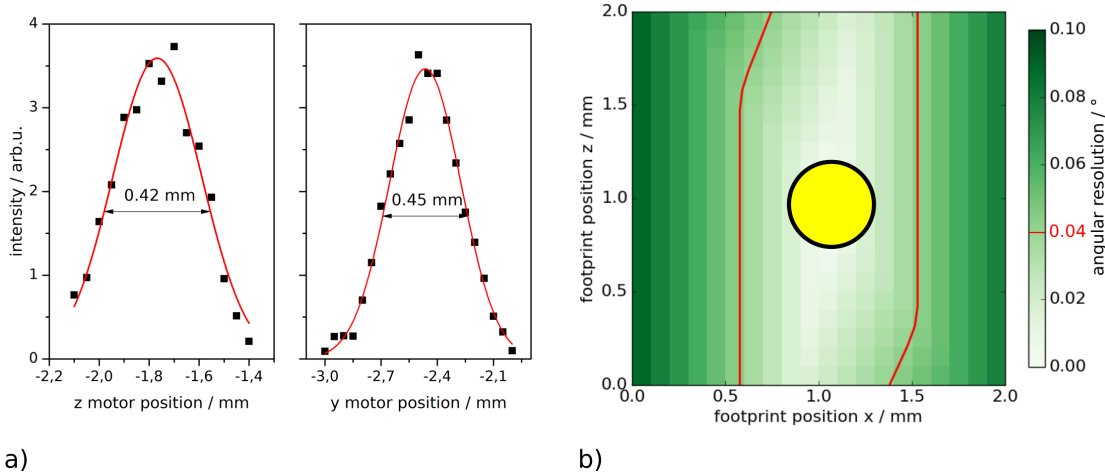


Figure 6.3.: a) Intensity scans of a $500\text{ }\mu\text{m}$ pinhole through the pivotal point of the goniometer. The width (FWHM) of the beam profile is less than 0.5 mm . b) Impact of the footprint size on the angular resolution of the GEXRF measurements for the applied geometry. The red line indicates an upper limit of the allowed footprint size not to affect the angular resolution. The yellow disc illustrates the maximum footprint size during the measurements.

steps are completed, the alignment of the goniometer to the KB focus and the alignment of the KB focus itself are checked. For this purpose, a pinhole with $500\text{ }\mu\text{m}$ diameter is scanned through the focus spot position and the respective intensity is recorded (the CMOS is not available during this beamtime). As can be seen in Figure 6.3 a), the profiles show a Gaussian-like shape with full widths at half maximum (FWHM) of less than 0.5 mm in the vertical and horizontal axis and thus the FWHM of the focus spot is less than 0.5 mm . Note that the spot size can be even smaller but is unresolved by the applied pinhole. Figure 6.3 b) shows the impact of the footprint size in the sample plane to the angular resolution of the GEXRF measurements for the actual setup geometry (from Section 6.2.4). A detailed description of the computation of the graph and its interpretation can be found in Section 2.3.2 for a general case. Here, the results show that even with an upper limit of the footprint size of $0.5 \times 0.5\text{ mm}^2$, the influence of the footprint size on the angular resolution is negligible.

To check the position of the KB focus at the beginning and at the end of each measurement day, a fluorescent screen is applied. The screen has a quadratic shape of $< 1 \times 1\text{ mm}^2$ and its position on the sample holder is determined just after the alignment of the spectroscopy chamber. For this purpose, the sample holder is moved while the LPP source is in operation, until the fluorescence light from the screen is visible and the spot size is minimized. For the daily control of the position of the KB focus, the corresponding motor positions of the fluorescence screen are adjusted and the fluorescence light checked

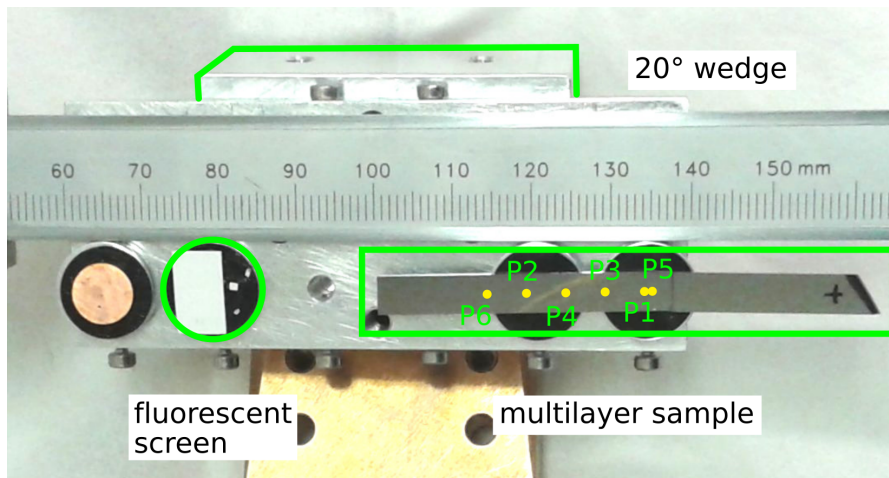


Figure 6.4.: Photograph of the specimen holder with the fluorescent screen and the multilayer sample part P. Indicated are also the measurement positions for the GEXRF analysis.

visually. During the whole measurement period, no misalignment of the KB optics is detected.

Sample Holder

The specimen holder is equipped with the 20° wedge (Section 5.2.5), on which the samples are mounted (Figure 6.4). On part P, which is the half of the multilayer sample with larger bilayer thickness, GEXRF measurements are performed at positions P1, P2, ... P6. On part Q, a single GEXRF measurement is performed at position Q1. The lateral positions of the measurements are given in Table 6.2.1.

Sample alignment is performed by measuring the sample-induced shadowing similar as in Section 5.2.5, but making use of the direct beam and the X-ray sensitive diode mounted on the 2θ axis. The relative distances between the first measurement point on the multilayer sample and the fluorescence screen are determined with a slide gauge. Thus, the position can be set into the focus of the KB optics by movement of the specimen holder with the x and y motors. Then, alignment of the zero angle (θ scan) and radial position (x - z scan) are carried out. For the final GEXRF geometry, the sample is rotated by $\theta = 84.2^\circ$ to get the full angular scale on the pnCCD chip. For the measurements of positions P1 to P6 on the same part of the multilayer sample, the sample surface is shifted through the pivotal point of the goniometer by using only the y motor. For these measurements, the whole geometry with respect to the pnCCD chip stays the same, which allows to use the same angular calibration for these measurements

Table 6.1.: C/Ni-bilayer thickness on several GEXRF measurement positions interpolated from XRR measurements.

measurement	position / mm	XRR bilayer thickness / nm
P1	36 \pm 1	out of range
P2	21 \pm 1	5.63 \pm 0.05
P3	31 \pm 1	5.90 \pm 0.05
P4	26 \pm 1	5.78 \pm 0.05
P5	37 \pm 1	out of range
P6	16 \pm 1	5.48 \pm 0.05
Q1	-3 \pm 2	4.89 \pm 0.05

(see section 6.2.4).

As can be seen in Figure 6.5, the data for the determination of the zero angle and the alignment of the sample surface into the pivotal point of the goniometer are noisy. For the x - z scan (Figure 6.5 a)) the diode is read-out 50 times per measurement point, resulting in a total scan time of 165 s. For the θ scan, the mean of 150 read-outs is used per measurement point, resulting in a total scan time of over 15 minutes but still high statistical uncertainties. Since longer scan times are inconvenient, the uncertainties for the z and θ adjustment, which are estimated to be $\Delta z = 0.1$ mm and $\Delta\theta = 0.5^\circ$ cannot be reduced further. The high noise level of the measurement originates from an amplifier not optimized for the short pulses of the LPP source and the slow readout times of the X-ray sensitive diode from the applied LabVIEW software used for the readout. The rather high uncertainties in the sample alignment are compensated by the angular calibration with a reference and in the second beamtime (Section 6.3.1) circumvented by using an optical laser instead of the direct LPP beam.

pnCCD

In contrast to conventional CCDs, the pnCCD facilitates a fully depleted wafer volume, a frame store area and on-chip amplifiers for every pixel column [130, 116]. This allows for fast read-out (up to 1 kHz) while preserving low noise levels, making the detector suitable for single photon detection. The pnCCD used in this beamtime has 264×264 pixels with a size of $48 \times 48 \mu\text{m}^2$. It is mounted to the spectroscopy chamber via the CCD positioning system as described in Section 5.2.4. Since no optical laser is used for the alignment procedures, only the distance of the pnCCD is adjusted to the specimen holder. In the final position, the camera is fixed and not moved for the whole

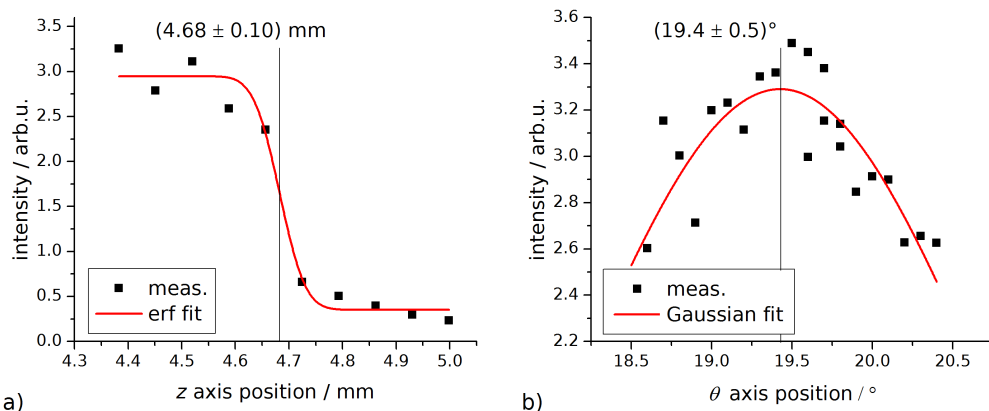


Figure 6.5.: a) x - z scan of the sample through the incoming beam with the surface parallel to the beam. At the half of the maximum intensity the sample shadows half of the beam. b) θ scan of the sample after its surface is adjusted to shadow half of the incoming beam. At maximum intensity, the surface is parallel to the beam.

measurement period. At the end of the beamtime, some parameters to describe the position of the camera are measured, while the other parameters are determined in an angular calibration procedure (see section 6.2.4). Using a cathetometer, the height of the 4 corners of the pnCCD chip and the height of the pivotal point of the goniometer (using the fluorescent screen aligned with the known motor positions, section 6.2.1) are determined. With this information, the tilt angle of the pnCCD relative to a vertical axis can be calculated to $\phi_{\text{CCD}} = (3.2 \pm 0.5)^\circ$ and the relative height of the pnCCD to $h_{\text{CCD}} = (4.1 \pm 0.2) \text{ mm}$. Furthermore, from the CAD model and the distance between flange and pivotal point, measured with slip gauges, the distance of the chip to the pivotal point of the goniometer is calculated to $d_{\text{CCD}} = (63 \pm 1) \text{ mm}$.

For the GEXRF measurements, the pnCCD is cooled down to -70° to minimize thermal noise. The readout of the camera is triggered with the laser trigger of the LPP source. This allows to take a frame with the pnCCD for every shot of the LPP source (1.2 ns pulse every 10 ms). Due to the quick readout times, a shutter, preventing radiation to reach the detector during readout, is not necessary.

6.2.2. Data Recording and Image Processing

After setup alignment and positioning of the θ axis of the sample to the GEXRF measurement value (which is 84.2° to use the full detector area) the LPP source is put into operation and the pnCCD starts recording images. A measurement for one measurement position consists of several hundred thousand frames in 1-2 hours. Each frame is background corrected by subtracting a master dark frame (calculated from some tens

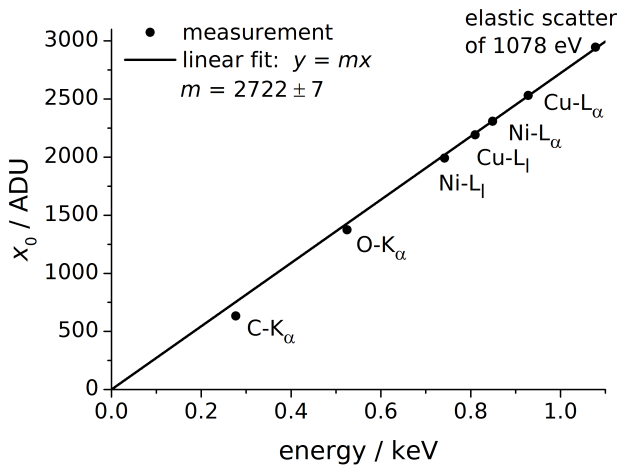


Figure 6.6.: Energy calibration function for the measurements performed with the pnCCD.

to hundreds of dark frames, which are recorded without the LPP source running), and by correction of gain and charge transfer efficiency [130, 131]. Noise is discriminated by setting all pixel values with intensities of less than a multiple of the standard deviation of a single dark frame to zero. Split events occur with a maximum of 4 pixels belonging to the same photon event, which means that the charge cloud is much smaller than the pixel size*. These split events are recombined by adding the pixel intensity of the adjacent pixels, providing the event intensity. The event position is set to the position of the pixel with maximum intensity. Thus, information about energy and position of each detected photon are obtained.

6.2.3. Integral XRF Spectrum

An integrated spectrum over the whole angle range (integral spectrum) can be created by plotting the number of photon events as a function of their intensity. From measurements on the C/Ni-multilayer and on a solid Cu pallet, peak positions of the fluorescence lines are evaluated to obtain an energy calibration for the pnCCD measurements. Figure 6.6 shows in first approximation a linear response for the energy calibration, but the detected charge intensity seems to be underestimated for the low energy fluorescence photons of C-K α and O-K α . This effect might originate from incomplete charge collection due to low signal to noise ratios of the single photon events in this energy region. Nevertheless, the shown energy calibration will be used for the further illustrations of the spectra. In Figure 6.7 a) the integral spectrum of measurement P2 of the multilayer sample is

* In [130] a charge cloud radius of about 10 μm is given for a pnCCD

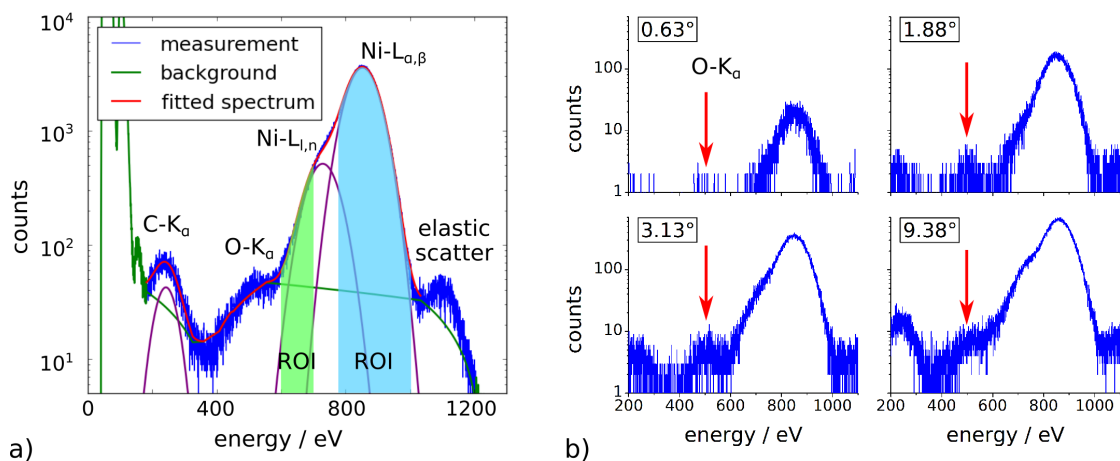


Figure 6.7.: a) Integral X-ray fluorescence spectrum of the C/Ni-multilayer sample. 1.4 million Ni-L photon events are detected in a measurement time of 140 minutes. Reprinted with permission from [84]. Copyright 2017 American Chemical Society. **b)** XRF spectrum for shallow angle regions as indicated $\pm 0.6^\circ$. The oxygen peak is marked with a red arrow.

shown. The spectrum intensity increases sharply at about 38.7 eV (105 ADU), which is the cut-off intensity for the noise discrimination. All channels up to 184.5 eV (500 ADU) are dominated by noise events. Fluorescence lines that can be attributed to C-K_α, Ni-L_{l,n}, Ni-L_{α,β} and elastically scattered radiation at 1078 eV are expected from the C/Ni-multilayer sample and clearly visible. O-K_α originates most likely from sample contamination or surface oxidation, as the spectra in Figure 6.7 b) indicate. Here, the angular calibration (see section 6.2.4) is already used to discriminate photons, which are emitted at shallow angles, only. It can be seen that the oxygen signal relative to the nickel signal is strongest at about 3°, which is an indication that the signal originates from a surface near region.

The integral spectrum shows a possibility to use the setup in a conventional XRF mode. Indeed, by irradiating the sample at e.g. 45° and scanning the sample in the surface plane, the CCD detector can be used as efficient energy-dispersive detector for soft X-ray fluorescence analysis with the LPP source (note that a single SDD detector suffers from pile-up effects because of the short X-ray pulses). In the following, the integral spectrum in Figure 6.7 a) is used to estimate lower limits of detection (LLD) for carbon and nickel. Peak intensities are retrieved from the spectrum by subtracting a background based on linear interpolation between supporting points and using Gaussian fits for the fluorescence peaks (shown in Figure 6.7 a)). The energy resolution at the Ni-L_{α,β} line obtained from the Gaussian fit is 113 eV. The data evaluated for the integral spectrum is recorded at P2 of the multilayer sample. For this position, the bilayer

Table 6.2.: Estimated lower limit of detection (LLD) from an integral spectrum of the C/Ni-multilayer recorded with the pnCCD. The sample is excited with 1078 eV photons from the laser-produced plasma source and a reference time of 1000 s is used.

element	LLD / ng cm ⁻²	LLD / atoms cm ⁻²	LLD / g
nickel	200	2×10^{15}	1×10^{-10}
carbon	1000	6×10^{16}	6×10^{-10}

thickness is $d = 5.63$ nm with a thickness ratio of $\Gamma = d_{\text{Ni}}/d_{\text{bilayer}} = 0.45$ and the densities for nickel and carbon are $\rho_{\text{Ni}} = 8.21$ g/cm³ and $\rho_{\text{C}} = 2.75$ g/cm³ according to the XRR measurements. This yields a total mass deposition for nickel and carbon of

$$\begin{aligned}\hat{m}_{\text{Ni}} &= 15 d \Gamma \rho_{\text{Ni}} = 31.2 \text{ }\mu\text{g/cm}^2 \quad \text{and} \\ \hat{m}_{\text{C}} &= 15 d (1 - \Gamma) \rho_{\text{C}} = 12.8 \text{ }\mu\text{g/cm}^2.\end{aligned}$$

The LLDs are now calculated by

$$\text{LLD}_i = \hat{m}_i \frac{3 \sqrt{N_{i,j}^{\text{det}}}}{N_{i,j}^{\text{det}}} \times \sqrt{\frac{t}{t_0}}, \quad (6.2.1)$$

with the measurement time $t = 140$ min., a reference time of $t_0 = 1000$ s and $N_{i,j}^{\text{det}}$ being the number of detected photons of Ni-L _{α,β} and C-K _{α} , respectively. The results are shown in Table 6.2 in various units for reason of comparison. For the last column, the size of the excitation footprint is multiplied to the relative LLDs, yielding absolute detection limits.

Typical detection limits for conventional XRF with an X-ray tube based spectrometer are in the range of 10^{-6} to 10^{-8} g [132]. In TXRF geometry, usually the analytes are deposited on a reflecting wafer surface and thus the scattering background produced in the wafer is drastically reduced. This leads to detection limits of 10^{-9} g to 10^{-11} g [133] or even further to the fg range [42] when applying monochromatic synchrotron radiation. The estimated absolute LLDs for the laboratory GEXRF setup are well in the range of typical TXRF detection limits, even though the angular range up to 12° is used, which exceeds the critical angle for total external reflection. Indeed, when exciting with monochromatic soft X-rays, the larger photoionization cross section as compared to hard X-ray excitation and the lower resonant scattering background in contrast to polychromatic excitation strongly enhance the LLDs. In the future, it might be possible to monitor the incident flux on the sample (since it cannot be assumed to

Table 6.3.: Determination of the geometric parameters with various methods as indicated in the table. l_{CCD} is not measured directly.

parameter	determination	determined value
d_{CCD}	slip gauge and CAD	$(63 \pm 1) \text{ mm}$
l_{CCD}	-	-
h_{CCD}	cathetometer	$(4.1 \pm 0.2) \text{ mm}$
ϕ_{CCD}	cathetometer	$(3 \pm 1)^\circ$
θ_{CCD}	defined by setup	$(0 \pm 2)^\circ$
ω_{CCD}	defined by setup	$(0 \pm 2)^\circ$
ω_{sample}	motor position	$(5.800 \pm 0.001)^\circ$

be constant over time because of accumulation of debris on filters in the beam path and thus increasing absorption) and use standard samples to properly calibrate the setup and perform quantitative trace element analysis.

6.2.4. Angular Calibration

For the present measurements of the first beamtime, the optical laser to define the coordinate system and the geometry of the setup, is not applied. Therefore, the coordinate system to describe the geometry (LAB system) has to be defined differently. It proves reasonable to define the LAB system such, that the surface normal of the sample after sample alignment points in the x direction of the LAB system (towards the pnCCD) and the origin is still defined by the pivotal point of the goniometer.

After sample alignment (sample surface is parallel to the incident X-ray beam, $\omega_{\text{sample}} = 90^\circ$), the θ motor of the goniometer is moved by 84.2° , to shift the zero-angle of the fluorescence emission to one edge of the pnCCD and thus make use of the whole detector chip for the measurements. However, this tilt of the sample surface, $\omega_{\text{sample}} = 5.8^\circ$ with respect to the x axis of the LAB system, needs to be considered in the angular calibration.

Table 6.3 summarizes the knowledge of the various geometric parameters (GPs, defined in Figure 5.8 on page 95) determined by independent measurements using e.g. slide gauge or cathetometer. Note that ϕ_{CCD} is measured with respect to a horizontal plane (the cathetometer is aligned with a spirit level) and not with respect to the coordinate system described above. Due to the unavoidable tilt of the sample normal on the specimen holder with respect to the horizontal plane, the uncertainty of ϕ_{CCD} is increased.

The GPs ϕ_{CCD} , d_{CCD} and l_{CCD} have the strongest influence on the angular axis and

l_{CCD} is not directly measured. This prohibits the use of an absolute angular calibration and makes a reference measurement (see Section 5.3.1) and the application of a fitting algorithm necessary. The other GPs are fixed according to their measured value in Table 6.3. The GEXRF profile for the calibration is provided by one of the GEXRF measurements, namely the measurement at position P2. The simulated GEXRF profile of the respective measurement is based on the sample structure derived from X-ray reflectometry measurements. The interpolated values of the XRR measurements at P2 yield a bilayer thickness of 5.63 nm, densities for the Ni and C layers of 8.21 g/cm³ and 2.75 g/cm³, respectively and a thickness ratio $\Gamma = d_{\text{Ni}}/d_{\text{bilayer}} = 0.45$. For the GEXRF profiles of Ni-L _{α,β} , the intensities of Ni-L _{α_1} , Ni-L _{α_2} and Ni-L _{β_1} are calculated and summed. The GEXRF profiles of Ni-L _{l,n} consist of the summed GEXRF profiles of Ni-L _{l} and Ni-L _{n} . Measured and simulated GEXRF profiles are used in the fitting algorithm for the angular calibration described in the following.

In a first step of the fitting algorithm, ϕ_{CCD} is optimized by maximizing the feature contrast in the measured Ni-L _{α,β} GEXRF profile (Figure 6.8 a)). For this purpose, values for d_{CCD} and l_{CCD} are taken from Table 6.3 as starting parameters and (measured) Ni-L _{α,β} GEXRF profiles are compiled for a set of ϕ_{CCD} values from 0° to 6°. Each profile is smoothed using a Savitzky-Golay filter and the contrast is defined as the difference between the maximum intensity close to the Bragg angle and the local minimum intensity. For the next fitting step, the ϕ_{CCD} value which gives the maximum contrast is used (Figure 6.8 b)).

In the second step of the fitting algorithm, the angular scale of the measured GEXRF profile is stretched and shifted by adapting d_{CCD} and l_{CCD} , to identify the best match with the simulated profile. It is found that the best result in terms of convergence and stability is achieved by using a brute force algorithm. Therefore, (measured) GEXRF profiles are compiled for a grid of 15 × 15 values (15 values for d_{CCD} and l_{CCD} , each) and compared to the simulated GEXRF profile. The shapes of measured and simulated curves show significant deviations (see section 6.2.5), preventing to use the whole curves for the evaluation. However, at least two criteria are needed for the unambiguousness of the algorithm (due to the two fit values). These criteria are chosen to be on the one hand the difference of the local intensity minimum position in the measured and simulated Ni-L _{α,β} GEXRF profile (Figure 6.8 a)) and on the other hand the angle difference of the inflection point of the measured and simulated Ni-L _{l,n} GEXRF profiles (Figure 6.8 c)). To find now the best d_{CCD} and l_{CCD} values in the brute force grid, the couple is chosen, where the maximum of the two angle differences (inflection point and minimum position) is minimized (Figure 6.8 d)).

Finally, the process is repeated iteratively 4 times, while always the grids for ϕ_{CCD} in

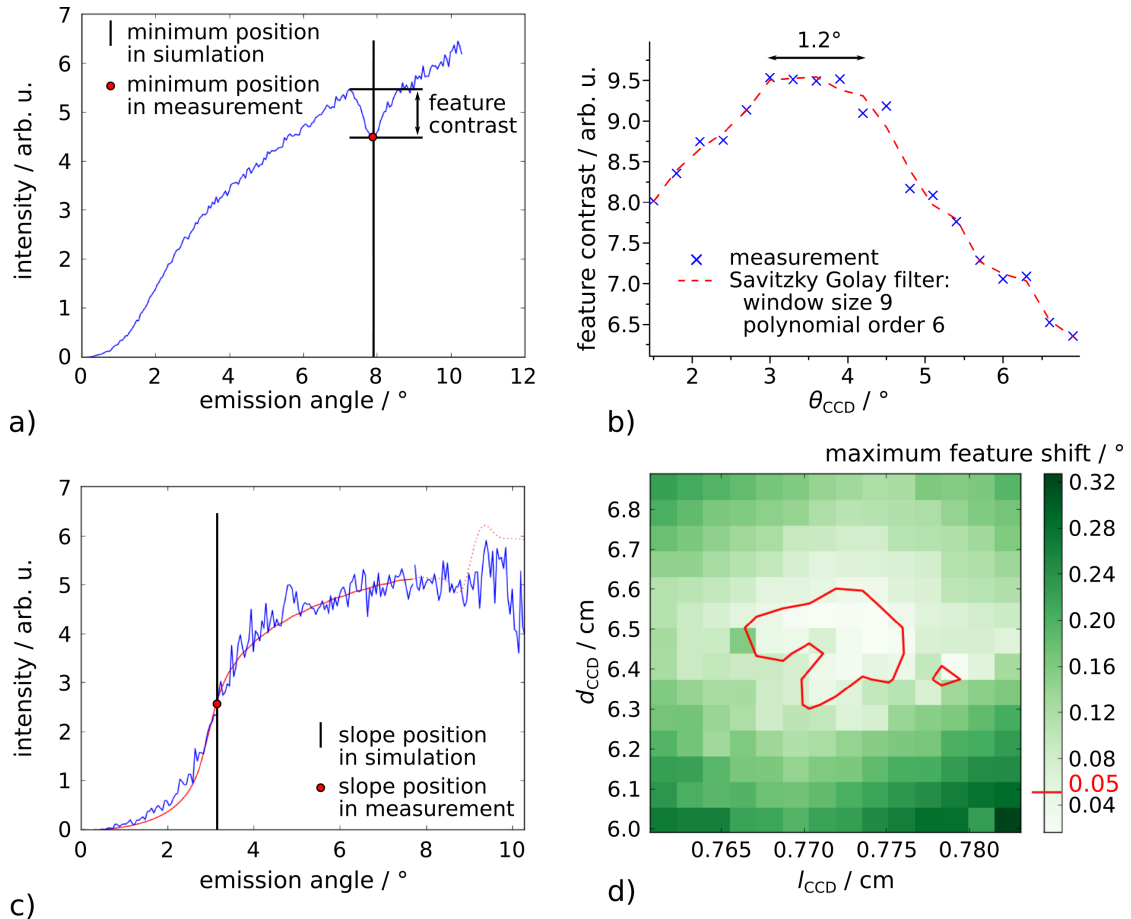


Figure 6.8.: Results of final iteration step for the angular calibration. a) Compiled Ni-L_{α,β} GEXRF profile and comparison of feature minimum position of measured and simulated data. b) Change of the feature contrast (see a)) with respect to ϕ_{CCD} . c) Compiled Ni-L_{l,n} GEXRF profile and comparison of inflection point position of measured and simulated data. d) Maximum of angle differences for the inflection point and the minimum position for a given set of d_{CCD} and l_{CCD} . The red line indicates the angular resolution due to pixel size (0.05°), which is used to estimate uncertainties for d_{CCD} and l_{CCD} .

Table 6.4.: Result of the angular calibration procedure. In addition to the actual value of each GP, its (estimated) uncertainty and influence on the shift of the minimum position are given.

parameter	determination	determined value	estimated uncertainty	shift of int. min.
d_{CCD}	fit algorithm	65.0 mm	1.3 mm	0.02°
l_{CCD}	fit algorithm	7.70 mm	0.06 mm	0.04°
h_{CCD}	measured	4.1 mm	0.2 mm	0.04°
ϕ_{CCD}	fit algorithm	3.6°	1.2°	0.06°
θ_{CCD}	defined by setup	0°	2°	0.02°
ω_{CCD}	defined by setup	0°	2°	0.03°
ω_{sample}	motor position	5.80°	0.001°	0.03°

the first step and d_{CCD} and l_{CCD} in the second step are refined.

The four frames in Figure 6.8 show the final fitting steps. The uncertainties of the fitted GPs are estimated to be for ϕ_{CCD} of the length of the plateau in Figure 6.8 b) and for d_{CCD} and l_{CCD} about size of the area in Figure 6.8 d), where the maximum feature shift is less than 0.05°, which is about the pixel resolution of the measurement.

Table 6.4 summarizes the results of the geometric parameters used in the angular calibration and also shows their influence on the angular scale. The latter is determined by calculating GEXRF profiles with an angular calibration where all but one GP are kept at the values shown in Table 6.4. The given influence is then the difference in the minimum position of the Ni $L_{\alpha,\beta}$ GEXRF profile created with two angular calibrations, one with the parameter as in the table and the other one with the estimated uncertainty added.

Figures 6.9 a) and b) show the result of the angular calibration in terms of fluorescence emission angles and solid angles of detection for each pixel on the pnCCD. An angular range of about 10° will be measured with decreasing pixel numbers contributing to the high angular range above 10° due to the tilt of the CCD. The calculated solid angles of detection will be used to normalize each angular region to its total solid angle of detection. The overall solid angle of detection is $\Omega_{\text{Det}}=0.038 \text{ sr}$.

6.2.5. GEXRF Profiles

GEXRF measurements are performed at 7 positions of the multilayer sample, corresponding to 7 different bilayer thicknesses (Table 6.2.1 in Section 6.2.1). On each posi-

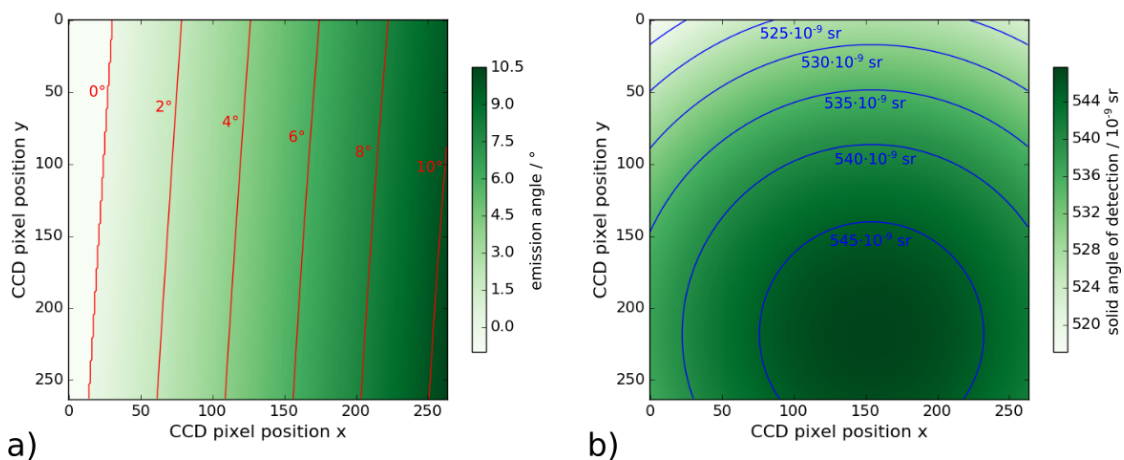


Figure 6.9.: Distribution of a) detected fluorescence emission angles and b) solid angles of detection for each pixel on the pnCCD chip according to the angular calibration.

tion, several thousand to a few millions of frames are recorded in up to a couple of hours measurement time. In every frame on average 3 to 5 single photon events (SPEs) are detected and evaluated with respect to event position and intensity. The photon event position can be converted to an emission angle using the angular calibration described in the previous Section 6.2.4. The photon event intensity can be used to further evaluate the photon events of a specific bandwidth of the fluorescence spectrum, enabling to generate GEXRF profiles of specific fluorescence lines, only. For this purpose, regions of interest (ROIs) are defined in the integral spectrum (Figure 6.7 in Section 6.2.3). Using the deconvolution of the integral spectrum, the lower and upper limits of the defined ROIs for $\text{Ni-L}_{\alpha,\beta}$ and for $\text{Ni-L}_{l,n}$ are chosen to maximize the integral intensity on the one hand and on the other hand guarantee the spectral purity of the respective lines (Appendix I).

The GEXRF profiles are compiled by counting the number of photons in the specific ROIs and angle increments, for all frames of one measurement. The angle increment for every emission angle is set to 0.05° and corresponds roughly to the pixel size resolution. Plotting the photon number against the emission angle provides the GEXRF profiles. The results of measurement P1 and P2 are shown together with corresponding simulations in Figure 6.10. The general shape of the GEXRF profiles follows the simulation, featuring a stronger intensity increase at shallow angles compared to steeper angles and also a local intensity minimum close to the Bragg angle is visible. However, a direct comparison shows also significant deviations from the simulation. First, the steep increase at shallow angles is overestimated in the simulation and, second, the predicted intensity maximum close to the Bragg angle is strongly damped. Typically, in GI- and

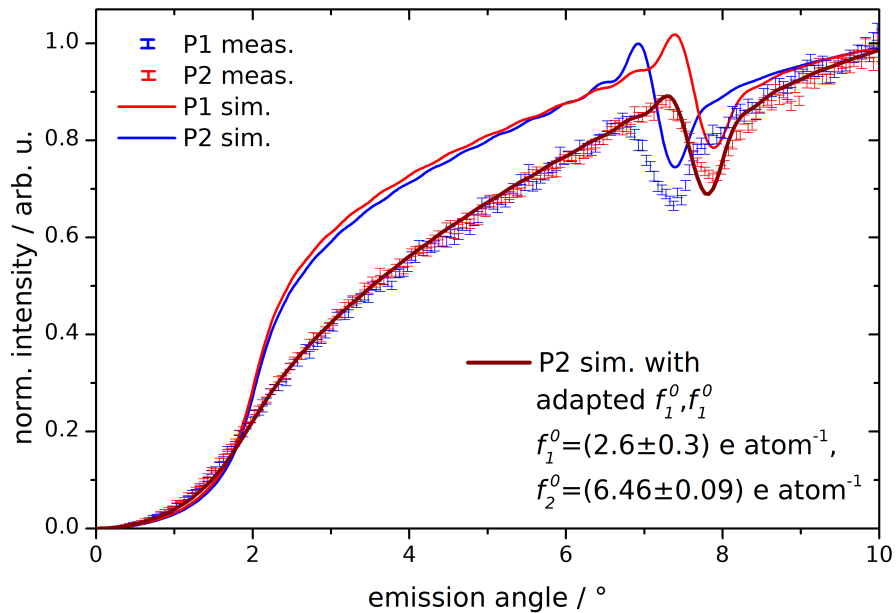


Figure 6.10.: Simulated and measured GEXRF profiles for measurement points P1 and P2. While the simulations with the tabulated atomic scattering factors show strong deviations from the measurements, f_1^0 and f_2^0 can be changed to fit the simulation to the measured data.

GEXRF analysis, such deviations are compensated by fitting the model of the sample, allowing then to determine the sample structure, layer density, roughness or to detect diffusion processes. In the present case, changing all these parameters cannot satisfactorily explain the deviations. Yet, if the atomic scattering factors f_1^0 and f_2^0 for nickel are used as fit parameters, the simulation can well describe the measured GEXRF profiles (see 6.10, purple curve). In the fit result, f_1^0 is reduced by a factor 0.6 and f_2^0 is increased by a factor 3.2 compared to the data for f_1^0 and f_2^0 taken from the Chantler database [40] for nickel at the Ni-L_{α1} fluorescence line (849 eV). As is described in section 2.2.1, f_2^0 is directly linked to the absorption behavior of the material. Therefore, an increase of f_2^0 means increased absorption, damping the features in the GEXRF profile, as can be observed in the measurement.

The applied adaptions to f_1^0 and f_2^0 are quite drastic. Chantler states in [40] uncertainties for the atomic scattering factors of about 1% in the high energy range, which can increase to 10% to 20% for energies between 30 eV and 1 keV. However, these values do not explain the strong adaptions necessary in the present study. In Figure 6.11, database values of the atomic scattering factors of nickel are shown from compilations of Chantler [40] and Henke et al. [39]. Clearly, the L resonances strongly affect the atomic scattering factors. For the GEXRF profiles with adapted atomic scattering factors, photons of

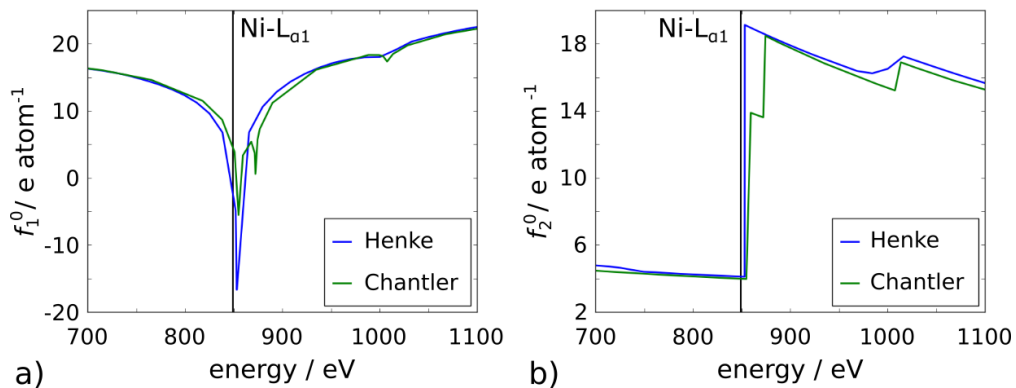


Figure 6.11.: Database values for the atomic scattering factors a) f_1^0 and b) f_2^0 taken from Chantler [40] and Henke et al. [39].

the Ni-L_{α1} fluorescence are simulated with an energy of 849 eV (according to the Elam database [32]), which is near the L3 absorption edge of nickel (853 eV). Consequently, a small uncertainty in the energy scale of the databases can lead to changes in the atomic scattering factors by e.g. a factor of 5 for f_2^0 . Also, the different databases show strong deviations between each other, indicating high uncertainties for the values close to resonances. This supports the validity of the fitted atomic scattering factors. Since the shape of the GEXRF profiles can be altered so strongly with the variation of atomic scattering factors, and the uncertainties of these are so drastic, any further evaluation on diffusion or roughness is doubtful and is not performed for the presented proof of principle measurements.

Nevertheless, the difference of the minimum position of the simulated GEXRF profiles with database values and fitted values for f_1^0 and f_2^0 is less than 0.03°. Also, moderate changes in the layer densities, Debye-Waller factors (modeling interlayer roughness [134]) or implementing surface contamination do not change the minimum position significantly

Table 6.5.: Effect of parameter variation in simulated Ni-L_{α1} GEXRF profiles on the minimum position close to the Bragg angle of the C/Ni-multilayer sample.

parameter	variation	shift of minimum
carbon layer density	± 10%	<0.005°
nickel layer density	± 10%	<0.005°
Debye-Waller factor	0 nm - 2 nm	0.02°
carbon contamination layer	0 nm - 10 nm	0.015°
Ni thickness ratio Γ	± 10%	0.065°

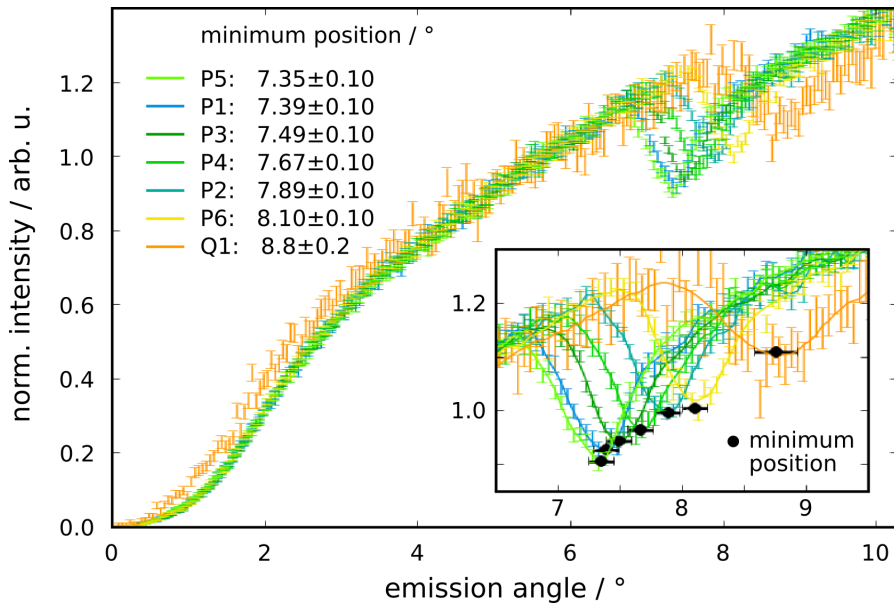


Figure 6.12.: Measured GEXRF profiles for all 7 measurement points. The inset shows the determined minimum position and the estimated angular uncertainty.

with respect to the angular resolution (Table 6.5). Only the relative thickness ratio for nickel Γ , varied by $\pm 10\%$, changes the minimum position in the range of the angular resolution, so that uncertainties in Γ might slightly increase the uncertainties of the bilayer thickness determination. Uncertainties for Γ are estimated to a few percent by the manufacturer of the multilayer [135] and therefore the influence on the angular scale smaller than in Table 6.5. In total, uncertainties due to the used sample model are in the range of 0.05° and thus it is possible to use the minimum position as a measure of the bilayer thickness of the multilayer. Furthermore, the given uncertainties due to the sample model are systematic and therefore, for the current measurements, are compensated by the angular calibration to a reference measurement. However, they need to be taken into account for the second beamtime, where an absolute angular calibration is applied (Section 6.3).

In Figure 6.12, the normalized GEXRF profiles for all measurements are shown. The profiles are smoothed using a Savitzky-Golay filter and the local minimum of the smoothed curve is used to determine the bilayer thickness. For this purpose, GEXRF profiles are simulated using the model of the multilayer (with the unchanged database values for f_1^0 and f_2^0 from Chantler [40]) with varying bilayer thicknesses from 3 to 7 nm with an increment of 0.02 nm. The minimum position of the simulations is evaluated similar to the measurements and provides the dependency of this position with the bilayer thickness (Figure 6.13). This allows for the assignment of measured minimum

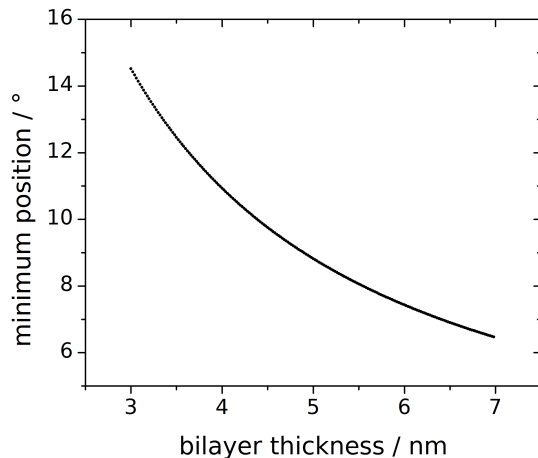


Figure 6.13.: Minimum positions close to the Bragg angle of the simulated Ni-L_{α,β} GEXRF profiles for the multilayer sample with various bilayer thicknesses.

position to a bilayer thickness. The estimated uncertainties for the minimum position are 0.1°, including the pixel resolution for the angular calibration, the precision of the determination of the minimum position and all above mentioned effects (density, roughness, etc.). For measurement Q1 the uncertainties are increased because of the poor statistics of the data and an additional contribution from sample alignment (ω_{sample}), since part Q of the multilayer is mounted separately on the sample holder. The minimum position uncertainties are directly transferred to thickness uncertainties using the data in Figure 6.13.

Figure 6.14 shows the bilayer thickness results of the GEXRF approach in comparison to the complementary methods from Figure 6.1 b) on page 120. Since XRR data is used to calibrate the angular scale of the GEXRF measurements at position P2, the thickness results of these two methods agree perfectly at this point. However, also for the other positions, there is a good match between values obtained by XRR and GEXRF. As already mentioned in Section 6.1.1, TEM measurements overestimate the XRR results, while the thickness values of the conventional XRF approach are systematically lower. Nevertheless, the bilayer thickness gradient is in good agreement for all four methods.

The uncertainties of the bilayer thickness determined by GEXRF are dominated by the angular resolution of the setup and the angular calibration. If necessary, they could be improved by smaller pixel sizes of the detector, the application of center of gravity methods yielding sub-pixel resolution (Section 5.4.1) or larger sample-to-detector distances. Indeed, via the CCD positioning system, a larger sample-to-detector distance is easily adjusted and the angular resolution can be improved at the expense of signal

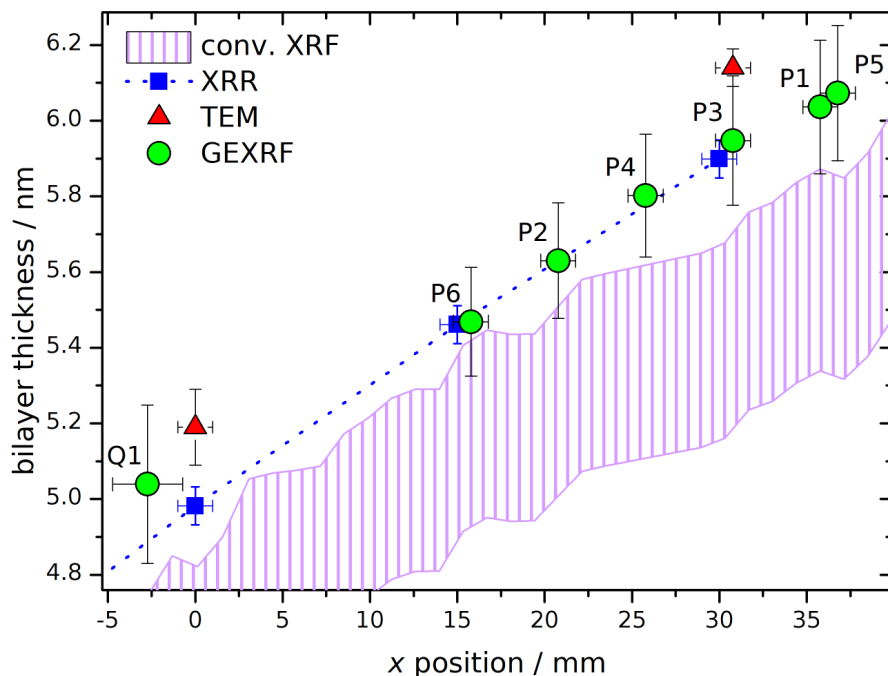


Figure 6.14.: Bilayer thickness results for a part of the C/Ni-multilayer sample deduced with conventional XRF, X-ray reflectometry (XRR), transmission electron microscopy (TEM) and grazing emission XRF (GEXRF). The latter are calibrated to the XRR measurements at P2. Nevertheless, the thickness gradient obtained with GEXRF is in good agreement with the other methods. Reprinted with permission from [84]. Copyright 2017 American Chemical Society.

intensity.

The GEXRF results demonstrate the feasibility of the method for the analysis of multilayer structures and serve as proof of principle for depth profiling approaches. The recorded GEXRF data is of high quality concerning energy (113 eV at Ni-L_α) and angular resolution (0.05°) and measurement times (1 to 2 hours) are already practical with the presented laboratory setup, especially when considering the early stage of development. Several major setup improvements (e.g. absolute angular calibration, enhanced excitation conditions) can be envisaged and are partly already implemented in this thesis, as will be described in the following Section 6.3.

Finally, if precise optical constants of the investigated sample were available, a fit of the complete GEXRF profile could be performed. This would not only increase the accuracy of the analysis, but also allow to investigate the sample structure, e.g. roughness, density and diffusion processes, more thoroughly.

6.3. Second Beamtime - Setup Development and Characterization

The pnCCD, which is used for the first proof of principle measurements, is costly in price and complex in operation. Therefore, in a second beamtime with the laser-produced plasma source, the suitability of a conventional CCD camera for scanning-free GEXRF measurements is investigated. Furthermore, some changes in the setup and alignment strategies are developed and applied. All the improvements concerning the general setup and the methodology that is proposed for scanning-free GEXRF measurements are already described in Chapter 5. They will be briefly named hereafter and compared to the measurements in the first beamtime (Section 6.2). However, the main part of this chapter will be concerned with the stability of the modified setup, the reproducibility of the absolute angular calibration and the comparison of the GEXRF profiles of the C/Ni-multilayer sample to those obtained before.

6.3.1. Setup Development

The main goals for the setup modification are the implementation of a less complex CCD camera, reduced measuring times and an angular calibration independent on reference measurements.

As stated in Section 2.3.1, also conventional CCDs can be used as energy-dispersive detectors if operated in a single photon counting mode. Therefore, a back-illuminated CCD (Greateyes GE 2048 512 BI) with 2046×515 pixels of $13.5 \times 13.5 \mu\text{m}^2$ size is implemented in the setup. It can be adjusted with the same positioning system used for the measurements with the pnCCD, applying a further adapter flange (see also Section 5.2.4). Since the CCD chip is rectangular with an aspect ratio of 1 to 4, the CCD can be mounted with the larger dimension in the direction of strongest change of the detected emission angles (y direction in the LAB system) or perpendicular to it. For all measurements shown hereafter, the latter geometry is chosen to maximize the solid angle of detection at the expense of angular dynamic range. Thus, regions of interest in the GEXRF profiles have to be chosen for each measurement (e.g. the angular range close to the Bragg angle for the C/Ni-multilayer sample) or successive measurements can be performed with tilted ω_{sample} and merged subsequently. For future applications, it might even be worthwhile to consider a diagonal alignment of the CCD to make use of large solid angles of detection for emission angles detected in the center of the CCD chip and still enable a rather wide angular dynamic range. One of the major drawbacks of the conventional CCD is the long readout time. Typically, a readout frequency of 1 MHz is chosen as a good compromise between introduced readout noise (which is increasing

with higher readout frequencies) and convenient readout time, which is about 1 s for the applied CCD chip. However, since noise contribution is critical to single photon event evaluation, especially in the soft X-ray range, measurements are also performed with a readout frequency of 250 kHz (lowest possible setting), resulting in readout times of up to 4 s. With a recording time per frame of 500 ms to 1 s it is obvious that total measurement times are limited by the slow readout in the present setup. This has to be considered if further optimizing the setup with respect to the detector system.

The somewhat declined readout conditions are compensated in the new setup by improvements with respect to excitation condition. Instead of the Kirkpatrick-Baez mirrors, two toroidal optics are implemented (Section 5.2.2). Because of the better total angle of acceptance and higher efficiency (only one reflection instead of two for focusing), the total flux in the sample plane is increased compared to the KB optics. Furthermore, optics alignment is comparatively easy and the focus size in the sample plane is reduced from $100 \times 500 \mu\text{m}^2$ to $70 \times 80 \mu\text{m}^2$ with the new optics.

To make the angular calibration independent of reference measurements, an optical alignment laser is applied. This is used to exactly define the geometry of the setup and also allows for precise alignment of the sample surface into the pivotal point of the goniometer (see Section 5.2.5).

6.3.2. Measurement Stability and Reproducibility

Adapted Operation Mode of the LPP Source

Because of the fast readout times of the pnCCD (below 1 ms), it is possible to use the trigger signal of the LPP source to guarantee readout between two subsequent X-ray pulses and a continuous operation of the LPP source. With the conventional CCD, readout times are in the range of seconds. During this time, no photon should hit the detector to avoid smearing of the GEXRF profile. Therefore, a mechanical shutter is triggered by the CCD, to block the seed laser pulse of the LPP laser system and thus plasma formation during readout (“staccato” operation).

The stability of the toroidal focus is investigated by recording images with the CMOS detector in the focal plane during “staccato” operation of the LPP source. The recording of 3 sequences consisting of 3 dark frames and subsequent 3 GEXRF measurement frames is simulated by opening the shutter for the measurement frames only. The recording time is set to 1 s and the laser pulse energy is 150 mJ. The CMOS detector records a movie of the focus spot of the toroidal optics. For the evaluation, the bright frames of the movie are extracted, which gives a set of $3 \times 3 \times 18 \pm 1$ frames (sequences \times measurement frames per sequence \times CMOS frames per measurement frame). For each frame, the mean value

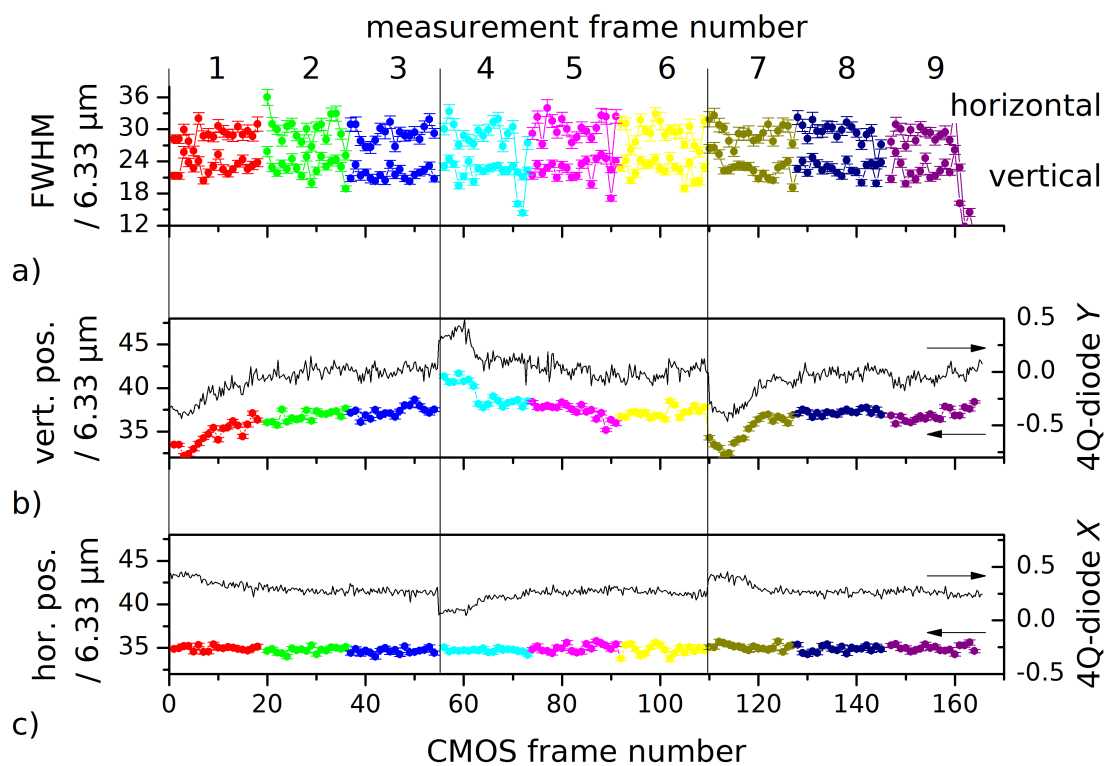


Figure 6.15.: Stability investigation of a) the toroidal focus width and b) and c) position in units of the CMOS pixel size along the horizontal and vertical direction. Real GEXRF measurement conditions are simulated by operating the LPP source in a “staccato” mode and taking three times 3 dark frames (vertical black lines) and 3 measurement frames (indicated by the different colors).

of the rows, respectively columns, is computed and a Gaussian function fitted to the focus peak position, yielding results for the horizontal (mean value of rows) and vertical (mean value of columns) direction in the laboratory. The position and full width at half maximum (FWHM) values of all fits are displayed in Figure 6.15 together with the X and Y signal of the 4Q-diode (see Section 2.5.2). Figure 6.15 a) shows that the peak width is rather stable and that the FWHM in the horizontal direction is slightly larger than in the vertical direction. The standard deviation of the FWHM is 8% for both, horizontal and vertical direction. The mean value of the FWHM is $(142 \pm 5) \times (186 \pm 7) \mu\text{m}^2$, which is overestimated with respect to the $70 \times 80 \mu\text{m}^2$ of a single toroidal optics (Section 5.2.2) because of the overexposed CMOS detector.

Figure 6.15 b) and c) show the stability of the focus position for the vertical and horizontal axis in the laboratory system. In the vertical direction, there are sudden displacements visible (at frame numbers 3, 54, 62, 110) of up to $30 \mu\text{m}$. The Y value of the 4Q-diode (same Figure) shows a similar behavior, correlating the focus position in the CMOS frames directly to the plasma position of the LPP source. The displacements originate from the missing correction of the target (performed also in the vertical direction) during the time when the 4Q-diode gets no signal and the subsequent sudden correction as soon as the plasma is created again. This effect is especially strong after recording of the dark frames, so before every three measurements, because of the longer time without plasma. The readout (and thus missing signal) is not strongly affecting the position of the focus, since the readout times are too small to induce a drastic target misalignment. The horizontal position of the focus is much more stable, even though there also appear displacements in the X signal of the 4Q-diode. The 4Q-diode is adjusted in a way that plasma displacements along the radius of the copper cylinder are monitored with Y , while not affecting X . Since a change of the laser position is not expected, the displacements in X can originate either from a small misalignment of the 4Q-diode or an effect of the determination of the X value. Concerning the latter, the change of total intensity detected by the 4Q-diode in combination with a non-Gaussian shape of the plasma image on the 4Q-diode can lead to differences in X . The standard deviation of the focus position is $10 \mu\text{m}$ for the vertical direction and $2.5 \mu\text{m}$ for the horizontal direction, thus smearing of the average focus size is stronger in the vertical direction, but still small compared to the focus size.

Figure 6.16 a) shows the intensity distribution of the two superimposed optics foci in the focus plane measured with the CMOS detector and averaged over all bright frames used for the stability investigations. The shape of the combined foci with its diagonal tails is similar to a single focus and indicates the good spatial overlay. The spot size (FWHM in center row and column) of $126 \times 177 \mu\text{m}^2$ is again overestimated as compared to the focus size with a single optics (Section 5.2.2) because of the overexposed CMOS

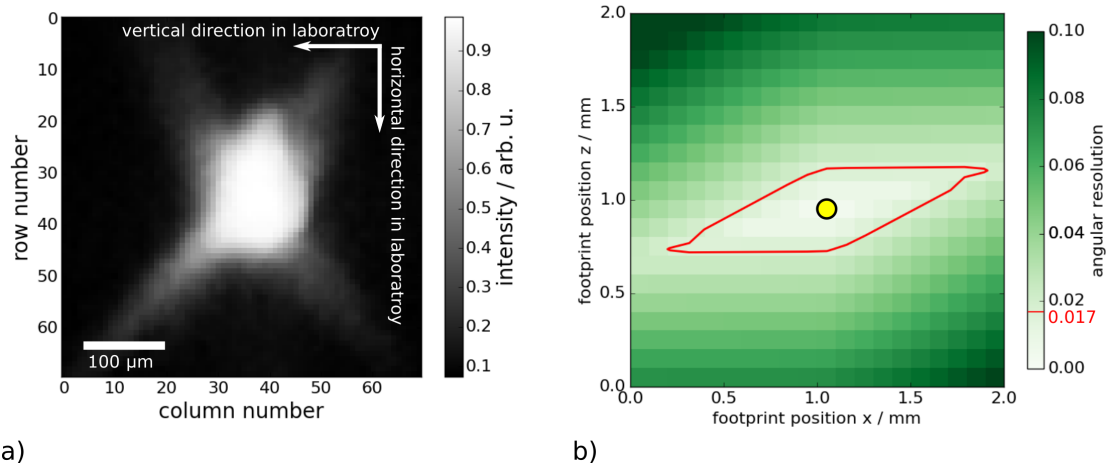


Figure 6.16.: a) Average intensity map of the two toroidal mirror foci superimposed in the sample plane recorded with the CMOS detector. b) Impact of footprint size on the angular resolution of the GEXRF measurements calculated for the final measurement geometry. The red line indicates a footprint size which would affect the angular resolution similar to the pixel size of the detector. The yellow disc illustrates a footprint shape with 100 μm diameter and shows that the angular resolution is not affected by the footprint size.

detector. In summary, the average spot size is well suited for GEXRF measurements and does not influence the angular resolution, as can be seen in Figure 6.16 b).

Usually, every laser pulse of the LPP source is focused onto a fresh spot on the rotating copper cylinder. After the whole surface of the target cylinder is used for plasma formation, which is the case after 11 hours of continuous operation, the target cylinder is replaced by a twin that has been turned down on a lathe and polished. The use of this two target cylinders makes daily operation possible, but about two hours (including venting and evacuating the vacuum chamber) are needed to change the target cylinder. To overcome this, the target cylinder is not changed, but used again a second time during this beamtime. The influence of the somewhat rougher target surface on the focus stability of the toroidal optics is investigated by using the same area of the target cylinder up to four times and recording images with a CCD camera in the focus plane of one of the toroidal mirrors. The laser pulse energy is set to 200 mJ and the recording times are 1 s. Figure 6.17 shows the results for the evaluation of the focus position and size. Similar to the evaluation of the CMOS images, rows, respectively columns are summed and a one-dimensional Gaussian fit is used for the evaluation. Note that due to the chosen evaluation of rows and columns to get direct correlation to changes in the corresponding direction and a probably imperfect adjustment, values for the focus size are larger than compared to the results of [113] in Section 5.2.2. It seems that position

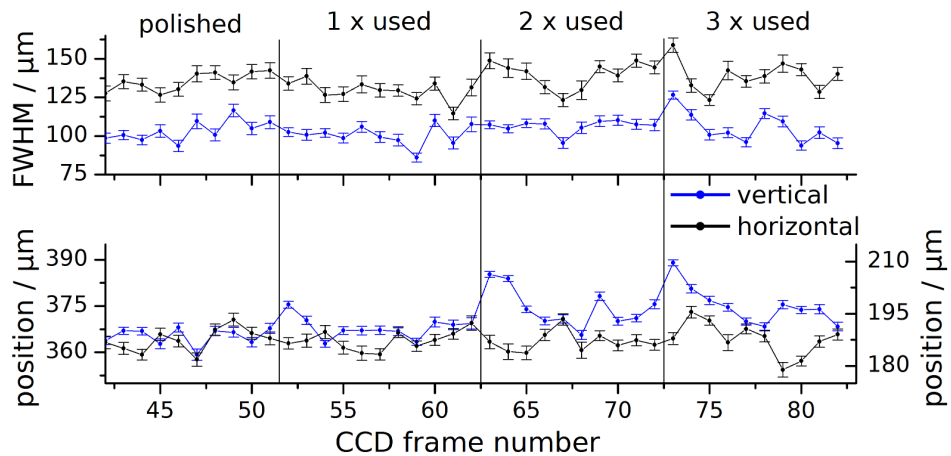


Figure 6.17.: Size (FWHM) and position variation of a single toroidal mirror focus recorded with a CCD camera in the focus plane. A target area of the LPP source is reused several times.

Table 6.6.: Mean values and standard deviation σ of the size (FWHM) and position of the focus spot from measurements in Figure 6.17.

target	horiz. FWHM		horiz. pos.
	mean / μm	σ / μm	σ / μm
polished	103 ± 4	6.1	3.9
1 × used	101 ± 4	6.3	5.7
2 × used	106 ± 4	3.9	6.0
3 × used	105 ± 4	9.9	5.9

target	vert. FWHM		vert. pos.
	mean / μm	σ / μm	σ / μm
polished	135 ± 5	5.4	3.1
1 × used	131 ± 5	7.9	2.5
2 × used	140 ± 5	8.2	2.7
3 × used	139 ± 5	9.4	4.7

and focus size fluctuations are induced with increasing number of used target material, probably because of the increased surface roughness of the target material. However, with a maximum standard deviation of the focus size (FWHM) of $\approx 10 \mu\text{m}$ and of the focus position of $\leq 6 \mu\text{m}$ in the horizontal and vertical direction, the effect is rather small (Table 6.6). It can be stated that the copper target can be used at least 4 times for GEXRF measurements without drastically reducing the lateral or angular resolution.

Reproducibility of Absolute Angular Calibration

In the following, the stability of the absolute angular calibration is investigated with data from the second beamtime and uncertainties for the angular scale are determined. During the whole beamtime, 8 sample alignments and angular calibrations are performed on different samples, each yielding values for the geometric parameters (GPs) defining the setup geometry (see Section 5.3.2). At first, $\omega_{\text{CCD}} = (5.9 \pm 0.5)^\circ$ and $\theta_{\text{CCD}} = (0.0 \pm 0.5)^\circ$ are determined using Equation 5.3.2. Then, all other GPs are calculated with the data of an angular scan of the sample (θ axis of the goniometer) and the position of the direct adjustment laser beam on the CCD, as is described in Section 5.3.2. Figure 6.18 summarizes the results for all the angular calibrations. In Figure 6.18 a) it can be seen that the position of the alignment laser on the CCD changes arbitrarily in the range of a few tens of micro meters on the CCD. Whether this shift is mainly caused by a change of the laser or CCD position (e.g. by thermal influence) or by the laser alignment through the pivotal point of the goniometer (performed prior to each angular calibration) is difficult to identify. Both effects will change the beam position on the CCD slightly, but as long as the position is known, all these shifts are compensated for during the angular calibration. In Figure 6.18 b) and d), the variation of the CCD tilt ϕ_{CCD} and of the goniometer position θ_0 , when the sample surface is aligned parallel to the adjustment laser (i.e. $\omega_{\text{sample}} = 0^\circ$), can be seen. Angular calibrations with the numbers (1,2), (3,4,5) and (7,8) are performed on the same sample without changing the sample holder but at different dates. A corresponding grouping of ϕ_{CCD} and θ_0 is visible. The angular calibration number 6 is performed on the same sample as used for (1,2), but the sample holder is load locked in between. This might result in the differences visible in ϕ_{CCD} , since this angle is defined with respect to the sample surface, which might be tilted for the various samples. Here, a reference sample holder should lead to more reproducible values. The effect is also seen in the variation of θ_0 in Figure 6.18 d), where the same correlation between θ_0 values and samples is visible. The results for the CCD chip-to-sample distance, d_{CCD} , are shown in Figure 6.18 c). Here, the values are all in good agreement to each other but for the angular calibration number 2. In the beginning of the beamtime the cable for the shutter signal is plugged into the CCD

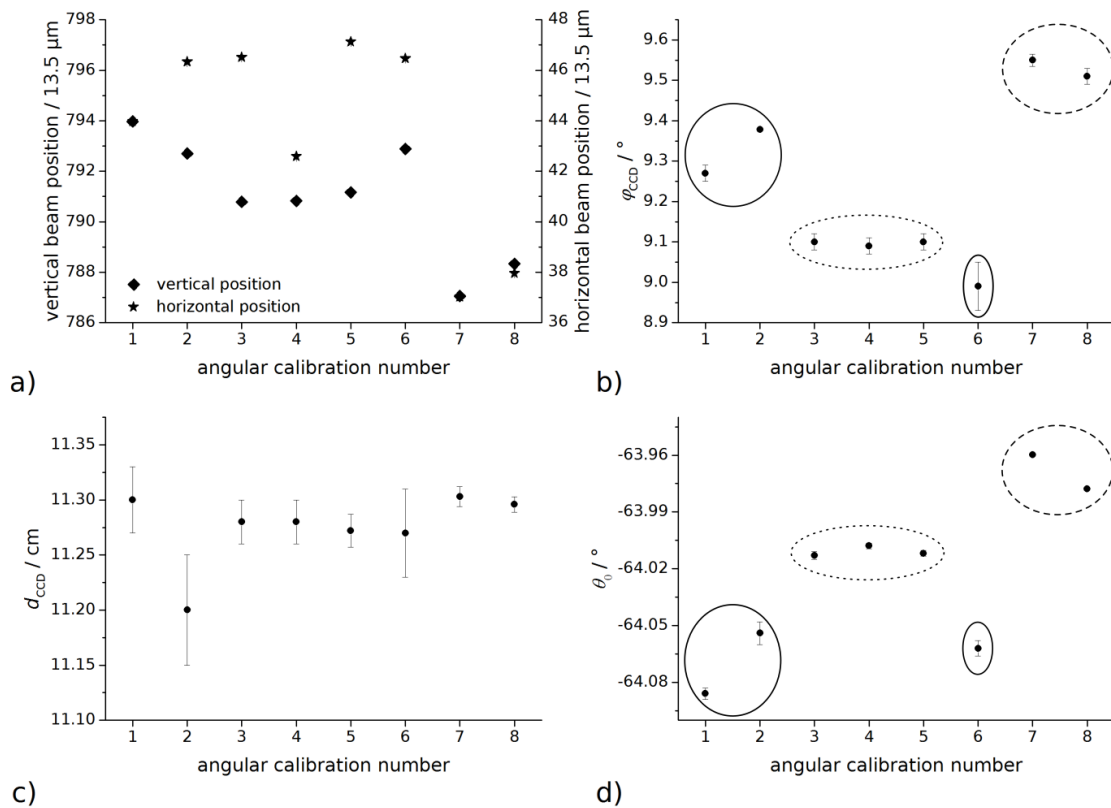


Figure 6.18.: Results for geometric parameters obtained with 8 different angular calibrations. a) shows the position of the direct adjustment laser beam. b) and d) show the angular tilt of the CCD θ_{CCD} and the zero angle ($\omega_{\text{sample}} = 0$) position of the goniometer θ_0 . The 3 different samples that are used for the angular calibration are illustrated by the circle with solid, dashed and dotted line. c) shows the determined CCD chip-to-sample distance. All the given uncertainties result from the fitting procedures described in Section 5.3.2.

directly. This might have affected the CCD position slightly and is changed for the subsequent measurements. Also, a slight misalignment of the sample surface into the pivotal point of the goniometer could affect the calculated distance.

Table 6.7 illustrates the effect of the uncertainties on the angular calibration. For this purpose, a GEXRF measurement from the next Section 6.3.3 on the C/Ni-multilayer is used and the GEXRF profile of the Ni-L fluorescence line is obtained by using the respective absolute angular calibration. Now, the GEXRF profiles are evaluated similar to the procedure in Section 6.2.5, once for the GPs given in Table 6.7 and once for each GP with the respective uncertainty added to the GP's value. The influence on the angular scale is estimated as the angular change of the intensity minimum in the respective GEXRF profiles. As can be seen, all shifts but the one for l_{CCD} are $\leq 0.006^\circ$,

Table 6.7.: Results of the absolute angular calibration. The influence of the uncertainties of the GPs on the angular scale is determined as the shift of the minimum position in the Ni-L GEXRF profile when adding the uncertainty to the respective GP, while leaving all other GPs fixed.

	value	shift of int. min.
d_{CCD}	$113.0 \text{ mm} \pm 0.3 \text{ mm}$	0.003°
l_{CCD}	$0.60 \text{ mm} \pm 0.05 \text{ mm}$	0.03°
h_{CCD}	$3.10 \text{ mm} \pm 0.05 \text{ mm}$	0.005°
ϕ_{CCD}	$9.27^\circ \pm 0.02^\circ$	0.003°
θ_{CCD}	$0.0^\circ \pm 0.5^\circ$	0.006°
ω_{CCD}	$5.9^\circ \pm 0.5^\circ$	0.006°
ω_{sample}	$5.956^\circ \pm 0.004^\circ$	0.004°

and thus their influence on the angular resolution small compared to the influence of the pixel size, which yields 0.011° . The uncertainty of l_{CCD} of $50 \mu\text{m}$, resulting in an angular shift of about 0.03° , is estimated from the sample alignment accuracy, which is performed online and will be improved in the future. Some aspects about the sample alignment can be found in Appendix J. In total, the uncertainty of the angular scale is estimated with 0.04° for all the measurements of the second beamtime.

6.3.3. GEXRF Profiles of the C/Ni-multilayer

During this second beamtime, several measurements at different dates and with varying CCD camera parameters are performed at position P2 of the C/Ni-multilayer already investigated in Section 6.2 and described in Section 6.1. The multilayer sample is mounted together with the CMOS detector, the $500 \mu\text{m}$ pinhole (both for adjustment control of the LPP focus and the optical laser), some fluorescent screen (to get a reference for the x and y position of the goniometer close to the sample) and the thermoelectric sample DM0149A, as can be seen in Figure 6.19. Also, the 20° wedge is applied to reduce the achievable camera-to-sample distance (see Section 5.2.4).

First, the setup needs to be aligned according to the procedure in Section 5.2.5. To exclude misalignment during the measurement, before and after each measurement, the position of the toroidal focus and of the adjustment laser for the angular calibration and sample alignment are monitored by the CMOS detector. Then, by visual inspection, the surface of the fluorescent screen is aligned into the focus plane of the toroidal optics to obtain a reference value for the position of the x and y axes of the goniometer. These axes

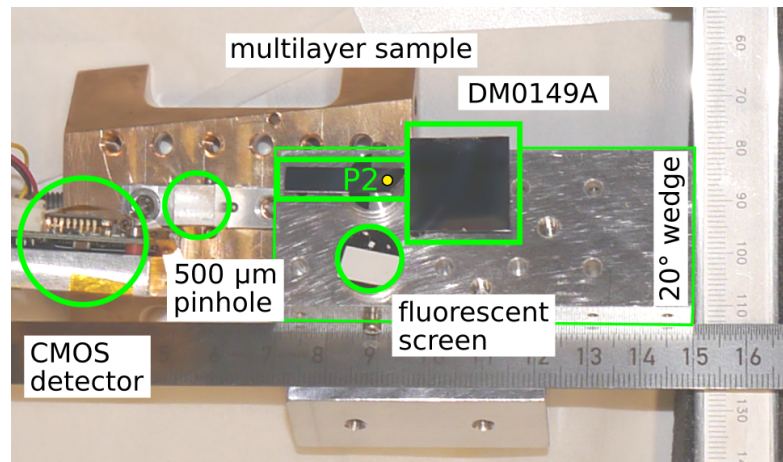


Figure 6.19.: Sample holder as it is used in the second beamtime. On the multilayer sample measurement spot P2 is indicated.

are shifted according to the distances measured on the photograph of the sample holder, to align the measurement spot of the sample into the toroidal focus. By this procedure, uncertainties reach about 1 mm for the lateral alignment, which is satisfactory for the current purposes. The precision in the lateral alignment can be increased if necessary, if the sample edges are scanned and for each position spectra with the CCD detector are recorded. Then, accuracies in the range of the focus size ($< 100 \mu\text{m}$) can be achieved. Now, alignment of the z and θ axes of the goniometer is performed with the adjustment laser and the CCD camera (see Section 5.2.5). The final θ scan is used for an absolute angular calibration (Section 5.3.2).

Figure 6.20 shows exemplarily the fluorescence emission angle and solid angle of detection distribution on the CCD chip for the angular calibration of measurement 1. In Figure 6.20 a), it can be seen that the angular range covers 4.8° to 10.4° . Furthermore, some parts of the CCD image are not used for the final compilation of the GEXRF profiles (marked black). These parts include first of all a frame border of 3 pixels width, to prevent counting a charge cloud that is not fully detected on the CCD chip. Secondly, in dark frames recorded at room temperature, some hot pixels are detected. These, and all the pixels in the direction of the readout of the CCD chip are also excluded preventively, since they might alter single photon event (SPE) intensities. Finally, some spots on a bright CCD image appear darker, probably because of dust particles on the chip. Soft X-ray photons might be absorbed in these dust particles, so that the corresponding pixels have a reduced detection efficiency and are also excluded from the evaluation.

In Figure 6.20 b) the distribution of the solid angle of detection of each pixel is shown. The maximum differences on the whole chip are $\approx 4\%$ and will be increased for shorter

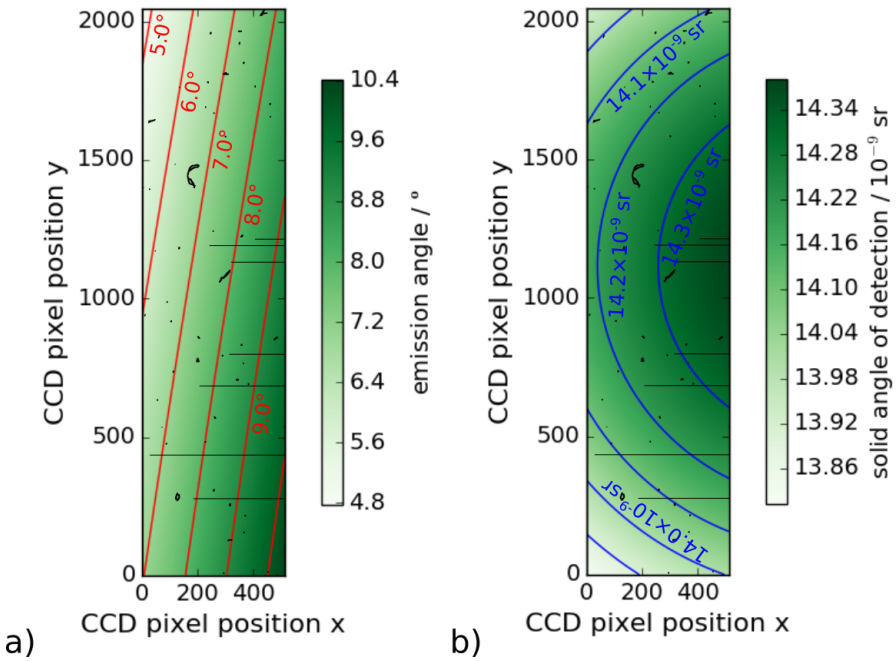


Figure 6.20.: a) Detected fluorescence emission angle and b) solid angle of detection for each pixel of the CCD chip according to the angular calibration of measurement number 1. Dark regions in the image are likely to create distorted signals and are thus excluded from the compilation of GEXRF profiles.

sample-to-detector distances (which should be the aim for such measurements). The sum of the solid angle of detections of all pixels yields 0.015 sr. Compared to the setup of the first beamtime with the pnCCD, both, the covered emission angle range and the solid angle of detection are about half as large. That means, even though the angular dynamic range is reduced, the solid angle of detection per angular range is similar. On the other hand, the angular resolution is more than 4 times better for the measurements with the conventional CCD, which reduces the uncertainties in the determination of the bilayer thickness of the C/Ni-multilayer.

From the aligned position, the θ axis of the goniometer can be used to adjust the segment of fluorescence emission angles, which is detected by the CCD chip. For the measurements of the C/Ni-multilayer, θ is moved by $\approx 6^\circ$. At the final position, CCD images are recorded while the LPP source is operated in the “staccato” mode, i.e. the seed laser pulse of the LPP laser system is blocked during dark frame recording and readout. Typically, sequences of 3 dark frames and subsequent 50 measurement frames are recorded, using an in-house labview control for the CCD camera. Measurements at P2 of the multilayer are performed with camera temperatures below $(-45 \pm 1)^\circ\text{C}$ and with varying exposure times, readout frequencies and with or without binning of two

Table 6.8.: CCD settings for the GEXRF measurements performed at P2 of the C/Ni multilayer sample and the achieved resolving power measured at the Ni-L_{α,β} line in the integral spectra. CCD chip temperature is (-45 ± 1)°C for all measurements. The values in brackets of the column 'frames recorded' indicate the number of dark frames and measurement frames for each sequence.

number	meas.	frames	exposure	readout	1 × 2	resolving
	time / min.	recorded	time / ms	freq. / kHz	binning	power
1	72	9 × (3+50)	1000	250	no	3.05
2	46	10 × (3+50)	1000	1000	no	2.67
3	46	13 × (3+50)	500	250	yes	3.40
4	37	9 × (3+50)	1000	250	yes	3.39
5	15	6 × (3+50)	1000	1000	yes	2.92

pixels in the direction of the smaller aspect ratio of the camera. The binning of pixels in the other direction can only be performed software-wise, so without decreasing readout time or noise, and is thus disregarded. The various measurement settings are listed in Table 6.8.

The recorded CCD images are evaluated as described in Section 5.4. The 4px-Area-Clustering method shows the best performance with respect to resolving power for the applied CCD and is therefore chosen for all further evaluations. The influence of the two noise thresholds on the integral spectra of the GEXRF measurement number 1 is investigated in Figure 6.21. First, the low resolving power compared to the spectra recorded with the pnCCD ($E/\Delta E = 7.5$ at Ni-L_{α,β} in Figure 6.7 on page 131) is apparent. With the conventional CCD, the Ni-L_{l,n} and Ni-L_{α,β} peaks cannot be resolved. Furthermore, the contributions of cluster events consisting of up to 7 pixels are shown in the plotted spectra of Figure 6.21. The global threshold factor n'_σ is influencing the cut-off at the low energy side of the spectrum and thus reduces the intensity of the noise peak. The local threshold factor n''_σ on the other hand reduces the contributions of n -px SPEs with $n > 4$, thereby enhancing the resolution of the main fluorescence peak but also reducing and maybe distorting the pile-up intensity. As compromise between the reduction of noise, the enhancement of resolution and keeping the pile-up peak unaffected, $n'_\sigma=n''_\sigma=4$ is chosen for all further investigations.

Besides the measurement conditions, Table 6.8 also shows the respective resolving power at the Ni-L_{α,β} line in the integral spectra evaluated with the 4px-Area-Clustering method and $n'_\sigma=n''_\sigma=4$. Reducing the readout frequency (measurement number 2 → 1 and 5 → 4) and using binning (1 → 4 and 2 → 5), both increase the resolving power

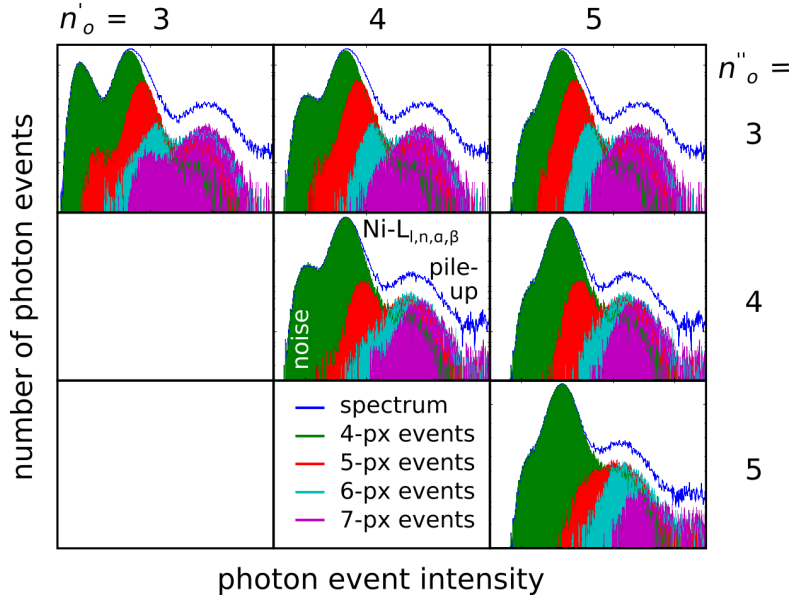


Figure 6.21.: Integral spectra of GEXRF measurement 1 (see Table 6.8) on the C/Ni multilayer, evaluated with the 4px-Area-Clustering method using the given factors n'_σ and n''_σ for the noise threshold.

by about 15% and 10%. While the former reduces the readout noise contribution in the CCD images, the latter leads to a more complete SPE recombination without additional noise contribution due to additional pixels assigned to the SPE. The measuring time ($4 \rightarrow 3$) has no significant influence on the resolving power, indicating that the dark noise current, and thus the camera temperature, are sufficiently low. Indeed, the CCD camera is cooled with an external water cooling system to achieve chip temperatures down to -45°C . For future applications it could be tested, if the CCD operation at -25°C , which can be reached by the air venting system of the CCD camera only and simplifies operation, is sufficient.

With the SPE evaluation and the angular calibration at hand, the GEXRF profiles can be compiled by summing the number of detected fluorescence photons in all the angular areas on the CCD chip, which include the same angular range, i.e. $\psi_H \pm 0.5 \times \Delta\psi_H$, with $\Delta\psi_H$ being the angular resolution due to the pixel size. To reduce background contributions from noise events and to properly handle pile-up, only SPEs in specific regions of interest (ROIs) of the integral spectrum are used for the compilation of the GEXRF profiles. The lower and upper limits of the two ROIs for the fluorescent peak and for the first pile-up peak are defined by the peak center x_0 and the width (FWHM) of the peak, i.e. $x_0 \pm \text{FWHM}$. For the GEXRF profile, the events in the pile-up ROI are counted double, since each event consists of two photons.

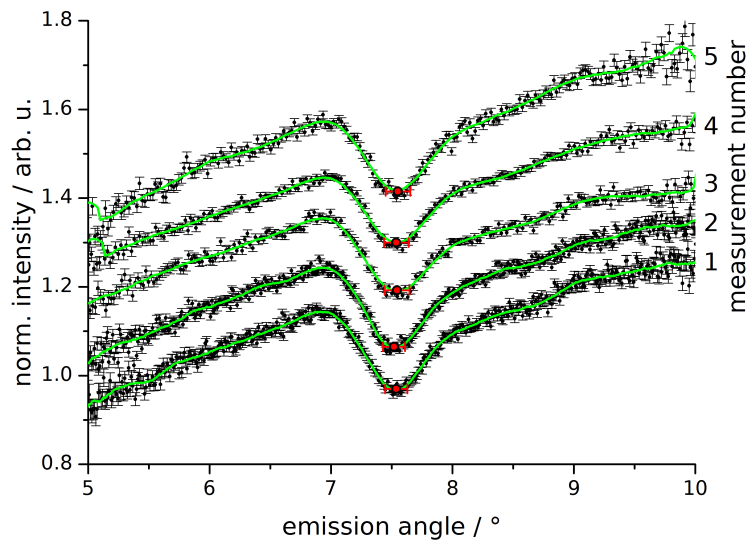


Figure 6.22.: Normalized GEXRF profiles of Ni-L fluorescence of the C/Ni-multilayer. For the determination of the minimum position (red dot) the profiles are smoothed with a Savitzky-Golay filter with window size 37 and of order 3 (green curve). An offset is added to the curves for reasons of clarity.

Figure 6.22 shows the GEXRF profiles of all 5 measurements with some offset for reasons of clarity. As can be seen, the local intensity minimum close to the Bragg angle is well reproduced in all measurements. Its position is again used to determine a bilayer thickness with the same model for the sample as in Section 6.2 and with the same procedure, but now taking into account the reduced energy resolution by summing the GEXRF profiles of Ni-L_{α_1} , $-\text{L}_{\alpha_2}$, $-\text{L}_{\beta_1}$, $-\text{L}_1$ and $-\text{L}_n$ for the simulation. The bilayer thickness results are compared in Figure 6.23 with complementary methods and the results of the GEXRF measurements of the first beamtime, where a reference for the angular calibration is used (Sections 6.1 and 6.2). The inset shows the bilayer thickness results of all 5 measurements with absolute angular calibration. Measurement numbers 1 and 2 and measurement numbers 3 and 4 have the same sample alignment and angular calibration, resulting in 3 different sample alignments and angular calibrations for the 5 measurements. The results of the bilayer thickness of all 5 measurements are identical with respect to their uncertainties, which shows the excellent reproducibility for the 5 measurements. Furthermore, uncertainties are similar compared to the measurements of the first beamtime. However, now these uncertainties are dominated by the sample alignment (contributing with 0.03°) and uncertainties of the model structure (contributing with 0.05° , see Section 6.2.5), while the uncertainty of the actual determination of

the intensity minimum is estimated with the value of the pixel resolution of about 0.01° . The former two uncertainties can be expected to be reduced by further investigations concerning the sample alignment procedure (see also Appendix J) and better known optical scattering factors to improve the simulations. In the main panel of Figure 6.23, the mean value of the five measurements is plotted (red dot). It can be seen that the bilayer thickness results of the second beamtime are systematically higher than the XRR measurements, and thus also the GEXRF measurements of the first beamtime, which are calibrated to the XRR measurements at P2. To exclude a drastic change of the sample composition (e.g. by oxidation) and an increase of the bilayer thickness over time, a further XRR measurement directly at P2 is carried out by the manufacturer AXO Dresden GmbH. The result is added to the graph and also used for the comparison in the inset. Even though the new XRR value for the bilayer thickness seems to be slightly increased, it does not fully explain the overestimation of the GEXRF measurements. Thus, some further systematic error seems to be present and needs to be investigated in future work. New measurements on a multilayer without thickness gradient and with a main component, whose fluorescence photon energy is not close to an absorption edge (which would reduce uncertainties of the atomic scattering factors), might be envisaged.

Whatever the outcome, it can still be concluded that the GEXRF measurements with an absolute angular calibration are in general successfully performed. GEXRF profiles in the soft X-ray range can be acquired even with a conventional CCD in good measurement times of down to 15 minutes. Indeed, due to the excellent efficiency of the toroidal optics, the bottleneck concerning measurement time is the long readout time of the conventional CCD. The actual recording time for all measurements is only 5 to 9 minutes for the whole GEXRF profile. Further increasing the readout frequency on the other hand would lead to significant additional noise, and thus reduced energy resolution. To circumvent this correlation, some other type of CCD might be optimal for soft X-ray GEXRF measurements. For example, in [136, 61], an electron multiplying (EM-) CCD is presented, which amplifies the signal of each pixel before readout, allowing to use much higher readout frequencies without distortion of the signal-to-noise ratio. Thus, the enhanced signal-to-noise ratio leads directly to an enhanced resolving power and also allows for more accurate split event recombination, again beneficial for the total resolving power. On the other hand, the amplification process induces some noise on the signal itself and it might be indeed worthwhile to analyze the effective gain in resolving power. In the end, the EM-CCD could be a good compromise between applicability for soft X-ray GEXRF and cost.

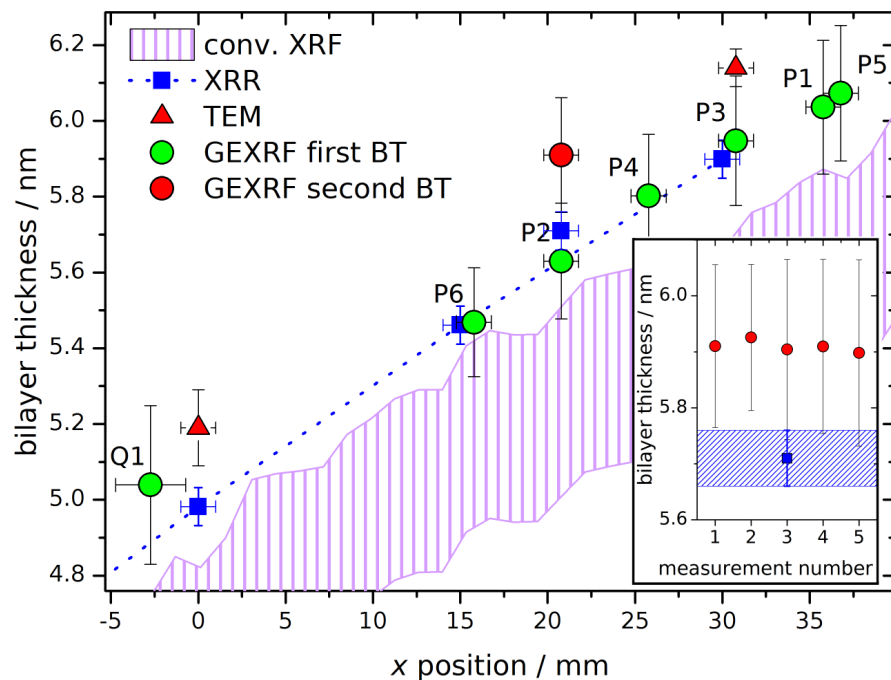


Figure 6.23.: Results of the bilayer thickness of the C/Ni-multilayer. The mean value of the 5 GEXRF measurements of the second beamtime (red dot) is compared to the results of the first beamtime (green dots) and complementary methods. The inset shows each of the 5 results in comparison to the result from repeated XRR measurements at the same measurement point P2. Reprinted with permission from [84]. Copyright 2017 American Chemical Society.

6.3.4. GEXRF Profiles of Thermoelectric Nanofilms

Besides the measurements on the C/Ni-multilayer for characterization purposes of the setup, GEXRF profiles of the thermoelectric nanofilm DM0149A are also recorded. In Section 4.5 the same sample is investigated by synchrotron radiation based grazing incidence XRF and it is found that the surface contamination prevents precise depth profiling of the thermoelectric nanofilms using the oxygen signal. Also, the Cu GIXRF profile in the shallow angular range is not trustworthy because of high uncertainties originating from sample misalignment and the effective solid angle of detection. However, some model for the contamination is found, which can explain the shape of the GIXRF profiles. Especially the carbon profile can be modeled by introducing carbon contamination into the thermoelectric thin film. Concerning the laboratory based GEXRF measurements, the low energy resolution and high noise levels of the conventional CCD make an evaluation of the oxygen signal difficult and of the carbon signal impossible. On the other hand, the solid angle of detection in the GEXRF setup changes only slightly with the detected fluorescence emission angle, leading to a low susceptibility of the GEXRF profile to uncertainties in the solid angle of detection. Thus, a depth profiling approach for DM0149A is pursued in the following.

Since the sample is mounted on the same sample holder as the C/Ni-multilayer (see Figure 6.19 on page 152) and measured during the same beamtime, measurement conditions and geometry are very similar. Of course, a separate sample alignment and thus also angular calibration are performed according to the procedure described in Sections 5.2.5 and 5.3.2. To record a wider angular range, 3 GEXRF measurements are performed at the same sample spot (and with the same calibration) but tilting the sample by 3° and 6° for the second and third measurement, respectively. The measurement parameters are listed in Table 6.9. The total measurement time of 3 hours is reasonable. The camera settings are chosen to maximize the expected resolving power for the measurements, i.e. exposure time is 500 ms, readout frequency is 250 kHz and 1×2 binning is used. The chip temperature is (-51± 1)°C for the first and (-48± 1)°C for the second and third GEXRF measurement.

All GEXRF frames are evaluated as described in Section 5.4 with the 4px-Area-Clustering method. However, the small oxygen signal in the measurement is only hardly detected due to the overall low resolving power of the (not optimized) conventional CCD camera. To get any signal at all, further refinement of the evaluation with the aim to enhance the resolving power have to be performed. First of all, the master dark image, which is subtracted from the GEXRF frames, is smoothed with a median filter, which puts in every pixel the median of the 5×5 square, centered at this pixel. By this procedure, some high frequency oscillation of very low amplitude is found in the spectra.

Table 6.9.: Measurement parameters for the GEXRF measurements on the thermoelectric nanofilms.

number	$\omega_{\text{sample}} / {}^\circ$	meas.	frames
		time / min.	recorded
1	-0.048 \pm 0.003	104	30 \times (3+50)
2	2.952 \pm 0.003	46	13 \times (3+50)
3	5.952 \pm 0.003	18	5 \times (3+50)

Since this artefact is hardly distinguishable from statistical noise, it should not affect the further evaluation. Second, the noise threshold factors n'_σ and n''_σ are increased to 6 (instead of 4 in the previous measurements on the C/Ni-multilayer).

A resulting spectrum of single photon events with a fluorescence emission angle between 3.98° and 4.20° is shown in Figure 6.24. As mentioned in Section 5.5, the further computation of the GEXRF profiles can be performed by using a region of interest (ROI) or a proper deconvolution to obtain energy discrimination. Both is performed for the measurements on DM0149A to compare the resulting profiles, since the spectra show strong noise contribution, which can distort the GEXRF profiles. The ROIs are chosen as is indicated in Figure 6.24 with channels 75 to 90 for the O-K $_\alpha$ fluorescence and $x_0 \pm w$ for the Cu-L $_{l,n,\alpha,\beta}$ and pile-up peak, x_0 being the respective peak position and w the width (FWHM) of the peak. For the deconvolution, an exponentially decreasing background signal $A_n \exp(-x/t_n)$ is found empirically. The origin of this background is not clear, since rather a Gaussian noise peak (and thus a decrease with quadratic exponent) is expected. It could arise either from the split event recombination of noise, single photon and pile-up events, or from an additional noise contribution to the GEXRF frames by e.g. stray light, as is suspected to be present in Section 5.4.2. Therefore, it is difficult to judge, whether the background does or does not originate from fluorescence photons. A wrong treatment of the background could introduce artifacts to the GEXRF profile, especially to the low intensity line of O-K $_\alpha$. Nevertheless, assuming the empirical background model and 4 Gaussian shaped peaks for O-K $_\alpha$, Cu-L $_{l,n,\alpha,\beta}$ and two pile-up peaks, the whole spectrum can be fitted satisfactorily. In the implemented fitting routine, besides the slope t_n and the amplitude A_n of the exponentially decreasing background intensity, the intensities I_j , positions $x_{j,0}$ and widths Δx_j ($j \in \{0, 1, 2, 3\}$) of the Gaussian functions are chosen as free parameters. Width and position are set as free parameters to compensate for small variations of these (especially O-K $_\alpha$), probably induced by a variation of the noise contribution. The GEXRF profiles are then compiled by plotting the area in the ROIs, respectively of the Gaussian functions, against the

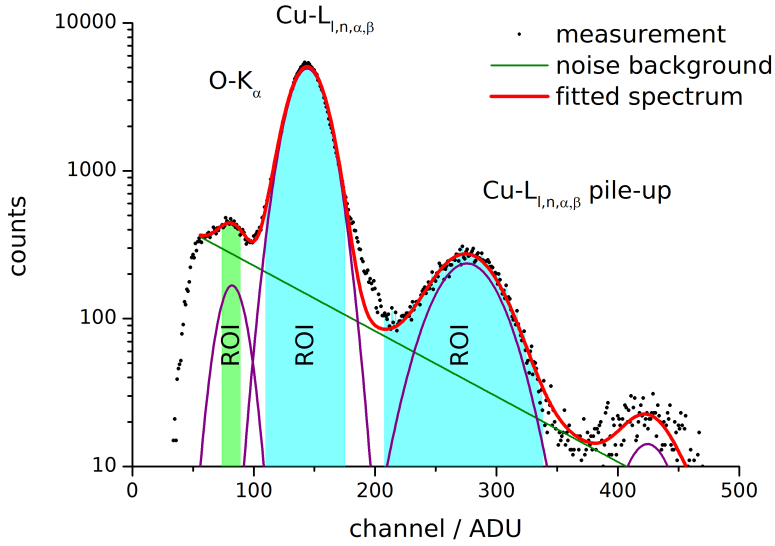


Figure 6.24.: Spectrum of DM0149A excited with 1078 eV photons of the LPP source and recorded with a conventional CCD. The fluorescence emission angle of the detected photons is between 3.98° and 4.20 degree. For the further computation of the GEXRF profiles, energy discrimination is achieved by using only the photons belonging to the ROIs as indicated or by deconvolution of the spectra with Gaussian functions and an exponentially decreasing background signal.

fluorescence emission angle. The pile-up signal of the first pile-up peak is added with twice its intensity to the Cu signal (since 2 photons contribute to a single pile-up event) for both the ROI and the deconvolution approach.

Figure 6.25 shows the O-K_α and Cu-L_{l,n,α,β} GEXRF profiles of the thermoelectric nanofilm DM0149A compiled with ROIs (a) and c)) on the one hand and using the deconvolution (b) and d)) on the other hand. The three subsequent measurements with rotated sample are concatenated by applying an intensity factor to the second and third measurement, so that the mean of an angular overlap of the profiles is the same. As can be seen, the angular resolution for the deconvolution approach is worse compared to the ROI evaluation, since a larger angular range (10× pixel resolution) is chosen to achieve better statistics in the deconvolved spectra. Furthermore, the Cu-L_{l,n,α,β} GEXRF profiles of both methods are very similar, since the high signal-to-noise ratio reduces the effect of the background treatment. However, the oxygen GEXRF profiles show distinct differences. While there is a maximum at about 5° in the deconvolution approach, no such feature is present in the evaluation with the ROI method. Such a maximum in a GEXRF profile can appear for thin layers of the fluorescing material, but

is not present in the calculations of 30 nm thick Cu₂O or CuO. Therefore, the layer from where the fluorescence radiation originates must be somewhat thinner. It could be an indication for a surface contamination of a few nm with high oxygen content or a highly oxidized thin surface layer (CuO) on top of less oxidized material (Cu_xO_{1-x}, $x > 0.5$). The errors given in the plots of Figure 6.25 refer to counting statistics only. Thus, the strong scattering of the data points in the O GEXRF profile using the deconvolution approach probably arises from the deconvolution itself. A better understanding of the background and more appropriate modeling might reduce this effect. For this purpose, a better energy resolution of the CCD camera should be envisaged.

When applying the N -layer model of Section 4.5.2 to the GEXRF measurements, the curves can be fitted simultaneously by varying the total layer thickness d^{tot} , the Cu atomic concentrations $x(n)$ and scaling factors for the fluorescence intensity s_{Cu} and s_{O} . The resulting GEXRF simulations for both evaluation methods, ROI and deconvolution, are also shown in Figure 6.25 for $N = 1, 2$ and 5 . Similar as for the GIXRF measurements in Section 4.5.2, the Cu signal can be well reproduced already with $N = 1$, apart from some overestimation above 8° . In the present data, counting statistics for the last measurement (above $\approx 6^\circ$) are comparatively large, so that the fit allows for the biggest deviation in that region. Probably, the actual discrepancy between model and data is rather in the low angular range and there caused by, e.g. the roughness of the sample or the rather simple density model (linear interpolation between bulk densities of Cu, Cu₂O and CuO) applied.

In the case of the O GEXRF profile, using at least 2 layers in the N -layer model seems to slightly increase the fit result. But still, for the evaluation using the ROI method (Figure 6.25 c)), the rise of the slope cannot be explained with the applied model. Since contributions from the noise peak to the O-K _{α} ROI are also likely, it is difficult to judge, whether the rise of the slope originates from the fluorescence intensity or from an evaluation artifact. The simulated and measured GEXRF profiles evaluated with the deconvolution approach are in better agreement to each other for $N > 1$. The maximum at about 5° is reproduced by the simulations and also the slope at shallow angles is in better agreement. But also here, the huge scattering of the data, which does not have to be statistically distributed and thus could conceal the actual shape of the GEXRF profile, makes any quantification using this data questionable.

Figure 6.26 summarizes the fitting results if only the rather trustworthy data of the Cu-L _{l,n,α,β} GEXRF profile (from the deconvolution) is used. As for the fits mentioned above, the simulated and measured GEXRF curves (Figure 6.26 a)) are in fair agreement, but some small deviations are present for all tested $N = 1, 2$ and 5 , probably because of the simplicity of the model. Interestingly, even though the O GEXRF profile is not fitted,

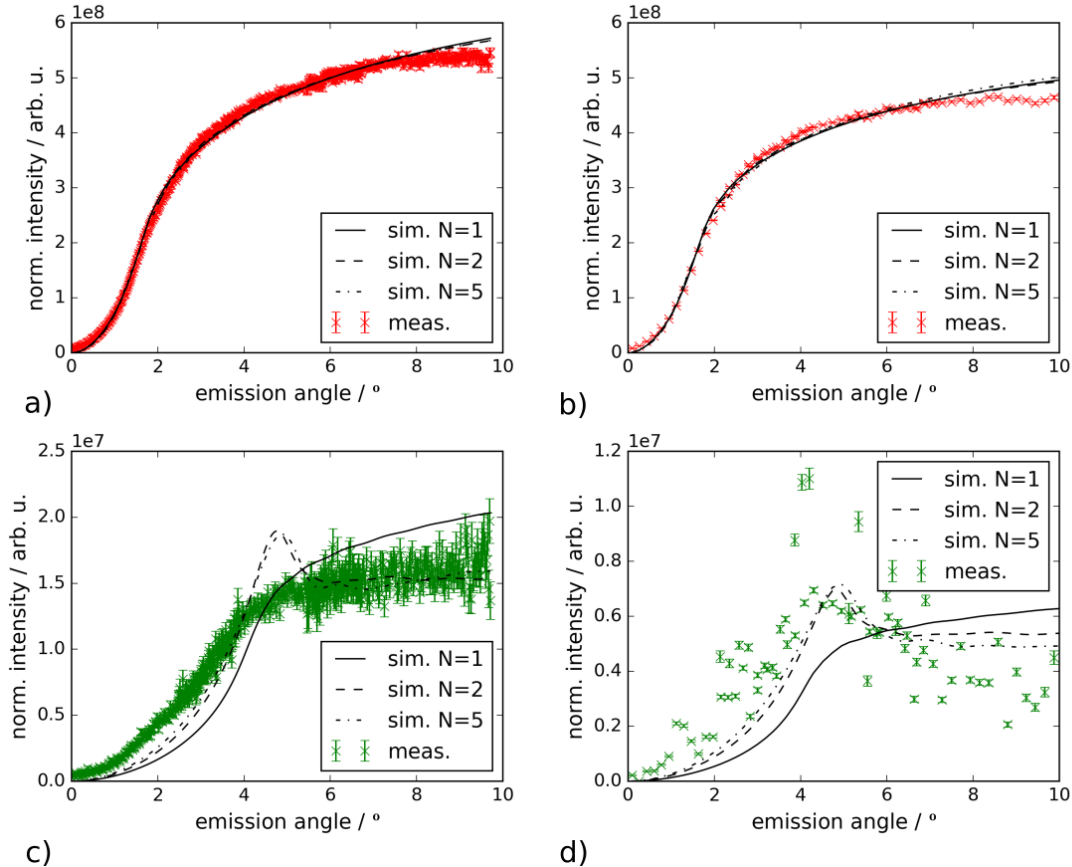


Figure 6.25.: a) and b) Cu- $L_{l,n,\alpha,\beta}$ and c) and d) O- K_α GEXRF profiles of the thermoelectric nanofilm DM0149A measured with the laboratory scanning-free GEXRF setup. The profiles are compiled out of 3 measurements, the second (3° - 7°) and third (6° - 10°) are scaled and concatenated to the first one (0° - 4°). The left side (a) and c)) show the results using ROIs and the right side (b) and d)) using a deconvolution approach for energy discrimination. Also shown are simulated GEXRF profiles from a fit result with the N -layer model (see text).

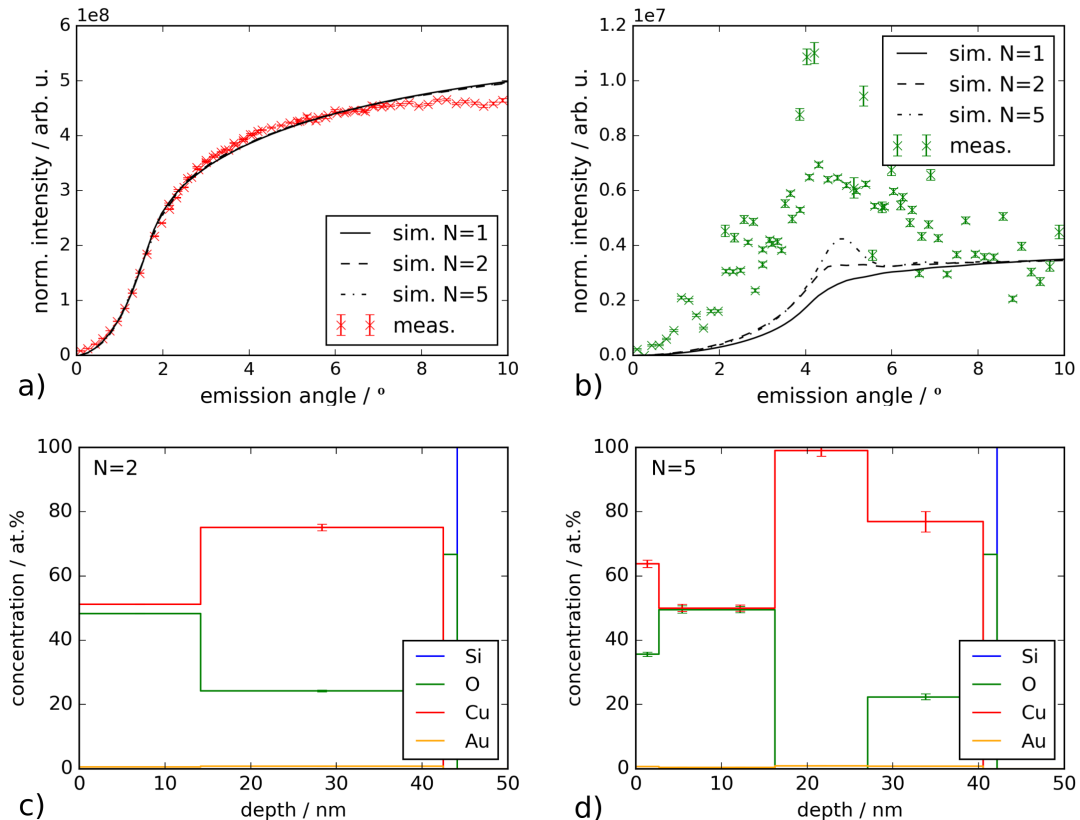


Figure 6.26.: a) Measured and simulated $\text{Cu-L}_{l,n,\alpha,\beta}$ GEXRF profiles using only the deconvolved Cu signal in the fit with the N -layer model. The same fit resulted in the O-K_α GEXRF profiles in b), which are normalized to the mean of the last 10 measurement points. c) and d) Results for the concentration profiles of the N -layer model with $N = 2$ and 5.

Table 6.10.: Fit results for the N -layer model using the Cu-L $_{l,n,\alpha,\beta}$ GEXRF profile from deconvolved spectra.

	$N = 1$	$N = 2$
$s_{\text{Cu}} / 10^{12}$	4.864 ± 0.010	4.63 ± 0.03
$d^{\text{tot}} / \text{nm}$	48.3 ± 0.2	42.5 ± 0.4
$x(1) / \text{at.\%}$	50.00 ± 0.07	51.16 ± 0.12
$x(2) / \text{at.\%}$	-	75.1 ± 1.1
$\hat{m}_{\text{Cu}} / (\text{ng} \times \text{cm}^{-2})$	24020 ± 80	24600 ± 300
$\hat{m}_{\text{O}} / (\text{ng} \times \text{cm}^{-2})$	5990 ± 20	3100 ± 30
$\hat{m}_{\text{Au}} / (\text{ng} \times \text{cm}^{-2})$	732 ± 3	751 ± 7

the fit of the Cu signal leads to a model, whose calculated O GEXRF profile exhibits some intensity maximum at about 5° for $N > 1$ (Figure 6.26 b)). As can be seen in Figure 6.26 c) and d), where the resulting concentration depth profile of the model is plotted for $N = 2$ and 5, the intensity maximum in the O GEXRF profile arises from a strong surface oxidation. This is qualitatively in agreement with the findings of the GIXRF-NEXAFS measurements in Section 4.4. Also, since only the Cu signal is fitted here, confusion with a signal from oxygen in contaminants on top of the surface, which is the case in the GIXRF study in Section 4.5.3, is unlikely. However, the quantitative values of the depth profile are questionable due to the simplicity of the model and the rather low sensitivity of the Cu GEXRF profile for such oxidation changes.

In Table 6.10, the fitted parameters and calculated mass depositions \hat{m} from the fitted model are listed. First of all, it should be mentioned again that the uncertainties given in the table are the estimates from the fitting procedure, which are only correct, if the applied model is correct and uncertainties in the data are purely Gaussian distributed. While the Poisson distribution of the counting error for large photon numbers is a good approximation to a Gaussian distribution, uncertainties due to the angular calibration for example are clearly not normal distributed. Furthermore, the simplicity of the model (limited number of layers, fixed density, no roughness) and uncertainties in the model from fundamental parameters and atomic scattering factors will surely lead to underestimated uncertainties from the fitting procedure. But as in Section 4.5.2, the uncertainties can be used to identify probable interferences in the chosen parameters, which are low in the present case.

The results of the total layer thickness d^{tot} for $N = 2$ are in agreement with the values obtained from the measurements at the PGM beamline (Section 4.5.2). On

the one hand, this is not surprising, since a similar model is used and GIXRF and GEXRF are based on the same physical principles. On the other hand, the result shows that a quantitative, reference-free approach for single layers is basically possible with laboratory based scanning-free GEXRF. The mass depositions of Cu, \hat{m}_{Cu} , are higher than the respective results from the integral quantification of the PGM beamline measurements ($\hat{m}_{\text{Cu}} = (18500 \pm 1300) \text{ ng/cm}^2$) and rather support again the results from the GIXRF approach ($\hat{m}_{\text{Cu}} = (20500 \pm 1200) \text{ ng/cm}^2$) and from the commercial setup ($\hat{m}_{\text{Cu}} = (22100 \pm 300) \text{ ng/cm}^2$, Chapter 3). The mass deposition for O, \hat{m}_{O} , agrees for $N=2$ much better with the results obtained from the integral quantification ($4300 \pm 900 \text{ ng/cm}^2$, Section 4.3), than the results for $N=1$, again indicating a better quality of the model with $N > 1$.

In contrast to the GIXRF measurements and fits in Section 4.5.2, the scaling factor s_{Cu} applied here does not only compensate for uncertainties in the fundamental parameters, but also for life time, detector efficiency and primary photon flux. Thus, with a life time of the first measurement of ≈ 750 s, a detector efficiency close to 1 and neglecting the uncertainties of the fundamental parameters, approximately 6×10^9 primary photons per second hit the sample in the toroidal focus. This is only 1 order of magnitude lower than the 4×10^{10} photons / s at a similar energy of 1060 eV during the measurements of the PGM beamline at BESSY II and demonstrates the performance of the laser-produced plasma source in combination with the toroidal mirrors. Furthermore, due to the application of the scanning-free GEXRF concept, a large solid angle of detection of 1.5×10^{-2} is achieved, allowing already in this early stage of development measurement times (3 hours) comparable to the synchrotron radiation based GIXRF measurements of the same sample (2 hours).

7. Summary

In this thesis, a laboratory spectrometer for soft X-ray fluorescence (XRF) measurements, using excitation with 1078 eV radiation, is successfully developed and established at the Berlin Laboratory for Innovative X-ray Technologies (BLiX). The presented measurements provide the first analytical XRF results obtained with a laser-produced plasma source in the soft X-ray range. It is shown that not only micro-XRF analysis is rendered feasible by applying a two-dimensional, energy-dispersive area detector in a single photon counting mode, but even elemental depth profiling in the nanometer regime is achieved via scanning-free, grazing emission (GE-) XRF measurements.

To render highly efficient, scanning-free GEXRF measurements possible, the sample-to-detector distance is minimized, which requires a precise knowledge of the detection geometry. Therefore, methodologies for the angular calibration based on the precise determination of sample-to-detector distances and tilt angles are developed, which additionally enables an absolute angular calibration. Furthermore, a part of the work focuses on the evaluation of soft X-ray single photon events (SPEs) detected with a conventional charge-coupled device (CCD). Due to the low signal-to-noise ratio at the low photon energies of soft X-rays, algorithms are developed to optimize the energy-dispersive properties of the CCD while maintaining the best possible efficiency in the evaluation process.

High stability, accuracy and reproducibility of setup and methodology are tested and confirmed by recording GEXRF profiles of a well-defined C/Ni-multilayer sample. Subsequently, the spectrometer is applied to thermoelectric gold-doped copper oxide nanofilms, demonstrating the relevance of the setup for research and development cycles of renewable energy sources.

In the following, the main results of the thesis concerning the setup development of the laboratory-based, scanning-free GEXRF spectrometer and the analytical findings of the gold-doped copper oxide nanofilms are discussed in some detail.

7.1. Methodological Development of the Laboratory Scanning-Free GEXRF Setup

The key components of the setup are a laser-produced plasma (LPP) source, providing highly brilliant radiation in the soft X-ray regime (1078 eV photons are used for XRF), efficient focusing multilayer optics with large solid angle of acceptance and a scanning-free approach utilizing a two-dimensional, energy-dispersive area detector. The latter maximizes the solid angle of detection and allows to circumvent pile-up due to the short LPP X-ray pulses of 1.2 ns, which prohibit the use of conventional energy-dispersive detectors. The scanning-free GEXRF setup described in this thesis is developed in several steps and tested in two beamtimes, i.e. BT1 and BT2.

In BT1, two reflective multilayer optics in Kirkpatrick-Baez (KB) geometry produce a $100 \times 500 \mu\text{m}^2$ spot in the sample plane. The sample is aligned by detecting the shadowing of the primary beam with an X-ray sensitive diode. For the detection of fluorescence measurements, a pnCCD is applied and the geometry of the setup defined by a combination of direct distance measurements and calibration with a reference GEXRF profile.

To demonstrate the feasibility of the setup and the alignment procedures, measurements on a C/Ni-multilayer sample with a one-dimensional thickness gradient are performed. The thickness of each of the 15 bilayers varies from 5 nm to 6 nm over a length of 40 mm. A single, integral (no angular discrimination) measurement is used to estimate a lower limit of detection (LLD) of 10^{-10} g, which is comparable to laboratory TXRF measurements. The bilayer thickness is determined by GEXRF measurements at 7 different positions, the measurement time for one position being 1-2 hours. Because of (at present) high uncertainties in the atomic scattering factors, it is not possible to use the whole GEXRF profile for the GEXRF evaluation*. Instead, the minimum position of the Kossel lines in the GEXRF profiles is exploited. The reproduced gradient is in good agreement with results from complementary measurements like X-ray reflectometry, transmission electron microscopy and conventional XRF[†].

In BT2, several setup and methodological improvements are developed. Instead of two one-dimensionally focusing multilayer optics in Kirkpatrick-Baez geometry, now two two-dimensionally focusing toroidal optics are applied. These optics reduce the focus excitation spot down to $100 \times 100 \mu\text{m}^2$ (BT2) while improving the photon flux

* Indeed, the energetic proximity of the L_α fluorescence line to the L_3 resonance, will complicate GEXRF measurements using the L_α fluorescence line for samples with main compositions of elements with $Z < 28$. On the other hand, the measurements could be used to gain access to the atomic scattering factors, if the sample composition and structure is well-known.

[†] Conventional XRF uses only one non-shallow incident and detection angle.

on the sample to about 10^9 photons/s due to a larger solid angle of acceptance and a more robust alignment. Furthermore, an optical alignment laser is implemented for sample alignment and to enable an accurate and reproducible measurement of the whole detection geometry. This allows an absolute angular calibration, which makes the typical use of a reference GEXRF profile (e.g. from a reference sample) for the angular calibration obsolete. Finally, instead of the complex and costly pnCCD, a conventional CCD is applied for SPE detection. The slow readout time of the CCD, which is at the moment the bottleneck for faster measurements, is overcompensated by the large increase of efficiency in the excitation channel. Therefore, measurement times applied to the C/Ni-multilayer sample are < 1 hour. The high accuracy and reproducibility of the absolute angular calibration are confirmed with independent angular calibrations on the same sample position of the C/Ni-multilayer sample.

To compile GEXRF profiles for different X-ray fluorescence lines (allowing compositional sensitivity), the energy discrimination of a CCD, when operated in a single photon counting mode, is used. In BT1, the single photon evaluation is performed by PNSensor, providing also the pnCCD detector for the measurements. However, with the conventional CCD in BT2, the SPE evaluation is more challenging due to increased noise level and severe splitting of the SPEs to more than one pixel. Therefore, various split event recombination methods are developed, characterized and compared, to optimize the energy resolution for the GEXRF measurements. For the applied detector, it is found that using a quadratic four-pixel box plus adjacent significant pixels yields the best compromise between resolving power and correct pile-up identification. The latter is important for correct GEXRF compilation when using the CCD at high count rates, allowing to reduce the measurement time. The resolving power achieved with the conventional CCD (≈ 3.4) is worse than with the pnCCD (7.5), because of higher CCD noise and larger charge cloud size. Simulations show that reducing both would significantly improve the resolving power, while especially the signal-to-noise ratio of every photon event is of importance. Probably the commercial CCD can be optimized for single photon detection in close cooperation with the manufacturer. Otherwise, an electron multiplying (EM) CCD, which can strongly increase the SNR in the soft X-ray range, might be a good compromise between enhanced energetic resolution and cost, while also allowing faster readout times.

Besides the SPE evaluation, also the operation of the LPP source must be adapted due to the utilization of the commercial CCD. Since readout times are in the order of seconds, a mechanical shutter is used during readout to prevent distortion of the CCD images. Blocking the seed laser pulse of the LPP laser system proves to be suitable to also reduce the sputter rate on the debris protection foils, while maintaining high stability of the X-ray focus in the sample plane. In combination with positive tests of

multiply using the copper target cylinder of the LPP source, maintenance shifts from once a day for two hours (BT1) are reduced to about 3 hours per week (BT2).

7.2. Thermoelectric Nanofilms

Two gold-doped copper oxide nanofilms are prepared in the research group of Prof. K. Rademann in the department of physical chemistry at the Humboldt University of Berlin. First, Au and Cu are simultaneously magnetron sputtered on a Si wafer. Then, one of the samples (DM0150A) is stored and oxidized in ambient conditions and the second sample (DM149A) is intentionally oxidized by tempering.

Characterization of the samples is accomplished by various laboratory-based and synchrotron radiation-based XRF methods. Conventional XRF mapping is performed with a commercially available device, revealing a slowly decreasing mass deposition \hat{m}_{Cu} of Cu towards the edges of the samples, caused by the non-uniformity of the plasma in the sputter coater. In a $2 \times 2 \text{ mm}^2$ area close to the center of the sample, \hat{m}_{Cu} is homogeneous within a 1% limit and the Au mass deposition \hat{m}_{Au} within at least 10% for both samples. For a more accurate statement concerning \hat{m}_{Au} , statistics could be increased in future measurements with measurement times of several days, which is possible for a laboratory setup. With the conventional setup, a first estimation of the layer thickness yields $\approx 25 \text{ nm}$ for both samples when assuming bulk densities for Cu. However, to get access to the mass deposition of oxygen, the oxidation state of copper and elemental depth profiling capabilities of the nanofilms, further analysis with synchrotron radiation (SR) is applied.

All SR-based measurements are performed at the laboratories of the Physikalisch Technische Bundesanstalt (PTB) at the synchrotron radiation facility BESSY II in Berlin. The oxidation state of Cu in the nanofilms is qualitatively investigated by near edge X-ray absorption fine structure (NEXAFS) analysis at the Cu-L₃ edge in combination with different shallow incident angles to vary the excitation depth. As reference, NEXAFS spectra of pure Cu₂O and CuO are measured and compared to literature data. The initially strong deviations due to self-absorption effects are reduced by normalizing the Cu-L _{α,β} to the O-K _{α} fluorescence intensity and the same procedure is used for the angular dependent NEXAFS scans. As expected, the main contribution to the NEXAFS spectra of the non-treated sample DM0150A is Cu₂O, showing the oxidation of the gold-doped Cu layer due to exposure to ambient conditions. For the tempered sample DM0149A, surface-near regions probed at the shallowest incident angles display main contributions of CuO, indicating the progressed oxidation because of thermal activation. However, for larger depths Cu₂O is dominant, revealing that only a surface-near region

is affected by the further oxidation.

To get more quantitative information about the depth dependent concentration profiles for Au, Cu and O, GIXRF measurements are performed at two different beamlines, providing access to Cu-L_{α,β}, O-K_α and C-K_α on the one hand and Cu-K_α and Au-M_α on the other hand. The GIXRF profiles of Cu-K_α and Au-M_α are found to be similar in the limits of the methods' sensitivity, indicating a similar depth distribution. As for the GIXRF measurements at larger wavelengths, severe surface contamination is found. In a three-step evaluation process with increasing complexity of the applied model of the sample, it is shown that the surface contamination prohibits accurate reconstruction of the oxygen depth profile due to interferences of the O-K_α signal from the contamination and the gold-doped copper oxide layers. Furthermore, a misalignment of the sample increases the uncertainties of the effective solid angle of detection for shallow angles below 1.5°, decreasing the sensitivity of the depth profiles. This prevents reliable statements concerning the elemental depth profiles from the Cu-L_{α,β} GIXRF profiles.

Nevertheless, the measurements are used to obtain information about the contaminants. By using additionally the C-K_α GIXRF profile, a model for the contamination is found, which can reproduce the measurements (within their uncertainties). According to these findings, the GIXRF signal of the contaminants originates from larger particles with diameters of several 100 nm. Furthermore, on the measurement spot of DM0150A one particle or a few particles with diameters in the micrometer range are present. The detection of similar particle sizes in atomic force micrographs of the thermoelectric nanofilm surfaces supports this model. According to the GIXRF measurements, these particles do not only contain carbon, but also oxygen and are thus probably consisting of organic compounds and water. For the tempered sample DM0149A, a further contribution to the C-K_α GIXRF signal from C implemented in the gold-doped copper oxide nanofilm has to be assumed. To find further evidence of C implemented in the thermoelectric nanofilm, and if this contamination is introduced during the tempering process, future measurements could be performed with in-vacuum sample preparation, storage and transfer to the beamline. Studies on potential positive or negative effects of carbon implementation into the nanofilms with respect to the thermoelectric behavior could also be envisaged. The whole study on contamination illustrates the importance of sample preparation for precise measurements and the benefits of short feedback loops from analysis to sample preparation and development.

Finally, the thermoelectric nanofilm DM0149A is analyzed in BT2 with the laboratory scanning-free GEXRF spectrometer developed in this thesis. Because of the high efficiency of the laboratory scanning-free GEXRF setup, measurement times for the analysis of the thermoelectric nanofilms are about 3 hours, which is well in the range of

7. SUMMARY

the applied measurement times of 2 hours at the synchrotron radiation facility. Yet, the rather small oxygen signal in combination with the low energy resolution and large noise peak of the conventional CCD makes spectrum evaluation challenging. Therefore, not only a region of interest (ROI) method is chosen to compile the GEXRF profiles, but also a deconvolution of the angular dependent spectra is pursued. It is found that some additional noise contribution, probably due to stray light in the spectroscopy chamber, has to be considered and needs to be further analyzed for future measurements. Both O-K_α GEXRF profiles (ROI and deconvolution approach) are subject to distortions and thus not used in a depth profiling approach. However, when applying the sample model of the GIXRF measurements to the Cu-L_{α,β} GEXRF profiles, evidence for surface oxidation is found and the calculated (not fitted) O-K_α GEXRF profile shows similarities to the measured O-K_α GEXRF profiles using the deconvolution approach.

The GEXRF measurements on the thermoelectric gold-doped copper oxide nanofilms demonstrate the applicability of the spectrometer to a scientific case with relevance for renewable energy sources.

From the measurements at BESSY II and from the laboratory measurements at BLiX, several quantification results for the mass depositions of O, Cu and Au in the thermoelectric nanofilms are obtained. Table 7.1 summarizes the findings for A) conventional XRF with a commercially available spectrometer (Section 3.2), B) and C) conventional SR-based XRF in the soft and hard X-ray regime (Section 4.3), D) SR-based GIXRF in the soft X-ray regime (Section 4.5, using additional information about the Au-to-Cu ratio from B)) and E) GEXRF with the laboratory scanning-free GEXRF spectrometer at BLiX from Section 6.3.4.

First, it has to be mentioned again, that the uncertainties should be understood as lower limits. The uncertainties of B) and C) can be directly traced to uncertainty estimations of the well-characterized measurement equipment of the PTB and the uncertainties of the applied fundamental parameters (FPs). The latter are also only estimated values from [100] and [99] and can easily be over- or underestimated, especially in the soft X-ray range. In D) and E), the influence of the fundamental parameters, on which the calculated fluorescence intensity depends linearly (i.e. the FPs in $\xi_{i,j,s}(E_{\text{pr}})$ in Equation 2.1.1) is canceled out by a fitting parameter, which explains the low values of the uncertainties. However, modeling and fitting is necessary and the given uncertainties for D) and E) are retrieved from the estimated covariance matrix of the fit. This alone is not quite accurate as is described throughout the thesis, since the models are probably no sufficient description of the sample. Particularly the influence of uncertainties in the FPs and atomic scattering factors would need thorough investigations. Thus, the small uncertainties in E) mainly originate from the good counting statistics and neglect the

Table 7.1.: Summary of the quantification results of the thermoelectric nanofilms. A) conventional XRF (laboratory), B) conventional SR-based XRF in the hard X-ray regime (KMC and BAMline beamlines), C) conventional SR-based XRF in the soft X-ray regime (PGM and information from B)), D) SR-based GIXRF (PGM and BAMline beamlines), E) laboratory-based, scanning-free GEXRF.

	mass deposition \hat{m}_i / (ng×cm ⁻²)					
	DM0150A			DM0149A		
	Cu	O	Au	Cu	O	Au
A)	23600±300	-	600±300	22100±300	-	600±300
B)	18900±1400	-	580±80	18500±1300	-	560±80
C)	18000±5000	3800±800	600±170	18000±5000	4300±900	560±160
D)	22600±800	3490±110	740±90	20500±1200	3350±200	620±80
E)	-	-	-	24020±80	5990±20	732±3

above-mentioned effects. Indeed, further validation of uncertainties obtained by fitting approaches of GIXRF and GEXRF measurements is a challenge for the still maturing methodology in the future. Probably using (time consuming) statistical methods like bootstrapping as is mentioned in Section 2.4.2 in combination with uncertainty validation (through standard samples) can lead to more reliable uncertainty estimates. As for A), FP modeling of the sample is applied and uncertainties of the FPs should be included. Yet, how accurate the overall uncertainties are for arbitrary samples is not known by the user.

In principle, all quantification approaches in Table 7.1 lead to similar values for the mass depositions of Cu, O and Au and no large outliers are obtained. For copper, \hat{m}_{Cu} is about 20000 ng cm⁻² for both samples DM0150A and DM0149A and probably slightly larger for DM0150A, originating from the sputtering process. The oxygen and gold mass depositions \hat{m}_{O} and \hat{m}_{Au} are about 4000 ng cm⁻² and 600 ng cm⁻², respectively. From the quantification measurements, it is difficult to judge, whether, and how much, additional oxygen is incorporated into the copper oxide nanofilm by the tempering process. The best evidence for an oxygen increase is given by C) in the direct comparison of the O signal, but this could also originate from contaminants.

If using a part of the GEXRF profile for the quantification of a single layer, as in E), and when applying superior techniques for the determination of reliable uncertainties (e.g. bootstrapping, validation of uncertainties with reference materials), reference-free thin film analysis can be performed even without a fully calibrated setup. This might be also one of the future applications for the laboratory scanning-free GEXRF setup developed in this thesis. A second possibility to perform quantitative measurements

could be the use of the integral spectrum of the CCD and thorough calibration of the setup by monitoring the X-ray flux variation and using standard samples. Then, also quantitative micro-XRF mapping in the soft X-ray regime could be envisaged.

7.3. Future Perspective

Large-scale synchrotron radiation facilities provide highly brilliant X-ray beams over a wide spectral range, which can be optimized with respect to spatial or energetic resolution for individual experiments. However, access to beamlines is usually restricted and the process of beamtime application can be time-consuming and its success uncertain for routine investigations during the development of novel materials. Clearly, there is a need for reliable, sensitive and readily available laboratory setups, which can perform similar analysis.

The laboratory scanning-free GEXRF spectrometer developed in this thesis applies high-efficiency concepts for the utilized source, optics, detector and detection geometry. This results in already competitive GEXRF measurement times as compared to SR-based GIXRF for the analysis of elemental depth profiles in nanofilm materials. Additionally, further development in LPP sources, optics and methodology can be expected. In the future, this possibly leads to a wider availability of this or a similar spectrometer concept to support research and development processes and advancements in e.g. renewable energy sources.

With respect to the present scanning-free GEXRF setup, specific scientific questions with relevance for thin film solar cells could be approached. For example, the investigation of copper depletion close to the surface (below 100 nm) of Cu(In,Ga)Se₂ absorbers or diffusion processes in perovskite thin films of only 70 nm thickness are envisaged.

Furthermore, the measurement principle of the scanning-free GEXRF spectrometer and the methodologies implemented for a precise sample alignment and angular calibration can be transferred to applications with other excitation sources. By using X-ray or electron nanoprobe in synchrotron radiation facilities or electron microscopes, the combination of nanometer lateral and in-depth resolution could be possible. Such a device might further enable the characterization and development of nano-structured devices, which until now is challenging with modern GIXRF analysis [137, 138]. On the other hand, the application of an X-ray tube in the excitation channel would result in an overall effective and low-cost GEXRF spectrometer (if using the conventional CCD) with excellent angular and good energy resolution. Such a device, due to the relatively low cost, could even further expand the availability of non-destructive depth profiling to a wider user community.

Appendix

A. Angular Limits of the Sherman Equation

The Sherman equation after solving the integral yields

$$\begin{aligned}
 N_{i,j} &= N_{\text{pr}}(E_{\text{pr}}) G(E_{i,j}) \xi_{i,j,s}(E_{\text{pr}}) C_i \frac{1 - \exp(-\mu_{\text{tot}}^*(E_{\text{pr}}, E_{\text{fl}})\rho d)}{\mu_{\text{tot}}^*(E_{\text{pr}}, E_{\text{fl}})}, \text{ with} \\
 G(E_{i,j}) &= \epsilon_{\text{det}}(E_{i,j}) \frac{\Omega}{4\pi \sin(\psi_{\text{pr}})} \\
 \xi_{i,j,s}(E_{\text{pr}}) &= \tau_{i,s}(E_{\text{pr}}) \omega_{i,s} p_{i,j} \\
 \mu_{\text{tot}}^* &= \frac{\mu_{\text{tot}}(E_{\text{pr}})}{\sin(\psi_{\text{pr}})} + \frac{\mu_{\text{tot}}(E_{i,j})}{\sin(\psi_{\text{fl}})}
 \end{aligned} \tag{A.1}$$

and the notation as in Section 2.1.1.

For reasons of simplicity let hereafter $\epsilon_{\text{det}}(E_{i,j}) = 1$, $\Omega = 1$ and $N_{\text{pr}}(E_{\text{pr}}) = 1$ photon/s. Furthermore, a single element layer is considered. Then, for incident or emission angles approaching zero it follows

$$\psi_{\text{pr}} \rightarrow 0 : \mu_{\text{tot}}^*(E_{\text{pr}}, E_{\text{fl}}) \rightarrow \frac{\mu_{\text{tot}}(E_{\text{pr}})}{\sin(\psi_{\text{pr}})} \tag{A.2}$$

$$\psi_{\text{fl}} \rightarrow 0 : \mu_{\text{tot}}^*(E_{\text{pr}}, E_{\text{fl}}) \rightarrow \frac{\mu_{\text{tot}}(E_{i,j})}{\sin(\psi_{\text{fl}})} \tag{A.3}$$

which further leads in Equation A.1 to

$$\begin{aligned}
 \psi_{\text{pr}} \rightarrow 0 : N_{i,j} &\approx \frac{1}{4\pi \sin(\psi_{\text{pr}})} \xi_{i,j,s}(E_{\text{pr}}) \frac{1 - \exp\left(-\frac{\mu_{\text{tot}}(E_{\text{pr}})}{\sin(\psi_{\text{pr}})}\rho d\right)}{\frac{\mu_{\text{tot}}(E_{\text{pr}})}{\sin(\psi_{\text{pr}})}} \\
 &\approx \frac{1}{4\pi} \frac{\xi_{i,j,s}(E_{\text{pr}})}{\mu_{\text{tot}}(E_{\text{pr}})}
 \end{aligned} \tag{A.4}$$

for shallow incident angles and similar

$$\begin{aligned}
 \psi_{\text{fl}} \rightarrow 0 : N_{i,j} &\approx \frac{1}{4\pi \sin(\psi_{\text{pr}})} \xi_{i,j,s}(E_{\text{pr}}) \frac{1 - \exp\left(-\frac{\mu_{\text{tot}}(E_{i,j})}{\sin(\psi_{\text{fl}})}\rho d\right)}{\frac{\mu_{\text{tot}}(E_{i,j})}{\sin(\psi_{\text{fl}})}} \\
 &\approx \frac{\sin(\psi_{\text{fl}})}{4\pi \sin(\psi_{\text{pr}})} \frac{\xi_{i,j,s}(E_{\text{pr}})}{\mu_{\text{tot}}(E_{i,j})}
 \end{aligned} \tag{A.5}$$

for shallow detection angles.

B. Atomic Force Micrographs of the Silicon Substrate for the Thermoelectric Nanofilms

Figure B.1 shows 2 sections of an AFM image. The white lines mark height jumps of a few nm. Such structures are also visible on the copper oxide nanofilms, as well as similar particles due to (organic) contamination. The root mean squared roughness (RMS) in an area without particles (lower white square in right image) is 1.2 nm and thus similar to the value of the thermoelectric samples (≈ 1 nm).

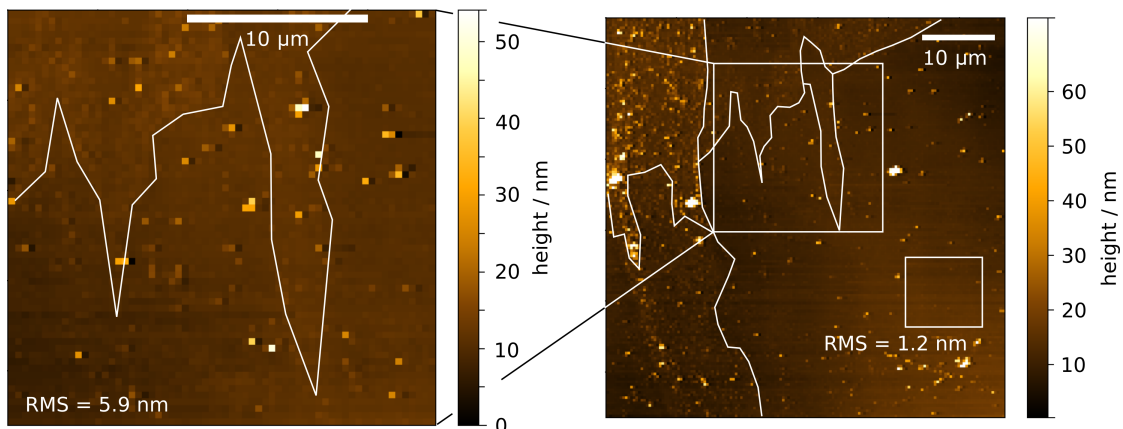


Figure B.1.: Atomic force microscopic image of a blank Si wafer similar to those used for the thermoelectric nanofilms.

C. Estimation of Uncertainties for Fluorescence Calculations

Table C.1 lists the applied uncertainties used for the quantification in reference-free XRF measurements.

Table C.1.: Estimated uncertainties for the fluorescence yield ω , transition probability p and attenuation coefficient μ from [99, 100] and for the geometric factor G from [42].

	C-K $_{\alpha}$	O-K $_{\alpha}$	Cu-L $_{\alpha}$	Cu-K $_{\alpha}$	Au-L $_{\alpha}$
$\Delta\omega/\omega$	20%	20%	25%	3%	3%
$\Delta p/p$	2%	2%	2%	2%	2%
$\Delta\mu/\mu$	2%	2%	2%	5%	2%
$\Delta G/G$	3%	3%	3%	3%	3%
total	21%	21%	26%	7%	6%

D. Effective Solid Angle of Detection for an Off-Axis Sample Surface

Figure D.1 a) sketches, how the footprint size can be taken into account when calculating the effective solid angle of detection for a GIXRF measurement with SDD. The footprint is approximated by a two-dimensional Gaussian profile in the sample plane. The profile is discretized by $N \times M$ positions and for every position the solid angle of the detector $\Omega_{N,M}$ is calculated using the formulas of [67]. The effective solid angle of detection Ω is then the Gaussian-weighted sum of the partial solid angles $\Omega_{N,M}$.

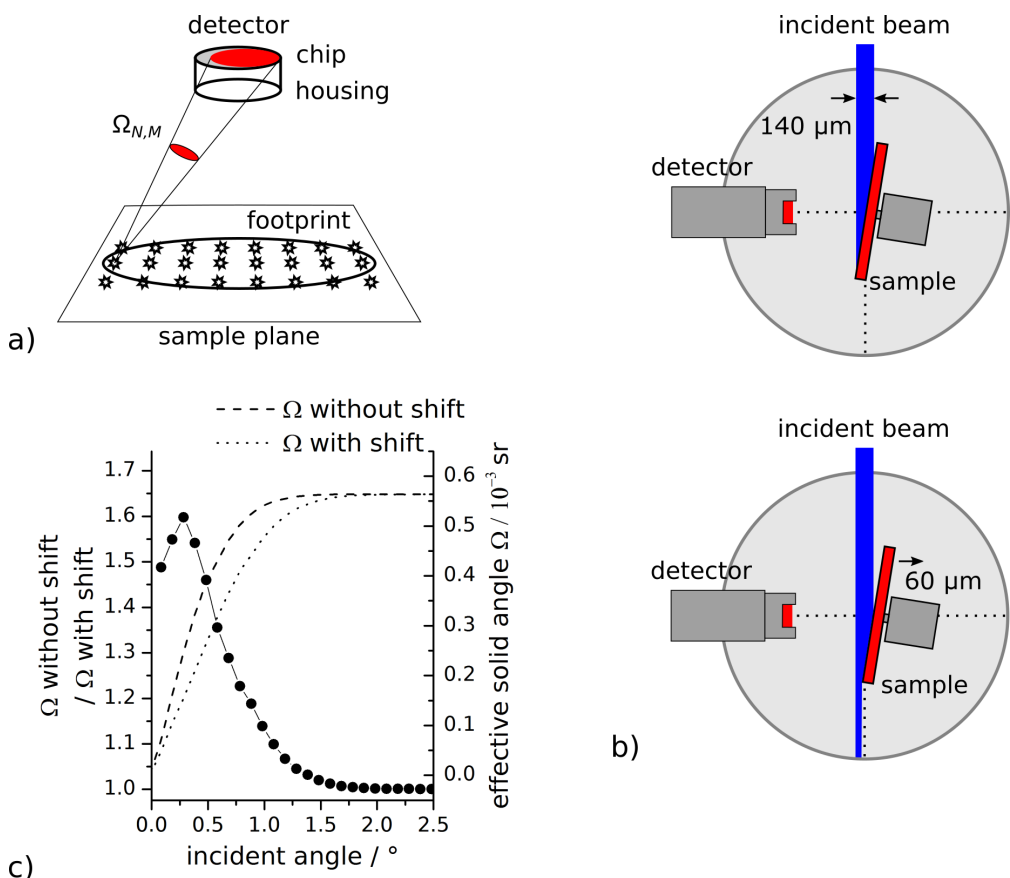


Figure D.1.: a) Sketch of how the effective solid angle of detection is calculated. b) Setup geometry with aligned sample (top) and misalignment of 60 μm (bottom). c) Calculated effective solid angles of detection and relative differences for shallow angles.

With this approach, the effective solid angle is calculated for the measurement geometry used in Section 4.5 once with perfectly aligned sample and once with a sample misalignment by 60 μm from the rotational axis (Figure D.1 b)). The relative difference for the effective solid angle of detection is plotted in Figure D.1 c).

E. Estimation of Efficiency of GI- and GEXRF Spectrometer Concepts

In the following, the solid angle of acceptance of a multilayer optics in the excitation channel of a spectrometer is estimated. The spectrometer shall utilize the laser plasma interaction chamber of the BLiX LPP source and the spectrometer chamber for sample positioning. Thus, the distance from source to optics and from optics to sample needs to be about $d = 550$ mm due to setup restrictions. The surface area of the multilayer optics is 200×25 mm².

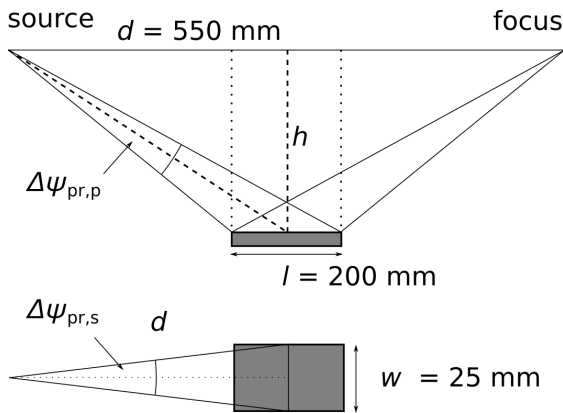


Figure E.1.: Schematic view of a multilayer optics applied to collect radiation from the LPP source.

In the case of parallelizing optics for GIXRF measurements, let the distance of the optics to the connecting line source-focus h be 1 mm (Figure E.1). Then

$$\begin{aligned} \Delta\psi_{\text{pr,p}} &= \arctan\left(\frac{h}{d - 0.5l}\right) - \arctan\left(\frac{h}{d + 0.5l}\right) \\ &= 0.04^\circ , \end{aligned} \quad (\text{E.1})$$

which is a reasonable value for the angular divergence for GIXRF experiments.

For the solid angle of acceptance, the second opening angle $\Delta\psi_{\text{pr,s}}$ (in the plane of projection in Figure E.1 bottom) is also of importance. This angle can be estimated by the width of the optics w and the distance d via

$$\Delta\psi_{\text{pr,s}} = 2 \arctan\left(\frac{0.5w}{d}\right) \approx 2.6^\circ \quad (\text{E.2})$$

With the two opening angles, the projected area A of the optics is calculated with

$$A = 2 d \tan(0.5 \Delta\psi_{\text{pr,p}}) \times 2 d \tan(0.5 \Delta\psi_{\text{pr,s}}) \quad (\text{E.3})$$

and the solid angle of acceptance $\Omega_{\text{opt}}^{\text{GI}}$

$$\Omega_{\text{opt}}^{\text{GI}} = \frac{A}{d^2} \approx 3.1 \times 10^{-5} \text{ sr} \quad (\text{E.4})$$

In the case of focusing optics for GEXRF measurements, a shallow incident angle with respect to the optics surface of $\approx 7.8^\circ$ and $h = 75$ mm is feasible. Indeed, these are the values applied for the Kirkpatrick-Baez and toroidal multilayer optics utilized in the GEXRF setup. Then, a similar approach as above yields $\Delta\psi_{\text{pr,p}} = 2.9^\circ$ and the solid angle of acceptance is

$$\Omega_{\text{opt}}^{\text{GI}} \approx 2.3 \times 10^{-3} \text{ sr} , \quad (\text{E.5})$$

which is about 75 times larger than in the grazing incidence case.

F. Effect of Tilted CCD on Distance Calculation

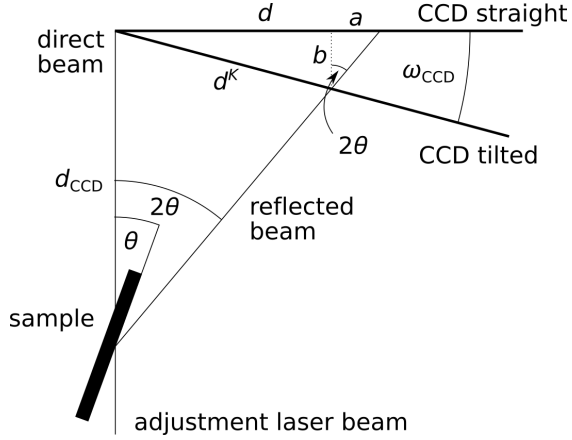


Figure F.1.: Schematic view of the distance calculation for a tilted CCD.

To calculate correctly the distance $d^K(\theta)$ of the reflected laser beams to the direct laser beam for a tilt angle θ of the sample and a tilt angle ω_{CCD} of the CCD, consider Figure F.1. Then, the following three trigonometric functions hold:

$$d^K(\theta) = \frac{b}{\sin(\omega_{\text{CCD}})} \quad (\text{F.1})$$

$$d^K(\theta) = \frac{d(\theta) - a}{\cos(\omega_{\text{CCD}})} \quad (\text{F.2})$$

$$a = b \tan(2\theta) \quad (\text{F.3})$$

with notation as in Figure F.1. Further, using Equation F.1 in F.3 yields:

$$a = d^K(\theta) \sin(\omega_{\text{CCD}}) \tan(2\theta) \quad (\text{F.4})$$

Using the result in Equation F.4 in F.2 leads to

$$d^K(\theta) = \frac{d(\theta)}{\cos(\omega_{\text{CCD}})} - d^K(\theta) \tan(\omega_{\text{CCD}}) \tan(2\theta), \quad (\text{F.5})$$

which is identical to the final expressions

$$\begin{aligned} d^K(\theta) &= d(\theta) \times (K(\omega_{\text{CCD}}, \theta))^{-1}, \text{ with} \\ K(\omega_{\text{CCD}}, \theta) &= \cos(\omega_{\text{CCD}}) + \sin(\omega_{\text{CCD}}) \tan(2\theta). \end{aligned} \quad (\text{F.6})$$

G. Study on the Influence of Noise Thresholds on CCD Spectra using the Clustering Method

As can be seen in Figure G.1, both noise thresholds $n'_\sigma \times \sigma_{\text{meas}}$ and $n''_\sigma \times \sigma_{\text{meas}}$ have a huge influence on the integral spectra evaluated with the Clustering method. In the top row, n'_σ is varied from 2 to 6. This shifts the sharp low-energy cut-off to photon event intensities $n'_\sigma \times \sigma_{\text{meas}}$ (rows). An increase of n''_σ leads to a red-shift of the fluorescence peak and pile-up peak, thus to a compressed energy scale (columns).

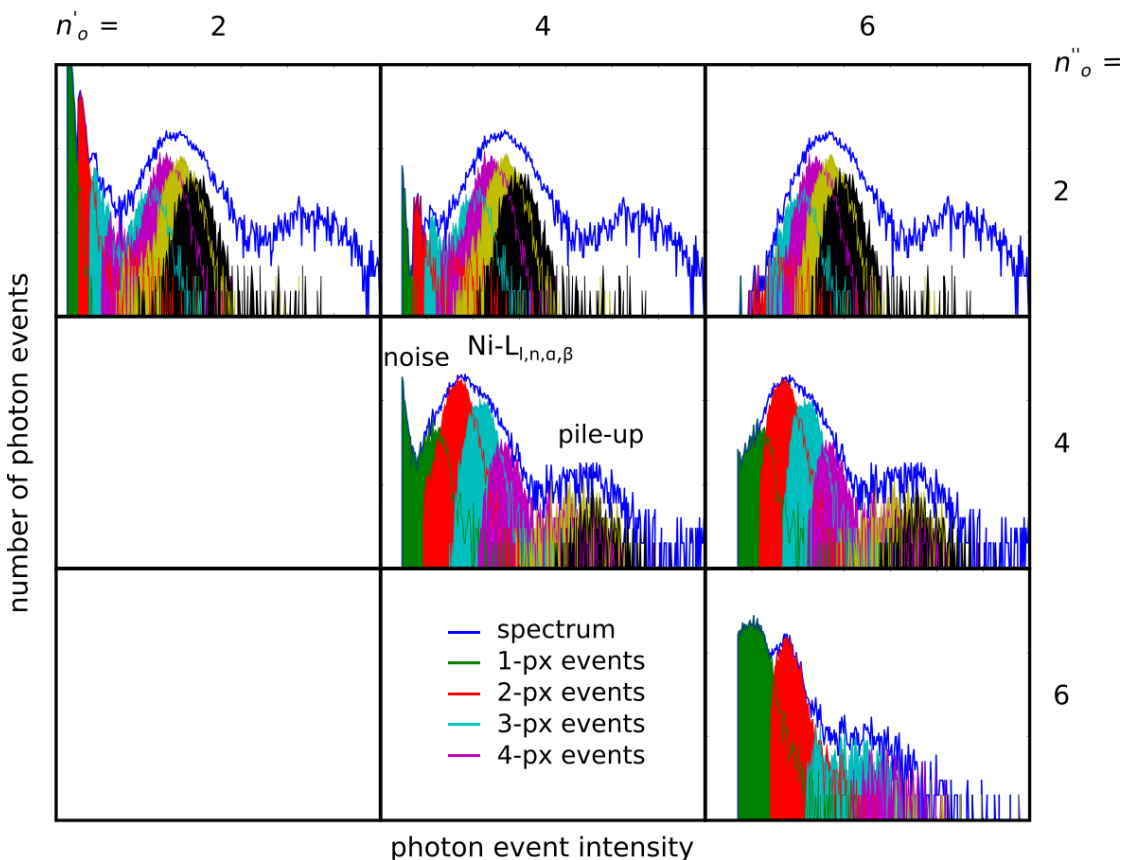


Figure G.1.: Integral spectra of the C/Ni-multilayer evaluated with the Clustering method.
Spectra computed with various noise thresholds are shown.

It is also seen in Figure G.1, that the peaks in the various $n\text{-px}$ spectra are shifted by a constant value. Examination of the peak intensity positions suggests that this shift is just $n \times n''_\sigma \times \sigma_{\text{meas}}$. The interpretation is, that with every additional pixel contributing to the SPE cluster, a mean value of approximately the second noise threshold $n''_\sigma \times \sigma_{\text{meas}}$ is added to the SPE cluster intensity. More precisely, this is the minimum value added to the cluster intensity, but it is also the most likely (noise) value, since higher pixel

intensities due to noise become more and more unlikely.

As can be seen in Figure G.2 a) and b), a correction for this offset leads indeed to a narrower peak. However, the peak is also strongly red-shifted and the resolving power of 2.56 is only slightly increased with respect to the resolving power of 2.44 of the untreated spectrum. The ratio of the peak positions of the fluorescence peak and the first pile-up peak is in Figure G.2 a) 1.49 and in b) 1.55, indicating a probably non-linear compression of the energy scale.

A similar effect is also present in the spectra evaluated with the 4px-Area-Clustering method used in the evaluation procedures in this thesis. Because of the drastic treatment of the spectra and the low resolution enhancement, a correction of n -px spectra positions is not performed there. Nevertheless, in the future, this effect could be further investigated.

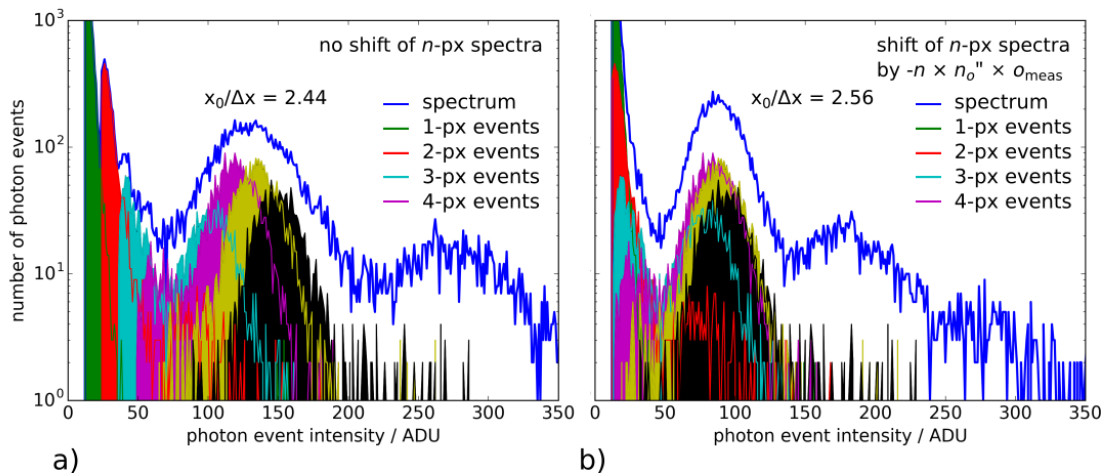


Figure G.2.: Comparison of the spectra from Figure G.1 with $n_\sigma' = n_\sigma'' = 2$ once with and once without shifting the n -px spectra.

H. Simulated Intensity Distribution of SPEs on a CCD Mesh

If a single photon is detected by a CCD camera, the charge collected in the potential minimum below the pixel structure is Gaussian-distributed in two dimensions (in the chip plane). Let the center position of the charge cloud with peak intensity A and widths σ_x and σ_y be (x_c, y_c) . The pixels are quadratic in the chip plane and have an edge length p . Then, integrating the two-dimensional Gaussian function over a pixel with center at (x', y') yields

$$I(x', y') = \int_{x' - \frac{p}{2}}^{x' + \frac{p}{2}} \int_{y' - \frac{p}{2}}^{y' + \frac{p}{2}} A \exp\left(-\frac{(x - x_c)^2}{2\sigma_x^2} - \frac{(y - y_c)^2}{2\sigma_y^2}\right) dx dy . \quad (\text{H.1})$$

The integral can be solved for the x and y coordinate separately, while the procedure is the same for both.

$$I(x', y') = \int_{x' - \frac{p}{2}}^{x' + \frac{p}{2}} A \exp\left(-\frac{(x - x_c)^2}{2\sigma_x^2}\right) dx \times \dots . \quad (\text{H.2})$$

Now, using the error function with codomain from -1 to 1 leads to

$$\begin{aligned} I(x', y') &= A 0.5 \left[1 + \operatorname{erf}\left(\frac{x - x_c}{\sqrt{2} \sigma_x}\right) \right]_{x' - \frac{p}{2}}^{x' + \frac{p}{2}} \times \dots \\ &= A 0.5 \left(\operatorname{erf}\left(\frac{x' + \frac{p}{2} - x_c}{\sqrt{2} \sigma_x}\right) - \operatorname{erf}\left(\frac{x' - \frac{p}{2} - x_c}{\sqrt{2} \sigma_x}\right) \right) \\ &\quad \times 0.5 \left(\operatorname{erf}\left(\frac{y' + \frac{p}{2} - y_c}{\sqrt{2} \sigma_y}\right) - \operatorname{erf}\left(\frac{y' - \frac{p}{2} - y_c}{\sqrt{2} \sigma_y}\right) \right) . \end{aligned} \quad (\text{H.3})$$

The final equation and the relation of the Gaussian peak intensity A with the number of charges in the charge cloud size (volume)

$$I_{\text{ph}} = 2\pi A \sigma_x \sigma_y \quad (\text{H.4})$$

is then used for the calculation of charges in every pixel of the CCD. Note that for the applied simulations $\sigma_x = \sigma_y = \sigma_{\text{cc}}$ is set. The intensities in the simulation are rounded to more physical natural numbers. This introduces a small noise, since no special care is taken to control that the integral over the whole pixel plane is indeed I_{ph} .

I. Choose ROIs

For setting the regions of interest (ROIs) for the evaluation of the Ni-L_{*l,n*} and the Ni-L_{*α,β*} GEXRF profiles in the first beamtime, the integral spectrum of a measurement (no angular discrimination) is considered. The spectrum between 600 eV and 1000 eV is fitted with two Gaussian functions for the Ni-L_{*l,n*} line and the Ni-L_{*α,β*} line, respectively. The result is shown in Figure I.1. The limits of the ROIs where then chosen in such a way that the intensity of the fitted Gaussian functions for the Ni-L_{*l,n*} and the Ni-L_{*α,β*} line are 99.6% and 80% of the total intensity at the corresponding limit. This results in a fraction of 94.1% of Ni-L_{*l,n*} fluorescence photons in the Ni-L_{*l,n*} ROI and 97.7% of Ni-L_{*α,β*} fluorescence photons in the Ni-L_{*α,β*} ROI. It has to be noted, firstly, that the Ni-L_{*n*} line and the Ni-L_{*β*} line are not resolved and are neglected together with further background contributions due to their low influence. Secondly, the intensity ratios of the Ni-L_{*l,n*} and Ni-L_{*α,β*} line change with the emission angle according to the grazing emission X-ray fluorescence profiles. Therefore, also the given numbers for the actual photon ratios in each of the ROIs might vary slightly, depending on the emission angle.

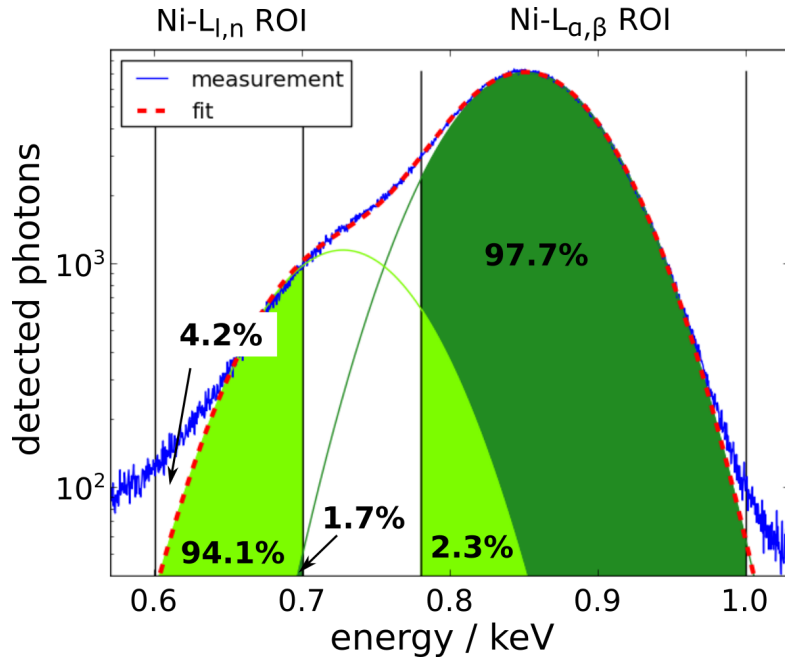


Figure I.1.: Section of the integral X-ray fluorescence spectrum of the first beamtime used for the definition of the regions of interest for the Ni-L_{*l,n*} and the Ni-L_{*α,β*} line.

J. Sample Alignment with a CCD

The radial sample alignment with an optical adjustment laser is performed by successively moving the sample into the laser beam and recording the beam intensity on the CCD, as is shown in Figure J.1 a). The intensity of the direct laser beam on the CCD will decrease due to increased shadowing of the beam. To evaluate the laser beam intensity on the CCD during the measurements, the intensity of every image in the scan is summed in a box of approximately 40 pixel width (Figure J.1 b). This already produces small variations in the reproducibility, since the box position is manually defined for every sample alignment. Figure J.1 c) shows the intensities of a radial scan for different box sizes. As can be seen in the plot on top and in the derivative at the bottom, the curves shift with the box size by about almost 100 μm for the shown box size range. Interestingly, the minimum position in the derivative plot does not change for large pixel boxes, suggesting that the effect originates from incomplete intensity summation. The difference between the minimum position applied in the measurements and the probably more accurate position obtained with large pixel boxes is about 50 μm . For future measurements, the evaluation with a two-dimensional Gaussian fit or fit with an Airy disk should also be tested.

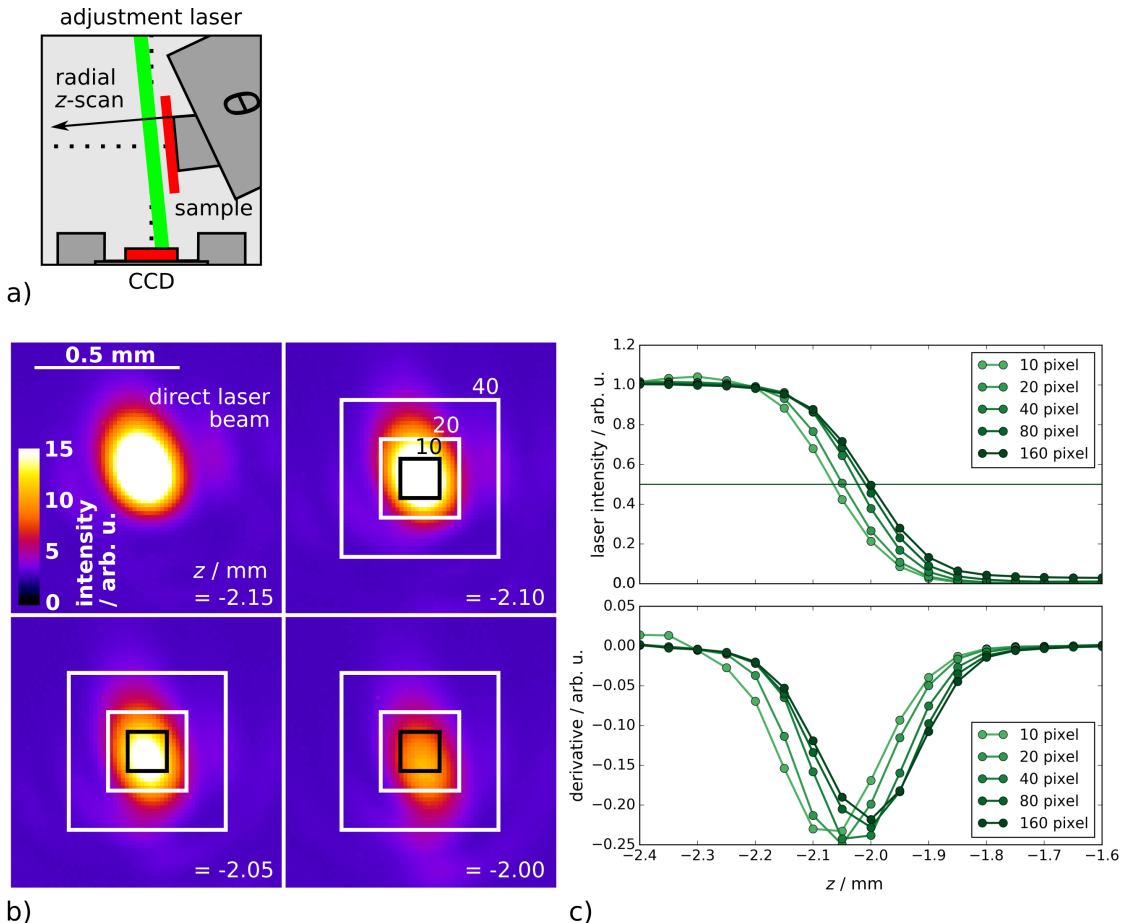


Figure J.1.: a) The principle of the radial scans is similar to a knife-edge scan. b) CCD images of the direct laser beam for 4 different radial positions of the sample. The intensity drops because of the increased shadowing of the laser beam by the sample. c) the laser intensity in the CCD image is integrated in a quadratic box. In a) such boxes with edge sizes of 10, 20 and 40 pixels are exemplarily shown.

List of Figures

2.1.	Electron configuration and X-ray transitions for Cu.	8
2.2.	ARXRF profiles of thin Cu layers from Sherman equation.	11
2.3.	X-ray reflectivities for vacuum-to-CuO and CuO-to-Si interface.	14
2.4.	XSW field intensity in front of and in a 30 nm thick CuO layer on a Si substrate.	15
2.5.	GI- and GEXRF profiles of thin Cu layers.	16
2.6.	CCD principle.	20
2.7.	SPE image of commercial CCD.	21
2.8.	Equi-angle lines on CCD chip.	23
2.9.	Geometric effects on angular resolution.	24
2.10.	Calculated degradation of angular resolution.	25
2.11.	Photograph of the copper cylinder in the plasma interaction chamber. . .	32
2.12.	Excitation with the LPP source.	33
3.1.	Photograph and schematic view of magnetron sputter coater.	36
3.2.	AFM image of a gold-doped copper oxide nanofilm.	37
3.3.	XRF maps of gold doped copper oxide nanofilms.	39
3.4.	XRF maps (small) of gold doped copper oxide nanofilms.	40
4.1.	Schematic view of the vacuum chambers of the PTB.	45
4.2.	Energy-dispersive spectra of sample DM0149A.	47
4.3.	Sample model used for the integral quantification.	52
4.4.	Cu-L ₃ NEXAFS of CuO and Cu ₂ O.	55
4.5.	Angular dependent Cu-L ₃ NEXAFS of thermoelectric nanofilms.	56
4.6.	O-K _α , Cu-K _α and Au-M _α GIXRF of thermoelectric nanofilms.	58
4.7.	C-K _α , O-K _α and Cu-L _{α,β} GIXRF of thermoelectric nanofilms.	60
4.8.	Schematic of the 1-layer model used in the fitting procedure of the GIXRF profiles.	61
4.9.	Simulated and measured GIXRF profiles of Cu and O for the copper oxide nanofilms using the 1-layer model.	62
4.10.	Schematic illustration of the <i>N</i> -layer model with increasing sublayer thickness.	64

LIST OF FIGURES

4.11. Simulated and measured GIXRF profiles of Cu and O for the copper oxide nanofilms using the <i>N</i> -layer model.	65
4.12. Zoom of the GIXRF profiles evaluated with the <i>N</i> -layer model.	68
4.13. Evaluated GIXRF profiles of Cu and O for the copper oxide nanofilms using the <i>N</i> -layer model with contamination.	70
4.14. Sketch of the <i>N</i> -layer model with contamination.	71
4.15. Evaluated GIXRF profiles of C and O for the copper oxide nanofilms using the <i>N</i> -layer model with contamination.	72
5.1. Schematic setup for the laboratory scanning-free soft X-ray GEXRF measurements.	80
5.2. Laser and plasma stability for 3 hours of LPP operation.	81
5.3. Vacuum setup and positioning stages for the reflective multilayer optics. .	83
5.4. Schematic view of spectroscopy chamber and sample manipulator at BLiX	85
5.5. Alignment of the toroidal optics foci into the pivotal point of the goniometer.	87
5.6. Figure 5.5 continued.	89
5.7. Schematic top view of the spectroscopy chamber with the optical alignment laser.	91
5.8. Schematic view of the GEXRF measurement geometry and definition of the geometric parameters.	95
5.9. Measuring the CCD tilt with the optical alignment laser.	96
5.10. CCD images of a θ scan for the absolute angular calibration.	97
5.11. Data and fits for the absolute angular calibration.	98
5.12. Single photon events detected with a CCD camera.	101
5.13. Histogram of master dark frame and clean GEXRF frame.	101
5.14. Principle of split event recombination methods.	104
5.15. Energy-dispersive spectra created with the three SPE recombination methods	105
5.16. Histogram of SPE types and SPE type share in total spectrum.	106
5.17. Comparison of the evaluation with the three SPE recombination methods.	109
5.18. Spectrum of SPE evaluation with the 4px-Area-Clustering method. . . .	111
5.19. Spectrum evolution for variation of several parameters.	112
5.20. Increase of resolving power when σ_{cc} or σ_{dark} are reduced.	114
5.21. Evaluation chart describing the computation of GEXRF profiles.	117
6.1. C/Ni-multilayer structure and bilayer thickness	120
6.2. Ni-L $_{\alpha,\beta}$ and Ni-L $_{l,n}$ GEXRF profiles of the C/Ni-multilayer sample. . . .	123
6.3. Footprint size and impact on the angular resolution.	126
6.4. Photograph of the specimen holder.	127

6.5.	Intensity scans for sample alignment.	129
6.6.	Energy calibration for the pnCCD.	130
6.7.	XRF spectra of the C/Ni-multilayer in the soft X-ray range	131
6.8.	Results of final iteration step for the angular calibration.	135
6.9.	Distribution of fluorescence emission angles and solid angles of detection on the pnCCD chip.	137
6.10.	Simulated and measured GEXRF profiles of the C/Ni-multilayer.	138
6.11.	Database values for the atomic scattering factors.	139
6.12.	Measured GEXRF profiles for all 7 measurement points.	140
6.13.	Simulated minimum positions of the C/Ni-multilayer GEXRF profiles. .	141
6.14.	Bilayer thickness results for the C/Ni-multilayer sample.	142
6.15.	Stability investigation of the toroidal focus width and position	145
6.16.	Intensity of the two superimposed toroidal mirror foci and impact on the angular resolution	147
6.17.	Influence on toroidal focus position and size if using the target of the LPP source several times.	148
6.18.	GP results obtained with 8 different angular calibrations.	150
6.19.	Sample holder as it is used in the second beamtime.	152
6.20.	Distribution of fluorescence emission angles and solid angle of detections on the conventional CCD chip	153
6.21.	Integral spectra of the C/Ni-multilayer for various noise thresholds.	155
6.22.	Normalized GEXRF profiles of Ni-L fluorescence of the C/Ni-multilayer. .	156
6.23.	Results of the bilayer thickness of the C/Ni-multilayer.	158
6.24.	Spectrum of DM0149A excited with 1078 eV photons.	161
6.25.	Cu-L _{l,n,α,β} and O-K _α GEXRF profiles of DM0149A.	163
6.26.	Fit results of GEXRF profiles and concentration profiles for DM0149A. .	164
B.1.	AFM image of a Si wafer.	177
D.1.	Effect of sample misalignment on effective solid angle of detection. . . .	178
E.1.	Schematic view of a multilayer optics applied to collect radiation from the LPP source.	179
F.1.	Schematic view of the distance calculation for a tilted CCD.	181
G.1.	Integral spectra of the C/Ni-multilayer evaluated with the Clustering method.	182
G.2.	Effect of shifting the n-px spectra.	183
I.1.	Section of the integral XRF spectrum used for the definition of the ROIs in the first beamtime.	185
J.1.	Evaluation of radial scans with the sample into the adjustment laser beam.187	

List of Tables

3.1.	Quantification results of the thermoelectric nanofilms with Fischerscope. . .	38
4.1.	Quantification results of the thermoelectric nanofilms from hard X-ray SR. .	50
4.2.	Quantification results of the thermoelectric nanofilms with soft X-ray SR. .	51
4.3.	Parameters and settings for the non-linear least square fit in the N -layer model.	65
4.4.	Results of the fitted parameters for the N -layer model.	66
4.5.	Fit results of the approach with the N -layered model with contamination. .	73
5.1.	Evaluation of the resolving power for the Ni-L _{α} peak.	108
6.1.	GEXRF measurement positions and C/Ni-bilayer nominal thickness.	128
6.2.	Estimated LLDs from an integral spectrum of the C/Ni-multilayer.	132
6.3.	GPs determined with various methods.	133
6.4.	Result of the angular calibration procedure with reference sample.	136
6.5.	Effect of sample parameter variation on the GEXRF profiles' minimum position.	139
6.6.	Size (FWHM) and position of the focus spot from measurements in Figure 6.17.	148
6.7.	Results of the absolute angular calibration.	151
6.8.	CCD settings and resolving power	154
6.9.	Measurement parameters for the GEXRF measurements on the thermoelectric nanofilms.	160
6.10.	Fit results for the N -layer model	165
7.1.	Summary of the quantification results of the thermoelectric nanofilms. . .	173
C.1.	Estimated uncertainties of the applied FPs	177

Nomenclature

ADU	analog/digital unit
AFM	atomic force microscopy
ARXRF	angular resolved X-ray fluorescence
BESSY	Berlin Electron Storage Ring Society for Synchrotron Radiation (Ger.: Berliner Elektronenspeicherring-Gesellschaft für Synchrotronstrahlung)
BLiX	Berlin Laboratory for Innovative X-ray Technologies
BT	beamtime
CCD	charge-coupled device
CMOS	complementary metal-oxide-semiconductor
FP	fundamental parameter
FWHM	full width at half maximum
GD-OES	glow-discharge optical emission spectrometry
GEXRF	grazing emission X-ray fluorescence
GIXRF	grazing incidence X-ray fluorescence
GP	geometric parameter
IPCC	Intergovernmental Panel on Climate Change
KB	Kirkpatrick-Baez
LLD	lower limit of detection
LPP	laser-produced plasma
NEXAFS	near edge X-ray absorption fine structure
PGM	plane-grating monochromator
PTB	national metrology institute of Germany (Ger.: Physikalisch-Technische Bundesanstalt)
ROI	region of interest
RRS	resonant Raman scattering
SDD	silicon drift detector
SIMS	secondary ion mass-spectrometry
SNR	signal-to-noise ratio

NOMENCLATURE

SPE	single photon event
SR	synchrotron radiation
TEG	thermoelectric generator
TEM	transmission electron microscopy
TXRF	total reflection X-ray fluorescence
XRF	X-ray fluorescence
XRR	X-ray reflectometry
XSW	X-ray standing wave
Yb:YAG	ytterbium:yttrium aluminum garnet

Bibliography

- [1] Intergovernmental Panel on Climate Change, World Meteorological Organization, and United Nations Environment Programme, *Climate change: The 1990 and 1992 IPCC assessments, IPCC First Assessment Report overview, policymaker summaries and 1992 IPCC supplement*. Geneve: IPCC, 1992.
- [2] J. T. Houghton, ed., *Climate Change 1995: IPCC Second Assessment Report, The science of climate change (IPCC)*. Cambridge and New York: Cambridge University Press, 1998.
- [3] J. T. Houghton, ed., *The scientific basis; contribution of Working Group I to the Third Assessment Report of the Intergovernmental Panel on Climate Change*. Climate change 2001, Cambridge: Cambridge Univ. Press, 2001.
- [4] S. Solomon, D. Qin, M. Manning, Z. Chen, M. Marquis, K.B. Averyt, M.Tignor, and H.L. Miller, eds., *Summary for Policymakers: The Physical Science Basis - Contribution of Working Group I to the Fourth Assessment Report of the Intergovernmental Panel on Climate Change*. Cambridge, United Kingdom and New York, NY, USA: Cambridge University Press, 2007.
- [5] Core Writing Team, R.K. Pachauri and L.A. Meyer, ed., *Climate change 2014: Synthesis report - Contribution of Working Groups I, II and III to the Fifth Assessment Report of the Intergovernmental Panel on Climate Change*. Geneva, Switzerland: IPCC, 2015.
- [6] Edenhofer, Edenhofer, Ottmar, Ipcc, & Intergovernmental Panel on Climate Change Ueberordnung, *Renewable energy sources and climate change mitigation: Special report of the Intergovernmental Panel on Climate Change [SRREN]*. Cambridge [u.a.]: Cambridge Univ. Press, 1. publ ed., 2012.
- [7] Z. Abdin, M. A. Alim, R. Saidur, M. R. Islam, W. Rashmi, S. Mekhilef, and A. Wadi, “Solar energy harvesting with the application of nanotechnology,” *Renewable and Sustainable Energy Reviews*, vol. 26, pp. 837–852, 2013.
- [8] J. P. Rojas, D. Singh, S. B. Inayat, G. A. T. Sevilla, H. M. Fahad, and M. M. Hussain, “Review—Micro and Nano-Engineering Enabled New Generation of Thermo-electric Generator Devices and Applications,” *ECS Journal of Solid State Science and Technology*, vol. 6, no. 3, pp. N3036–N3044, 2017.

- [9] M. Collinet-Fressancourt, N. Nuns, S. Bellayer, and M. Traisnel, “Characterization by TEM and ToF-SIMS of the oxide layer formed during anaphoretic paint electrodeposition on Al-alloys,” *Applied Surface Science*, vol. 277, pp. 186–191, 2013.
- [10] F. Pianezzi, S. Nishiwaki, L. Kranz, C. M. Sutter-Fella, P. Reinhard, B. Bissig, H. Hagendorfer, S. Buecheler, and A. N. Tiwari, “Influence of Ni and Cr impurities on the electronic properties of Cu(In,Ga)Se₂ thin film solar cells,” *Progress in Photovoltaics: Research and Applications*, vol. 23, no. 7, pp. 892–900, 2015.
- [11] P. Sanchez, B. Fernández, A. Menéndez, D. Gómez, R. Pereiro, and A. Sanz-Medel, “A path towards a better characterisation of silicon thin-film solar cells: depth profile analysis by pulsed radiofrequency glow discharge optical emission spectrometry,” *Progress in Photovoltaics: Research and Applications*, pp. 1246–1255, 2013.
- [12] D. Abou-Ras, R. Caballero, C.-H. Fischer, C. A. Kaufmann, I. Lauermann, R. Mainz, H. Möning, A. Schöpke, C. Stephan, C. Streeck, S. Schorr, A. Eicke, M. Döbeli, B. Gade, J. Hinrichs, T. Nunney, H. Dijkstra, V. Hoffmann, D. Klemm, V. Efimova, A. Bergmaier, G. Dollinger, T. Wirth, W. Unger, A. A. Rockett, A. Perez-Rodriguez, J. Alvarez-Garcia, V. Izquierdo-Roca, T. Schmid, P.-P. Choi, M. Müller, F. Bertram, J. Christen, H. Khatri, R. W. Collins, S. Marsillac, and I. Kötschau, “Comprehensive comparison of various techniques for the analysis of elemental distributions in thin films,” *Microscopy and microanalysis : the official journal of Microscopy Society of America, Microbeam Analysis Society, Microscopical Society of Canada*, vol. 17, no. 5, pp. 728–751, 2011.
- [13] C. Streeck, B. Beckhoff, F. Reinhardt, M. Kolbe, B. Kanngießer, C. A. Kaufmann, and H. W. Schock, “Elemental depth profiling of Cu(In,Ga)Se₂ thin films by reference-free grazing incidence X-ray fluorescence analysis,” *Nuclear Instruments and Methods in Physics Research Section B: Beam Interactions with Materials and Atoms*, vol. 268, no. 3-4, pp. 277–281, 2010.
- [14] B. Caby, F. Brigidì, D. Ingerle, E. Nolot, G. Pepponi, C. Streli, L. Lutterotti, A. André, G. Rodriguez, P. Gergaud, M. Morales, and D. Chateigner, “Study of annealing-induced interdiffusion in In₂O₃/Ag/In₂O₃ structures by a combined X-ray reflectivity and grazing incidence X-ray fluorescence analysis,” *Spectrochimica Acta Part B: Atomic Spectroscopy*, vol. 113, pp. 132–137, 2015.
- [15] T. Noma, H. Miyata, and S. Ino, “Grazing exit x-ray fluorescence spectroscopy for thin-film analysis,” *Jpn. J. Appl. Phys. (Japanese Journal of Applied Physics)*, vol. 31, no. 7A, pp. 900–903, 1992.
- [16] H. J. Sánchez and C. A. Pérez, “Study of copper surface oxidation by grazing angle

- X-ray excitation,” *Spectrochimica Acta Part B: Atomic Spectroscopy*, vol. 65, no. 6, pp. 466–470, 2010.
- [17] P. Hönicke, B. Beckhoff, M. Kolbe, D. Giubertoni, van den Berg, Jaap, and G. Pepponi, “Depth profile characterization of ultra shallow junction implants,” *Analytical and bioanalytical chemistry*, vol. 396, no. 8, pp. 2825–2832, 2010.
- [18] Y. Kayser, P. Hönicke, D. Banaś, J.-C. Dousse, J. Hoszowska, P. Jagodziński, A. Kubala-Kukuś, S. H. Nowak, and M. Pajek, “Depth profiling of low energy ion implantations in Si and Ge by means of micro-focused grazing emission X-ray fluorescence and grazing incidence X-ray fluorescence,” *J. Anal. At. Spectrom.*, vol. 30, no. 5, pp. 1086–1099, 2015.
- [19] M. Müller, P. Hönicke, B. Detlefs, and C. Fleischmann, “Characterization of High-k Nanolayers by Grazing Incidence X-ray Spectrometry,” *Materials*, vol. 7, no. 4, pp. 3147–3159, 2014.
- [20] Y. Kayser, J. Sá, and J. Szlachetko, “Nanoparticle characterization by means of scanning free grazing emission X-ray fluorescence,” *Nanoscale*, vol. 7, no. 20, pp. 9320–9330, 2015.
- [21] de Bokx, P. K. and H. P. Urbach, “Laboratory grazing-emission x-ray fluorescence spectrometer,” *Review of Scientific Instruments*, vol. 66, no. 1, p. 15, 1995.
- [22] R. D. Pérez and H. J. Sánchez, “New spectrometer for grazing exit x-ray fluorescence,” *Review of Scientific Instruments*, vol. 68, no. 7, pp. 2681–2684, 1997.
- [23] A. Kubala-Kukuś, D. Banaś, W. Cao, J.-C. Dousse, J. Hoszowska, Y. Kayser, M. Pajek, M. Salomé, J. Susini, J. Szlachetko, and M. Szlachetko, “Observation of ultralow-level Al impurities on a silicon surface by high-resolution grazing emission x-ray fluorescence excited by synchrotron radiation,” *Physical Review B*, vol. 80, no. 11, 2009.
- [24] Y. Kayser, J. Szlachetko, and J. Sà, “Scanning-free grazing emission x-ray fluorescence by means of an angular dispersive arrangement with a two-dimensional position-sensitive area detector,” *Review of Scientific Instruments*, vol. 84, no. 12, p. 123102, 2013.
- [25] J. Weber, K. Potje-Kamloth, F. Haase, P. Detemple, F. Völklein, and T. Doll, “Coin-size coiled-up polymer foil thermoelectric power generator for wearable electronics,” *Sensors and Actuators A: Physical*, vol. 132, no. 1, pp. 325–330, 2006.
- [26] D. Crane, J. LaGrandeur, V. Jovovic, M. Ranalli, M. Adldinger, E. Poliquin, J. Dean, D. Kossakovski, B. Mazar, and C. Maranville, “TEG On-Vehicle Performance and Model Validation and What It Means for Further TEG Development,” *Journal of Electronic Materials*, vol. 42, no. 7, pp. 1582–1591, 2013.

BIBLIOGRAPHY

- [27] T. Kuroki, R. Murai, K. Makino, K. Nagano, T. Kajihara, H. Kaibe, H. Hachiuma, and H. Matsuno, “Research and Development for Thermoelectric Generation Technology Using Waste Heat from Steelmaking Process,” *Journal of Electronic Materials*, vol. 44, no. 6, pp. 2151–2156, 2015.
- [28] D. Coster and R. D. L. Kronig, “New type of auger effect and its influence on the x-ray spectrum,” *Physica*, vol. 2, no. 1-12, pp. 13–24, 1935.
- [29] J. Sherman, “The theoretical derivation of fluorescent X-ray intensities from mixtures,” *Spectrochimica Acta*, vol. 7, pp. 283–306, 1955.
- [30] B. Beckhoff, B. Kanngießer, N. Langhoff, R. Wedell, and H. Wolff, *Handbook of practical X-ray fluorescence analysis*. Berlin and New York: Springer, ©2006.
- [31] de Boer, D. K. G., “Calculation of x-ray fluorescence intensities from bulk and multilayer samples,” *X-Ray Spectrometry*, vol. 19, no. 3, pp. 145–154, 1990.
- [32] W. T. Elam, B. D. Ravel, and J. R. Sieber, “A new atomic database for X-ray spectroscopic calculations,” *Radiation Physics and Chemistry*, vol. 63, no. 2, pp. 121–128, 2002.
- [33] H. Ebel, R. Svagera, M. F. Ebel, A. Shaltout, and J. H. Hubbell, “Numerical description of photoelectric absorption coefficients for fundamental parameter programs,” *X-Ray Spectrometry*, vol. 32, no. 6, pp. 442–451, 2003.
- [34] P. K. de Bokx, C. Kok, A. Bailleul, G. Wiener, and H. P. Urbach, “Grazing-emission X-ray fluorescence spectrometry; principles and applications,” *Spectrochimica Acta Part B: Atomic Spectroscopy*, vol. 52, no. 7, pp. 829–840, 1997.
- [35] D. T. Attwood, *Soft x-rays and extreme ultraviolet radiation: Principles and applications*. Cambridge: Cambridge University Press, 1999.
- [36] R. Klockenkämper and A. von Bohlen, *Total-reflection X-ray fluorescence analysis and related methods*, vol. 181 of *Chemical analysis*. Hoboken, NJ: Wiley, 2. ed. ed., 2015.
- [37] de Boer, D. K. G., “Glancing-incidence x-ray fluorescence of layered materials,” *Physical Review B*, 1991.
- [38] J. D. Jackson, *Klassische Elektrodynamik*. De Gruyter Studium, Berlin: de Gruyter, 5. aufl. ed., 2014.
- [39] B. L. Henke, E. M. Gullikson, and J. C. Davis, “X-Ray Interactions: Photoabsorption, Scattering, Transmission, and Reflection at $E = 50\text{--}30,000 \text{ eV}$, $Z = 1\text{--}92$,” *Atomic Data and Nuclear Data Tables*, vol. 54, no. 2, pp. 181–342, 1993.
- [40] C. T. Chantler, “Theoretical Form Factor, Attenuation, and Scattering Tabulation for $Z=1\text{--}92$ from $E=1\text{--}10 \text{ eV}$ to $E=0.4\text{--}1.0 \text{ MeV}$,” *Journal of Physical and Chemical Reference Data*, vol. 24, no. 1, p. 71, 1995.

- [41] L. G. Parratt, "Surface Studies of Solids by Total Reflection of X-Rays," *Physical Review*, vol. 95, no. 2, pp. 359–369, 1954.
- [42] B. Beckhoff, R. Fliegauf, M. Kolbe, M. Müller, J. Weser, and G. Ulm, "Reference-free total reflection X-ray fluorescence analysis of semiconductor surfaces with synchrotron radiation," *Analytical chemistry*, vol. 79, no. 20, pp. 7873–7882, 2007.
- [43] C. Streeck, S. Brunken, M. Gerlach, C. Herzog, P. Hönicke, C. A. Kaufmann, J. Lubeck, B. Pollakowski, R. Unterumsberger, A. Weber, B. Beckhoff, B. Kanningießer, H.-W. Schock, and R. Mainz, "Grazing-incidence x-ray fluorescence analysis for non-destructive determination of In and Ga depth profiles in Cu(In,Ga)Se₂ absorber films," *Applied Physics Letters*, vol. 103, no. 11, p. 113904, 2013.
- [44] H. P. Urbach and de Bokx, P. K., "Calculation of intensities in grazing-emission x-ray fluorescence," *Physical Review B*, vol. 53, no. 7, pp. 3752–3763, 1996.
- [45] R. S. Becker, J. A. Golovchenko, and J. R. Patel, "X-Ray Evanescent-Wave Absorption and Emission," *Phys. Rev. Lett.*, vol. 50, no. 3, pp. 153–156, 1983.
- [46] M. Wu, K. Le Guen, J.-M. André, V. Ilakovac, I. Vickridge, D. Schmaus, E. Briand, S. Steydli, C. Burcklen, F. Bridou, E. Meltchakov, S. de Rossi, F. Delmotte, and P. Jonnard, "Kossel interferences of proton-induced X-ray emission lines in periodic multilayers," *Nuclear Instruments and Methods in Physics Research Section B: Beam Interactions with Materials and Atoms*, vol. 386, pp. 39–43, 2016.
- [47] J. Szlachetko, D. Banaś, A. Kubala-Kukuś, M. Pajek, W. Cao, J.-C. Dousse, J. Hoszowska, Y. Kayser, M. Szlachetko, M. Kavčič, M. Salome, and J. Susini, "Application of the high-resolution grazing-emission x-ray fluorescence method for impurities control in semiconductor nanotechnology," *Journal of Applied Physics*, vol. 105, no. 8, p. 086101, 2009.
- [48] L. Strüder, P. Holl, G. Lutz, and J. Kemmer, "Device modeling of fully depletable CCDs," *Nuclear Instruments and Methods in Physics Research Section A: Accelerators, Spectrometers, Detectors and Associated Equipment*, vol. 253, no. 3, pp. 386–392, 1987.
- [49] E. Pinotti, H. Bräuninger, N. Findeis, H. Gorke, D. Hauff, P. Holl, J. Kemmer, P. Lechner, G. Lutz, W. Kink, N. Meidinger, G. Metzner, P. Predehl, C. Reppin, L. Strüder, J. Trümper, C. Zanthier, E. Kendziorra, R. Staubert, V. Radeka, P. Rehak, G. Bertuccio, E. Gatti, A. Longoni, A. Pullia, and M. Sampietro, "The pn-CCD on-chip electronics," *Nuclear Instruments and Methods in Physics Research Section A: Accelerators, Spectrometers, Detectors and Associated Equipment*, vol. 326, no. 1-2, pp. 85–91, 1993.
- [50] M. Campbell, E. Heijne, G. Meddeler, E. Pernigotti, and W. Snoeys, "A readout

- chip for a 64×64 pixel matrix with 15-bit single photon counting,” *IEEE Transactions on Nuclear Science*, vol. 45, no. 3, pp. 751–753, 1998.
- [51] C. Brönnimann, R. Baur, E. F. Eikenberry, S. Kohout, M. Lindner, B. Schmitt, and R. Horisberger, “A pixel read-out chip for the PILATUS project,” *Nuclear Instruments and Methods in Physics Research Section A: Accelerators, Spectrometers, Detectors and Associated Equipment*, vol. 465, no. 1, pp. 235–239, 2001.
- [52] M. C. Peckerar, W. D. Baker, and D. J. Nagel, “X-ray sensitivity of a charge-coupled-device array,” *Journal of Applied Physics*, vol. 48, no. 6, pp. 2565–2569, 1977.
- [53] M. C. Peckerar, D. H. McCann, and L. Yu, “X-ray imaging with a charge-coupled device fabricated on a high-resistivity silicon substrate,” *Applied Physics Letters*, vol. 39, no. 1, pp. 55–57, 1981.
- [54] M. G. Vasin, Y. Ignatiev, A. E. Lakhtikov, A. P. Morovov, and V. V. Nazarov, “Energy-resolved X-ray imaging,” *Spectrochimica Acta Part B: Atomic Spectroscopy*, vol. 62, no. 6-7, pp. 648–653, 2007.
- [55] M. Alfeld, K. Janssens, A. Sasov, X. Liu, A. Kostenko, K. Rickers-Appel, G. Falkenberg, M. Denecke, and C. T. Walker, “The Use Of Full-Field XRF For Simultaneous Elemental Mapping,” in *X-ray optics and microanalysis: Proceedings of the 20th International Congress*, AIP Conference Proceedings, pp. 111–118, AIP, 2010.
- [56] F. P. Romano, C. Caliri, L. Cosentino, S. Gammino, L. Giuntini, D. Mascali, L. Neri, L. Pappalardo, F. Rizzo, and F. Taccetti, “Macro and micro full field x-ray fluorescence with an X-ray pinhole camera presenting high energy and high spatial resolution,” *Analytical chemistry*, vol. 86, no. 21, pp. 10892–10899, 2014.
- [57] G. C. Holst, *CCD Arrays Cameras and Displays*. JCD Publishing, 2nd ed., 1998.
- [58] E. Miyata, M. Miki, J. Hiraga, H. Kouno, K. Yasui, H. Tsunemi, K. Miyaguchi, and K. Yamamoto, “Application of the Mesh Experiment for the Back-Illuminated Charge-Coupled Device: I. Experiment and the Charge Cloud Shape,” *Jpn. J. Appl. Phys. (Japanese Journal of Applied Physics)*, vol. 41, no. Part 1, No. 9, pp. 5827–5834, 2002.
- [59] A. Abboud, S. Send, N. Pashniak, W. Leitenberger, S. Ihle, M. Huth, R. Hartmann, L. Strüder, and U. Pietsch, “Sub-pixel resolution of a pnCCD for X-ray white beam applications,” *Journal of Instrumentation*, vol. 8, no. 05, p. P05005, 2013.
- [60] G. Ghiringhelli, A. Piazzalunga, C. Dallera, G. Trezzi, L. Braicovich, T. Schmitt, V. N. Strocov, R. Betemps, L. Patthey, X. Wang, and M. Grioni, “SAXES, a high resolution spectrometer for resonant x-ray emission in the 400–1600 eV energy

- range,” *Review of Scientific Instruments*, vol. 77, no. 11, p. 113108, 2006.
- [61] D. J. Hall, M. Soman, J. Tutt, N. Murray, A. Holland, T. Schmitt, J. Raabe, V. N. Strocov, and B. Schmitt, “Improving the resolution in soft X-ray emission spectrometers through photon-counting using an Electron Multiplying CCD,” *Journal of Instrumentation*, vol. 7, no. 01, pp. C01063–C01063, 2012.
- [62] D. Lawrence, P. O’Connor, J. Frank, and P. Takacs, “Model-independent Characterization of Charge Diffusion in Thick Fully Depleted CCDs,” *Publications of the Astronomical Society of the Pacific*, vol. 123, no. 907, pp. 1100–1106, 2011.
- [63] J. Hiraga, H. Tsunemi, K. Yoshita, E. Miyata, and M. Ohtani, “How Big Are Charge Clouds inside the Charge-Coupled Device Produced by X-Ray Photons?,” *Jpn. J. Appl. Phys. (Japanese Journal of Applied Physics)*, vol. 37, no. Part 1, No. 8, pp. 4627–4631, 1998.
- [64] A. Amorese, G. Dellea, L. Braicovich, and G. Ghiringhelli, “Enhancing spatial resolution of soft x-ray CCD detectors by single-photon centroid determination,” *ArXiv e-prints*, 1410.1587, 2014.
- [65] J. Szlachetko, J.-C. Dousse, J. Hoszowska, M. Berset, W. Cao, M. Szlachetko, and M. Kavcic, “Relative detection efficiency of back- and front-illuminated charge-coupled device cameras for X-rays between 1 keV and 18 keV,” *The Review of scientific instruments*, vol. 78, no. 9, p. 093102, 2007.
- [66] K. C. Gendreau, *X-ray CCDs for Space Applications: Calibration, Radiation Hardness, and Use for Measuring the Spectrum of the Cosmic X-ray Background*. Dissertation, Massachusetts Institute of Technology, Berlin, 1995.
- [67] J. S. Asvestas and D. C. Englund, “Computing the solid angle subtended by a planar figure,” *Optical Engineering*, vol. 33, no. 12, p. 4055, 1994.
- [68] F. Förste, *Winkelkalibrierung eines Aufbaus zur Röntgenoreszenzspektroskopie unter streifenden Detektionswinkel für Elementtiefenprofilmessungen*. Bachelor’s thesis, Technical University of Berlin, Berlin, 2015.
- [69] W. H. Press, S. A. Teukolsky, W. T. Vetterling, and B. P. Flannery, *Numerical recipes: The art of scientific computing*. Cambridge: Cambridge Univ. Press, 3. ed. ed., 2007.
- [70] P. R. Bevington and D. K. Robinson, *Data reduction and error analysis for the physical sciences*. Boston, Mass.: McGraw-Hill, 3. ed. ed., 2003.
- [71] M. A. Branch, T. F. Coleman, and Y. Li, “A Subspace, Interior, and Conjugate Gradient Method for Large-Scale Bound-Constrained Minimization Problems,” *SIAM Journal on Scientific Computing*, vol. 21, no. 1, pp. 1–23, 1999.
- [72] The Scipy community, “<http://scipy.github.io/devdocs/generated/scipy.optimize.html>.

- least_squares.html#scipy.optimize.least_squares,” 05/14/2017.
- [73] J. Falta, T. Möller, and F. Beckmann, *Forschung mit Synchrotronstrahlung: Eine Einführung in die Grundlagen und Anwendungen*. Studium, Wiesbaden: Vieweg + Teubner, 1. aufl. ed., 2010.
- [74] A. Gianoncelli, B. Kaulich, R. Alberti, T. Klatka, A. Longoni, A. de Marco, A. Marcello, and M. Kiskinova, “Simultaneous soft X-ray transmission and emission microscopy,” *Nuclear Instruments and Methods in Physics Research Section A: Accelerators, Spectrometers, Detectors and Associated Equipment*, vol. 608, no. 1, pp. 195–198, 2009.
- [75] K. V. Kaznatcheev, C. Karunakaran, U. D. Lanke, S. G. Urquhart, M. Obst, and A. P. Hitchcock, “Soft X-ray spectromicroscopy beamline at the CLS: Commissioning results,” *Nuclear Instruments and Methods in Physics Research Section A: Accelerators, Spectrometers, Detectors and Associated Equipment*, vol. 582, no. 1, pp. 96–99, 2007.
- [76] M. Muller, F.-C. Kuhl, P. Grossmann, P. Vrba, and K. Mann, “Emission properties of ns and ps laser-induced soft x-ray sources using pulsed gas jets,” *Optics express*, vol. 21, no. 10, pp. 12831–12842, 2013.
- [77] B. A. M. Hansson and H. M. Hertz, “Liquid-jet laser–plasma extreme ultraviolet sources: From droplets to filaments,” *Journal of Physics D: Applied Physics*, vol. 37, no. 23, pp. 3233–3243, 2004.
- [78] F. Zamponi, Z. Ansari, C. Korff Schmising, P. Rothhardt, N. Zhavoronkov, M. Woerner, T. Elsaesser, M. Bargheer, T. Trobitzsch-Ryll, and M. Haschke, “Femtosecond hard X-ray plasma sources with a kilohertz repetition rate,” *Applied Physics A*, vol. 96, no. 1, pp. 51–58, 2009.
- [79] I. Mantouvalou, K. Witte, D. Grötzsch, M. Neitzel, S. Günther, J. Baumann, R. Jung, H. Stiel, B. Kannegießer, and W. Sandner, “High average power, highly brilliant laser-produced plasma source for soft X-ray spectroscopy,” *The Review of scientific instruments*, vol. 86, no. 3, p. 035116, 2015.
- [80] K. Witte, *Röntgenabsorptionsspektroskopie mit einer Laser-Plasma-Quelle im L-Kantenbereich von Übergangsmetallen*. Master’s thesis, Technical University of Berlin, Berlin, 2012.
- [81] K. Witte, *Einzelschuss Röntgenabsorptionsspektroskopie an organischen Molekülen*. PhD thesis, Technische Universität, Berlin, 2017.
- [82] J. Baumann, *Charakterisierung eines Labor-Röntgenmikroskops und erste Anwendungen*. Master’s Thesis, Technische Universität, Berlin, 2012.
- [83] I. Mantouvalou, K. Witte, W. Martyanov, A. Jonas, D. Grötzsch, C. Streeck,

- H. Löchel, I. Rudolph, A. Erko, H. Stiel, and B. Kanngießer, “Single shot near edge x-ray absorption fine structure spectroscopy in the laboratory,” *Applied Physics Letters*, vol. 108, no. 20, p. 201106, 2016.
- [84] J. Baumann, C. Herzog, M. Spanier, D. Grötzsch, L. Lühl, K. Witte, A. Jonas, S. Günther, F. Förste, R. Hartmann, M. Huth, D. Kalok, D. Steigenhöfer, M. Krämer, T. Holz, R. Dietsch, L. Strüder, B. Kanngießer, and I. Mantouvalou, “Laboratory Setup for Scanning-Free Grazing Emission X-ray Fluorescence,” *Anal. Chem.*, vol. 89, no. 3, pp. 1965–1971, 2017.
- [85] K. Bethke, *Thermoelectric nano films*. Diploma thesis, Humboldt-Universität zu Berlin, Berlin, 2014.
- [86] F. Senf, U. Flechsig, F. Eggenstein, W. Gudat, R. Klein, H. Rabus, and G. Ulm, “A plane-grating monochromator beamline for the PTB undulators at BESSY II,” *Journal of synchrotron radiation*, vol. 5, no. Pt 3, pp. 780–782, 1998.
- [87] B. Beckhoff, R. Fliegauf, G. Ulm, J. Weser, G. Pepponi, C. Streli, P. Wobrauschek, T. Ehmann, L. Fabry, S. Pahlke, B. Kanngießer, and W. Malzer, “TXRF Analysis of Low Z Elements and TXRF-NEXAFS Speciation of Organic Contaminants on Silicon Wafer Surfaces Excited by Monochromatized Undulator Radiation,” *Solid State Phenomena*, vol. 92, pp. 165–170, 2003.
- [88] P. W. Hönicke, *Charakterisierung nanoskaliger Schichtstapel durch eine Kombination aus referenzprobenfreier Röntgenspektroskopie unter streifendem Einfall und der Röntgenreflektometrie*. Dissertation, Technische Universität, Berlin, 2016.
- [89] B. Pollakowski, *Entwicklung und Validierung der Methode GIXRF-NEXAFS zur Analyse von tief vergraben Nanoschichtsystemen*. Dissertation, Technische Universität, Berlin, 2011.
- [90] M. Krumrey, “Design of a four-crystal monochromator beamline for radiometry at BESSY II,” *Journal of synchrotron radiation*, vol. 5, no. Pt 1, pp. 6–9, 1998.
- [91] M. Krumrey and G. Ulm, “High-accuracy detector calibration at the PTB four-crystal monochromator beamline,” *Nuclear Instruments and Methods in Physics Research Section A: Accelerators, Spectrometers, Detectors and Associated Equipment*, vol. 467-468, pp. 1175–1178, 2001.
- [92] W. Görner, M. P. Hentschel, B. R. Müller, H. Riesemeier, M. Krumrey, G. Ulm, W. Diete, U. Klein, and R. Frahm, “BAMline: The first hard X-ray beamline at BESSY II,” *Nuclear Instruments and Methods in Physics Research Section A: Accelerators, Spectrometers, Detectors and Associated Equipment*, vol. 467-468, pp. 703–706, 2001.
- [93] A. Rack, S. Zabler, B. R. Müller, H. Riesemeier, G. Weidemann, A. Lange,

- J. Goebbels, M. Hentschel, and W. Görner, "High resolution synchrotron-based radiography and tomography using hard X-rays at the BAMline (BESSY II)," *Nuclear Instruments and Methods in Physics Research Section A: Accelerators, Spectrometers, Detectors and Associated Equipment*, vol. 586, no. 2, pp. 327–344, 2008.
- [94] M. Kolbe, B. Beckhoff, M. Krumrey, and G. Ulm, "Thickness determination for Cu and Ni nanolayers: Comparison of completely reference-free fundamental parameter-based X-ray fluorescence analysis and X-ray reflectometry," *Spectrochimica Acta Part B: Atomic Spectroscopy*, vol. 60, no. 4, pp. 505–510, 2005.
- [95] J. Lubeck, B. Beckhoff, R. Fliegauf, I. Holfelder, P. Hönicke, M. Müller, B. Polakowski, F. Reinhardt, and J. Weser, "A novel instrument for quantitative nanoanalytics involving complementary X-ray methodologies," *The Review of scientific instruments*, vol. 84, no. 4, p. 045106, 2013.
- [96] P. Eisenberger, P. M. Platzman, and H. Winick, "Resonant x-ray Raman scattering studies using synchrotron radiation," *Physical Review B*, vol. 13, no. 6, pp. 2377–2380, 1976.
- [97] M. Müller, B. Beckhoff, G. Ulm, and B. Kanngießer, "Absolute determination of cross sections for resonant Raman scattering on silicon," *Physical Review A*, vol. 74, no. 1, 2006.
- [98] H. A. Kramers, "XCIII. On the theory of X-ray absorption and of the continuous X-ray spectrum," *Philosophical Magazine Series 6*, vol. 46, no. 275, pp. 836–871, 1923.
- [99] M. O. Krause, "Atomic radiative and radiationless yields for K and L shells," *Journal of Physical and Chemical Reference Data*, vol. 8, no. 2, pp. 307–327, 1979.
- [100] G. Zschornack, *Handbook of X-Ray Data*. Berlin, Heidelberg: Springer-Verlag Berlin Heidelberg, 2006.
- [101] T. L. Barr, "An ESCA study of the termination of the passivation of elemental metals," *The Journal of Physical Chemistry*, vol. 82, no. 16, pp. 1801–1810, 1978.
- [102] S. Eisebitt, T. Böske, J.-E. Rubensson, and W. Eberhardt, "Determination of absorption coefficients for concentrated samples by fluorescence detection," *Physical Review B*, vol. 47, no. 21, pp. 14103–14109, 1993.
- [103] A. Iida and T. Noma, "Correction of the Self-Absorption Effect in Fluorescence X-Ray Absorption Fine Structure," *Jpn. J. Appl. Phys. (Japanese Journal of Applied Physics)*, vol. 32, no. Part 1, No. 6A, pp. 2899–2902, 1993.
- [104] P. Pfalzer, J.-P. Urbach, M. Klemm, S. Horn, M. L. denBoer, A. I. Frenkel, and J. P. Kirkland, "Elimination of self-absorption in fluorescence hard-x-ray absorp-

- tion spectra,” *Physical Review B*, vol. 60, no. 13, pp. 9335–9339, 1999.
- [105] R. Carboni, S. Giovannini, G. Antonioli, and F. Boscherini, “SelfAbsorption Correction Strategy for Fluorescence Yield Soft Xray Near Edge Spectra,” *Physica Scripta*, p. 986, 2005.
- [106] M. Grioni, J. B. Goedkoop, R. Schoorl, de Groot, F. M. F., J. C. Fuggle, F. Schäfers, E. E. Koch, G. Rossi, J.-M. Esteva, and R. C. Karnataka, “Studies of copper valence states with Cu L3 x-ray-absorption spectroscopy,” *Physical Review B*, vol. 39, no. 3, pp. 1541–1545, 1989.
- [107] A. Nilsson, D. Nordlund, I. Waluyo, N. Huang, H. Ogasawara, S. Kaya, U. Bergmann, L.-Å. Näslund, H. Öström, P. Wernet, K. J. Andersson, T. Schiros, and L. Pettersson, “X-ray absorption spectroscopy and X-ray Raman scattering of water and ice; an experimental view,” *Journal of Electron Spectroscopy and Related Phenomena*, vol. 177, no. 2-3, pp. 99–129, 2010.
- [108] A. Sharma, M. Varshney, J. Park, T.-K. Ha, K.-H. Chae, and H.-J. Shin, “XANES, EXAFS and photocatalytic investigations on copper oxide nanoparticles and nanocomposites,” *RSC Adv*, vol. 5, no. 28, pp. 21762–21771, 2015.
- [109] M. Grioni, J. F. van Acker, M. T. Czyżyk, and J. C. Fuggle, “Unoccupied electronic structure and core-hole effects in the x-ray-absorption spectra of Cu₂O,” *Physical Review B*, vol. 45, no. 7, pp. 3309–3318, 1992.
- [110] M. Kolbe and P. Hönicke, “Fundamental parameters of Zr and Ti for a reliable quantitative X-ray fluorescence analysis,” *X-Ray Spectrometry*, vol. 44, no. 4, pp. 217–220, 2015.
- [111] M. Spanier, C. Herzog, D. Grötzsch, F. Kramer, I. Mantouvalou, J. Lubeck, J. Weser, C. Streeck, W. Malzer, B. Beckhoff, and B. Kanngießer, “A flexible setup for angle-resolved X-ray fluorescence spectrometry with laboratory sources,” *The Review of scientific instruments*, vol. 87, no. 3, p. 035108, 2016.
- [112] A. Jonas, *Komponentenentwicklung für Röntgenfluoreszenzanalyse unter streifendem Einfall mittels einer Laser-Plasma-Quelle*. Master’s thesis, Technical University of Berlin, Berlin, 2015.
- [113] R. Reusch, *Justage und Charakterisierung von doppelt gekrümmten Multilayer-Optiken an einer Laser-Plasma-Quelle*. Bachelor’s thesis, Technical University of Berlin, Berlin, 2017.
- [114] L. Bauer, *Winkelkalibrierung eines Scan-freien Labormessplatzes für Tiefen\auflösende Röntgenfluoreszenzanalyse*. Bachelor’s thesis, Technical University of Berlin, Berlin, 2016.
- [115] Y. Kayser, D. Banaś, W. Cao, J.-C. Dousse, J. Hoszowska, P. Jagodziński,

- M. Kavčič, A. Kubala-Kukuš, S. Nowak, M. Pajek, and J. Szlachetko, “Depth profiles of Al impurities implanted in Si wafers determined by means of the high-resolution grazing emission X-ray fluorescence technique,” *Spectrochimica Acta Part B: Atomic Spectroscopy*, vol. 65, no. 6, pp. 445–449, 2010.
- [116] L. Strüder, “High-resolution imaging X-ray spectrometers,” *Nuclear Instruments and Methods in Physics Research Section A: Accelerators, Spectrometers, Detectors and Associated Equipment*, vol. 454, no. 1, pp. 73–113, 2000.
- [117] S. Staeck, *Detection optimization for grazing emission fluorescence spectroscopy with a soft X-ray laboratory source*. Master’s thesis, Technical University of Berlin, Berlin, 2017.
- [118] V. A. Solé, E. Papillon, M. Cotte, P. Walter, and J. Susini, “A multiplatform code for the analysis of energy-dispersive X-ray fluorescence spectra,” *Spectrochimica Acta Part B: Atomic Spectroscopy*, vol. 62, no. 1, pp. 63–68, 2007.
- [119] A. Kubec, K. Melzer, J. Gluch, S. Niese, S. Braun, J. Patommel, M. Burghammer, and A. Leson, “Point focusing with flat and wedged crossed multilayer Laue lenses,” *Journal of synchrotron radiation*, vol. 24, no. Pt 2, pp. 413–421, 2017.
- [120] N. F. Brejnholt, R. Soufli, M.-A. Descalle, M. Fernandez-Perea, F. E. Christensen, A. C. Jakobsen, V. Honkimaki, and M. J. Pivovaroff, “Demonstration of multilayer reflective optics at photon energies above 0.6 MeV,” *Optics express*, vol. 22, no. 13, pp. 15364–15369, 2014.
- [121] Y.-I. Chen, Z.-T. Zheng, W. Kai, and Y.-R. Huang, “Oxidation behavior of Ru–Al multilayer coatings,” *Applied Surface Science*, vol. 406, pp. 1–7, 2017.
- [122] Y. Ogata, T. Shimura, M. Ryu, and Y. Iwazaki, “X-ray absorption fine structure analysis of molybdenum added to BaTiO₃ -based ceramics used for multilayer ceramic capacitors,” *Jpn. J. Appl. Phys. (Japanese Journal of Applied Physics)*, vol. 56, no. 4, p. 041101, 2017.
- [123] Y. Tu, Y. Yuan, K. Le Guen, J. M. André, J. Zhu, Z. Wang, F. Bridou, A. Giglia, and P. Jonnard, “X-ray fluorescence induced by standing waves in the grazing-incidence and grazing-exit modes: study of the Mg-Co-Zr system,” *Journal of synchrotron radiation*, vol. 22, no. 6, pp. 1419–1425, 2015.
- [124] A. Haase, S. Bajt, P. Honicke, V. Soltwisch, and F. Scholze, “Multiparameter characterization of subnanometre Cr/Sc multilayers based on complementary measurements,” *Journal of applied crystallography*, vol. 49, no. Pt 6, pp. 2161–2171, 2016.
- [125] G. Sberveglieri, “Recent developments in semiconducting thin-film gas sensors,” *Sensors and Actuators B: Chemical*, vol. 23, no. 2-3, pp. 103–109, 1995.

- [126] M. Kormunda, D. Fischer, A. Hertwig, U. Beck, M. Sebik, and N. Esser, “Preparation of pulsed DC magnetron deposited Fe-doped SnO₂ coatings,” *physica status solidi (a)*, vol. 213, no. 9, pp. 2303–2309, 2016.
- [127] W. Kossel, V. Loeck, and H. Voges, “Die Richtungsverteilung der in einem Kristall entstandenen charakteristischen Röntgenstrahlung,” *Z. Physik (Zeitschrift für Physik)*, vol. 94, no. 1-2, pp. 139–144, 1935.
- [128] X. Jianc, T. H. Metzger, and J. Peisl, “A Novel Mechanism for the Kossel Effect Due to Coherent X-Ray Scattering in Periodic Amorphous Multilayers,” *physica status solidi (b)*, vol. 179, no. 2, pp. 299–306, 1993.
- [129] G. Faigel, G. Bortel, and M. Tegze, “Experimental phase determination of the structure factor from Kossel line profile,” *Scientific reports*, vol. 6, p. 22904, 2016.
- [130] S. Send, A. Abboud, R. Hartmann, M. Huth, W. Leitenberger, N. Pashniak, J. Schmidt, L. Strüder, and U. Pietsch, “Characterization of a pnCCD for applications with synchrotron radiation,” *Nuclear Instruments and Methods in Physics Research Section A: Accelerators, Spectrometers, Detectors and Associated Equipment*, vol. 711, pp. 132–142, 2013.
- [131] O. Scharf, S. Ihle, I. Ordavo, V. Arkadiev, A. Bjeoumikhov, S. Bjeoumikhova, G. Buzanich, R. Gubzhokov, A. Gunther, R. Hartmann, M. Kuhbacher, M. Lang, N. Langhoff, A. Liebel, M. Radtke, U. Reinholz, H. Riesemeier, H. Soltau, L. Struder, A. F. Thunemann, and R. Wedell, “Compact pnCCD-based X-ray camera with high spatial and energy resolution: a color X-ray camera,” *Analytical chemistry*, vol. 83, no. 7, pp. 2532–2538, 2011.
- [132] R. Jenkins, R. W. Gould, and D. Gedcke, *Quantitative X-ray spectrometry*. New York: Dekker, (1981).
- [133] G. Tölg and R. Klockenkämper, “The role of total-reflection X-ray fluorescence in atomic spectroscopy,” *Spectrochimica Acta Part B: Atomic Spectroscopy*, vol. 48, no. 2, pp. 111–127, 1993.
- [134] P. Debye, “Interferenz von Röntgenstrahlen und Wärmebewegung,” *Annalen der Physik*, vol. 348, no. 1, pp. 49–92, 1913.
- [135] M. Krämer, *AXO DRESDEN GmbH*. personal communication, 02-28-2017.
- [136] J. H. Tutt, A. D. Holland, N. J. Murray, R. D. Harriss, D. J. Hall, and M. Soman, “Electron-multiplying CCDs for future soft X-ray spectrometers,” *Journal of Instrumentation*, vol. 7, no. 02, pp. C02031–C02031, 2012.
- [137] D. Eisenhauer, B. Pollakowski, J. Baumann, V. Preidel, D. Amkreutz, B. Rech, F. Back, E. Rudigier-Voigt, B. Beckhoff, B. Kanngießer, and C. Becker, “Grazing incidence X-ray fluorescence analysis of buried interfaces in periodically structured

BIBLIOGRAPHY

- crystalline silicon thin-film solar cells,” *physica status solidi (a)*, vol. 212, no. 3, pp. 529–534, 2015.
- [138] P. Hönicke, B. Beckhoff, M. Kolbe, S. List, T. Conard, and H. Struyff, “Depth-profiling of vertical sidewall nanolayers on structured wafers by grazing incidence X-ray flourescence,” *Spectrochimica Acta Part B: Atomic Spectroscopy*, vol. 63, no. 12, pp. 1359–1364, 2008.

Teile dieser Arbeit wurden auf mehreren nationalen und internationalen Konferenzen, sowie in der nachfolgenden Veröffentlichung präsentiert.

- Baumann, J.; Herzog, C.; Spanier, M.; Grötzsch, D.; Lühl, L.; Witte, K.; Jonas, A.; Günther, S.; Förste, F.; Hartmann, R.; Huth, M.; Kalok, D.; Steigenhöfer, D.; Krämer, M.; Holz, T.; Dietsch, R.; Strüder, L.; Kanngießer, B.; Mantouvalou, I. (2017): *Laboratory Setup for Scanning-Free Grazing Emission X-ray Fluorescence*. In: Anal. Chem. 89 (3), S. 1965-1971. DOI: 10.1021/acs.analchem.6b04449.

Für die folgenden Veröffentlichungen, die kein Bestandteil dieser Arbeit sind, liegt eine Co-Autorenschaft vor.

- Eisenhauer, D.; Pollakowski, B.; Baumann, J.; Preidel, V.; Amkreutz, D.; Rech, B.; Back, F.; Rudigier-Voigt, E.; Beckhoff, B.; Kanngießer, B.; Becker, C. (2015): *Grazing incidence X-ray fluorescence analysis of buried interfaces in periodically structured crystalline silicon thin-film solar cells*. In: Phys. Status Solidi A 212 (3), S. 529-534. DOI: 10.1002/pssa.201400112.
- Mantouvalou, I.; Witte, K.; Grötzsch, D.; Neitzel, M.; Günther, S.; Baumann, J.; Jung, R.; Stiel, H.; Kanngießer, B.; Sandner, W. (2015): *High average power, highly brilliant laser-produced plasma source for soft X-ray spectroscopy*. In: The Review of scientific instruments 86 (3), S. 35116. DOI: 10.1063/1.4916193.

Danksagung

Ein ereignisreicher Lebensabschnitt ist abgeschlossen und viel Kraft, Zeit und Mühen, aber auch Ideen, Spaß und Freude sind in diese Arbeit eingeflossen. Und das nicht allein von mir, sondern von all den Personen, die mich bei diesem Projekt direkt und indirekt unterstützt haben. Dafür gilt allen mein herzlichster Dank.

An erster Stelle möchte ich Birgit Kanngießer, ohne die nicht einmal der Gedanke an diese Arbeit in mir gekeimt wäre, für die Betreuung meiner Promotion danken. Danke für dein Vertrauen in mich, diese Promotion bestreiten zu können. Nur durch deinen Schubser in Richtung SALSA, noch rechtzeitig vor meiner Reise nach Südamerika, konnte ich, nach abenteuerlichen TOEFL-Tests in Peru und Skypekonferenzen aus Bolivien, das Stipendium ergattern, welches die Grundlage meiner Promotion werden sollte. Aber auch darüber hinaus danke ich dir für dein stets offenes Ohr, deine ehrliche Meinung und dein Bestreben in anderen das Nach- und Hinterfragen zu fördern.

Auch Herr Professor Rademann möchte ich für die Ermöglichung und Betreuung dieser Arbeit danken. Ich werde mit Freude und einem Lächeln an die teils ausschweifenden aber interessanten und manchmal persönlichen Gespräche mit Ihnen zurückdenken.

Ein ganz herzliches Dankeschön gilt auch Dr. Ioanna Mantouvalou, für das Näherbringen der Laserplasmaquelle, die gemeinsamen und lehrreichen Arbeiten im Labor und das unermüdliche und stets mit einem Lächeln vollzogene Gegenlesen meiner Arbeit. Auch für deinen Rat, deine Unterstützung und dein Verständnis in Bezug auf mein großes privates Projekt Familie möchte ich dir danken und bin gespannt, welche ähnlichen Mauern wir da noch erklimmen.

Beatrix Pollakowski möchte ich für die ermöglichten Strahlzeiten und deren Betreuung bei BESSY danken. Ohne dich würde ich vielleicht immernoch im Dschungel der Bürokratie und dem finsternen Wald von IDL stecken. Danke auch an Philipp Hönicke für die Diskussionen zu den nicht ganz einfachen Auswertungen der thermoelektrischen Schichten.

Kevin Bethke möchte ich für die Bereitstellung der Proben und der AFM Messungen danken, sowie dem Bestreiten gemeinsamer Strahlzeiten und WinFTM Programmierungen.

Außerdem gilt mein Dank Malte Spanier, Veronika Szwedowski, Daniel Grötzsch,

Adrian Jonas, Steffen Staech und Katharina Witte für die vielen vielen gemeinsamen spannenden und spaßigen Stunden im Labor, bei Planungen oder im Büro, sowie Wolfgang Malzer, Christian Herzog und Lars Lühl für Diskussionen und die Einführung in die xrlfupa und die xrfLibrary. Aber eigentlich müsste ich jeden einzelnen der Arbeitsgruppe Analytische Röntgenphysik hier nennen, sei es wegen fruchtbare Diskussionen, moralischem Beistand oder einfach nur für die schöne Atmosphäre. Bitte fühlt euch alle angesprochen.

Nicht zu vergessen sind außerdem Sabine Remus, Sven-Uwe Urban und das ganze Team der Feinmechanischen Werkstatt, die einen reibungslosen Ablauf in so vielen Belangen erst ermöglichen.

Sodann danke ich all den Mitarbeitern und Doktoranden der School of Analytical Sciences Adlershof. Thank you all for this interdisciplinary and intercultural experience!

Meine Freunde gehören ebenfalls an diese Stelle gesetzt, auch wenn ihre Hilfe eher passiver Natur und dadurch geprägt war, dass sie in den letzten Monaten viel auf mich verzichten mussten. Danke, dass ihr trotzdem an mich denkt und jedes Wiedersehen an der alten Verbundenheit anknüpfen kann.

Ich habe es schon einmal formuliert, meine Eltern sind die Besten. Der Rückhalt, den ich durch euch in allen Situationen und jederzeit erfahre hat mich erst dahin gebracht, wo ich jetzt stehe. Ihr habt alles richtiggemacht und ich hoffe, dass ich das an meine Kinder weitergeben kann. Danke!

Die letzten Worte sollen meiner jungen Familie gelten. Es war nicht immer einfach, aber durch die frühe Gewöhnung an den Schlafmangel hat dieser mir in den letzten Monaten kaum noch etwas ausgemacht. Wenn ihr das mal irgendwann lesen solltet, Hannah und Leonard, ihr seid einfach großartig und ihr gebt all dem so viel Sinn. Jana liebste, ohne dich wäre diese Arbeit nicht denkbar gewesen. Danke dir, für die Zeit, die du mir gegeben hast, dein Verständnis und deine Liebe.